

### 3. SITE 896<sup>1</sup>

#### Shipboard Scientific Party<sup>2</sup>

#### HOLE 896A

**Date occupied:** 11 February 1993  
**Date departed:** 8 March 1993  
**Time on hole:** 15 days, 23 hr, 45 min  
**Position:** 1°13.006'N, 83°43.392'W  
**Bottom felt (drill-pipe measurement from rig floor, m):** 3459.0  
**Distance between rig floor and sea level (m):** 11.23  
**Water depth (drill-pipe measurement from sea level, m):** 3447.8  
**Water depth (precision depth recorder, m):** 3439.8  
**Total depth (from rig floor, m):** 3928.00  
**Penetration (m):** 469.00  
**Number of cores (including cores with no recovery):** 30  
**Total length of cored section (m):** 273.90  
**Total core recovered (m):** 73.68  
**Core recovery (%):** 26.9  
**Hard rock:**  
**Depth (mbsf):** 469.00  
**Nature:** Moderately phyric plagioclase-olivine and olivine-plagioclase basalt  
**Measured velocity (km/s):** 4.63–6.12

**Principal results:** Site 896 is located 1 km southeast of Hole 504B at a water depth of 3439.8 m (1°13.006'N, 83°43.392'W). The site is situated on a bathymetric high overlying a basement topographic high. These coincide with a local heat-flow maximum where low-temperature hydrothermal fluids are upwelling through most of the 179-m sediment section that was spot-cored during Leg 111.

Three scientific objectives were to be addressed at Site 896. The first goal was to examine local variability in volcanic stratigraphy, areal extent of laval flows, and horizontal and vertical variations in igneous geochemistry. The second goal was to examine the effects of off-axis hydrothermal activity on the basement, relating the composition of upwelling fluids (determined on Leg 111 and from a Leg 111 site survey) in a high heat-flow area to alteration of basement rocks. Physical properties and hydrogeology of the site could also be examined to test models of off-axis convection. The third goal was to drill the second of a pair of deep basement sites. Hole 504B penetrates two possible faults (at about 800 meters below seafloor [mbsf] in the lower volcanics and at 2111 mbsf in the lower dikes), whereas Site 896 is located on the inferred footwall, south of Hole 504B. Variations in alteration between uplifted and downdropped basement will be examined, as will the possible role of the fault in alteration and whether the fault may have influenced volcanism and volcanic stratigraphy. The new site also provides the opportunity for future geophysical experiments between the paired boreholes, Holes 896A and 504B.

Site 896 was occupied while waiting for fishing tools to arrive for further work at Site 504 on 11–20 February 1993, and then again 28

February–4 March and 6–7 March. Four days were devoted to setting a reentry cone and casing, eight days were spent coring, and three days were relegated for logging.

Basement was first encountered in Hole 896A at 179 mbsf where rubble material was felt by the drill bit, and the hole was cored from 195.1 to 469 mbsf, which is 290 m into basement. Mainly pillow basalts and minor massive flows and breccias were recovered in 30 cores for an average recovery of 26.9% (73.68 m of rock). Igneous lithology and magnetic and physical properties suggest that the core can be divided into upper and lower sections.

Four types of volcanic units were identified: massive basalt, pillow lavas, breccias, and dikes. Massive units comprise about 38% of the drilled section and lack chilled margins, have a larger, more uniform grain size, and may be lava flows, or possibly interiors of very large pillows. Two dikes, identified by steeply dipping (74°–78°) margins chilled against host rock, were recovered. The dike margins are characterized by a lack of variolitic textures and exhibit a different series of quench crystallization textures than pillow margins. Pillow lavas comprise approximately 57% of the drilled section and are characterized by chilled and/or glassy margins and relatively fine grain size.

Breccias comprise 5% of the drilled section and are of several types:

1. Hyaloclastites formed on the sea floor by fragmentation of glassy pillow rims and consist of clasts of volcanic glass in a matrix of clay and altered glass.
2. A second type of breccia that consists of millimeter- to centimeter-sized clasts of basalt and less common glass fragments, cemented by carbonate and/or clay minerals. Basalt clasts show evidence for alteration, oxidation, and vein development prior to cementation. Such breccias may have formed as talus at the base of a slope or within fissures in the basement.
3. The third type of breccia is characterized by a "jigsaw puzzle" fabric where the various clasts can be fit back together, and are cemented by carbonate and clay matrix and veins. These breccias probably formed nearly in situ beneath the seafloor by fragmentation in the uppermost crust during extension.

The basalts are sparsely to highly phyric tholeiites. Fifty lithologic units were recognized, of which all but two are sparsely to highly phyric plagioclase-olivine basalts or olivine-plagioclase basalts, both commonly containing spinel. The two exceptions are moderately olivine-phyric basalts. The volcanic section can be divided into upper and lower sections: plagioclase-olivine phyric basalts make up 90% of the units in the upper basement (195.1–390.1 mbsf), whereas olivine-plagioclase phyric lavas make up 72% of the lower section (390.1–469 mbsf). Clinopyroxene is also present as a phenocryst phase from 353.1 to 392.1 mbsf. The basalts contain a variety of megacrysts and glomerocrysts, including plagioclase, plagioclase-olivine, plagioclase-clinopyroxene, and plagioclase-olivine-clinopyroxene.

Plagioclase phenocrysts range in size from less than 0.1 mm to more than 5 mm. Olivine phenocrysts range from less than 0.1 mm microphe-nocrysts to 5 mm megacrysts and commonly contain inclusions of glass or spinel. Clinopyroxene phenocrysts range from less than 0.5 mm to 7 mm and are partly resorbed. Spinel is a minor mineral, ranging in size from 10  $\mu$ m to 200  $\mu$ m.

The basalts are extremely depleted tholeiites, generally similar to those from nearby Hole 504B, but basalts from the upper 100 m of Hole 896A are even more depleted than rocks from Hole 504B. Chemical variations

<sup>1</sup> Alt, J.C., Kinoshita, H., Stokking, L.B., et al., 1993. *Proc. ODP, Init. Repts.*, 148: College Station, TX (Ocean Drilling Program).

<sup>2</sup> Shipboard Scientific Party is as given in the list of participants preceding the contents.

in Hole 896A in part reflect cyclic trends in fractional crystallization and phenocryst abundances. Variations in the compositions of the rocks cannot all be explained by these processes, however, suggesting that two or more magma sources may be indicated.

All of the rocks from Hole 896A are slightly (<10%) altered, except for pillow rims, where fresh glass is present. Based on comparison with other sites, the alteration is all low temperature (<100°C). A pervasive background (reducing) alteration is characterized by the gray color of the rocks and by saponite and rare pyrite replacing olivine and filling pore spaces. Plagioclase is rarely slightly replaced by saponite. Oxidative alteration effects are characterized by dark gray to yellow and red alteration halos, up to 20 mm wide, which commonly occur around smectite veins in pillow and massive basalts, but are more common in the coarser grained massive lavas. The red and yellow colors result from Fe-oxyhydroxides replacing olivine, filling interstitial space and staining the primary silicates. Diffuse pale-brown halos, a few millimeters wide, are only observed in the pillow lava samples.

Dark-green and light-green saponite are the most common veins in both pillow and massive lavas. Calcium carbonate, commonly aragonite, is present as a later phase following smectite. Analcite was observed in veins of several hand specimens, and one occurrence each of fibrous zeolite (possibly natrolite) and pyrite were observed. Most of the veins are less than 1 mm thick, but some range up to several millimeters in thickness, especially in the upper half of the core. Phillipsite is also present in the cement of the hyaloclastites where it formed after saponite and before carbonate.

Two types of veins were characterized structurally: fibrous and non-fibrous. Veins filled with blocky carbonate and/or vermicular clay have characteristics suggesting growth of crystals into open spaces. The orientation of all non-fibrous veins are clearly non-random, with a tendency toward steeper dips. These veins are common in massive lavas, and may represent steeply dipping cooling joints.

Fibrous veins are generally relatively late and formed after filling of cracks and voids by non-fibrous carbonate and clay. Textures of the fibrous veins indicate that they formed by the crack-seal mechanism caused by fluid overpressure. The dips of fibrous veins are distinct from those predicted for random planes, with shallow dips being more common.

Magnetic properties suggest that Hole 896A can be divided into two sections: an upper part above 370 mbsf; and a lower part below 370 mbsf. The boundary between the upper and lower sections is the top of a thick series of massive units. This surface may represent a hiatus in volcanic eruption, or a boundary controlling alteration.

In the upper part of the hole the intensity of natural remanence ( $J_0$ ) is relatively high ( $11.9 \pm 4.0$  A/m), the median destructive field (MDF) is high ( $22.6 \pm 12.9$  mT), and the bulk susceptibility is high ( $0.015 \pm 0.008$  SI units). Isothermal remanent magnetism (IRM) acquisition experiments indicate that the rocks generally saturate in fields less than 0.2 T, consistent with the carriers being (titano)magnetite and/or (titano)maghemite; probably very fine-grained single-domain material. These properties are common to both pillowed and massive units. Stable inclinations measured from samples from the upper part of the hole are consistent, with a mean value of  $-9.5^\circ \pm 10.4^\circ$ .

In the lower part of the hole  $J_0$  is significantly lower ( $3.9 \pm 2.5$  A/m), MDFs are lower ( $12.3 \pm 7.3$  mT), and bulk susceptibilities are higher ( $0.033 \pm 0.014$  SI units). Alternating field demagnetization often isolates 2 components: a low-coercivity phase, probably carried by (titano)magnetite and/or (titano)maghemite; and a higher coercivity phase. The presence of a small proportion of high-coercivity material in these samples is also indicated by IRM acquisition experiments. Stable inclination data exhibit a high degree of variation, which may reflect large-scale disruption of the units cored in the lower part of the hole.

Anisotropy of magnetic susceptibility (AMS) measurements reveal weak (<9%), dominantly prolate, magnetic fabrics. The maximum principal AMS axes are dominantly sub-horizontal, toward  $283^\circ$ , but it is unlikely that this represents a flow fabric.

The physical properties of most of the samples from Hole 896A are typical of moderately altered basalt: bulk densities range for the most part between 2.80 and 2.95 g/cm<sup>3</sup>; the porosities are moderately high (2%–10%); resistivities are low, ranging between 40–250 Ωm; velocities are fairly low (5.5–6.0 km/s) and thermal conductivities range between 1.6–

1.8 W/(m·K). The unusual recovery of glassy pillow margins, interpillow hyaloclastic breccias and flow breccias cemented by clays and calcite suggests that the crust at Site 896 is at least partially sealed by alteration products. While these materials have very low densities (2.2–2.7 g/cm<sup>3</sup>), velocities (3.6–4.7 km/s) and resistivities (10–20 Ωm), they are much higher than those of seawater (1.035 g/cm<sup>3</sup>; 1.5 km/s; 0.2 Ωm at room temperature) and will strongly affect the overall properties of the formation, causing  $V_p$ , density, and resistivity to rise, porosity to decrease, and heat flow to approach conductive values. There is a marked increase in scatter in  $V_p$  and thermal conductivity below 350 mbsf, which we attribute to increasingly variable alteration with depth.

Prior to the last bit run and following eight days of fishing and logging in Hole 504B, which allowed the borehole temperatures to recover from drilling somewhat, a combined temperature and geochemical log was run in Hole 896A. The measured temperature profile suggests a conductive heat flow of 275 mW/m<sup>2</sup>, and a temperature of about 50°C at the basement-sediment interface. These values are consistent with detailed surface heat flow measurements and modeling of off-axis convection in the region and are not indicative of downhole flow as occurred when Hole 504B was first drilled.

Following the last drill bit in Hole 896A, a series of logs including the sonic density tool, dual laterolog, FMS, magnetometer, and packer permeability experiments were run in Hole 896A. Two passes were made with the FMS, which provided excellent images of the borehole walls to 440 mbsf.

The BRG magnetometer was run to 438 mbsf in Hole 896A. The measured anomalies are generally large, ranging up to 5000 nT, but the bottom 30 m have rather small anomalies, <100 nT. Anomaly amplitudes imply reverse magnetization with negative inclinations, consistent with measurements on minicores and with location of the site within a reversed magnetic interval.

The packer was set at depths of 106 mbsf (in the casing), 233 mbsf, and 385 mbsf. The uppermost few tens of meters of basement appear quite permeable, much like in Hole 504B. Permeabilities decrease deeper in Hole 896A, but probably remain large enough to support off-axis circulation in the uppermost basement.

The most significant lithological differences between Sites 896 and 504 include the following: (1) the abundant breccias from Hole 896A; (2) the greater proportion of pillow units at Hole 504B; and (3) the greater proportion of massive units at Hole 896A. Clinopyroxene appears as a phenocryst phase only at depths greater than about 100 m into basement at both sites, but no detailed lithologic correlations yet exist between the two holes. The greater abundance of recovered breccias from Hole 896A, the thicker and more abundant smectite and carbonate veins in the upper half of Hole 896A, the lack of flow of bottom seawater down into Hole 896A (compared to the occurrence of such flow into Hole 504B in the past), all suggest that, although still permeable, the Site 896 section is more extensively sealed than at Site 504. This effect may be related to location of Site 896 on a basement topographic high and a heat flow maximum.

## BACKGROUND AND OBJECTIVES

After considering alternatives for drilling near Site 504 (see “Summary and Conclusions” section, Site 504 chapter), the shipboard party came to a general consensus to revisit Site 678, which is located on a small bathymetric high about 1 km southeast of Hole 504B. This new site is numbered as Site 896. It is situated on a local heat-flow maximum over a basement topographic high, where low-temperature hydrothermal fluids are upwelling through most of the 170-m sediment section that was cored during Leg 111. A reentry cone was to be set along with casing for basement drilling.

Three main scientific objectives were proposed. The first goal was to examine local variability in volcanic stratigraphy, areal extent of flows, and horizontal and vertical variations in igneous geochemistry. The second goal was to examine the effects of off-axis hydrothermal activity on the basement, relating the composition of upwelling fluids (determined on Leg 111 and from a Leg 111 site survey) in a high heat-flow area to alteration of basement rocks. Physical properties and hydrogeology of the site could also be examined to test models

of off-axis convection. The third goal was to drill the second of a pair of sites situated across a fault. Hole 504B is located on the hanging wall and penetrates two possible faults (at about 800 mbsf in the lower volcanics and at 2111 mbsf in the lower dikes), whereas Site 896 is located on the footwall, south of Hole 504B. Variations in alteration between uplifted and down-dropped basement and the role of the fault in alteration will be examined, as well as the possible influence of the fault on volcanism and volcanic stratigraphy.

### Background

Site 896 is a reoccupation of Site 678, which was cored originally as part of a contingency plan for drilling at Site 504 during ODP Leg 111. Detailed information about the site is given in Becker, Sakai, et al. (1988) and in the Site 678 site survey, which consisted of a detailed program of heat-flow measurements and sediment pore-water chem-

istry from piston cores in a 10 km × 10 km area (Langseth et al., 1988). The bathymetry of the area around Sites 896, 678, and 504 is characterized by linear east-west ridges and troughs (Fig. 1) that are primarily controlled by basement topography, which is formed by tilted fault blocks with the steeper slopes facing north (Fig. 2). Hole 504B is located on the southern slope of an asymmetric tilted fault block, whereas Site 896 is located about 1 km to the southeast, at a water depth of 3439.8 m, near the crest of a small hill that rises about 30 m above the surrounding seafloor. This hill lies near the center of a 4-km-wide trough that runs east-west through the area.

Two holes were drilled at Site 678 on Leg 111 (Becker, Sakai, et al., 1988): Hole 678A was aborted after two failures to obtain a mudline core (making it the shortest hole ever drilled by DSDP and ODP); a mudline core was recovered in Hole 678B, which was then spot-cored to basement at 170.8 m. Three sedimentary units and one basaltic unit were recognized in Hole 678B:

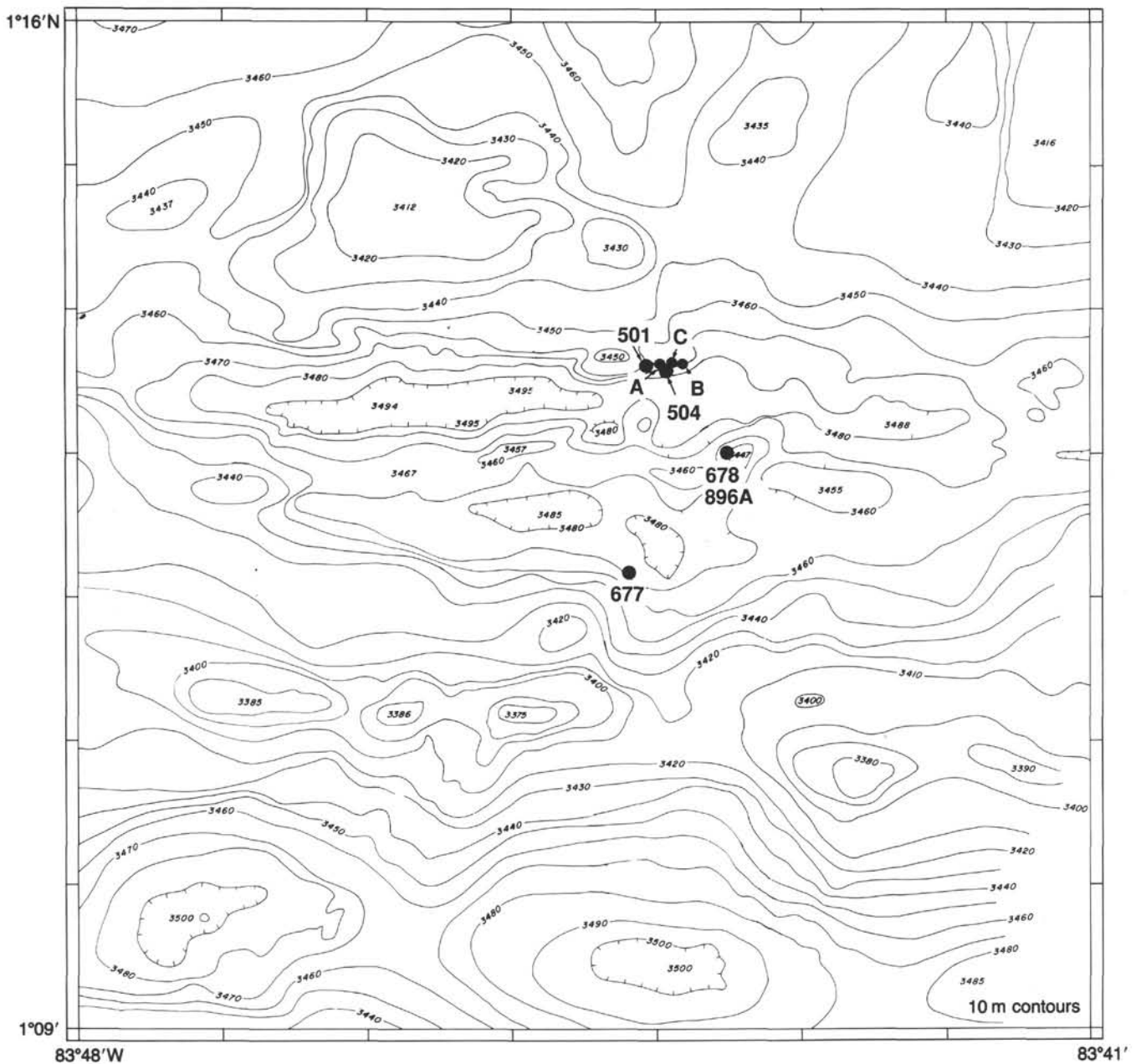


Figure 1. Contour map of seafloor bathymetry in the five site area. Locations of Holes 501, 504, 504A-C, and Sites 677, 678, and 896 are also shown. From Langseth et al. (1988).

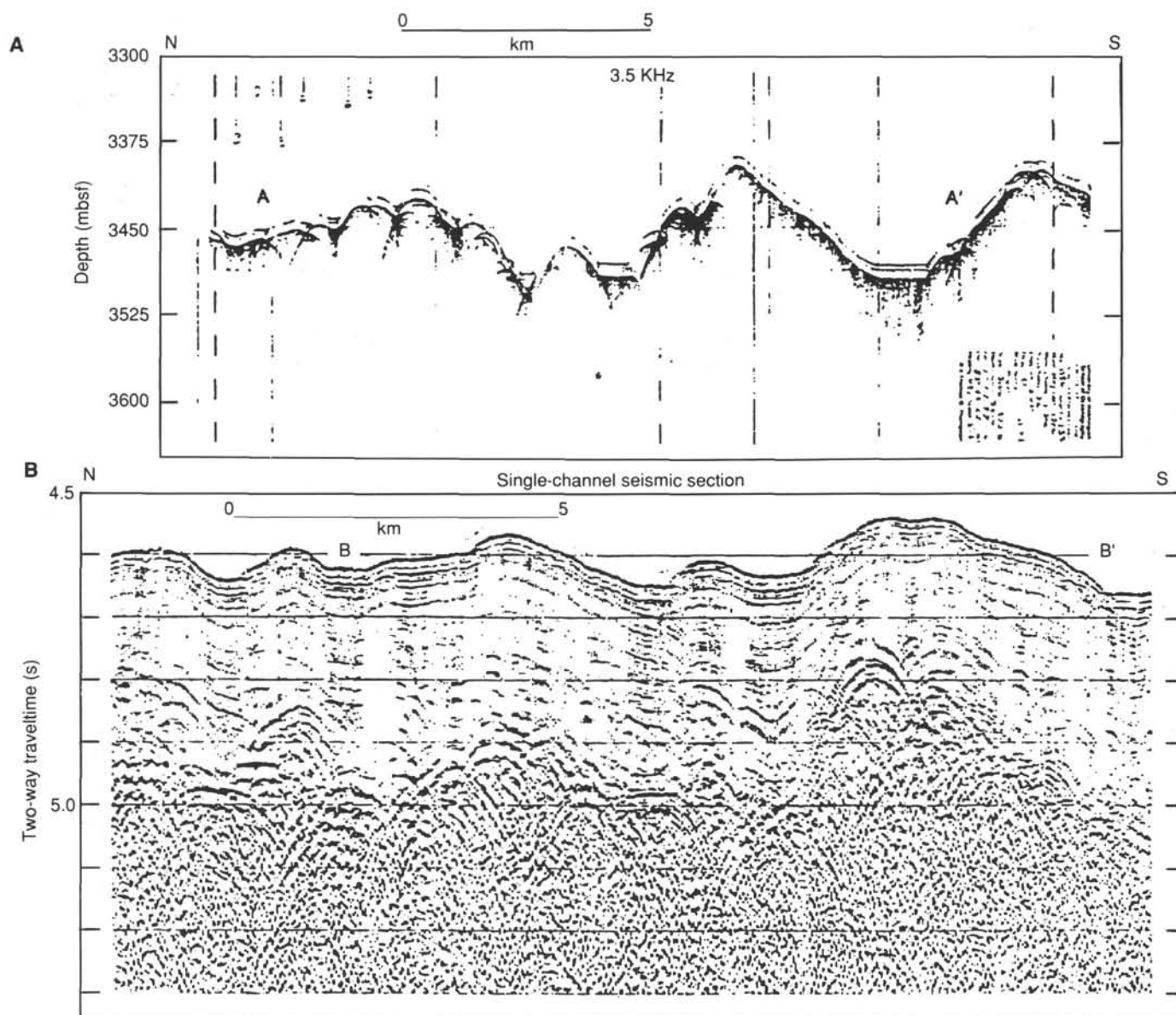


Figure 2. A. Reproduction of the 3.5-kHz record along line A-A' (see Fig. 3). B. Single-channel seismic section along line B-B' (see Fig. 3). From Langseth et al. (1988).

1. Unit I: radiolarian and diatom ooze (0–27.2 mbsf).
2. Unit II: clayey diatom-nannofossil chalk (95.5–111.8 mbsf).
3. Unit III: limestone (111.8–169.8 mbsf).
4. Unit IV: metal-rich muds intercalated with basalt pebbles and conglomerates with white calcitic material (169.8–170.1 mbsf).

Paleontologic age of the basal sediment in Hole 678B is 5.8–6.4 m.y., consistent with the ages for basement and basal sediments at Site 504 (5.9 m.y.), and indicating that the basaltic rubble penetrated at the bottom of Hole 678B is the top of the basement. Seismic refraction evidence suggests sediment thicknesses in excess of 250 m around Site 896, however, so the small bathymetric hill upon which Sites 678 and 896 are located is underlain by a basement peak or ridge. The sediment thickness is much greater (309 m) at Site 677, which is located in a low heat-flow bathymetric trough 2 km to the southwest (Fig. 1), indicating that sediment accumulation was greater in the basement troughs and less on the highs.

Heat flow in the five site area (Sites 501, 504, 677, 678, and 896) fluctuates around the value predicted for 5.9-m.y. crust (194 m/Wm<sup>2</sup>,

Parsons and Sclater, 1977; Langseth et al., 1983, 1988). General east-west undulations in seafloor heat flow roughly follow the bathymetry, with broad heat-flow lows in the troughs and smaller-area highs on the ridges (Fig. 3). Measured values of heat flow range from 166 to 395 m/Wm<sup>2</sup>, with a mean of 218 ± 36 m/Wm<sup>2</sup> (Langseth et al., 1988).

Pronounced vertical and lateral gradients occur in Ca<sup>2+</sup>, Mg<sup>2+</sup>, and alkalinity in sediment pore waters from Leg 69 and from piston cores in the area (Mottl et al., 1983; Mottl, 1989). Ca concentrations increase downward, whereas Mg exhibits a corresponding 1:1 decrease. These changes are characteristic of reaction of seawater with basaltic material within the sediments or underlying basement (Gieskes and Lawrence, 1981). There is a general positive correlation of chemical and thermal gradients in the area, and Ca<sup>2+</sup> and Mg<sup>2+</sup> profiles are convex upward at Site 678 and other high heat-flow zones. The profiles at Site 678 change exponentially with depth and asymptotically reach inferred compositions of basement fluids at about 40 mbsf (Fig. 4). These changes are consistent with the upward flow of basement waters through the sediments at velocities of a few millimeters per year. Movement of fluids at such velocities can cause

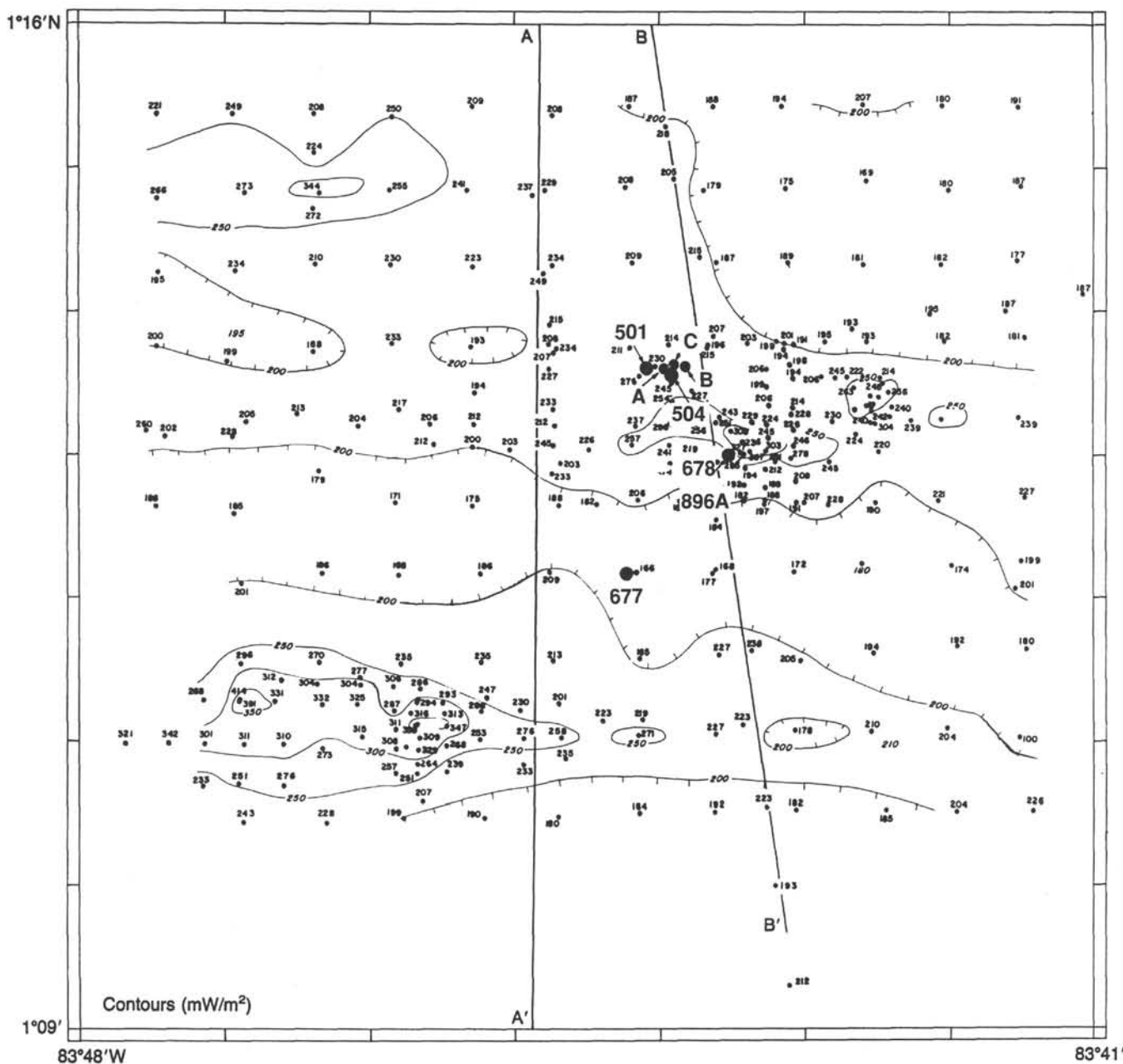


Figure 3. Map showing measured heat flow in the five site area. Drill hole locations are shown, and lines A-A' and B-B' are locations of profiles shown in Figure 2. From Becker, Sakai, et al. (1988).

significant changes in pore-water chemical gradients, but is not detected by heat-flow measurements at the relatively high ambient heat flow (Langseth et al., 1988). The compositions of interstitial waters in sediments at the nearby low heat-flow Site 677 are nearly constant in the upper 90 m, but approach the inferred basement water composition in the lowermost 40 m, suggesting the possibility that seawater is being advected downward through the sediment in heat-flow lows. The uniformity of inferred basement compositions suggests that fluids move at velocities of up to several tens of centimeters per year within the basement (Langseth et al., 1988; Mottl, 1989).

The wavelength of surface heat-flow variations in the five-site area is on the order of 4–7 km. At this wavelength, numerical models assuming a uniform permeability medium would generally find convection cells extending a kilometer or more into the crust (e.g., Fehn et al., 1983). Measurements of crustal permeability in Hole 504B reveal

very low permeabilities at depth in the sheeted dikes, however, (i.e.,  $\sim 10^{-19}$  m<sup>2</sup>) with only the uppermost 200 m of lavas exhibiting significant permeability ( $10^{-14}$  to  $10^{-13}$  m<sup>2</sup>; Anderson, Honnorez, Becker, et al., 1985). Fisher et al. (1990) demonstrate that convection can occur with large aspect ratio convection cells mainly in the uppermost 200–300 m of the crust. Convection in the model is induced by a combination of buoyancy fluxes, due to heating from below and topographic variations on the seafloor and at the basement-sediment interface.

Modeling of convection in the 3256 area (Sites 501 + 504 + 677 + 678 + 896 = 3256) predicts generally underpressured fluids within basement (Fisher et al., 1990), consistent with a measured underpressure of 8 bars in the upper 200 m of basement in Hole 504B (Anderson and Zoback, 1982). Model-predicted underpressures in the basement vary, however, and fluids could have slightly positive hot hydrostatic pressures (Fisher et al., 1990), although these are very small and

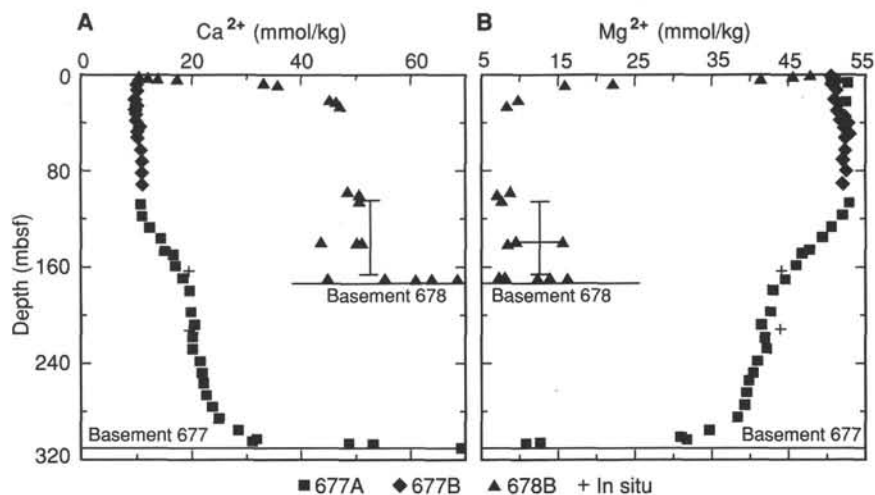


Figure 4. Concentrations of (A)  $\text{Ca}^{2+}$ , and (B)  $\text{Mg}^{2+}$  vs. depth in sedimentary sections at Sites 677 and 678. Core 678B-4W is a wash core and therefore has an uncertain depth range, as indicated by the vertical bar. From Becker, Sakai, et al. (1988).

would almost certainly be overwhelmed by the high density of cold seawater pumped into the hole during drilling, which would cause flow of bottom seawater down the casing and into the upper basement.

## OPERATIONS

On 11 February the *JOIDES Resolution* left Site 504 to set a reentry cone and to core at Site 896 while awaiting fishing equipment and a fishing consultant. Drilling objectives at this site are presented in the "Background and Objectives" section, this chapter.

### Jetting, Casing, and Reentry Cone

Prior to setting a reentry cone a test was performed to determine the depth to which the 16 in. casing could be jetted to partially support the 11-3/4-in. casing. The reentry cone was assembled while a 14-3/4-in. bit and bottom hole assembly (BHA) were run to the seafloor. A smaller truncated reentry cone that had been built several years earlier and left aboard ship was to be used. The eight panels of the cone that comprise the octagonal structure are 20 in. shorter than those in a standard reentry cone. Two sonar reflectors were installed on the rim of the cone, and the interior of the cone was painted with black and white stripes. One of the eight panels was painted completely black for orientation during re-entries.

The jetting BHA was run to the seafloor for the jet test. The 14-3/4-in. bit was jetted to 96 mbsf, with a weight on bit of 15,000 lb. The jetting assembly was returned to the rig floor, and preparations were made to run six full joints of 16-in. casing, plus one 8.37-m joint above the shoe. That configuration would achieve the maximum depth that could accommodate the BHA, putting the 14-3/4 in. bit 6 in. inside the casing shoe. The casing was latched into the reentry cone and the 14-3/4-in. drilling assembly was prepared with the double-J tool in the BHA and landed in the hanger. Hole 896A was spudded at 0350 UTC on 13 February, and the casing string was jetted in by 0815 UTC with a maximum weight on bit of 20,000 to 25,000 lb. The 16-in. casing shoe was at a depth of 86.15 mbsf, which placed the mat of the reentry cone directly on the seafloor.

The 14-3/4-in. hole was drilled initially using a tri-cone bit. Erratic torque was encountered while drilling a rubble zone from 179.0–186.5 mbsf. When the 14-3/4-in. hole was drilled to 195.1 mbsf, the drill string was pulled to the 16 in. casing shoe. After returning to bottom with no drag, 6.5 m of hole fill was reamed, and a 50-bbl sweep of high-viscosity mud was pumped. This was then displaced with mud

that was left in the hole while pulling out to run the 11-3/4-in. casing through the rubble zone.

A string of thirteen 11-3/4-in. joints of casing was designed to fit both the drilled hole depth and a stinger assembly that included three bumper subs. After reentering the hole and slowly running in the casing, fill was encountered 6.5 m off bottom. The hole was circulated and washed for an hour, but the casing did not move downwards. The ship was moved forward in DP mode for about 5 min and the casing began to slide into the hole. The 11-3/4 in. casing shoe was set at 191.46 mbsf. The running tool was released from the casing and 77 bbl of cement was pumped and displaced with seawater. Once above the reentry cone on the pipe trip out of the hole, the drill string was circulated thoroughly and tripped to the surface.

### Coring and Logging

#### Coring Run 1

An RBI C-7 coring bit with a center bit was chosen to drill the cement, plug, and shoe at the bottom of the 11-3/4-in. casing. No progress was made after 6.5 hr of drilling with a center bit, so the center bit was pulled and a core barrel was sent down the pipe. When this failed to help, the core barrel was pulled, and a chisel-type center bit was dropped into the pipe. The shoe was drilled in 70 min and a 40-bbl high-viscosity mud sweep was pumped. The chisel center bit was retrieved and the first core was drilled (Table 1). The coring parameters for the C-7 bit were 25,000 lb weight on bit, at 50 rpm. At the end of every core in Hole 896A, a 40-bbl sweep of high-viscosity mud was pumped.

Penetration rate increased from 2.42 m/hr for Core 148-896A-5R to 4.62 m/hr for Core 148-896A-8R. As in Hole 504B, however, as penetration rate increased, the percent recovery typically decreased. Rates of penetration were only 3.06 m/hr for Core 148-896A-9R and 3.05 m/hr for Core 148-896A-10R. After cutting Core 148-896A-11R, a trip was made for another bit.

#### Coring Run 2

The second coring bit used in Hole 896A was a Smith series-9 bit. This type of bit had not been chosen to drill Hole 504B because the legs of the cones were long and had insufficient gauge protection. The BHA contained a non-magnetic monel drill collar so that the hard-rock orientation system (HRO) could be used to orient alternate cores (see "Paleomagnetism" section, this chapter).

**Table 1. Coring summary, Hole 896A.**

Core	Date (1993)	Time (UTC)	Sub-bottom top (m)	Sub-bottom bottom (m)	Meters cored	Meters recovered	Percent recovered
148-896A-							
1R	16 Feb.	1430	195.1	200.9	5.8	0.78	13.4
2R	16 Feb.	1820	200.9	209.9	9.0	0.89	9.9
3R	16 Feb.	2305	209.9	218.9	9.0	1.38	15.3
4R	17 Feb.	300	218.9	228.4	9.5	1.06	11.1
5R	17 Feb.	825	228.4	237.9	9.5	4.50	47.3
6R	17 Feb.	1240	237.9	247.4	9.5	3.59	37.8
7R	17 Feb.	1645	247.4	257.1	9.7	1.21	12.5
8R	17 Feb.	2000	257.1	266.7	9.6	1.14	11.9
9R	18 Feb.	30	266.7	276.4	9.7	1.96	20.2
10R	18 Feb.	450	276.4	286.0	9.6	1.38	14.4
11R	18 Feb.	1730	286.0	295.6	9.6	3.49	36.3
12R	19 Feb.	740	295.6	305.1	9.5	1.83	19.2
13R	19 Feb.	1315	305.1	314.6	9.5	0.12	1.3
14R	19 Feb.	1825	314.6	324.3	9.7	3.55	36.6
15R	19 Feb.	2255	324.3	333.9	9.6	2.29	23.8
16R	20 Feb.	440	333.9	343.5	9.6	3.99	41.5
17R	20 Feb.	925	343.5	353.1	9.6	5.23	54.5
18R	20 Feb.	1800	353.1	356.0	2.9	2.10	72.4
19R	2 March	1040	356.0	363.5	7.5	1.60	21.3
20R	2 March	1715	363.5	373.0	9.5	1.21	12.7
21R	2 March	2205	373.0	382.6	9.6	2.66	27.7
22R	3 March	245	382.6	392.1	9.5	4.62	48.6
23R	3 March	845	392.1	401.8	9.7	3.25	33.5
24R	3 March	1250	401.8	411.3	9.5	6.09	64.1
25R	3 March	1700	411.3	421.0	9.7	3.15	32.5
26R	3 March	2215	421.0	430.5	9.5	3.06	32.2
27R	4 March	205	430.5	440.0	9.5	2.89	30.4
28R	4 March	650	440.0	449.7	9.7	1.75	18.0
29R	4 March	1050	449.7	459.3	9.6	1.59	16.5
30R	4 March	1530	459.3	469.0	9.7	1.32	13.6
Total					273.9	73.68	26.90

An obstruction at 282.6 mbsf was encountered while reaming the last two stands of drill pipe to bottom; it was washed through. Over 7 m of rubble at the bottom of the hole was reamed and washed, and Core 148-896A-12R was drilled. Core 148-896A-13R, which required 4.08 hrs to cut, recovered only 0.12 m of basalt that had jammed the HRO scribe in the core catcher. Cores 148-896A-14R to -18R were drilled successfully with a weight on bit of 23,000–28,000 lb, at 50 rpm. The drill string was pulled out of the hole and the ship departed for Site 504 at 1410 UTC, 20 February, to clean out Hole 504B.

#### Logging: Phase 1

The *JOIDES Resolution* returned to Site 896 on 1 March to log Hole 896A (see "Downhole Measurements" section, this chapter). The induced gamma-ray spectroscopy tool (GST), aluminum clay tool (ACT), natural-gamma spectroscopy tool (NGT), and temperature logging tool (TLT) were run in combination successfully from 120.73 to 347 mbsf (11 mm above the bottom of the hole).

#### Coring Run 3

The next coring run in Hole 896A was another Smith series-9 bit, again in conjunction with a monel drill collar and with the HRO system used on alternate cores. The drill string was run to the bottom of the hole (356 mbsf) and encountered no rubble. Cores 148-896A-19R to -22R were drilled with weight on bit of 25,000 to 28,000 lb, at 50–55 rpm. Near the end of drilling Core 148-896A-23R, the weight on bit was increased to between 30,000 and 32,000 lb, but did not improve penetration rate, so the weight was decreased to 28,000 lb. Drilling continued until 4 March when Core 148-896A-30R was cut and coring operations ceased to allow the ship to return to Site 504 for additional downhole measurements. The rate of penetration for the final bit run averaged 2.91 m/hr, for an overall recovery of 29.4%.

#### Logging: Phase 2

After completing operations at Site 504 on 6 March the *JOIDES Resolution* returned to Site 896 to log. The first logging string contained the dual laterolog, the sonic density tool, and the natural-

gamma tool. The suite was run successfully from 117.28 to 429 mbsf. The packer experiment was conducted next, with measurements at 105.6, 233, and 396.55 mbsf. The magnetometer then logged from 117.28 to 325 mbsf, and finally, the Formation MicroScanner was run to 373 mbsf (see "Downhole Measurements" section, this chapter).

The drill string was pulled out of the hole, and the ship left Site 896 on 8 March for a two day transit to port. Leg 148 ended when the ship docked in Balboa, Panama, on 10 March.

## IGNEOUS PETROLOGY

### Introduction

The rocks recovered from Hole 896A on Leg 148 are primarily pillow basalts that are similar to the basalts recovered at Site 504 on DSDP Legs 69 and 70 (Cann, Langseth, Honnorez, Von Herzen, et al., 1983). In addition to pillow basalts, thin flows or massive units, breccias, and one or two dikes have been identified. Most of these rocks have plagioclase as the most abundant phenocryst mineral and olivine as the second most abundant. Pyroxene phenocrysts rarely occur. These rocks are classified as olivine tholeiites.

### Lithologic Units

Lithologic units were based primarily on changes in mineral abundance and mineral type, and the lithology of each of the 51 units at Site 896 is described in Appendixes A and B. The units are shown graphically in Figure 5. Units with 1% to 2% phenocrysts were classified as sparsely phyrlic, with more than 2% and less than 10% phenocrysts as moderately phyrlic, and with 10% or more phenocrysts as highly phyrlic. No aphyric basalts (less than 1% total phenocrysts) were recovered. Based on the mineral abundances determined in hand specimen (Appendix A), 3 units were sparsely to moderately phyrlic, 30 units were moderately phyrlic, 15 units were moderately to highly phyrlic, and 2 units were highly phyrlic. Again based only on the hand specimen descriptions, plagioclase was the dominant mineral phase in about 40 of the units and olivine was the most abundant phenocryst in the others. Pyroxene was present in minor amounts in some units.

### Volcanic Stratigraphy

In addition to the mineralogical subdivision into lithological units, the core was subdivided into volcanic units, which were based on the gross structure and texture of the recovered rocks (Fig. 5). Boundaries of these lithostratigraphic units are not necessarily coincident with boundaries of the mineralogically defined units, but are intended to provide information on the volcanic stratigraphy of the drilled section. It must be emphasized that the stratigraphy shown on Figure 5 has been reconstructed from 28% core recovery, and refinements may be possible by comparison with logging results (i.e., the Formation MicroScanner and dual lateral log). Four types of volcanic unit were identified: massive, pillow lavas, dikes, and breccias.

### Massive Units

Massive units comprise about 38% of the drilled section (based on the expanded thicknesses in Figure 5). A massive unit was defined on the basis of a lack of curved glassy or chilled margins, the presence of well-developed brown oxidative alteration, generally higher recovery and longer sections of contiguous core than in pillowed units, and a fracture pattern that appears more regular than in the pillow lavas (Fig. 6). In such units the grain size varies from microcrystalline to fine grained. The thicker massive units (e.g., Cores 148-896A-23R-1, Piece 5, to -24R-6, Piece 1) are probably lava flows, whereas less extensive intervals (e.g., Core 148-896A-1R-1, Pieces 4 and 5) are probably the interiors of large pillows. If the classification schemes of Adamson (1985) and Shipboard Scientific Party (1989) are applied, many of the massive units could be classified as thin flows (i.e., homogeneous zones of >1 m thick, expanded thickness).

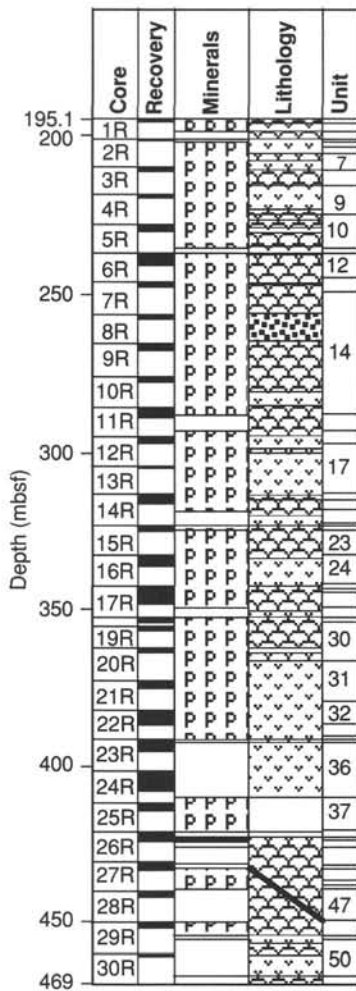


Figure 5. Drilling and recovery at Hole 896A on Leg 148. Black bars show recovery relative to core length. In the minerals column the P pattern indicates the dominance of plagioclase; otherwise, olivine is dominant. The lithology column indicates the eruptive type of the basalt: pillow basalts = convex upward, massive = v, and breccia = solid dots. The diagonal solid line indicates a mixture of pillow basalts, pillow-breccias, breccias.

**Dikes**

Two chilled margins interpreted to be dike contacts were recovered: Core 148-896A-21R-2, Pieces 9B and C, and Core 148-896A-22R-4, Pieces 3-5, where microcrystalline-cryptocrystalline rocks are in contact with considerably coarser-grained massive units. These margins are characterized by steep dips (74°-78°), a lack of obvious glass and variolitic textures in hand specimen, and the presence of veins or breccia zones separating the chilled margin from host rock (see "Structure and Deformation" section, this chapter). In thin section the chilled material in Sample 148-896A-21R-2, Piece 9, has a thin glassy margin, unusual in chilled dike margins from Hole 504B, but a considerably different series of quench crystallization textures than the majority of pillows; using the criteria of Kempton (1985) it would be classified as a dike margin.

**Pillow Lavas**

Pillow lavas comprise approximately 57% of the drilled section. A pillow lava was characterized by curved to planar or irregular chilled and/or glassy margins, an interior variolitic zone (Fig. 7), poorly developed oxidative alteration, abundant fracturing and veining, more abundant and thick (>1 mm) veins, and a relatively fine grain size.

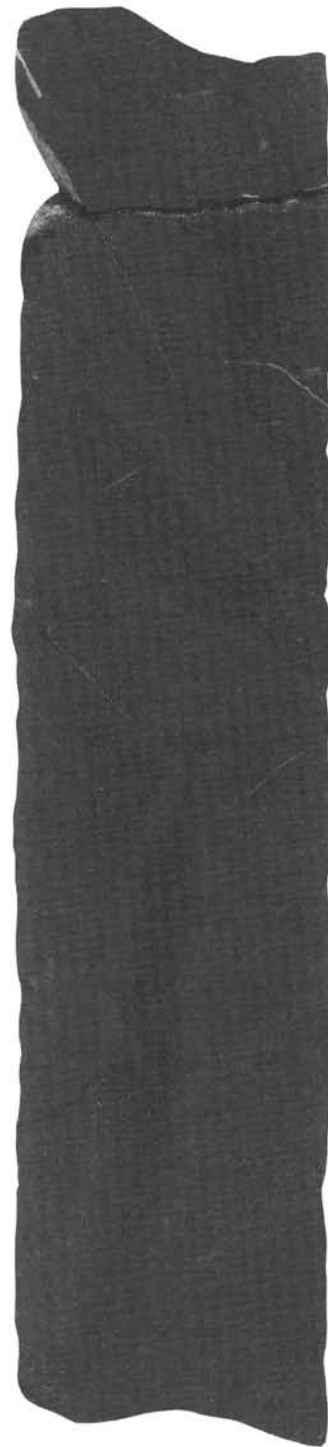


Figure 6. Massive lava, weakly veined with complex oxidative alteration halos. Sample 148-896A-16R-2, Piece 1E.

Where both margins of a pillow were recovered, minimum pillow thicknesses were determined to be from 5 to 28 cm (Fig. 8) and up to 35 cm in a single piece, where only one margin was recovered. Where rims are missing the cores of large pillows may have been classified as massive units. Contacts between pillows are rare, although some adjacent pieces both had glass rims and could have been the margins of stacked pillows. One intact contact between pillows was recovered, in Core 148-896A-5R-2, Piece 7 (Fig. 9). The contact in this piece is

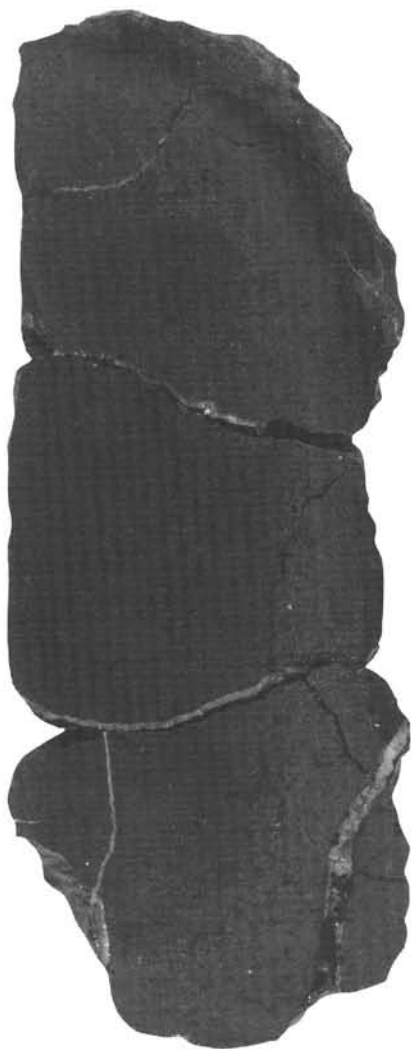


Figure 7. Example of a single pillow, with glassy and chilled rind, variolitic zone, and microcrystalline core. Sample 148-896A-7R-1, Pieces 10A and B.

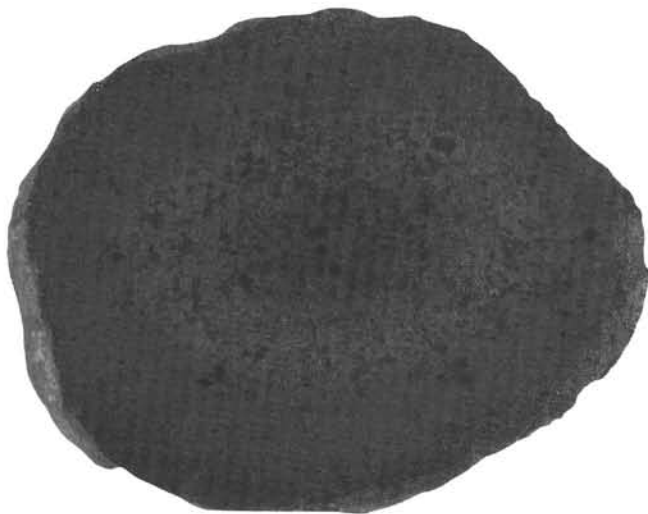


Figure 8. Single small pillow with variolitic zone. Sample 148-896A-11R-1, Piece 1.

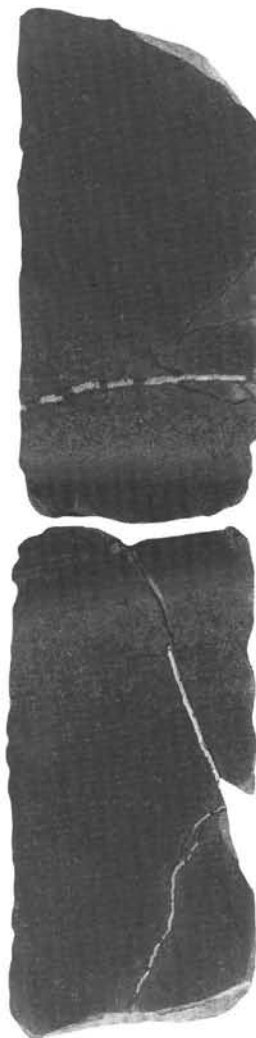


Figure 9. Planar and horizontal contact between two pillows. Sample 148-896A-5R-2, Pieces 1C and D.

nearly horizontal, similar to approximately 20% of the chilled rinds in the pillowed units. Adamson (1985) classified sequences with planar horizontal chilled margins spaced at intervals of  $<0.5$  m as sheet flows. In only one interval, Core 148-896A-17R-3, Pieces 1, 2, 5, 13, and 14, is there a sequence of closely spaced horizontal chilled rinds, but Piece 8 of this section has a steeply dipping margin. We do not consider the evidence sufficient to describe this sequence as a sheet flow rather than pillow lavas.

#### **Breccias**

Breccias were recovered in many pieces but were only recorded as a unit where two or three pieces occurred together; units defined in this way comprise 5% of the drilled section. Two types of breccia, hyaloclastic and "matrix supported," were identified but were not differentiated in the visual core description (see "Cores," this chapter). "Matrix supported" breccias are lithologically variable, ranging from angular fragments in intensely veined zones to angular to rounded clasts in a matrix of clays  $\pm$  carbonate and finely comminuted basalt. This latter type is apparently polymict, with clasts having a range of grain sizes and alteration intensities. The origins and characteristics of these breccias are described further in the "Structure and Deformation" section of this chapter. Hyaloclastic breccias (Fig. 10, for example) are often preserved on the outer edge of chilled/glassy rinds and comprise



Figure 10. Hyaloclastite breccia with clay + carbonate groundmass. Sample 149-896A-8R1, Piece 1.

fragments of glass and devitrified glass in a matrix of clay or clay + carbonate, probably altered and devitrified glass. We speculate that this material comprises the majority of inter-pillow space, but it is poorly represented in the core recovered. Below Section 148-896A-20R-1 true hyaloclastic breccias are rare, whereas matrix-supported breccias are relatively abundant in both pillowed and massive units.

### Phenocryst Phases

#### Plagioclase

Plagioclase phenocryst range in size from less than 0.1 mm to more than 5 mm. They may range in shape from equant to needle shaped and they may be euhedral to anhedral. Chemical zoning that is evident in thin section is common and many grains have complex zonation that suggests changing conditions in the magma while the crystals grew. Other features of plagioclase phenocrysts are the presence of glass and spinel inclusions and their common agglomeration into crystal clots or glomerocrysts. Also they rarely show any significant amount of alteration.

#### Olivine

Olivine phenocrysts range in size from <0.1-mm microphenocrysts to 5-mm megacrysts. They are usually euhedral and sometimes have the skeletal overgrowths that result from rapid growth during quenching. Glass and spinel inclusions are frequently found within olivine grains, and in some cases 100- $\mu$ m plagioclase laths or anhedral grains are also included. The plagioclase inclusions are rare but the complete inclusion of olivine in plagioclase megacrysts or phenocrysts is never observed, which suggests that plagioclase precedes olivine in the crystallization sequence. Usually olivine is completely replaced by secondary minerals but, in some units, some or most of the olivine is preserved. Olivine is also commonly preserved where it is included in the glassy margins of pillow basalts.

#### Clinopyroxene

Clinopyroxene is present as phenocrysts in only a few lithologic units. Where it is found it ranges in size from <0.5 mm to 7 mm. Phenocrysts appear to have been reacting with their host magma before the magma was quenched because the phenocrysts are usually rounded. In hand specimen they appear as green phenocrysts that often are intergrown with plagioclase on their rims, similar to clinopyroxene seen in the dikes of Hole 504B (Fig. 11). Pyroxene also occurs in glomerocrysts with plagioclase and sometimes with plagioclase and olivine.

### Spinel

Spinel is a minor mineral that crystallizes at high temperatures (~1200°–1250°C) along with plagioclase and olivine. It ranges in size from 10  $\mu$ m to 200  $\mu$ m and usually forms equant grains that are euhedral to anhedral. The habit of most spinel grains from the thin sections are reported in Appendix C. The spinels' color may be yellow, yellowish green, yellowish brown, reddish brown, or black, and they are sometimes zoned. Zoning is evident in the lighter or darker colored rim in transmitted light or by a difference in reflectivity when observed in reflected light. The darker colors usually signify higher iron content (Fisk and Bence, 1980; Furuta and Tokuyama, 1983).

Spinel is often found included in plagioclase and olivine phenocrysts so that in many instances it may be the first mineral to crystallize in these magmas. This can be tested by chemically analyzing the host minerals by microprobe to determine if they are early formed crystals. Although spinel is found in most units, it is rare or absent in Units 33 to 36. This corresponds to the cores in which pyroxene is present and these two minerals may be incompatible.

The darker colored rims on many spinels found in the groundmass of the basalts are the typical result of differentiation resulting in higher iron content of the melt and the subsequent higher iron content of the spinel. In some cores that have low abundance of spinel, the spinels are often dark, which suggests that they crystallized late, possibly just before the appearance of pyroxene.

### Chilled Pillow Margins

#### Quench Textures

Various types of quench textures were found in the pillow basalts at Hole 896A and the textural terms applied to them were adopted from Bryan (1972), Lofgren (1971, 1980, 1983), and MacKenzie et al. (1982). The origin of the various types of quench textures depends on nucleation and growth mechanisms and rates, and the heterogeneities of the medium in which the crystallization takes place (e.g., Bryan, 1972; Lofgren 1971, 1980, 1983). Here we present some simplified sketches, photos, and descriptions of the most characteristic varieties that we consistently used in our descriptions. The terms, schematically illustrated in Figure 11, are as follows:

1. Variolitic texture, which includes various stages of dendritic to spherulitic growth.
2. Plumose texture.

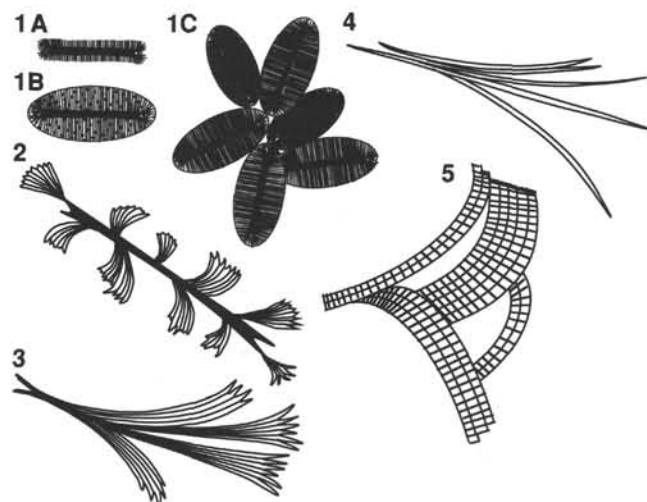


Figure 11. Sketches of the various quench textures referred to in the text. 1A, B, C show variolitic texture; 2 shows plumose texture; 3 shows sheaf-spherulitic texture; 4 shows branching texture; 5 shows comb texture.

3. Sheaf-spherulitic texture.
4. Branching texture.
5. Comb texture.

In the thin sections of chilled margins at least two of the above mentioned quench textures occur in close association, but in the majority of cases we can not systematically follow any progressive development. In some cases, however, the recovery of well-preserved pillow lava rims has enabled us to study the sequence of quench-textural development from the glass to the crypto- to micro-crystalline interiors of pillows. Below we describe and illustrate a traverse through this zone, commonly referred to as variolitic.

#### *The Glassy/Variolitic Zone*

The chilled part of pillows, when preserved, may be divided into five zones, and between each one there is complete gradation; they are classified as follows: (1) glass without quench crystals; (2) glass with the incipient crystallites, in which the first appearance of varioles occurs; (3) glass with individual and coalesced varioles; (4) only coalesced varioles; and (5) areas in which the typical variolitic texture grades into various morphologies of optically identifiable quench minerals. Figure 12 shows the gradation across the variolitic zone from glass only to cryptocrystalline material.

Zone 1 is often thin since the fragile glass spalls off as it forms and becomes interpillow hyaloclastite. The glass further breaks up during drilling. Thus, the maximum observed thickness of this zone in recovered samples is of the order of 1–2 mm. Within the glass, there are commonly small phenocrysts of plagioclase and olivine that had crystallized prior to chilling. It is mostly within this zone that olivine is preserved as a completely fresh mineral.

Zone 2, approximately 2–4 mm thick, is characterized by the scattered occurrence of small, oval varioles (Fig. 11), around 0.03 to 0.06 mm in the longest dimension. In some cases it can be seen that the varioles are defined by a central quench crystal of typically swallowtail plagioclase, around which there is sparse to dense dendritic growth of fibers, commonly 0.005–0.015 mm long (Fig. 13A), that cannot be identified mineralogically by petrographic microscope. These always grow perpendicular to the walls of the central crystal. Even though the length of the fibers may differ within very short distances, they are commonly of equal length around the same quench crystal. This seems to be different when they grow on already present phenocrysts, in which case parts of the host crystal may be completely without the fibrous overgrowth, and other parts may be densely overgrown, but for olivine there is commonly no fibrous overgrowth.

In Zone 3, approximately 6–8 mm thick, the amount of thin, quench swallowtail plagioclase crystals become increasingly more abundant, and hence the density of varioles increases. The length of the plagioclase quench crystals, onto which the spherulitic growth takes place, is commonly on the order of 0.015–0.05 mm, and in some cases two or more crystals occur together, either in a parallel or subparallel arrangement, or they may cross each other at various angles. The fibers (still impossible to identify optically) are longer than those within Zone 2, and they are commonly on the order of 0.03–0.05 mm. Since quench plagioclase is the dominant mineral on which the fibers nucleate, and the fibrous growth is always perpendicular to the crystal walls, the varioles are ellipsoidal to nearly spherical bodies. Since the ratio of length to thickness of the host crystal to that of the fibers is on the order of 1:10 to 1:20, one might expect varioles to invariably be oval in shape. It appears, however, that the length of the fibers on the long sides of the crystal is greater than on the short edges, thus making the production of spherical bodies possible. Irregular varioles result when fibers grow on quench crystals that are attached to plagioclase phenocrysts, or when phenocrysts of olivine and plagioclase occur together, and the fibers preferentially grow on the plagioclase crystals. At the inner half of Zone 3, most of the varioles occur as clusters of coalesced bodies, and

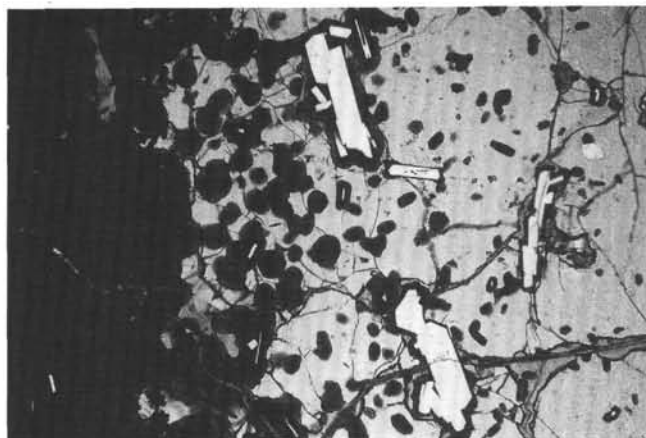


Figure 12. Profile across the variolitic zone from the outer glass rim (right) to the cryptocrystalline coalesced varioles (left). Thin-section photomicrograph of Sample 148-896A-4R-1, 75–80 cm, Piece 9. Obj. 2.5. Length of photograph is 5.7 mm. A single hexagonal olivine (near right edge) has no spherulitic overgrowth. Plagioclase phenocrysts are surrounded with spherulites.

the occurrence of glass becomes progressively less abundant. The shapes of the bodies become more spherical in character, and the lengths of the fibers are commonly 0.03–0.07 mm. Figure 13B shows the typical variole occurrence within Zone 3.

In Zone 4 there is a complete coalescence of the varioles with only an occasional occurrence of glass. The bodies are commonly 0.3 mm to 0.5 mm in diameter, and the lengths of the fibers are up to 0.15 mm. The boundaries between varioles take on a honeycomb arrangement. The fibrous crystallites may reach a sufficient size for optical identification. In seems that in the majority of cases the fibers consist of plagioclase or intergrown plagioclase and olivine.

In Zone 5 the well-defined honeycomb texture is gradually lost over a distance of approximately 4–6 mm (Fig. 13C), and the shapes of olivine and plagioclase quench crystals change and become more variable, and clinopyroxene quench crystals can be positively recognized.

#### *Plumose Texture*

This feather-like textural variety consists of dense, extremely thin and curved fibers, approximately 0.1–0.2 mm long (Fig. 13D). Its most frequent occurrence is within the inner part of the variolitic Zone 5. Otherwise it is commonly associated with the sheaf-spherical texture (described below). In no cases has it been possible to optically identify the mineral(s) of which it consists. In some cases this texture can be seen to have grown on swallowtail quench plagioclase. Because plagioclase is the liquidus mineral and because plagioclase preferentially nucleates on itself (Lofgren, 1983), the thin fibers may possibly also consist of plagioclase.

#### *Sheaf-spherical Texture*

This is by far the most commonly observed quench texture. It is characterized by straight to curved fibers 0.3 mm to 1 mm long, arranged in bundles of various length (Fig. 13E). The fibers that define this textural type are thicker and longer than those of the plumose texture, and they appear to consist of intergrown plagioclase and olivine.

#### *Branching Texture*

This texture consists of few straight, relatively thick and long fibers (Fig. 13F) and may be considered a coarser variety of the sheaf-spherical type, with which it is usually associated. In some cases it can be seen to consist of intergrown plagioclase and olivine and in some cases also clinopyroxene.

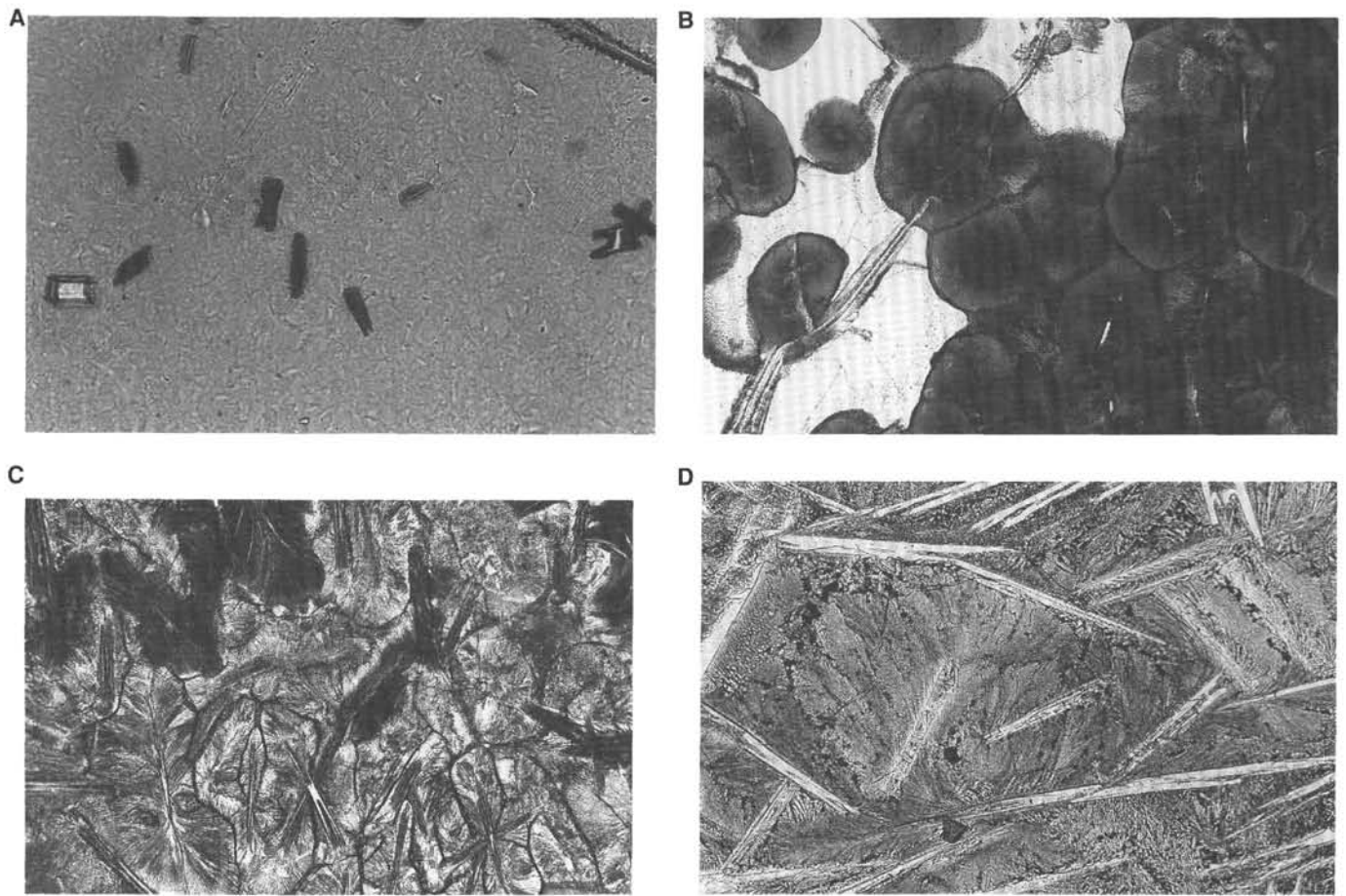


Figure 13. **A.** Dendritic growth (black, fuzzy overgrowths) on elongate plagioclase quench crystals. Thin section from Sample 148-896A-4R-1, 75–80 cm, Piece 9. Obj. 20. Length of photograph is 0.72 mm. **B.** Individual and coalesced varioles. White is fresh glass. From thin section 148-896A-4R-1, 75–80 cm, Piece 9. Obj. 20. Length of photograph is 0.72 mm. **C.** Honeycomb-like texture at the inner part of the variolitic zone. From thin section 148-896A-4R-1, 75–80 cm, Piece 9. Obj. 10. Length of photograph is 1.4 mm. **D.** Typical plumose texture (left of center), grading into the sheaf-spherical type. From thin section 148-896A-6R-1, 52–54 cm, Piece 5C. Obj. 20. Length of photograph is 0.72 mm. Euhedral spinel trapezoid is below center. **E.** Typical sheaf-spherical texture below center. From thin section 148-896A-6R-2, 88–91 cm, Piece 10A. Obj. 10. Length of photograph is 1.4 mm. **F.** Typical branching type texture right of center. From thin section 148-896A-11R-3, 48–53 cm, Piece 8. Obj. 20. Length of photograph is 0.72 mm. **G.** Comb texture (right of center). From thin section 148-896A-17R-1, 1–3 cm, Piece 1A. Obj. 20. Length of photograph is 0.72 mm. **H.** Curved comb texture (right of center). From thin section 148-896A-17R-1, 1–3 cm, Piece 1A. Obj. 20. Length of photograph is 0.72 mm.

#### *Comb Texture*

This texture, with its comb-like appearance, has a variety of forms. In some cases the back of the comb is straight (Fig. 13G), in other cases it is bent, and occasionally it may define semi-circles (Fig. 13H). This texture is most commonly associated with the branching and sheaf-spherical varieties, and occasionally with the plumose type, but has not been seen within the variolitic zone.

#### *Secondary Textural Development in the Glass*

Along cracks within the rim of pillows, straight zones to highly irregularly shaped patches with a vermicular texture often occur adjacent to the fresh glass. These zones may vary in thickness from 5–30  $\mu\text{m}$ . The diameter of the round, oval to worm-like bodies is commonly 1–2  $\mu\text{m}$ . Also along the grain edges of altered glass fragments in hyaloclastites are dense populations of similarly sized and shaped bodies as those along the cracks in the fresh glass mentioned above. These occurrences are commonly seen to be rooted at 1–2  $\mu\text{m}$  inside the edges of the glass fragments. They develop perpendicularly into the fragment as strings, or in a funnel-shape pattern (up to 40  $\mu\text{m}$  long), to finally become irregularly shaped patches with diffuse to sharp

boundaries to the adjacent fresh to slightly altered glass. The individual bodies have a light brown inner part and a darker brown rim.

The shipboard facilities for high-power magnification and chemical analyses of these bodies are not available, so we have not determined their composition or the fine details of their texture. However, they have the same size, shape, and texture as features produced by bacterial activity on glass surfaces in Icelandic hyaloclastites (Thorseth et al., 1992). These features, possibly biogenically produced, will be analyzed in detail as a post-cruise study.

#### *Zoning Patterns of Plagioclase*

Plagioclase occurs as megacrysts, phenocrysts, microlites, and glomerocrysts. Microlites have the simplest zoning and morphology, which corresponds to their location in the pillows and massive basalts. Microlites near chilled margins are fine-grained, elongated needles. The width of microlites increases toward the interiors of pillow and massive basalts. These microlites are zoned with a rapid continuous decrease in An content from the core to the rim.

Zoning of megacrysts, phenocrysts and glomerocrysts are generally complex, but all have a sharp boundary between the core or mantle and rim with low An contents. The width of the phenocryst

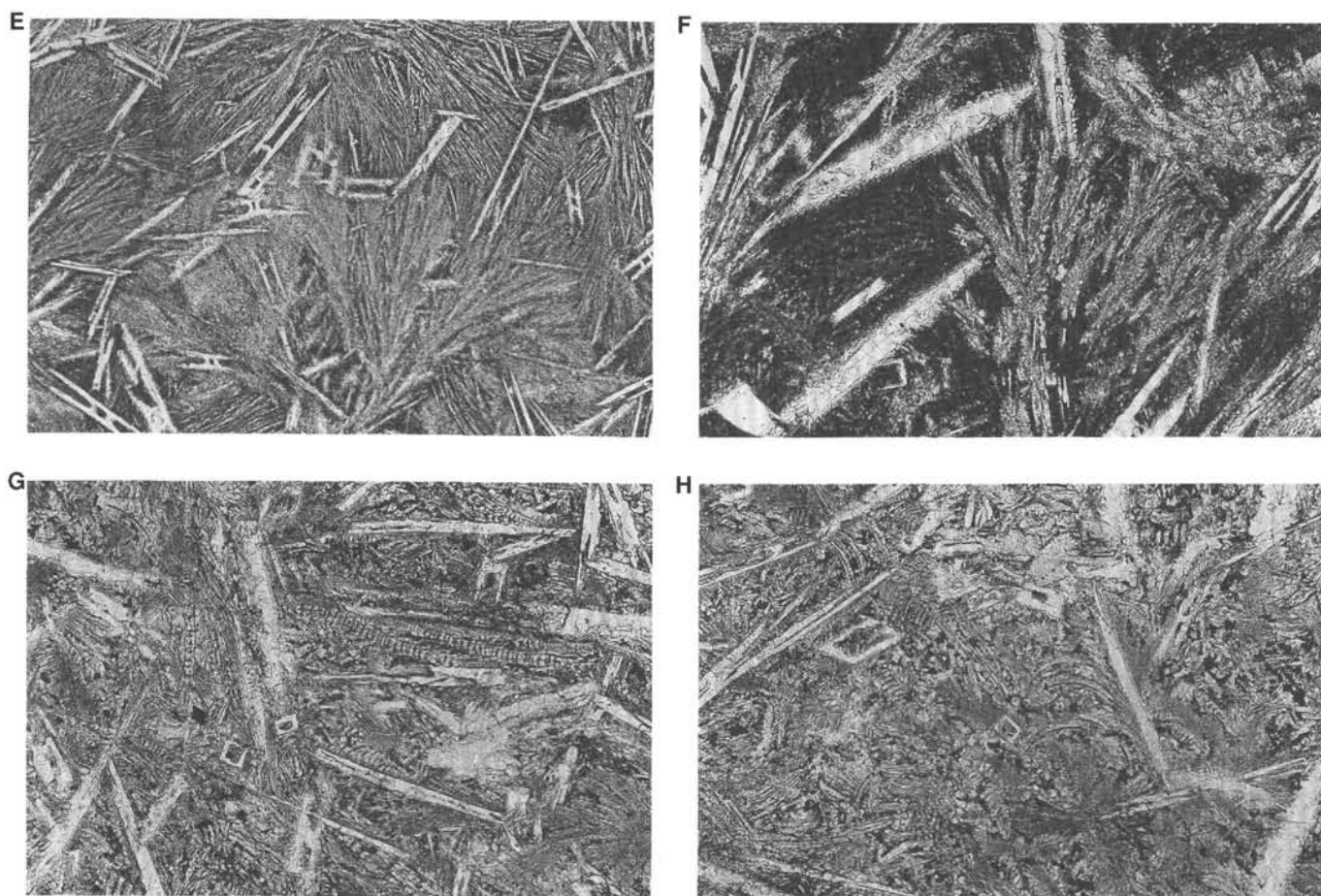


Figure 13 (continued).

rim is similar to the width of microlites in the same thin section. Phenocryst rims vary from about  $2\ \mu\text{m}$  at near the chilled margin to  $30\ \mu\text{m}$  at near the center of pillows or in the massive lavas. This indicates that these rims correspond to the same stage of crystal growth as the plagioclase microlites.

The zoning of the cores may include normal, reverse, fine oscillatory, undulatory, patchy, and sector zoning, and combinations of these patterns exist. The simplest pattern is a comparatively uniform core sometimes with fine oscillation. This zoning is observed in some megacrysts and in prismatic phenocrysts. A second pattern consists of euhedral core, mantle, and rim. The euhedral core is surrounded by a sharp boundary, by mantles then rims. This type of zoning may occur in comparatively coarse-grained phenocrysts, megacrysts, and glomerocrysts. The mantles are lower in An than the cores and range in thickness from 3 to  $150\ \mu\text{m}$  independent of the occurrence, unlike the rim. The mantle may also have fine oscillatory zoning. A representative example of this zoning is shown in Figure 14, which exhibits conspicuous fine oscillatory zoning in both mantle and core.

A third type is characterized by the appearance of a reversely zoned core, but it is otherwise like types one and two. The cores may have fine oscillatory zoning and be divided into two parts, an irregular inner core with low An content and an outer core high in An contents. Usually the outer core is euhedral and has a sharp boundary with the mantle. The inner core sometimes contains devitrified glass inclusions. Euhedral cores are most common but some are conspicuously anhedral or subhedral. Both gradual and sharp boundaries are observed between the inner core and outer core. These patterns are frequently found in megacrysts, large phenocrysts ( $>1\ \text{mm}$ ), and glomerocrysts.

A fourth type of zoning are sector-zoned plagioclases, which consist of (010) and (001) sectors. An contents are higher in the (010) sector than in the (001) sector, as found in previous studies (Lofgren, 1980; Meyer and Shibata, 1990). The sector-zoned plagioclases were found in 8 of the 58 thin sections. The sector-zoned plagioclases are always euhedral and tabular ranging from 0.4 to 1.5 mm in length



Figure 14. Plagioclase phenocryst showing fine oscillatory zoning. This 2-mm-long plagioclase consists of core and mantle, which both have fine oscillatory zoning. Sample 148-896A-11R-3 48-53 cm, Piece 8.

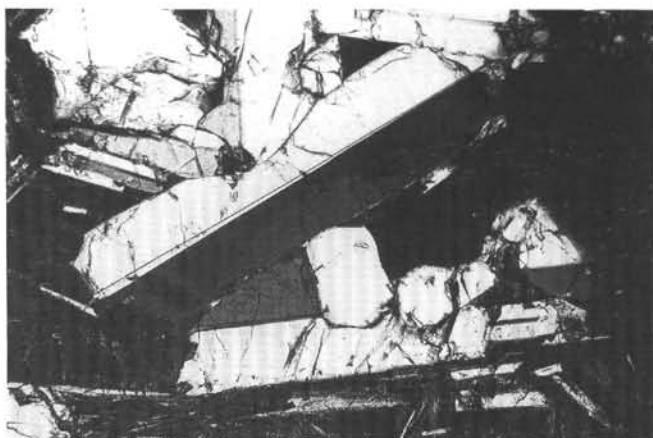


Figure 15. Sector-zoned plagioclase are usually tabular and euhedral. Twinned grain near center has weak sector zoning and is about 1 mm. Sample 148-896A-6R-2 130–133 cm, Piece 11D. See text for discussion.



Figure 16. Representative plagioclase showing complexed zoning. The plagioclase has a euhedral core that is weakly reversely zoned with fine oscillations and is surrounded by an inner low-An mantle with a sharp boundary. The outer margin of the inner mantle is embayed by a high-An outer mantle, followed by narrow rim with distinct boundaries. Diameter is about 0.5 mm. Sample 148-896A-3R-1, 41–44 cm, Piece 7.

with aspect ratios about 3 to 5 (Fig. 15). Sector-zoned plagioclase may be surrounded by a normally zoned rim or oscillatory zoned mantle. The sector-zoned plagioclases are found in glomerocrysts (Appendix E) and as medium- to coarse-grained phenocrysts.

In addition to the above four patterns are more complexly zoned plagioclases. As shown in Figure 16, the plagioclase has a euhedral core that is weakly reversed with fine oscillations and is surrounded by an inner low-An mantle with a sharp boundary. The outer margin of the inner mantle is embayed by a high-An outer mantle, followed by a narrow rim with distinct boundaries.

It is apparent that plagioclase microlites in groundmass grew in situ because of rapid cooling caused by the extrusion of magma on the seafloor. Narrow rims surrounding phenocrysts, megacrysts, and glomerocrysts were also produced during the same quenching event. The great variety of zoning patterns in plagioclases suggests that these magmas underwent complex processes prior to the emplacement.

Sector zoning has not been previously reported from the Costa Rica Rift, but it appears in 8 of the 58 thin sections from Hole 896A. It may be even more common, however, because sector zoning will only be observed in crystals in which the plane of the thin section intersects the core of the crystal and is nearly perpendicular to the

(010) plane. Generally, the sector zoning is believed to be due to rapid cooling and rapid crystal growth conditions (e.g., Bryan, 1972; Shipboard Scientific Party, 1988b). In this hole sector zoning exclusively appears as tabular grains up to 1.5 mm in length with aspect ratios of about 3 to 5, which suggests that they crystallized in a super-cooled magma before extrusion. Super-cooling could have been caused by an abrupt change in physical and chemical conditions (e.g., pressure and volatile contents of the magma). Under super-cooled conditions, the crystals grew rapidly initially, but as crystallization proceeded, the degree of super-cooling was reduced and equilibrium crystallization approached. The presence of sector-zoned plagioclase suggests that super-cooled conditions may have occurred frequently during the magmatic evolution of Hole 896A basalts.

Abrupt decreases in An contents outward at the core-mantle transitions of plagioclase phenocrysts may be produced by mixing a primitive magma containing plagioclase with a more evolved magma. Rapid release of volatiles from a magma in which plagioclases have been crystallizing may also be responsible for the rapid decrease in An contents, because decreasing volatile contents would shift the plagioclase loop toward higher temperatures. This implies that the crystallization of plagioclases was greatly promoted and the preexisting high-An plagioclases were rapidly enclosed with the mantle low in An contents.

Another common feature of zoning are reversely zoned plagioclases, which may contain numerous glass inclusions and have a partly resorbed cores. The reverse zoning can be produced by many causes (e.g., injections of less evolved magma into a more evolved magma where plagioclase had already crystallized; rapid uplift of magma with plagioclase suspended in the melt; initiation of crystallization under super-cooled conditions; and rapid increase in volatile contents as a result of contamination by wall rock). A wide variety of the reversely zoned plagioclases in the Hole 896A basalts suggests that multiple factors may have been involved in producing the reverse zoning.

Fine-scale oscillations in composition frequently observed in both the core and mantle are explained by crystal growth under rapidly changing conditions of temperature, pressure, or magma composition. Sharp and repeated occurrence of the oscillatory zoning may have been caused by abrupt fluctuations of volatile contents, recharge of the magma chamber with hot magma, or convective overturn that repeatedly carried crystals between hotter and cooler regions of the magma chamber.

On the basis of the above arguments, the growth processes of the plagioclase shown in Figure 14 may be interpreted as follows. At least five stages of crystal growth can be determined: (1) crystallization of primary low-An plagioclase accompanied by fine oscillation; (2) reversed zoning at the margin of the core; (3) abrupt decrease in An contents resulting from the overgrowth on the core; (4) resorption followed by euhedral overgrowth on the resorbed mantle; and (5) abrupt decrease in An contents by the final crystallization to produce the rim. Glass inclusions may be produced during the resorption and overgrowth stages. However, this is an only one example, the wide variety of zoning patterns in the plagioclases suggests that they underwent complex growth processes prior to the emplacement of magma and those with different growth history were mixed up during the extrusion of magma.

#### Glomerocrysts

The phenocrysts and megacrysts often define glomerophyric clusters. Glomerocrysts have been reported from basalts and diabbases recovered from Hole 504B during Legs 69, 83, 111, and 140. Various glomerocrysts were again found during Leg 148 from Hole 504B (Appendix F, "Site 504" chapter, this volume). Most of the basalts recovered from Hole 896A contain a variety of glomerocrysts and megacrysts. Glomerocrysts were classified by mineral assemblage as plagioclase, plagioclase-olivine, plagioclase-clinopyroxene, and plagioclase-olivine-clinopyroxene. For each glomerocryst, the number of crystals, grain size, and approximate modal composition were determined (Ap-

pendix E). The occurrences of plagioclase megacrysts and xenocrysts are also included in Appendix E. Some glomerocrysts contain spinels as inclusions in plagioclases or olivine, and these are indicated by asterisks in Appendix E. The glomerocrysts are usually closely packed and have little interstitial minerals, but some glomerocrysts are loosely packed with the interstices filled by groundmass material.

Plagioclase is the dominant glomerophytic mineral, and glomerophytic clusters consist of 5 to 50 grains with a wide variety of textures and grain sizes. Individual grains within the glomerocrysts range from euhedral to subhedral (Fig. 17), but anhedral grains are also found. Within single glomerophytic clusters, a variety of crystal shapes, sizes, and zoning patterns may occur in the plagioclase. For example, euhedral tabular plagioclases are often associated with large subhedral equant plagioclases. The former usually has concentric oscillatory zoning, whereas the latter may have a patchy zoned core surrounded by an undulatory to oscillatory zoned mantle. Sector zoning is occasionally found in the euhedral tabular grains (Fig. 18 and Appendix E), but some grains have concentric oscillatory zoning. Some glomerocrysts contain plagioclase grains up to 3 mm long with oscillatory-zoned mantles and resorbed cores with irregular, low-An patches. Such resorbed plagioclases frequently contain numerous glass inclusions. Details on a variety of the zoning patterns are described in a previous section of this chapter. The great variety of plagioclase suggests that



Figure 17. Representative example of plagioclase type glomerocryst, consisting of about 30 grains. Individual plagioclases are euhedral to subhedral and show fine oscillatory zoning and sector zoning. The width of photograph is 4 mm. Sample 148-896A-11R-3, 48–53 cm, Piece 8.

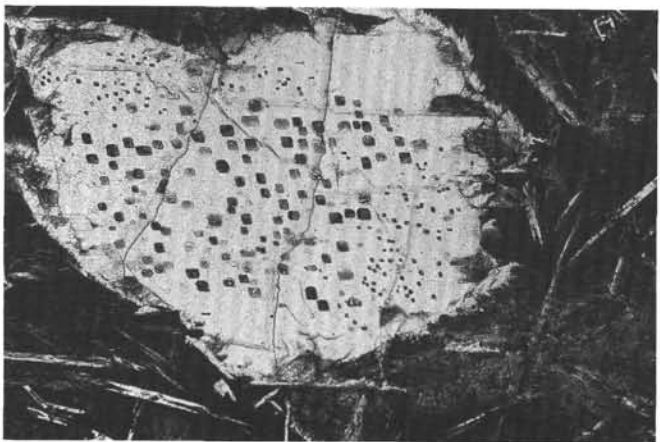


Figure 18. Anhedral plagioclase (1.1 × 0.9 mm) megacryst with numerous glass inclusions. Sample 148-896A-5R-2, 20–23 cm, Piece 1B.

individual grains in some glomerocrysts have different origins, and were mixed prior to and/or during the emplacement of magmas.

Plagioclase-olivine glomerocrysts are the next most abundant type, consisting of 4 to 30 grains each (Appendix E). The grain size ranges from 0.1 to 2.7 mm. The plagioclases again have a wide variety of sizes, shapes, and zoning patterns similar to the plagioclase type. Usually, plagioclases and olivines are found as separate aggregates in the glomerocrysts. These facts suggest that the plagioclases associated with olivines may be derived from various origins.

Plagioclase-clinopyroxene and plagioclase-clinopyroxene-olivine glomerocrysts are exclusive to Cores 148-896A-19R to -22R. Pyroxenes occur as prismatic grains up to 7 mm long, which sometimes include plagioclase laths or enclose equant to tabular plagioclases with poikilitic texture. Plagioclases are euhedral to subhedral and have patchy zoned cores. Strong zonation is not observed in the plagioclases inside the glomerocrysts, but some have faint oscillatory zoning.

Megacrysts of plagioclase commonly occur in many specimens and they may show complex zoning patterns and irregular (Fig. 18) or rounded shapes (Fig. 19) due to resorption. These megacrysts often contain numerous glass inclusions (Fig. 18).

### Phenocryst Mineralogy

A systematic study of phenocryst abundance was undertaken by point counting (500 points per thin-section) 80 thin sections. The samples range from aphyric (<1% phenocrysts) to highly phytic (33.4%) basalts, and plagioclase is the most abundant phenocryst in almost all samples (Appendix D). Megacrysts, which are present in most thin-sections as single crystals or glomerophytic clots, were point-counted separately. A separation between phenocrysts *sensu stricto* and megacrysts is convenient to distinguish between crystals grown during ascent and cooling of the melt and crystals of different origins that can greatly influence the mineralogic characteristics of a basalt (e.g., Bryan, 1983). However, in only a few samples of Hole 896A was the megacryst abundance high enough to significantly increase the abundance of the primary phenocryst minerals.

Phenocryst abundances show some systematic variations with depth. This is best demonstrated by the content of plagioclase phenocrysts, which increase from the top of the hole to near 330 mbsf, at Unit 20 (Fig. 20A). From this level to approximately 340 mbsf, there is a rapid decrease in the content of plagioclase phenocrysts, followed by an increase down to approximately 390 mbsf. Below this level plagioclase phenocryst abundance decreases suddenly, apparently followed by a poorly defined increase to the bottom of the hole. The two maxima correlate with major occurrences of thick massive basalt



Figure 19. Rounded plagioclase megacryst with numerous glass inclusions near a smectite-carbonate vein. Diameter is 1.6 mm. Sample 148-896A-15R-1, 101–106 cm, Piece 15.

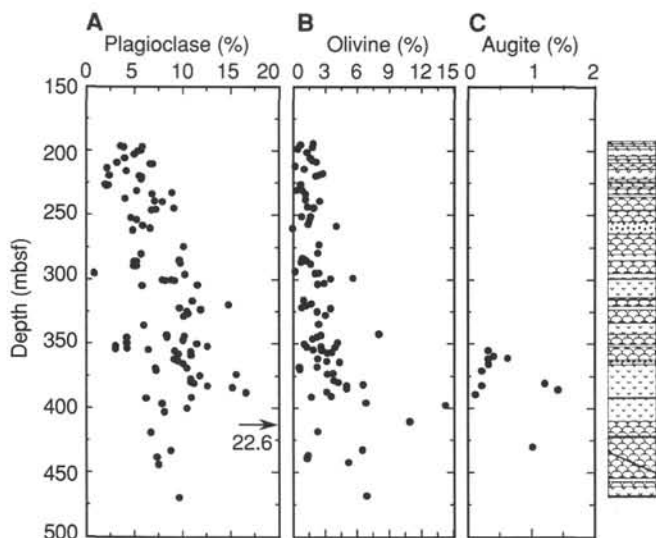


Figure 20. Modal abundance of (A) plagioclase, (B) olivine, and (C) augite vs. sub-bottom depth of the basalts from Hole 896A. The column to the right shows the volcanic lithostratigraphy (see Fig. 5 for legend).

units (Fig. 20A). At any depth throughout this profile, the difference in the minimum and maximum plagioclase content is between 5%–6%. Two samples, however, deviate strongly from this trend by containing significantly less plagioclase (Samples 148-896A-11R-3, Unit 15, and 148-896A-14R-2, Unit 20). The abundance of olivine phenocrysts also show variations with depth and is roughly coincident with the pattern defined by plagioclase phenocrysts (Fig. 20B). The occurrence of clinopyroxene phenocrysts is confined largely to the thick massive basalts in Units 31–36 (Fig. 20C).

In Figure 21A the sum of plagioclase, olivine, and clinopyroxene phenocrysts shows similar variation pattern as defined by plagioclase and olivine separately. The megacrysts of plagioclase, olivine, and clinopyroxene (>1 mm), do not show any correlation with depth (Fig. 21B), and thus cannot be regarded as responsible for the trend

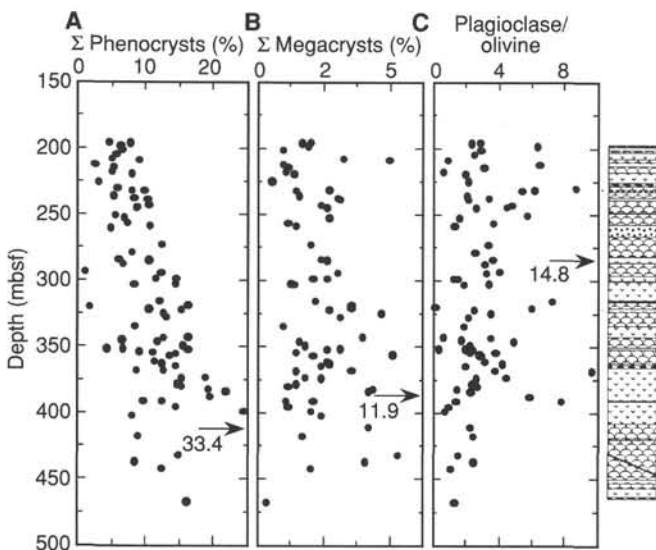


Figure 21. Modal percentages of (A) total phenocrysts content (plagioclase, olivine, and clinopyroxene), (B) megacrysts of plagioclase, olivine, and clinopyroxene, and (C) the plagioclase/olivine ratios of the basalts from Hole 896A. The column to the right shows the volcanic lithostratigraphy (see Fig. 5 for legend).

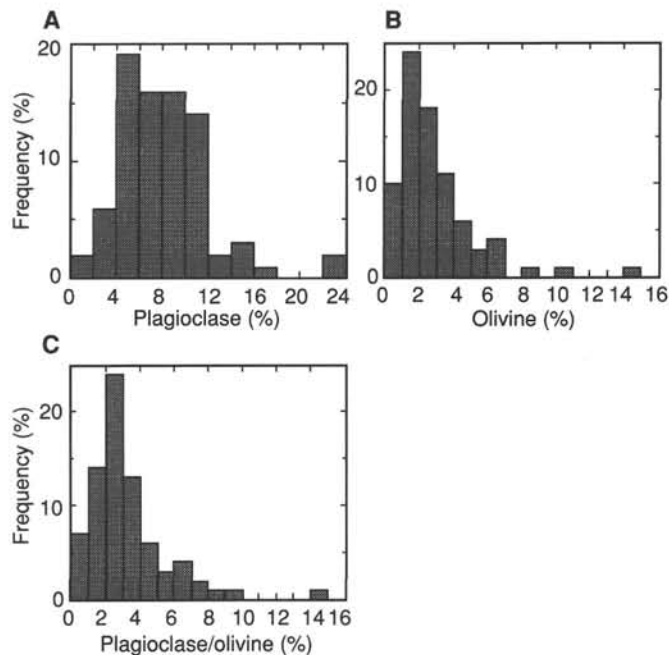


Figure 22. Frequency diagrams showing the distribution of the amount of (A) plagioclase phenocrysts, (B) olivine phenocrysts, and (C) the plagioclase/olivine ratio of the basalts from Hole 896A.

documented for the total sum of plagioclase and olivine (Fig. 21A). The plagioclase/olivine ratios show large variations from 0.14 to 14.8 (Fig. 21C). The high values are markedly different from the cotectic plagioclase/olivine proportion, which is around 2.

Figure 22A shows the modal distribution of percentage plagioclase phenocrysts, and demonstrates a broad peak between 4% and 10%. The modal distribution of olivine is shown in Figure 22B, and from the highest frequency around 1% to 2%, there is a gradual decrease in the frequency with increasing modal olivine content. The frequency distribution of the plagioclase/olivine ratio is shown in Figure 22C and demonstrates that in most basalts the ratio is near the cotectic ratio.

In addition to mineral abundances, grain size variations that may provide information on the magmatic history of basalts were studied in selected samples. The plagioclase occurs in three distinct sizes: (1) large (up to 5 mm) megacrysts, often as a part of glomerocrysts; (2) small (0.6–0.04 mm) acicular crystals, often with swallowtail textures; and (3) very fine (<0.04 mm) acicular needles in small patches. It appears that forms (2) and (3) formed during the magma transport and rapid cooling or quenching of the groundmass, and they have the characteristic bimodal distribution associated with this type of cooling history (e.g., Lofgren, 1980). In ocean floor basalts, plagioclase phenocrysts may be the products of either high level fractional crystallization of the magma, or they may represent xenolithic material derived from the magma chamber or its walls (Fig. 23A).

The crystal size distribution (CSD) model (Marsh, 1988) shows that phenocrysts developed by fractional crystallization form a log-normal size distribution, whereas the phenocrysts of xenolithic origin have a marked divergence from this size distribution. In Hole 896A, the size distribution of plagioclase phenocrysts and micro-phenocrysts in 34 thin sections from Cores 148-896A-1R to -18R were determined to evaluate the CSD. To obtain unbiased, representative counting statistics, we attempted to measure all of the large grains (>0.1 mm) that did not show any obvious features of quenching.

It was usual for the basalts from Hole 896A to contain 40 to more than 100 plagioclase crystals over 0.1 mm in size, per thin section. The numbers of olivine crystals are 50 to 60 in the two studied thin sections used to demonstrate the method (Fig. 24). The number of crystals per

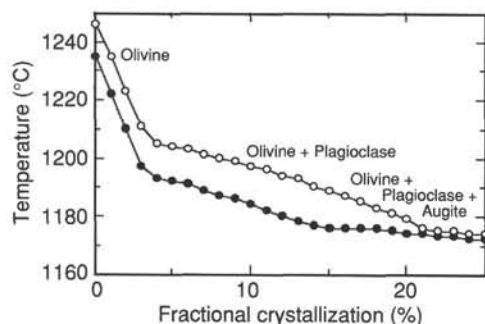


Figure 23. Crystallization sequences of two representative primitive Hole 504B Leg 69 lavas (Samples 69-504B-12R-2, 65–69 cm, Piece 736, and 69-504B-16R-4, 14–19 cm, Piece 1004, from Marsh et al., 1983). Filled circles = 69-504B-12R-2, 65–69, Open circles = 69-504B-16R-4, 14–19 cm, Piece 1004. Differentiation trends were calculated with the program of Nielsen (1990). Crystallization starts with olivine, joined by plagioclase after 4% crystallization. The olivine/plagioclase ratio along the calculated cotectic is about 2, which is largely coincident with most of the observed plagioclase/olivine phenocrysts ratios.

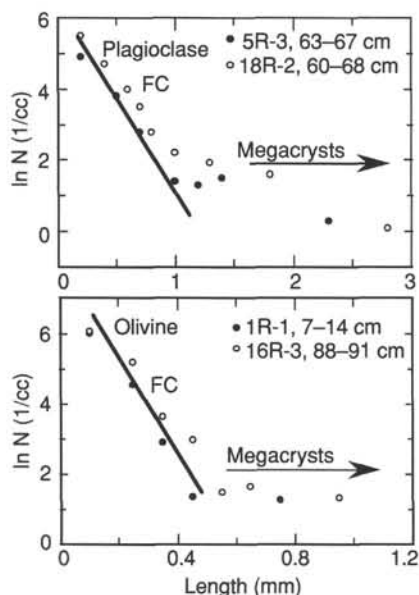


Figure 24. Crystal size distribution (CSD) data for representative samples from Hole 896A. The  $\ln(N)$  is the natural logarithm of the number of crystals in one class per  $\text{cm}^3$  calculated after the method of Saltykov (1967). Note that small grain sizes plot along a steep line representing a log-normal distribution. Plagioclase data for two thin sections and olivine data for two thin sections are presented. See text for detailed discussions.

$\text{cm}^3$  ( $N$ ) was calculated from the measured number of crystals per unit area according to the method of Saltykov (1967). The grain size range was then subdivided into 10 class intervals, with the number of grains in each class being recorded. The CSD pattern was obtained by plotting the  $N$  value vs. the class interval; representative CSD patterns for plagioclase and olivine are shown in Figure 24. Assuming simple closed system crystallization, the CSD should be a log-normal distribution and should follow the steep line in the diagram (Marsh, 1988). Grain size distributions in the studied samples follow a log-normal distribution up to crystal sizes of 0.9 and 0.4 mm for plagioclase and olivine, respectively. However, beyond such values, the distribution diverges from a log-normal form and has nearly flat profiles (Fig. 24).

Therefore, it would appear that a large portion of the olivine and plagioclase phenocrysts grew during closed-system fractional crystallization. However, the larger phenocrysts of plagioclase ( $>0.9$  mm) and olivine ( $>0.4$  mm) were not produced during this episode. Such megacrysts have been interpreted as (1) xenocrysts from the mantle or lower crust incorporated accidentally, (2) cognate phenocrysts in the sense of fragments of cumulate material derived from the margins of the magma chamber, and (3) phenocrysts crystallizing from a host magma or primitive melt that was later mixed with differentiated magmas (see Rhodes et al., 1979, for a more detailed discussion). Olivine megacrysts could have been formed during pressure release that accompanied uprising of the mantle (e.g., O'Hara, 1968). Mantle xenocrysts, however, are preserved only when the time interval between melt segregation in the mantle and eruption of the lavas is short. Biggar and Clarke (1976) implied from experimental studies that single crystals would not be expected to remain more than a few days. Assuming the existence of a magma chamber in which the melts accumulate and differentiate makes a mantle origin of the megacrysts unlikely. Plagioclase and olivine megacrysts mostly occur in the form of large glomerophytic assemblages often together with spinel. Single plagioclase megacrysts are less frequently observed, and they show mostly apparent resorption features. This observation together with the occurrence of gabbroic clots in dikes from Hole 504B point to a cognate nature of the megacrysts formed in a magma chamber. A preservation of large crystals during ascent of melts from a magma chamber is not unlikely, as the ascent velocities are high. Delaney and Pollard (1982) estimated that the ascent velocity was around 1 m/s. Assuming a depth of the magma chamber of 2 to 2.5 km, the ascent of melt occurs in less than 1 hr, which is sufficient to preserve cognate megacrysts from complete resorption.

Studying phenocryst systematics of Mid-Atlantic Ridge basalts, Bryan (1983) found high proportions of plagioclase as a characteristic of MORBs. In Figure 25, the Hole 896A data plot in the region of plagioclase dominance of the phenocryst assemblages, well within the field of N-MORBs from the Mid-Atlantic Ridge (Bryan, 1983). Lavas from the Galapagos Spreading Center and the Explorer Ridge show similar phenocryst assemblages (Perfit and Fornari, 1983; Michael and Chase, 1987), but they generally have lower total phenocryst abundances and clinopyroxene as a common minor phase.

In contrast, lavas from the southern part of the East Pacific Rise typically are plagioclase and clinopyroxene dominated with only minor or no olivine (Michael and Chase, 1987). Thus, phenocryst

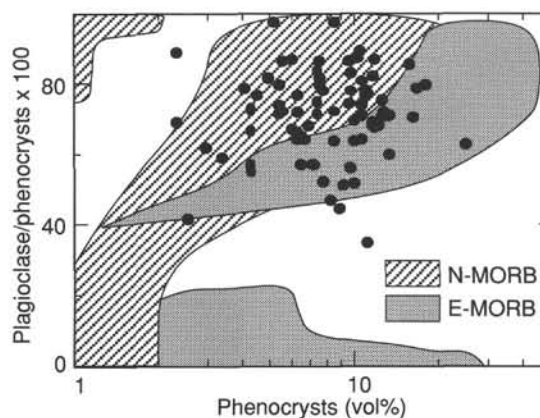


Figure 25. Modal percent of plagioclase/total phenocrysts vs. total phenocrysts volume percent (after Bryan, 1983). N-MORBs are plagioclase and olivine phryic basalts from the North Atlantic Ridge and E-MORB are LILE enriched basalts from the same area. In Hole 896A samples, plagioclase is the most abundant phenocryst and there are no olivine-rich units that plot along the  $x$ -axis in the field olivine-rich E-MORBs.

assemblages of Hole 896A lavas are comparable to low and medium rate spreading center lavas and are markedly different from super-fast spreading ridges.

As shown previously, the plagioclase/olivine ratios of most Hole 896A lavas are about two (Fig. 21C), suggesting that crystallization is largely along the olivine-plagioclase cotectic typically for an early stage of fractionation. Significantly higher plagioclase/olivine ratios, displayed by some samples, can be explained by different processes: (1) plagioclase was the first mineral to crystallize, followed by limited low-pressure fractionation of olivine; and (2) enrichment of plagioclase through flotation. Because of its low density, plagioclase is the only mineral that can float in these magmas, whereas olivine (and clinopyroxene) are more likely to be separated from the melt by gravitational settling (e.g., Bryan and Moore, 1977).

Studies of the crystallization sequences in Hole 504B diabases showed that plagioclase often is the first liquidus phase in the crystallization history of these rocks (Dick, Erzinger, Stokking, et al., 1992). The crystallization sequence in N-MORBs usually is olivine > olivine + plagioclase > olivine + plagioclase + augite (e.g., Bryan, 1983). To determine the crystallization sequence in representative Costa Rica Rift basalts, the crystallization models of Nielsen (1990) were applied. As shown in Figure 23, primitive basalts from Leg 69 (Marsh et al., 1983) display the common crystallization sequence beginning with olivine. Plagioclase joins olivine after 4% crystallization, and augite precipitation starts after 15% or 20% fractional crystallization. The general absence of clinopyroxene phenocrysts in the studied rocks from Hole 896A therefore probably indicates low degrees of differentiation. However, the absence of clinopyroxene is frequently observed in many MORBs, though they appear to fall on the plagioclase-olivine-clinopyroxene cotectic. This prominent clinopyroxene problem has been explained by high-pressure fractionation (e.g., Bender et al., 1978), magma mixing (Rhodes et al., 1979), and by gravitational settling of clinopyroxene in the magma chamber (Niu and Batiza, 1991). Plagioclase flotation depends on the temperature and composition of the melts, the composition of plagioclase, and possibly on the presence of inclusions in plagioclase. The latter might have influenced the densities of plagioclase in Hole 896A lavas as inclusions were commonly observed. Sparks et al. (1980) demonstrated that, starting from primitive basaltic melts, densities first slightly decrease and then increase as the melts cool and differentiate. Thus, plagioclase flotation is more likely to occur in cooler, more differentiated (denser) melts. Figure 26 shows density differences between plagioclase and lavas from Hole 504B Legs 69 and 70 with different compositions. Densities

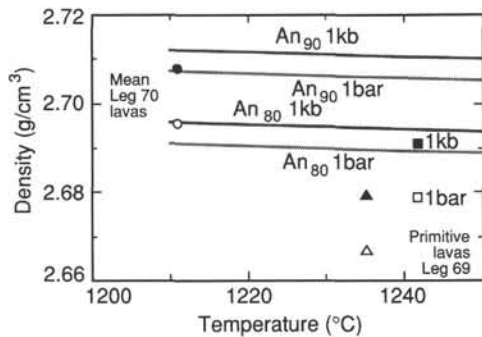


Figure 26. Densities of Hole 504B plagioclase and basaltic melts under varying pressure and temperature. Densities were calculated with the program DENSICAL by Niu and Batiza (1991). Average Leg 70 glass composition (circles) is from Emmermann (1985). Primitive basalts (triangles and squares) are the same as in Figure 23. Upper parallel lines show the density of An<sub>90</sub> plagioclase as a function of temperature and pressure. Lower parallel lines are for An<sub>80</sub> plagioclase. Open symbols are densities at 1-atmosphere and solid symbols are densities at 1 Kb. Plagioclase flotation is possible in slightly cooled melts and should be enhanced at higher pressures.

were calculated using the program DENSICAL by Niu and Batiza (1991). Plagioclase flotation appears to be possible only in moderately evolved lavas as represented by average compositions of Leg 70 basalts and glasses (Emmermann, 1985).

### Lithological and Mineralogical Comparison of Holes 504B and 896A

Most of the volcanism associated with the Costa Rica Rift is situated in an approximately 2-km-wide neovolcanic zone (rift-valley) that is bounded by fault scarps (van Andel and Ballard, 1979). The vast majority of the pillow and sheet flows are channeled parallel to a narrow zone centered on the ridge axis (Ballard et al., 1979; van Andel and Ballard, 1979). Toward the margin of the neovolcanic zone, ridge parallel faults create a rough topography formed by normal faults and tilted basement blocks. This effect is less pronounced on the southern side of the rift-system (Searle, 1983), although the tilted block basement topography is evident in the vicinity of Hole 504B (Becker, Sakai, et al., 1988).

Hole 896A is situated approximately 1 km to the south of Hole 504B, and assuming a spreading rate of 36 mm/yr (Dick et al. 1992) is situated in oceanic crust about  $2.8 \times 10^4$  years older than the Hole 504B basement. From the seismic data Site 896 is located in a different tilted block from Hole 504B; however, it is not known if a fault scarp existed between the two sites when they were located in the rift valley. The age difference between the two sites also suggests that Site 896 was near the margin of the rift valley when the Hole 504B basement was forming. This distance coupled with the potential fault-scarp separation makes it extremely unlikely that any one lava flow covered both sites.

The lithostratigraphy of Sites 504 and 896 is shown in Figure 27. The Hole 504B lithostratigraphy has been modified from Adamson (1985), such that thin flows and pillow lavas are grouped as pillows, as at Site 896, no distinction was made between these two morphological types. The relative abundance of lithologic units is shown in:

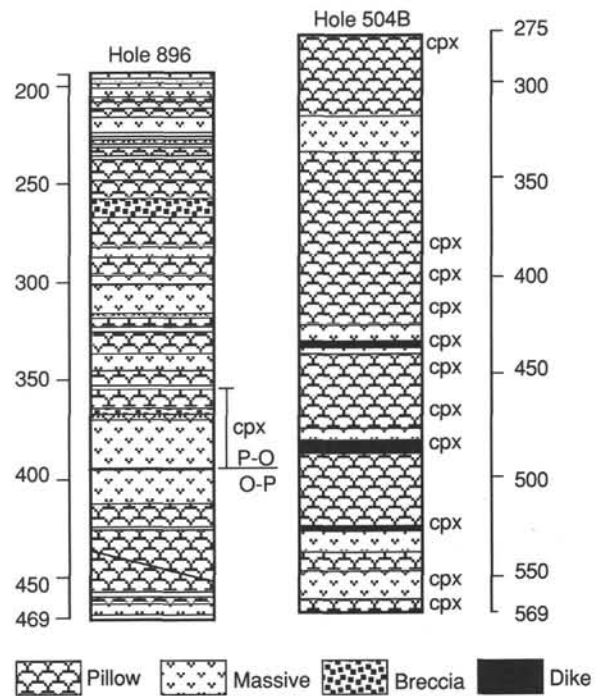


Figure 27. Lithostratigraphy of Holes 504B and 896A. Cpx indicates the position of clinopyroxene phyrification. In Hole 896A, P-O indicates the dominance of plagioclase-olivine phyrification and O-P olivine-plagioclase phyrification. The lithologies for Hole 504B are modified from Adamson (1985).

**Table 2. Proportions of volcanic units in Holes 504B and 896A.**

Volcanic unit	Hole	
	504B	896A
Pillow units	76	57
Massive units	2	38
Breccias	<1	5
Dikes	3	<1

Note: For Hole 504B the values relate to the upper 275 m of the basement.

Table 2. The most significant lithological differences between the two sites include the following: (1) the abundant breccias from Site 896, (2) the greater proportion of pillow units at Site 504, and (3) the greater proportion of massive units at Site 896. The most likely lithologies to be correlated are the massive units, because were they flows they would have the potential of being widespread in the rift-zone. However, it is also possible that these massive units represented lava lakes having limited areal extent, which would not form good lithostratigraphic markers. In Hole 896A the large massive units (Units 31–36) contain abundant euhedral cumulate olivine, which may indicate an origin as a lava lake. One further complication is added by the tendency of flows to be channelled along the axis of the rift valley, which would preclude the possible correlation of flows between the two drill sites because they lie on a line nearly perpendicular to the east-west oriented ridge axis.

The lavas at Hole 896A are dominated by plagioclase-olivine phyric basalts (90%) in the upper 195 m of the basement, below which olivine-plagioclase phyric lavas dominate (72%). In the entire Hole 896A only a short interval (40 m, Cores 18–22) contained clinopyroxene phenocrysts (Fig. 27). In contrast, the majority of Hole 504B lavas contain plagioclase as the dominant phenocrysts phase and clinopyroxene phenocrysts appears in Unit 1 and are common in the pillow and massive units below 105 m into basement. This marked change in the occurrence of clinopyroxene phyric lavas between the two sites probably represents a fundamental change in either the melting regime parameters supplying melt to the magma chambers or in the processes operating within the magma chambers related to the Hole 504B and Hole 896A lavas. It is therefore likely that there are no correlatable units between the two holes.

### Conclusions

The rocks recovered from Site 896 are primarily moderately phyric olivine tholeiites. The abundance of phenocrysts appears to decrease up through the section, suggesting that a change took place in the magma chamber over the time that these basalts erupted, which was probably less than 30,000 yr ago. This change can be seen in the composition of the spinel (as inferred from its color), in the type of glomerocrysts preserved in the lavas, and in the occurrence of clinopyroxene in some of the deeper units. All of these factors suggest that the magmas became hotter upsection.

Massive units may represent large single or multiple eruptions of magma, or they may be interpreted as localized ponds of magma. If they are the latter, then there is little reason to expect that large units can be correlated between Sites 504 and 896.

### ALTERATION

This section summarizes observations on the alteration of cored basalts as observed in hand specimen and in thin section. Alteration is manifest as secondary minerals replacing igneous phases and filling primary pore spaces of the rock (i.e., as background alteration and variously colored halos or bands) and as crosscutting veins and breccia cement.

### Secondary Mineral Identification

Clay minerals were identified as smectites in hand specimen. Their structural characteristics (e.g., expandable nature and octahedral site occupancy) were spot-checked by X-ray diffraction (Table 3). In thin-section descriptions they can be identified as green clay, or celadonite-nontronite, if they exhibit a bluish-green absorption color and are clearly birefringent. When their absorption color is green to yellowish green and they show low birefringence, they are called nontronite. The light tan to colorless clay minerals having distinct birefringence that sometimes reaches vivid tints of the second order are called saponite. These identifications must be regarded as very tentative until X-ray diffraction and chemical studies confirm them. A more general designation is also commonly used in this report, to wit, the generic terms smectite or clay (mineral) qualified with the absorption color.

Iddingsite designates a mixture of clay mineral and Fe-oxyhydroxide, which yields a characteristic red-orange or reddish brown color in thin section.

Chlorite was tentatively identified three times on the basis of weak, blue-green, pleochroic color; parallel extinction; and an anomalous bluish interference tint.

Calcite and aragonite were distinguished from one another by their conoscopic figure in sections perpendicular to an optic axis or by the extinction angle. X-ray diffraction runs aided in distinguishing calcite from aragonite (Table 4). When neither of these optical properties could be determined, the mineral was simply called "carbonate."

Phillipsite was recognized by its low relief and birefringence, its colorless prismatic habit in veins, or by the fibroradial habit with a brownish orange halo that it forms in hyaloclastites and pillow breccias.

Chabasite was tentatively identified on the basis of its low relief and birefringence, short subequant crystal habit, and common twinning lamellae. This identification requires confirmation by X-ray diffraction and/or electron microprobe analyses. Analcite, with characteristic euhedral icositetrahedral crystals, was recognized in hand specimen. Natrolite was tentatively identified in hand specimen by its characteristic finely fibro-radial aggregate habit.

### Alteration of the Bulk Rock

Alteration affected all of the rock pieces cored in Hole 896A. Except for pillow rims where fresh glass is commonly present, all of the samples studied are pervasively altered even though the amount of alteration is not high (i.e., it ranges from a few to less than 10% by adding the amounts of altered olivine and interstitial clay minerals). Alteration effects are commonly manifested as variously colored halos or bands, as veins, and as breccia cements.

### Halos

Three types of halos are distinguished on the basis of their color:

1. The most spectacular are the compound halos ranging from dark gray, to yellow to red, and which are the most common in the coarser grained massive lavas. The halos also occur in the fine-grained lavas but they are not as abundant nor as visible. They range in thickness from a few millimeters (as in the case of the dark gray portions) to 20 mm in the red portions. They commonly appear to be related to dark green smectite veins. The red part of the halo shows a sharp boundary toward the inner gray core. The red and yellow colors are result from Fe-oxyhydroxides or iddingsite replacing olivine, filling interstitial space and staining the primary silicates.

2. The pale brown halos are observed only in the pillow lava samples. These display diffuse, irregular boundaries and are a few millimeters thick.

3. The dark gray or black halos are the least common (i.e., they were observed in only three core pieces). Their thickness is centimeters in scale.

**Table 3. Summary of the results of shipboard X-ray diffraction studies on clays. Trioct = trioctahedral.**

Core, section, piece	D-spacing (angstroms)			Description	Mineral
	(060)	(001)	(001)-GLYC		
148-896A-					
1R-1, 11	1.54	14.94	16.33	Green	Trioct-smectite
1R-1, 11	1.53	15.17	16.36	Slur	Trioct-smectite
1R-1, 17	1.51-1.53	15.23	16.49	Clay from calcite	Trioct-smectite
2R-1, 11	1.54	15.49			Trioct-smectite
6R-2, 11D	1.53	15.32	17.09	Carbonate with black clay from vein	Trioct-smectite
6R-3, 4	1.53	15.32	16.70	Green + black clay	Trioct-smectite
7R-1, 15	1.54	15.56	16.41	Green	Trioct-smectite
9R-2, 2	1.53	15.30	16.96	Clear green crystals	Trioct-smectite
11R-1, 13	1.54	15.14			Trioct-smectite
11R-2, 8	1.53	15.22	16.11	Tan clay with minor calcite	Trioct-smectite
11R-2, 8	1.53	15.23	16.11	Tan matrix from glass clast	Trioct-smectite
15R-2, 11	1.54	15.29	16.61	Green balls	Trioct-smectite
16R-1, 3	1.53	15.38	16.64	Light green	Trioct-smectite
16R-1, 8A	1.53	15.28	17.17	Medium-green clay from vein	Trioct-smectite
16R-1, 8A	1.54	15.38	17.02	Red-brown clay from above vein	Trioct-smectite
16R-3, 5	1.54	15.67	16.90	Brown	Trioct-smectite
19R-1, 4	1.54	15.36	16.83	Hard black clay	Trioct-smectite + plagioclase
19R-1, 4	1.54	15.45	17.27	Soft gray-green clay from same vein as above	Trioct-smectite
19R-1, 12	1.54	15.25	17.48	Brownish-black clay	Trioct-smectite
19R-1, 13	1.54	15.10	17.21	White/green crystals	Trioct smectite + aragonite
23R-1, 12	1.54	15.65	17.10	Red brown	Trioct-smectite
23R-2, 1	1.54	14.90	17.50	Dark red	Trioct-smectite
23R-2, 4	1.53	13.98	17.19	Brown	Trioct-smectite
25R-1, 3	1.54	15.55	17.20	Gray	Trioct-smectite

### Examples of Bulk Rock Alteration

The alteration of the bulk rock of Hole 896A is documented in the alteration log (Appendix F). In effect, the alteration log is a record of the extent of oxidative alteration, because this is the characteristic that is most evident in hand specimen. It is possible that all oxidative alteration is associated with veins; however, the scale of such features may typically exceed the sampling scale (diameter) of the core.

Pristine material that retains both its original mineral assemblage and texture has not been observed from the Hole 896A core. In all rock types, olivine is completely (rarely partially) altered to clay minerals, though, commonly, the other main constituent minerals remain predominantly fresh. Most of the freshest material was identified as portions of pillow lavas on the basis of fine grain size and the abundant presence of chilled margins and hyaloclastic material. The freshest basalt is gray, with no evidence of oxidation visible in hand specimen. Olivine is only partly altered in the glassy margins of the pillow lavas. In non-glassy basalts, olivine phenocrysts are replaced by pale-colored clay minerals with very minor Ca-carbonate, whereas interstitial pore spaces are commonly clogged by similar clay material (Fig. 28). A dark brown sheen is exhibited by some of the finer grained pillow lavas and commonly a narrow (2–3 mm) band of orange oxidation is visible in the chilled margin along the boundary between the glass rim and the spherulitic material inside of the rim. Minor amounts of very fine-grained iron oxyhydroxides  $[\text{Fe}(\text{O},\text{OH})_x]$  may be present scattered throughout the groundmass and in particular around the margins of quenched groundmass pyroxene or along the diffuse boundaries of the spherulites.

Oxidation is developed within the pillow lavas as red-orange halos along dark brown smectite veins. Within these halos the clay replacements after olivine and interstitial material are commonly altered to orange-brown or dark red material (iddingsite) and the groundmass is host to abundant disseminated grains of dark red iron oxyhydroxides. Olivine grains are commonly surrounded by Fe oxyhydroxides and the margins and internal cracks in the plagioclase phenocrysts are commonly rust-stained. The abundance of Fe oxyhydroxides gives these oxidized halos a distinctive red-orange hue.

Oxidation is more prevalent in the fine- to medium-grained massive units that correspond to massive flows or interiors of large pillows. Oxidation halos are present in most pieces and “fresh” gray rock, as observed in the pillow lavas, is less common. Alteration is manifest by



Figure 28. Photomicrograph of an olivine phenocryst replaced by pale tan saponite and minor carbonate in Sample 148-896A-5R-3, Piece 8.

the abundance of disseminated red to red-brown Fe oxyhydroxides within the groundmass that replaces olivine and clinopyroxene. Oxidation halos have generally developed along the margins of fine (<1 mm), brown smectite veins and commonly a complex chronology of vein halos is recorded in the samples. Different generations of vein halos are delineated by their different colors, though a gradation of color may be present within a single alteration halo. Figures 29 and 30 illustrate typical examples of complex alteration halos.

Figure 29 is a sketch of Sample 148-896A-14R-1, Pieces 1A and 1B, in which both little altered and highly oxidized zones are present. The different alteration stages are described in the apparent chronological order. Nonoxidized basalt is present along the right side of the sample. This region is gray and the replacement of olivine by dark-green smectite is the only alteration effect visible in hand specimen. A swath of yellow alteration is present along the length of the core. In this region both olivine and interstitial material are replaced by bright yellow clays. Overprinting both the less altered gray basalt and the altered yellow region is a band of variable but intense oxidation

**Table 4. Summary of the results of shipboard X-ray diffraction studies on carbonates.**

Core, section, piece	Comments	Mineral
148-896A-		
1R-1, 1	White sugary	Calcite
1R-1, 11	White	Calcite
1R-1, 12	Sugary white	Calcite
1R-1, 17	Sugary white	Calcite
2R-1, 1	Fibrous white	Aragonite
2R-1, 17	Fibrous white	Aragonite
2R-1, 17	Blocky white (vein)	Aragonite
3R-1, 7	Fibrous/rosette	Aragonite
3R-1, 9A	White + green needles	Aragonite > calcite
3R-1, 9B	Sugary white mineral	Aragonite
5R-2, 1	Blocky white	Aragonite
5R-2, 11	White	Aragonite
6R-2, 11D	Fibrous with black clay	Aragonite
6R-3, 4	Fibrous white vein	Aragonite
7R-1, 7	White	Aragonite > calcite
7R-1, 14	Colorless	Aragonite
7R-1, 15	Colorless	Aragonite
7R-1, 21	Colorless + green	Aragonite
8R-1, 9	Colorless	Aragonite > calcite
8R-1, 10	White/colorless	Aragonite
8R-1, 25	Green	Calcite > aragonite
9R-1, 6	Green	Aragonite
9R-1, 8	Colorless	Aragonite
9R-1, 13	Colorless	Aragonite + minor calcite
9R-2, 2	Colorless + green	Aragonite
10R-1, 8		Aragonite
11R-1, 3A	White	Aragonite
11R-1, 13	Colorless	Aragonite
11R-2, 1	Colorless from rubble	Aragonite
11R-2, 8	In tan clay	Minor calcite
11R-2, 8	Colorless loose	Aragonite
11R-2, 13	Colorless	Aragonite
19R-1, 13	White green	Aragonite
21R-1, 10	White	Aragonite + calcite
23R-1, 5	White	Calcite
23R-3, 16	White sugary	Calcite
25R-1, 3	Gray	Aragonite with smectite
25R-1, 4	Colorless	Aragonite
25R-1, 11	White blades	Aragonite

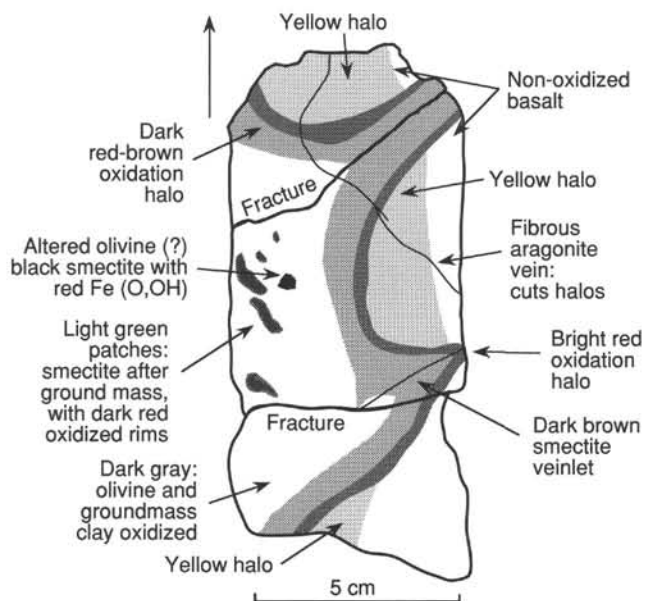


Figure 29. Sketch of Sample 148-896A-14R-1, Pieces 1A and 1B.

that passes through the central and right-hand portions of the core. This sharply delineated band comprises a  $\approx 5$ -mm-wide, bright red band of intense oxidation that grades into a 1-cm-wide, red-brown zone on the left, with the bulk of the latter comprising dark red-brown basalt in which the olivine and interstitial groundmass are completely or partially replaced by Fe oxyhydroxides. A number of  $<10$  mm-

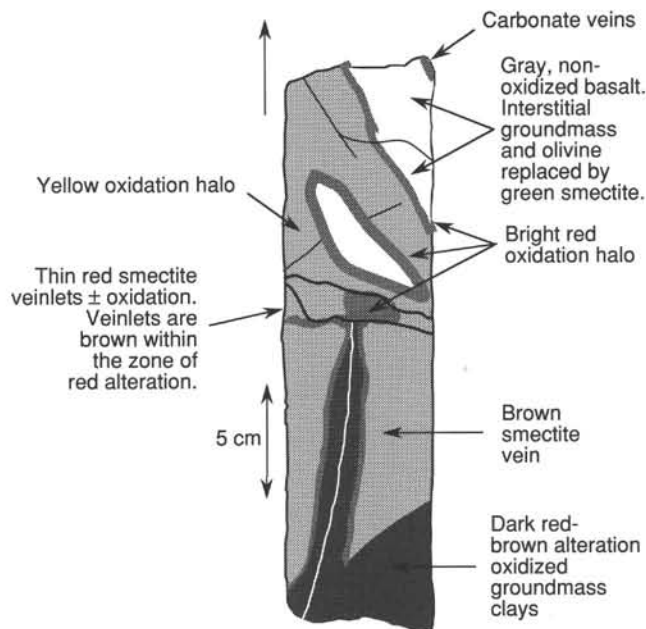


Figure 30. Sketch of 148-896A-16R-2, Piece 1E. For a core photograph of this piece see Figure 6.

diameter patches of pale green smectite are present within this halo, and the margins of these patches contain Fe oxyhydroxides. The latest stage of oxidation appears to have developed as a halo around two thin brown smectite veinlets. Oxidation extends across the core along the margins of these veinlets forming two cusps, with the yellow alteration zone preserved in the saddle between. The various halos are cut by a thin ( $<1$  mm) vein of fibrous aragonite. There is no apparent bulk rock alteration associated with the formation of this carbonate vein.

A similar chronology of halo development is observed in Sample 148-896A-16R-2, Piece 1E (Fig. 30). In this sample (and adjoining pieces) small rounded areas of nonoxidized basalt are preserved within halos of yellow alteration. A thin ( $\approx 5$  mm) intense red boundary separates the gray regions from the yellow zone. More intensive, red-black alteration has developed along the margins of a subvertical brown smectite vein that penetrates the center of the specimen and overprints the yellow alteration. A red halo of abundant Fe oxyhydroxides marks the sharp boundary between the yellow alteration and the dark red-black alteration present along the margin of the vein. The red boundary is more extensively developed at the tip of the red-black zone, where the subvertical smectite vein intersects a number of subhorizontal, thin brown smectite veinlets. Carbonate veinlets cut the alteration halos, but no associated halos have developed. In such complex oxidized halos, iddingsite commonly fills cracks in olivine crystals and surrounds the outlines of the crystals. The remainder of the olivine crystal is replaced by tan smectite (Fig. 31). Plagioclase cores are sometimes partly replaced by tan smectite (Fig. 32).

The relative timing of development of the different oxidation styles is commonly ambiguous. A thin section from Sample 148-896A-3R-1, Piece 17 (143–146 cm), contains an example of a red oxidation front that appears to overprint an area of gray lava. Within the gray rock, alteration is restricted to the presence of interstitial clays and the replacement of olivine by pale-colored smectite. At and behind the oxidation front Fe oxyhydroxides are very abundant, imparting a red hue, with the most intense colors at the boundary with the gray material. Within the oxidized zone relict olivine is present, and olivine coated in Fe oxyhydroxides is most abundant at the oxidation boundary. Relict olivine is not observed in the nonoxidized gray basalt. The configuration of the oxidized region suggests that this alteration has overprinted the basalt but the presence of fresh olivine within the oxidized zone requires that the oxidation occurred

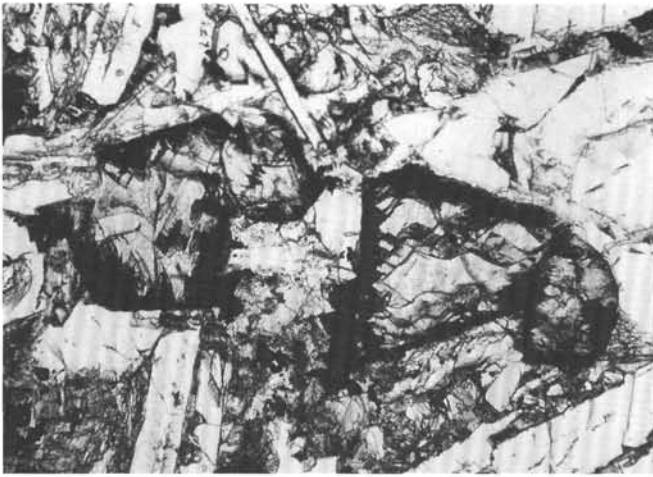


Figure 31. Photomicrograph of an olivine phenocryst replaced by iddingsite (black) and pale-brown saponite (gray) in Sample 148-896A-16R-2, Piece 4A.

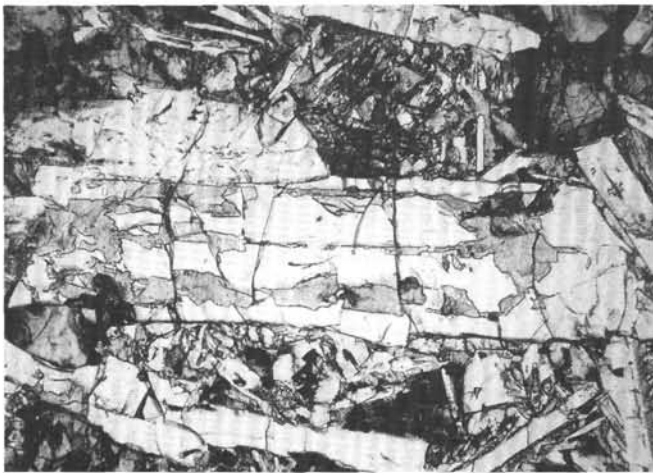


Figure 32. Photomicrograph of plagioclase partly replaced by pale-brown saponite in Sample 148-896A-16R-2, Piece 4A.

before the development of the background alteration assemblage (interstitial areas and olivine to clay) and that the Fe oxyhydroxides somehow armored the cores of the olivine grains against the breakdown to clay minerals. Alternatively, the gray nonoxidized zone in which all olivines are replaced by clay may represent a halo surrounding an unseen vein, and this halo simply may not have reached beyond the red oxidation front.

The more common relationship between oxidation and olivine breakdown is the situation in which relict cores of fresh olivine are present within gray basalt, and that olivine within the oxidized regions is completely replaced by oxidized clay minerals, Fe oxyhydroxides, and rarely aragonite.

**Variations of Alteration Mineralogy and Style with Depth**

There is very little change in the alteration mineralogy with depth in Hole 896A (Fig. 33), and the overall style of alteration is continuous with depth. A strong lithologic control on alteration style is readily apparent. Figure 34 illustrates the percentage of oxidative alteration for each piece, from the alteration log, plotted vs. depth below sea-floor. There is a correlation between intervals that are highly oxidized and rocks that were logged as massive basalts. Massive intervals always contain a high percentage of pieces that have a high percentage

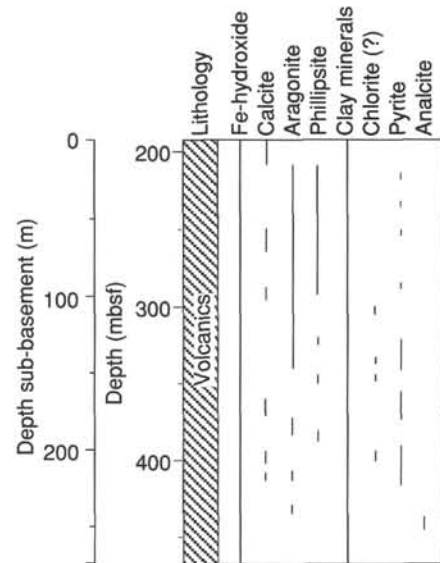


Figure 33. Diagram showing the occurrence of alteration minerals with depth in Hole 896A, based upon shipboard thin section and X-ray diffraction studies.

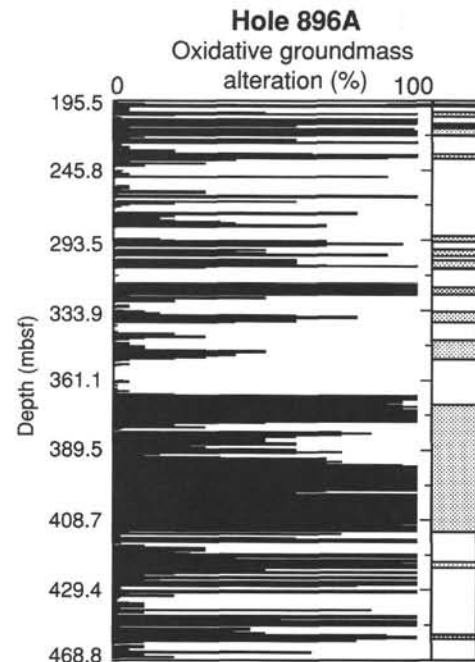


Figure 34. Diagram showing the percentage of oxidative alteration of each piece from the core of Hole 896A. At the right is a schematic representation of the distribution of pillowed and massive basalt units. Note that many massive units contain a large number of pieces exhibiting a high percentage of oxidation, whereas many pillow basalt units have only sporadic oxidative alteration. This suggests a strong lithologic control on the access of oxidizing fluids to the primary igneous rocks.

of oxidative alteration, whereas in pillow intervals only a few pieces exhibit high percentages of oxidative alteration.

**Veins**

Veins were observed in the archive half of every core from Hole 896A and were recorded in the vein log (Appendix G). A total of 1993 veins were logged, representing approximately 2 vol% of the recov-

ered samples. Based on their color in hand specimen, veins were classified in one of nine categories, including dark green, medium green, light green, dark green + light green, green + white, white, and brown + green. Other combinations or variants (e.g., orange, brown + dark green + white, dark green + metallic) occur infrequently. The particular shade of green (dark, medium, light) depends on whether the vein is dry or wet and should not be taken literally. Veins exhibiting two shades of green, however, for example dark + light are common and they are distinct from veins with only one shade. Table 5 summarizes the vein types recorded in the vein log.

The most common veins, occurring in both pillow lava and coarser grained massive lavas, comprise dark green and light green clay minerals (Fig. 35). Ca-carbonate, commonly aragonite, can be present as a last phase following the dark and light green clay minerals (Fig. 29). Other veins are formed by a dark green clay mineral alone and are the most common veins observed in pillow lavas. Analcite and a fibrous zeolite (possibly natrolite) were observed in veins and fractures in hand specimen several times and once, respectively (Fig. 36).

### Clay Veins

The dark- and/or light-green veins are composed of clay minerals. When checked by X-ray diffraction, they have uniformly been identified as trioctahedral smectite, with  $d(001) = 14 \text{ \AA}$ , expanding to about  $17 \text{ \AA}$  upon saturation with ethylene glycol. They are probably saponites. The thickness of the clay veins ranges from  $< 1 \text{ mm}$  to about  $3 \text{ mm}$  and averages  $< 1 \text{ mm}$  (Fig. 35).

### Carbonate-bearing Veins

The mineral reported as white in the vein log is generally either sugary, fibrous or blocky (meaning coarser and more vitreous than sugary). Some of the colorless crystals, whether associated with white crystals in veins or not, have also been reported as white. Almost all these minerals are either calcite or aragonite. A summary of carbonate mineral identifications by X-ray diffraction is given in Table 4. All the calcite crystals identified are sugary white, whereas aragonite is either white or colorless, or rarely appears green because it is mixed with clay minerals. Aragonite commonly occurs as fibers perpendicular to the vein edges (Fig. 37). The fibers exhibit inclined extinction, indicating that the aragonite is not elongated along a particular crystallographic direction, but is oriented randomly (see "Structure and Deformation" section, this chapter).

Veins described as carbonate alone in hand specimen always have a thin selvage of clay minerals when observed in thin section. These veins represent only 5% of the total veins logged, and they are all  $< 1 \text{ mm}$  thick. Composite clay + carbonate veins (clay present in sufficient volume to be observed in hand specimen) represent 25% of all the veins logged. In these, the carbonates occur in the center, with clay selvages varying from dark-green clay to light-green clay. Their width ranges from  $< 0.1 \text{ mm}$  to about  $4 \text{ mm}$ , with an average of less than  $1 \text{ mm}$ . The occurrence and frequency of several-millimeter-thick green and white veins is one of the most striking features of cores recovered in Hole 896A.

### Fe-Oxyhydroxide-bearing Veins

The brown, orange, and reddish veins are probably made of iron oxides and/or hydroxides mixed with clays. Most of them are  $< 1 \text{ mm}$  in thickness. Two of them are thicker ( $3\text{--}4 \text{ mm}$ ) and have a dark green

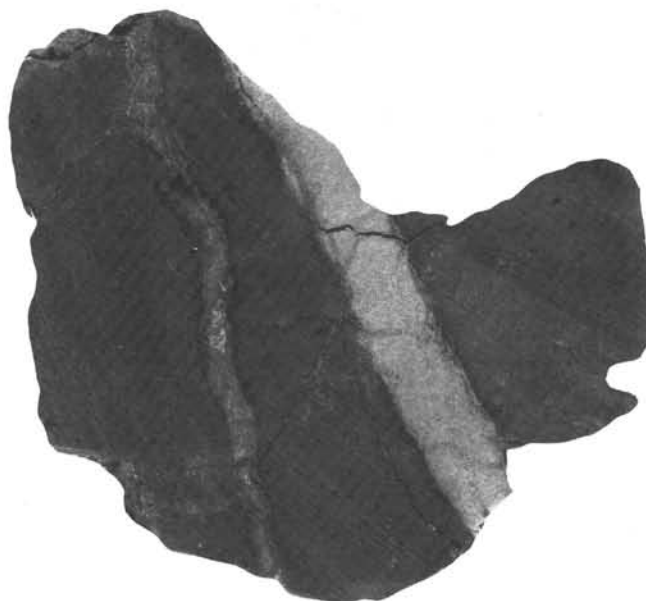


Figure 35. Pillow basalt piece crosscut by two thick (up to  $8 \text{ mm}$ ) veins composed of thin dark green clay selvage, and light green clay in center in Sample 148-896A-4R-1, Piece 5.

selvage and a brown center. One of these was analyzed by X-ray diffraction; the results indicated only the presence of smectite suggesting that if Fe-oxyhydroxide is present, there is too little of it or it is X-ray amorphous.

### Other Veins

A single occurrence of a dark green clay + pyrite vein has been reported (Sample 148-896A-16R-3, Piece 7). Another vein type, identified only in thin section is smectite with chalcopyrite.

A striking feature is the fact that numerous pieces of rock recovered from Hole 896A very quickly split open along clay veins (because of their swelling nature?), even when still wet (Fig. 37). This phenomenon continues, and after some days in the core lab, many pieces completely fell apart, making description and thin sectioning of the veins difficult or impossible. The crumbling of the cores to pieces is probably due to the alternatively wet and dry conditions and to the decompression of the clay veins after drilling. It is thus suggested that the cores be stored in a high and constant humidity environment both aboard ship and at the core repository.

Various additional vein types have been observed in thin section. Saponite  $\pm$  carbonate  $\pm$  phillipsite veins occur in and adjacent to brecciated pillow rims, cementing clasts of basaltic glass and filling adjacent cracks. These veins are described further in the "temporal relations" section below.

In glassy pillow margins, thin ( $< 0.1 \text{ mm}$ ) veins are generally composed of green or yellowish green clay grading to pale brown clay toward the pillow interior. The glass is locally altered to yellowish green clay when in contact with these veins.

The composition of a single vein commonly varies along strike, frequently in response to its entering different zones of alteration halos. For example, veins may change successively from Fe oxyhy-

Table 5. Summary of veins recorded in the vein log of Hole 896A.

Type	Minerals	Number	% of Total
Dark green $\pm$ medium green $\pm$ light green	Clays	1209	60.7
Dark green $\pm$ medium green $\pm$ light green + white	Clays + carbonates	467	23.4
Brown or red $\pm$ dark green $\pm$ medium green $\pm$ light green	Fe-oxyhydroxides + clays	188	9.4
Brown or red + dark green $\pm$ medium green $\pm$ light green + white	Fe-oxyhydroxides + clays + carbonate	30	1.5
White	Carbonates	99	5
Total		1993	100



Figure 36. Analcite and fibrous zeolite (possibly natrolite) coating a basalt piece (Sample 148-896A-27R-3, Piece 2).



Figure 37. Pillow basalt piece crosscut by two dark green clay, light green clay and aragonite veins in Sample 148-896A-6R-3, Piece 4. Note that the piece splits open along the veins.

droxide at the selvage + tan saponite at the center, to Fe-oxyhydroxide alone, then to green clay ("nontronite-celadonite," e.g., Sample 148-896A-17R-2, Piece 16). Another example involves samples having red-orange oxidation halos separated from gray, non-oxidized basalt. Here, green + white veins commonly cut the sharp boundary between two such zones: the vein as it traverses the gray zone is dominantly fibrous aragonite, whereas in the red oxidized zone the vein is predominantly light green clay with little or no carbonate.

#### Variations in Veins with Depth

The distribution of veins in Hole 896A varies as a function of depth. The veins are generally thinner below ~ 350 mbsf than in the upper portion of the hole: most veins below ~ 350 mbsf are less than 1 mm thick, and very few are 2 or 3 mm in thickness. Using the data from the vein log, the vein density in each core in terms of average number of veins per meter was calculated for different types of veins (Fig. 38). Veins bearing carbonate (alone, or in association with clay, zeolite, or Fe-oxyhydroxide) occur at a density of about 0 to 20 veins/m, and the density shows a steady decline with depth, with perhaps a steep decline at about 340 mbsf (Fig. 38A). Veins bearing clay alone occur with a density of 0 to almost 40 veins/m. The variation with depth shows a sharp increase at about 330 mbsf, then a slight decline with further depth (Fig. 38B). In contrast to carbonate-bearing and clay only veins, Fe-oxyhydroxide-bearing veins occur at a low density of 0 to 8 veins/m (Fig. 38C). Because many carbonate- and Fe-oxyhydroxide-bearing veins contain clay as well, a better idea of the overall distribution of clay-bearing veins is derived from examining the plot of total veins (Fig. 38D), which shows a fairly steady density of about  $30 \pm 20$  veins/m throughout Hole 896A.

Inspection of the vein log (Appendix G) reveals that the vast majority of the 1993 veins logged have widths less than 1 mm. Only 154 of those veins have widths greater than 1 mm. The thickest veins appear to be present in larger concentrations in the top half of Hole 896A. A plot of the number of veins ranging from 3 to 10 mm wide in each core (Fig. 39) confirms that the thick veins exhibit a maximum in Core 148-896A-11R (286–295.6 mbsf).

#### Hyaloclastites and Breccias

It is possible to distinguish among hyaloclastites, pillow breccias, and other basalt breccias. The former two rock types are observed at or near pillow lava rims. They are made up of clasts coming from the various parts of the pillow lava (i.e., they range in texture from holohyaline to variolitic to intersertal). One can commonly observe thin dark green or blackish veins progressively becoming more numerous and forming near pillow margins a network of irregular, bifurcating cracks that grades into in-situ pillow breccia at the glassy rim of the pillow lava (Fig. 40).

The other basalt breccias comprise angular to subangular fragments of basalt, sometimes exhibiting different textures and colors, as if they were derived from different lava units or from different halos from the same unit (Fig. 41). This observation indicates that, for instance, red or yellow oxidation halos predate the brecciation. Basaltic breccias occur within both pillowed and massive basalt intervals. They comprise angular to sub-rounded clasts of either pillow lava or holocrystalline basalt, the latter commonly affected by oxidative styles of alteration and set within a matrix of smaller clasts and individual igneous crystals. Such breccias are particularly abundant in Cores 148-896A-18R, -20R, -21R, -27R, -28R, and -30R (at depths greater than 350 mbsf).

The clasts are cemented by the same secondary minerals that form the veins (i.e., dark and light green clay minerals and more rarely Ca-carbonates). Veins are observed that are completely included in the clasts and they never appear to cut across both clasts and cement. This suggests that the veins formed in the rocks before the brecciation

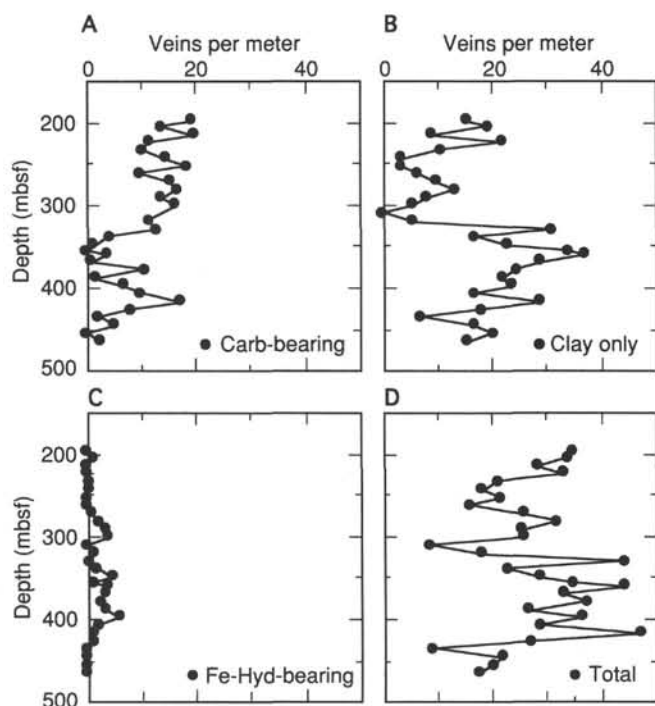


Figure 38. Plot of variation in vein composition and abundance with depth.

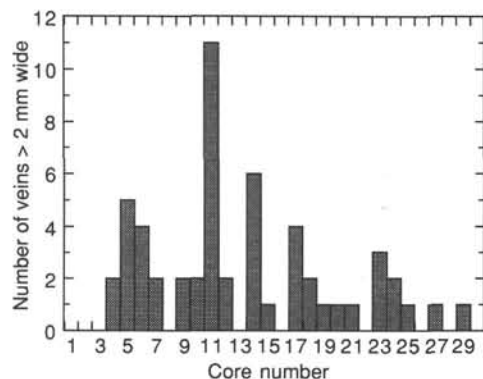


Figure 39. Histogram of veins greater than 2 mm wide (varying from 3 to 10 mm wide) for each core logged in Hole 896A. Note the maximum in Core 148-896A-11R, 286 to 295.6 mbsf.

of the latter. Such breccias could either be talus breccias resulting from mass wasting at the base of thick massive lava flow (i.e., sedimentary breccias) or they may represent the cementation of debris fallen into cracks of massive lava flow during their emplacement and cooling on the seafloor.

Both hyaloclastites and basaltic breccias were recovered sporadically in Hole 896A. Most hyaloclastites are restricted to intervals of pillow lavas and are commonly observed directly against glassy chilled margins of pillows. The clasts comprise blocky glass shards or angular clasts of subvolcanic basalt, of the order of 1–15 mm across, cemented either by dark green or black clays and/or green clay + carbonate (Fig. 42). Thin-section observations reveal that many breccia cements exhibit intricate concentric patterns in the dark clays, as well as the common presence of fibro-radial phillipsite (Fig. 43). Other breccias are cemented by green clays and blocky aragonite. These two types of breccia cement may be related temporally as in the clay-zeolite-aragonite veins, which invariably comprise early clay + zeolite (phillipsite) margins and later aragonite cores. Many clasts in hyaloclastites are completely altered to clays. Igneous olivine is



Figure 40. Network of thin, irregular, bifurcating veinlets grading into in-situ pillow breccia at the glassy rim of a pillow in Sample 148-896A-28R-1, Piece 18ABC.

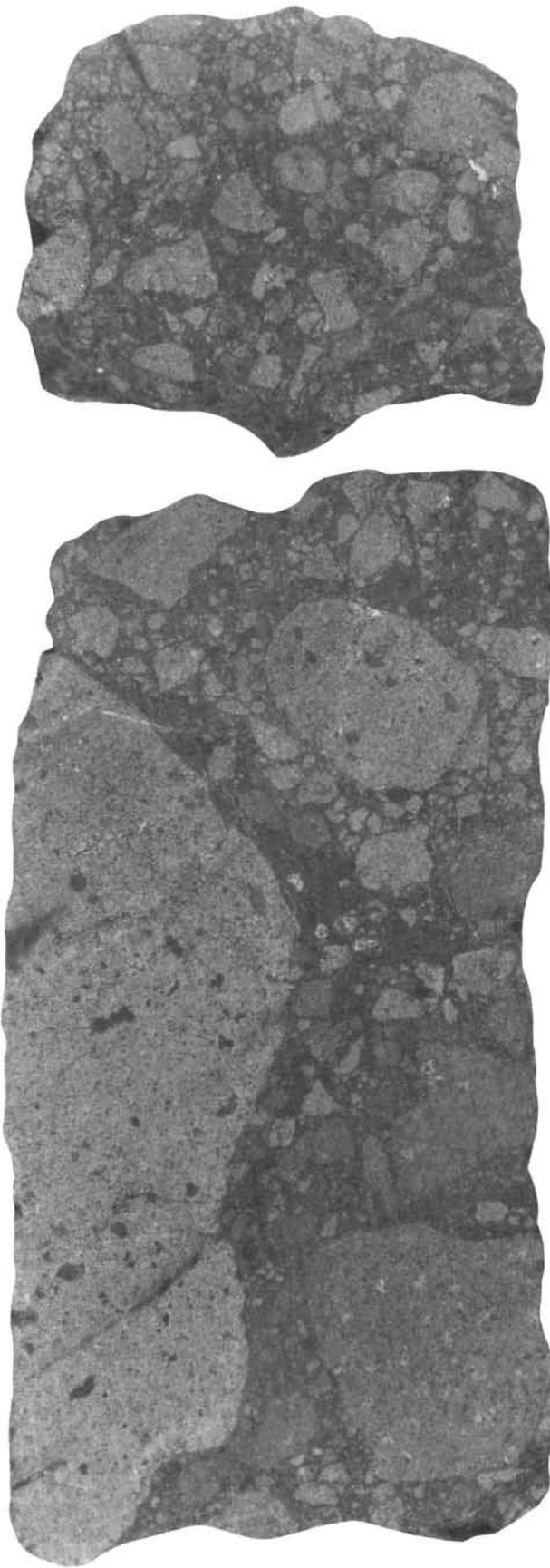


Figure 41. Regular breccia, Sample 148-896A-27R-2, Piece 5AB.

completely replaced by colorless clay, whereas plagioclase is usually fresh or partly altered to tan clay.

### Fluid Inclusions

Aragonite crystals, both blocky and fibrous varieties, that formed in veins and in the matrix of hyaloclastite breccias commonly contain fluid inclusions. The abundance of inclusions is low, and their distribution is highly irregular. Typical inclusions measure between about 2 and 10 mm in diameter, and are filled with one phase, probably liquid. Very few inclusions contain the two phases of liquid plus a vapor bubble.

Inclusions occur along sub-planar arrays, indicating that they were formed as a result of fracture healing in the presence of fluid (i.e., all are secondary inclusions). Commonly, such arrays cut intercrystalline boundaries, showing that the vein-filling aragonite fibers were fractured as a multicrystalline unit. Rarely, in fibrous aragonite veins, secondary inclusion trails form in parallel swarms that are subparallel to the vein walls and perpendicular to the fibers. In general, however, there is no preferred orientation of healed fractures. There are no unequivocal primary inclusions representing entrapment of the fluid from which the aragonite initially grew.

The fact that nearly all inclusions are single-phase suggests that the temperature of trapping, or fracture healing, was low enough that fluid contraction upon cooling to room temperature was insufficient to nucleate a vapor bubble. Generally such inclusions are formed at less than 60°–70°C. Those inclusions with vapor may have had favorable shapes for nucleating bubbles, in which case they will provide accurate estimates of trapping temperatures after heating studies. Alternatively, the bubbles may have appeared due to inclusion leakage, which can be discerned through the measurement of homogenization temperatures.

### Discussion and Conclusions

In this section, new observations of oceanic crustal alteration made on samples from Hole 896A are summarized and preliminary interpretations are given. We review evidence on the chronology of alteration of oceanic crust at Site 896 and conclude by presenting a detailed comparison of Hole 896A with the analogous upper part of Hole 504B, located 1 km away.

Two contrasting alteration styles dominate the Site 896 samples. These styles have been described above as oxidative and non-oxidative to emphasize the major distinguishing characteristic: the presence or absence of ferric iron-rich minerals. These styles could also be termed the oxidative and the saponitic types. A major question is whether the oxidative alteration overprints the non-oxidative saponite alteration. Details given above suggest that both sequences may have occurred in different individual samples.

Crosscutting and reopening relationships among veins generally indicate the following temporal depositional sequence of secondary minerals in open fractures: (1) brown Fe oxyhydroxides and/or dark green clay minerals; (2) light green clay minerals; and (3) carbonates. When phillipsite is present, the following sequence is observed: (1) green clay; (2) phillipsite; (3) pale brown smectite; (4) calcite; and (5) calcite or aragonite (Fig. 31, Sample 148-896A-8R-1, Piece 12).

The sequence is commonly ambiguous and one must be very cautious in such cases. For instance, in Sample 148-896A-7R-1, Piece 10B, a vein is composed of dark green clay + carbonate, each of these minerals occurring either at the selvage or in the center depending on which segment of the vein is observed. In Sample 148-896A-7R-1, Piece 6, two veins composed of light green clay at the selvage and carbonate in the center merge into one another. One of the veins is intersected by a light green clay vein. Such an observation can be interpreted either by inferring that the light green clay or the carbonate formed first.

In many samples, oxidative alteration halos are clearly linked to the presence of veins. In fine-grained pillow rims, thin millimeter-scale oxidation halos develop around thin, dark clay veins. In slightly

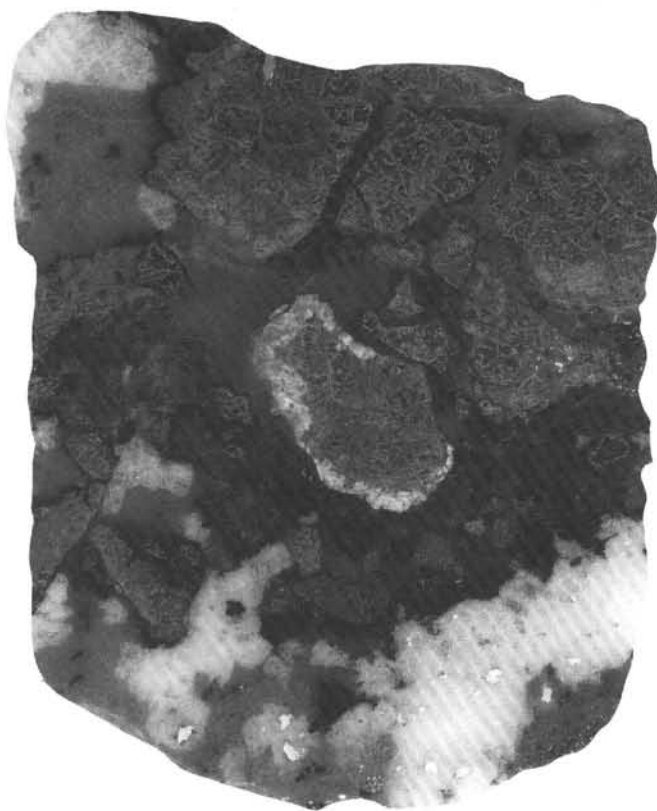


Figure 42. Hyaloclastite, Sample 148-896A-14R-1, Piece 5.

coarser-grained basalts (pillow interiors and the massive basalts), well-developed halos commonly flank clay veins symmetrically or, less commonly, asymmetrically. In contrast, oxidation halos do not flank the later carbonate-bearing veins. Many carbonate veins cut through oxidation halos at high angles. Thus, vein relations suggest that oxidative alteration was developed early, in general before the major development of carbonate in re-opened clay veins or in new carbonate-only veins.

One possible general sequence of alteration involves the early introduction of hydrothermal fluid having elevated oxygen fugacity (i.e., seawater). At relatively low temperatures (probably less than 100°C, based on experience from studies of similar oceanic rocks, and on the absence of higher-temperature minerals), this fluid may have reacted with the rock and developed clay-lined fractures that became flanked with oxidative alteration halos. Multiple episodes at this stage may have generated complex overprinting halo relations. Subsequent to the early oxidation, hydrothermal fluid having a paucity of oxygen may have permeated the basalts, introduced along fractures that eventually sealed with clays, zeolites, and then carbonates. This could represent the stage at which widespread saponite development occurred in the majority of the basalts. In this scenario, the saponitic alteration had little noticeable effect on the earlier-formed oxidation halos.

An alternate interpretation of the sequence of alteration involves early, incomplete saponitic, non-oxidative alteration, followed by oxidative alteration along a later generation of veins. A third vein generation, resulting in carbonate veins that cut oxidation halos, represents another low oxygen fugacity stage. This is the latest stage.

#### Comparison with the Hole 504B Upper Pillow Alteration Zone

As in Hole 896A, no cored sample from Hole 504B is totally fresh: all of the rocks contain alteration minerals partly replacing olivine and

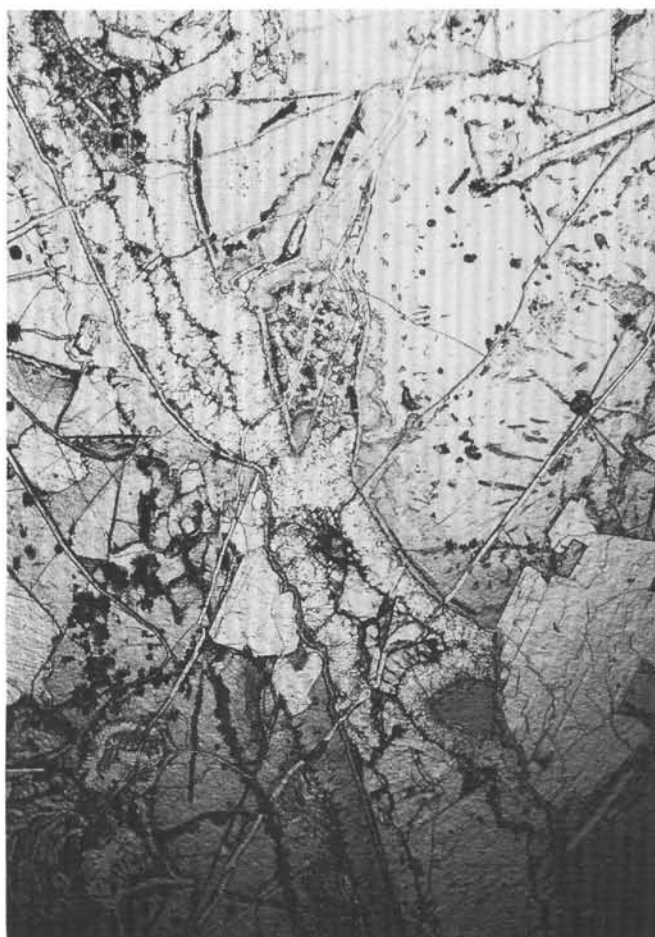


Figure 43. Photomicrograph of Sample 148-896A-7R-1, Piece 10, showing a breccia cemented by successive fillings: pale brown saponite, phillipsite, Ca-carbonate.

filling interstitial voids. The major alteration minerals and their occurrences observed in Hole 896A are similar to those identified in the uppermost 310 m of basement cored in Hole 504B during DSDP Legs 69 and 70 and forming the Upper Pillow Alteration Zone (UPAZ) of Hole 504B (Honnorez et al., 1983). Smectite, and more particularly saponite, is ubiquitous in basalts from both holes; it replaces olivine phenocrysts, fills or replaces interstitial voids, and occurs in veins and breccia cement. The UPAZ of Hole 504B is mainly comprised of pillow lavas, with few massive lava flows and basaltic breccia horizons. The basalts were affected by three alteration processes:

1. The outer parts of some of the samples are characterized by low-temperature oxidation resulting in reddish halos up to 50 mm in thickness. The red color is due to the presence of Fe oxyhydroxides and saponite (i.e., iddingsite) replacing most of the olivine phenocrysts, filling interstitial voids, and staining the igneous silicates. The red halos generally start from exposed surfaces or fissures now coated with or filled by secondary minerals. Red halos are progressively less frequent and lighter in color with depth in Hole 504B until they disappear at 584 mbsf (i.e., 310 m sub-basement).

2. The inner parts of the red-halo-bearing samples and of the bulk of the other samples without halos exhibit a uniform dark gray color. They contain saponite as the major secondary mineral filling interstitial voids, replacing the olivine phenocrysts, and sometimes partly replacing plagioclase phenocrysts when they are adjacent to veins. The contact between the outer red halos and the gray inner parts is generally sharp, even under the microscope. Small amounts of secondary pyrite are sometimes present in the gray zones.

3. The third alteration process observed in Hole 504B is more rare and far more limited in extent than the other two. It results in dark gray bands or black halos more commonly located between exposed surfaces and red halos than between the latter and the inner gray cores. These dark gray bands range from 2 to 10 mm in width. The dark gray bands and halos are characterized by the presence of green clay minerals (mixtures of or mixed-layer nontronite and celadonite) and Fe oxyhydroxides replacing the olivine phenocrysts and filling interstitial voids.

Most veins in the Hole 504B UPAZ are commonly less than 0.5 mm in thickness. In the black bands the veins mainly comprise celadonite/nontronite, whereas in the red halos, they contain iddingite. In the gray inner cores they are comprised of saponite and, less frequently, successively farther away from the selvages, phillipsite and a calcium carbonate (either calcite or aragonite). One fissure filled with Fe oxyhydroxides in a red halo extends into the adjacent dark gray rock as a saponite and pyrite filling.

The most obvious difference between rocks from Hole 896A and from Hole 504B is the greater size and abundance of the veins, and the larger proportion of carbonate, particularly aragonite in the former. Breccias and hyaloclastites are more abundant in the cores from Hole 896A. The general picture is that of a much more tightly cemented oceanic crust in Hole 896A than in Hole 504B.

## IGNEOUS AND METAMORPHIC GEOCHEMISTRY

### Introduction

Hole 896A drilled during Leg 148 penetrated 290 m of basement. Fifty-one lithological units of sparsely to highly phyrlic tholeiitic basalts were defined from this section, consisting mainly of pillow lavas (about 57%), some massive lava flows (about 38%), and minor pillow breccias and hyaloclastites. The basalts are predominantly plagioclase-olivine phyrlic in the upper part of the section, but commonly plagioclase-olivine-clinopyroxene phyrlic in the lower part (see Fig. 20). From Hole 896A, 64 samples were selected for geochemical analyses by the Shipboard Scientific Party.

### Results

The chemical composition of the basalts are shown in Table 6. They are strongly depleted, moderately evolved MORB (MgO: 6.69–9.74 wt%,  $\text{Fe}_2\text{O}_3^*$ : 8.10–10.32 wt%,  $\text{Mg}^*$ -value: 0.609–0.698, Ni: 82–198 ppm, Cr: 293–407 ppm, Zr: 32–53 ppm, Nb <3 ppm). Figures 44 and 45 show the major and trace elements plotted against the  $\text{Mg}^*$ -value, respectively. With the exception of MgO, none of the elements show significant correlation with the  $\text{Mg}^*$ -value when viewed as a total batch of data. A wide range of incompatible element abundances at similar  $\text{Mg}^*$ -values can be seen in Figure 44 for  $\text{TiO}_2$  and in Figure 45 for Sr and Zr. This variation is discussed later.

### Variation with Depth

Figures 46 and 47 show the variations in the major and trace elements with depth, respectively. For a number of the elements there are trends, shown by progressive increases or decreases down the section. The  $\text{SiO}_2$  content shows a general decrease downhole to a level of 316 mbsf, then increases rapidly to 350 mbsf, and then decreases down to 440 mbsf. The last six samples (below 450 mbsf) again show high  $\text{SiO}_2$  content (>50 wt%).  $\text{Al}_2\text{O}_3$  shows a general decrease downhole, with a minor jump to higher concentration at around 420 mbsf, whereas  $\text{Fe}_2\text{O}_3^*$  and MnO show rather steady downhole increases in concentrations. The CaO concentration shows a well-defined increase downhole to 260 mbsf, lower concentrations at around 270 mbsf and then an increase down to 325 mbsf, below which it decreases down to 390 mbsf, and then increases. The concentrations of  $\text{TiO}_2$ , Y, and Zr, in particular the former, show well-defined trends. From the top

of the basement to approximately 340 mbsf, the concentrations of these elements show a slight increase, then jump suddenly to higher concentrations, and subsequently decrease downhole. At around 435 mbsf two samples (Samples 148-896A-27R-2, 109–120 cm, and -896A-28R-1, 54–58 cm) show extreme depletions of  $\text{TiO}_2$ , Y, and Zr. V defines a downhole trend similar to that for  $\text{TiO}_2$ , whereas the trends of Ni and Cr are approximately antipathetic to that of  $\text{TiO}_2$ . Zn shows a steady increase downhole to 400 mbsf, where there is a sudden drop in concentration and then an increase downhole.

### Comparison between Holes 504B and 896A

Figure 48 shows the comparison between the geochemistry of the basalts from Holes 504B and 896A, with respect to  $\text{Al}_2\text{O}_3$ ,  $\text{TiO}_2$ , MnO, CaO, Cr, V, Y, Zr, and Zn. It is apparent that the concentration of these elements, as well as most of the downhole geochemical trends differ between the two holes. In general there is more scatter in the Hole 504B data than in those from Hole 896A. In the upper 150 m of basement, the Hole 896A basalts are higher in  $\text{Al}_2\text{O}_3$  and CaO, and lower in  $\text{TiO}_2$ , V, Y, Zr, and Zn. Below this level differences between the two holes are not so obvious, except for V.

### Alteration

In order to make some preliminary estimate of the extent to which elements may have been depleted or enriched as a result of alteration in Hole 504B, the element concentrations have been plotted against the  $\text{H}_2\text{O}^+$  content and percentage alteration (Figs. 45 and 46, "Site 504" chapter, this volume). In the basalts from Hole 896A, the  $\text{H}_2\text{O}^+$  content varies between 0.63–3.31 wt% (Table 6), whereas the alteration (replacement of primary minerals by secondary minerals) of the bulk rock is mostly much less than 10% (see "Alteration" section, this chapter). In Figure 49 a number of minor and trace elements have been plotted against  $\text{H}_2\text{O}^+$ . In the case of  $\text{TiO}_2$ , Zr, Y, Zn, and Ni there is no systematic change with increasing  $\text{H}_2\text{O}^+$ . For Sr and Cr a slight increase, and for V a slight decrease, in concentration can be seen with increasing  $\text{H}_2\text{O}^+$ . The high  $\text{K}_2\text{O}$  contents (>0.2%) and low S contents (<500 ppm) in Figures 46 and 47 are probably the results of low temperature alteration processes.

### Discussion

The spread in the immobile incompatible elements (i.e., Ti, Y, Zr) at a given  $\text{Mg}^*$ -value, as well as near total lack of correlation between elements and their  $\text{Mg}^*$ -values (Figs. 44 and 45), cannot be readily explained by simple closed-system crystal fractionation (Rayleigh fractionation) from magma batches of similar composition (e.g., Hagen and Neumann, 1990). The large spread in the above-mentioned elements, however, more probably reflects production of magma batches of different origin. Further fractional crystallization from such individual magma batches would produce smooth enrichment trends with respect to the incompatible elements and depletion trends for compatible elements. This may be reflected in the Zr and Ni versus  $\text{Mg}^*$  diagrams (Fig. 45). The uphole, rather smooth enrichment in  $\text{SiO}_2$ , interrupted by rapid resets, and the opposite trend with respect to CaO (Fig. 46), would also indicate fractionation cycles.

Compared to normal MORB (Sun and McDonough, 1989), the basalts from Hole 896A can be considered as highly depleted in incompatible elements, and in the upper 150 m of basement more depleted than the basalts at the same level in Hole 504B (Fig. 48). The depleted nature of the Costa Rica Rift basalts has been commented on, and two models have been proposed. Natland et al. (1983) and Emmermann (1985) suggested that the basalts represent highly primitive examples, whereas others (Autio and Rhodes, 1981, 1983; Kempton et al., 1985; Autio et al., 1989) propose multistage melting of a normal ocean ridge mantle source, followed by crystal fractionation. Our minor and trace element data, particularly  $\text{TiO}_2$ , Zr, and Ni, from

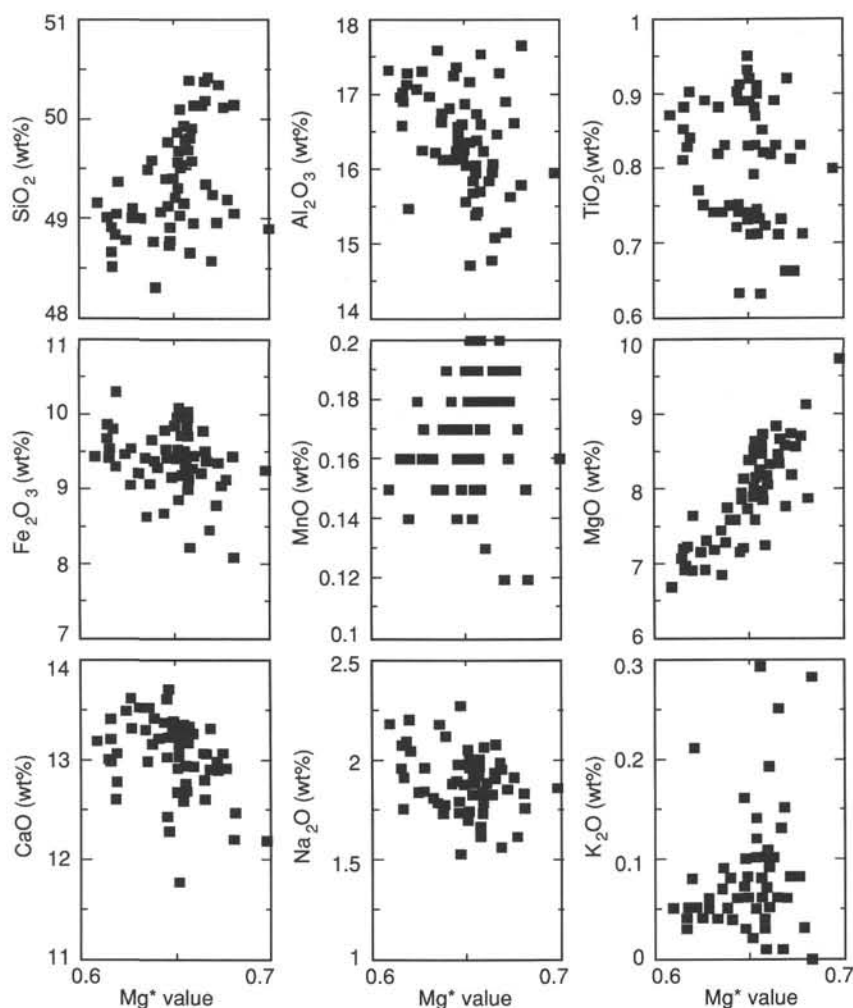


Figure 44. Major element geochemistry plotted against  $Mg^*$  fractionation index of the basalts from Hole 896A drilled during Leg 148.

Hole 896A may, to some extent, support the latter suggestion. However, if this process alone should account for the nature of the Hole 504B and Hole 896A basalts a progressive depletion uphole might be expected. To some extent this can be seen, but in the lower part of Hole 896A, the intercalation of highly depleted and less depleted basalts (see  $TiO_2$  and Zr plots of Fig. 48) can probably not be explained by multistage melting alone. This feature is even more clearly demonstrated in the comparative plots of  $TiO_2$  and Zr against depth from Hole 504B (Fig. 48). Some of the samples are highly phyrlic however, and the effect of removing the phenocrysts has not been considered here. An explanation for the sporadic appearance of less depleted to normal and even enriched MORB (the two latter types in Hole 504B, see  $TiO_2$  and Zr plots of Figs. 48 and 49), may be that these basalts belong to a magma chamber system not connected to that yielding the highly depleted basalts. This possibility will be investigated by some of the Leg 148 petrologists as part of the post-cruise research on the Costa Rica Rift basalts.

## STRUCTURE AND DEFORMATION

### Introduction

The rocks recovered at Hole 896A are the first from the upper part of Layer 2 of the ocean crust to be systematically studied by a group of shipboard structural geologists. Observed structures include veins, breccias, and rare dike margins. More than 600 veins were measured, and detailed structural observations were made on 30 cores (see the

Structural and Deformation Logs, Appendixes H and I). Techniques and methods utilized are discussed in the "Explanatory Notes" chapter, this volume.

### Veins

Veins are the most prominent structural features observed in rocks recovered from Hole 896A. The earliest veins are associated with alteration halos (see "Alteration" section, this chapter), and the rocks are commonly fractured along the walls of various vein types. Although veins oriented both parallel and perpendicular to glassy chilled margins of the pillow lavas are common, the orientation of veins, both in terms of azimuth and dip, is highly variable throughout the drilled sequence (see "Orientation" section below).

The most important distinction of vein types in Hole 896A is the presence or absence of fibers. The terms "fiber" and "fibrous" are used in reference to a crystal morphology characterized by extreme length to width ratio (Ramsay and Huber, 1983). Unlike crystals, which grow into open cavities, the elongated direction of fibers generally has no correlation with respect to crystallography. Fibers track the opening direction of a vein so that fibers oriented normal to the vein walls, such as the vast majority of the Hole 896A veins, indicate pure extension (Cox and Etheridge, 1983). Fibrous veins generally form by numerous cycles of opening and filling. In Hole 896A fibrous veins consist of aragonite and/or smectite. The aragonite fibers show no preferred crystallographic orientation, whereas the

Table 6. Geochemical analyses of Hole 896A basalts, Leg 148.

Leg	148	148	148	148	148	148	148	148	148	148	148	148	148	148	148	148	148	148	148
Hole	896A	896A	896A	896A	896A	896A	896A	896A	896A	896A	896A	896A	896A						
Core	1R	1R	1R	2R	2R	3R	4R	5R	6R	6R	7R	7R	8R	9R	10R	11R	11R	11R	12R
Section	1	1	1	1	1	1	1	1	2	2	1	1	1	1	1	3	3	3	1
Interval (cm)	7-14	14-21	47-55	41-50	94-101	38-41	68-70	38-40	52-54	89-91	58-60	80-83	29-32	138-141	116-118	12-17	48-53	78-81	
Piece	3	4	11	10	21	7	9C	1D	5C	10A	10A	13	7	25	9C	3	8	10B	
Unit	1	2	3	7	7	8	9	10	12	12	13	14	14	14	14	15	16	16	
Lithology	M-PO	M-PO	M-PO	M-PO	M-PO	M-P	M-PO	M-PO	H-PO	H-PO	M-PO	M-PO	H-PO	H-PO	M-PO	S-P	H-PO	H-PO	
Grain size	C-M	M-F	C-M	G-C	C-F	C-M	G-C	G-F	M-F	M-F	G-M	M-F	M-F	M-F	C-F	M-F	M-F	M-F	
Depth (mbsf)	195.17	195.24	195.57	201.31	201.84	210.28	219.58	229.7	238.42	240.27	247.98	248.2	257.39	268.08	277.56	289.04	289.4	296.38	
SiO <sub>2</sub> (wt %)	50.14	49.25	49.40	49.92	48.96	49.19	49.03	49.73	49.41	49.59	49.00	49.31	49.13	48.95	48.74	49.48	48.57	49.02	
Al <sub>2</sub> O <sub>3</sub>	17.64	17.27	17.25	17.52	16.89	16.59	17.15	16.72	16.58	16.72	16.95	16.86	17.35	16.23	16.49	16.22	16.46	16.33	
TiO <sub>2</sub>	0.71	0.73	0.72	0.73	0.66	0.66	0.71	0.71	0.74	0.74	0.74	0.73	0.75	0.72	0.74	0.82	0.71	0.73	
Fe <sub>2</sub> O <sub>3</sub> *	8.10	8.45	8.68	8.25	8.80	9.14	8.87	9.03	9.18	9.09	9.24	9.19	8.71	9.48	9.45	9.43	9.40	9.57	
MgO	7.87	7.76	7.16	7.24	8.19	8.70	7.57	7.86	7.71	7.27	7.20	7.78	7.22	8.36	7.87	7.45	8.61	8.16	
CaO	12.47	13.30	13.36	13.27	13.00	12.90	13.25	13.33	13.31	13.50	13.51	13.37	13.59	12.91	13.20	13.29	12.89	13.13	
Na <sub>2</sub> O	1.75	1.95	1.89	1.73	1.84	1.61	1.82	1.67	1.74	1.72	1.80	1.73	1.87	1.86	1.73	1.78	1.56	1.74	
K <sub>2</sub> O	0.28	0.08	0.06	0.09	0.08	0.03	0.05	0.03	0.06	0.05	0.04	0.06	0.07	0.10	0.08	0.07	0.06	0.10	
MnO	0.12	0.12	0.14	0.13	0.16	0.17	0.16	0.15	0.16	0.15	0.16	0.16	0.17	0.18	0.17	0.15	0.19	0.18	
P <sub>2</sub> O <sub>5</sub>	0.03	0.05	0.03	0.03	0.03	0.02	0.04	0.03	0.04	0.03	0.03	0.03	0.04	0.04	0.03	0.03	0.04	0.04	
LOI	0.63	0.81	0.95	0.75	1.00	0.76	0.98	0.55	0.99	0.76	1.00	0.93	0.83	1.13	1.11	1.15	1.23	0.90	
Total	99.74	99.77	99.64	99.66	99.61	99.77	99.63	99.81	99.92	99.62	99.67	100.15	99.73	99.96	99.61	99.87	99.72	99.90	
H <sub>2</sub> O <sup>+</sup>	n.a.	1.82	2.25	2.16	1.89	2.30	2.42	2.00	2.56	2.27	2.19	2.07	1.96	2.31	0.37	2.99	2.97	1.72	
CO <sub>2</sub>	n.a.	0.16	0.08	0.41	0.18	0.08	0.20	0.09	0.19	0.10	0.16	0.20	0.19	0.20	0.16	0.19	0.23	0.25	
SO <sub>2</sub>	n.a.	0.04	0.05	0.04	0.05	0.06	0.05	0.10	0.07	0.06	0.06	0.03	0.05	n.d.	0.07	0.02	0.06	0.04	
S (ppm)	812	454	1007	952	806	922	1060	1042	1077	978	1006	1015	978	473	710	1080	804	298	
Sc	48	48	49	47	40	40	44	45	37	41	46	50	46	40	42	46	44	43	
V	230	239	232	237	217	213	226	232	231	234	234	226	229	232	221	260	224	221	
Cr	385	379	399	407	376	369	384	371	387	385	387	363	406	379	366	387	367	347	
Ni	181	125	169	174	179	182	175	167	167	163	164	164	159	162	178	148	161	169	
Cu	93	91	99	100	96	99	89	97	98	99	92	93	95	95	98	100	90	90	
Zn	56	53	63	62	57	59	60	60	62	57	61	61	64	58	62	68	61	57	
Ga	13	15	14	12	14	13	14	14	14	15	14	14	13	13	14	16	16	16	
Rb	1	2	1	2	3	<1	1	<1	1	3	4	2	2	4	1	2	3	3	
Sr	70	69	66	72	67	61	66	63	63	67	72	69	72	66	67	70	61	74	
Y	18	23	21	22	20	21	20	21	22	22	21	22	21	22	22	24	20	21	
Zr	40	43	37	44	38	41	41	38	45	44	43	43	41	44	45	45	42	39	
Nb	<1	<1	1	<1	<1	1	1	<1	<1	<1	<1	2	2	2	<1	<1	<1	<1	
Ba	<8	<8	<8	12	<8	<8	9	16	<8	14	23	35	8	16	<8	20	16	10	
Mg <sup>+</sup> -value	0.681	0.669	0.645	0.659	0.672	0.677	0.653	0.657	0.649	0.638	0.632	0.651	0.646	0.66	0.647	0.635	0.668	0.652	

clay fibers are arranged with their (001) planes orthogonal or at a high angle to the vein walls.

### Non-fibrous veins

Non-fibrous veins consist of Fe-oxyhydroxide + brown clay, dark and light green clay, and blocky carbonate and/or clay. The Fe-oxyhydroxide-bearing veins are the least common and tend to be very thin (mm wide) compared to most carbonate- and clay-filled veins. They are generally irregular-to-sinuuous in shape and have wide, gray to red to orange alteration halos. In some samples they show branching and anastomosing character and green clay in the vein center, possibly due to reopening of the vein (Sample 148-896A-17R-5, 7-16 cm). In addition to the existence of Fe-oxyhydroxide + clay veins, intracrystalline cracks in plagioclase phenocrysts are filled with Fe-oxyhydroxide in some samples (Sample 148-896A-12R-1, 68-71 cm, Piece 9C; -12R-2, 9-12 cm, Piece 1C; -14R-2, 135-137 cm, Piece 19; -16R-1, 31-34 cm, Piece 3B; -16R-3, 88-91 cm, Piece 4B; -17R-4, 118-123 cm, Piece 12).

Blocky carbonate + clay veins and many light-green clay veins have spherical-like ("vermicular") aggregates evident in both hand specimen (Fig. 35) and thin section (see "Alteration" section, this chapter). These veins are generally relatively thick (1-8 mm wide), display a curvilinear to sinuous morphology, and are locally quite irregular (e.g., large vein-cutting chilled margin in Fig. 7). In thin section, the blocky carbonate (148-896A-5R-2, 20-23 cm, Piece 1B; -7R-1, 52-55 cm, Piece 10) consists of large crystals (up to about 2 mm in width) arranged in a mosaic texture.

Non-fibrous clay-filled veins are commonly thin (0.1 to 0.5 mm in width) occurring as planar to curvilinear single veins or as anastomosing and branching vein systems. Irregular clay veins <1 mm wide

are locally well-developed, part of a complex network of vein systems and/or incipient brecciation near the glassy chilled margins (i.e., Sample 148-896A-10R-1, 13-45 cm; -18R-1, 80-86 cm). Most of these veins are filled with dark-green clay. Vermicular clay + carbonate is commonly present in the vein networks, but in many cases it appears to have been deposited during subsequent vein reopening (see "Alteration" section, this chapter).

### Fibrous veins

Fibrous veins consisting of aragonite and/or clay show a broad range of width (0.5 mm to 8 mm) and range from planar and curvilinear to sinuous and irregular. The thinner fibrous veins (~0.5-1.00 mm wide) tend to be curvilinear, locally show abrupt changes in orientation, and are commonly discontinuous. Fibrous veins also display overlapping vein segments and triple-junction intersections characteristic of fracture propagation (Fig. 50). These veins are readily recognized in hand specimen by the presence of fibers and their silky luster.

Carbonate fibers are mostly oriented with their long axis orthogonal to the vein walls, and individual carbonate fibers extend from wall-to-wall with crystallographic continuity (Fig. 51; "stretched" fibers of Ramsay and Huber, 1983) (e.g., Sample 148-896A, 3R-1, 83-86 cm, Piece 9A). Carbonate fibers commonly become wider from the vein walls toward the vein center (Samples 148-896A-5R-3, 1-5 cm, Piece 1A; -7R-1, 5-8 cm, Piece 1; -7R-1, 135-139 cm, Piece 22) at the expense of other finer-grained fibers that pinch out inward. This change in fiber width is interpreted to be a result of incremental growth from the wall to the center of the veins (Ramsay and Huber, 1983). In some samples, carbonate fibers appear slightly curved (Samples 148-896A-3R-1, 143-146 cm, Piece 17; -6R-3, 6-9 cm,

Table 6 (continued).

Leg	148	148	148	148	148	148	148	148	148	148	148	148	148
Hole	896A	896A	896A	896A	896A	896A	896A	896A	896A	896A	896A	896A	896A
Core	12R	14R	14R	14R	14R	15R	15R	16R	16R	17R	17R	17R	17R
Section	2	1	2	2	2	1	1	1	3	1	1	3	4
Interval (cm)	9–12	38–41	28–31	58–61	113–115	23–29	103–106	31–34	88–91	1–3	82–84	89–93	99–102
Piece	1C	2B	3	7	16A	4	15	3B	4B	1A	10B	8	9
Unit	17	18	19	20	21	22	23	24	24	25	26	28	28
Lithology	H-PO	H-PO	H-PO	S-O	H-PO	H-PO	H-PO	M-PO	H-PO	H-PO	M-PO	H-PO	M-PO
Grain size	M-F	M-F	M-F	M-F	M-F	M-F	M-F	M-F	M-F	M-F	M-F	M-F	M-F
Depth (mbsf)	297.14	314.98	316.29	316.59	317.14	324.53	325.33	334.21	337.58	343.51	344.32	347.33	348.89
SiO <sub>2</sub> (wt %)	49.84	49.07	48.52	49.12	48.77	49.01	48.78	49.85	49.22	49.58	50.33	49.93	49.37
Al <sub>2</sub> O <sub>3</sub>	16.38	16.80	16.99	16.23	16.60	17.29	17.04	15.97	16.28	16.14	15.13	15.85	15.48
TiO <sub>2</sub>	0.74	0.75	0.81	0.89	0.74	0.75	0.77	0.83	0.74	0.89	0.92	0.88	0.90
Fe <sub>2</sub> O <sub>3</sub> *	9.18	9.31	9.46	9.57	9.67	9.07	9.48	9.34	9.51	9.41	9.36	9.53	10.32
MgO	8.00	7.59	6.91	7.32	7.75	6.93	7.16	8.09	8.01	7.96	8.74	8.21	7.64
CaO	13.15	13.18	13.40	13.30	13.15	13.61	13.49	13.21	13.27	13.03	12.87	12.93	12.78
Na <sub>2</sub> O	1.92	1.87	1.75	1.96	1.77	1.83	1.83	1.99	1.99	2.04	1.90	1.92	2.19
K <sub>2</sub> O	0.01	0.06	0.05	0.06	0.08	0.05	0.04	0.05	0.02	0.08	0.08	0.10	0.21
MnO	0.17	0.18	0.16	0.16	0.17	0.17	0.18	0.18	0.17	0.18	0.18	0.18	0.16
P <sub>2</sub> O <sub>5</sub>	0.04	0.05	0.03	0.05	0.04	0.04	0.04	0.04	0.03	0.06	0.05	0.05	0.06
LOI	0.61	0.80	1.56	0.88	0.83	0.78	0.81	0.40	0.68	0.48	0.08	0.10	0.55
Total	100.04	99.66	99.64	99.54	99.57	99.53	99.62	99.95	99.92	99.85	99.64	99.68	99.66
H <sub>2</sub> O*	1.52	2.39	2.37	2.64	2.01	2.63	2.16	1.40	1.50	1.35	1.12	n.a.	n.a.
CO <sub>2</sub>	0.29	0.24	0.35	0.18	0.18	0.21	0.20	0.14	0.24	0.23	0.21	n.a.	n.a.
SO <sub>2</sub>	0.09	n.d.	0.02	n.d.	n.d.	0.04	n.d.	n.d.	n.d.	n.d.	n.d.	n.a.	n.a.
S (ppm)	1590	797	835	1249	140	868	1038	147	94	695	921	571	102
Sc	39	42	46	50	39	44	48	38	38	45	43	44	47
V	224	238	246	272	225	231	238	253	232	264	284	260	277
Cr	353	341	354	360	342	346	334	335	328	307	317	293	301
Ni	166	156	152	109	151	162	143	164	161	121	183	132	82
Cu	95	91	95	98	96	97	92	67	76	82	113	87	63
Zn	63	59	67	72	61	62	60	65	56	65	75	70	63
Ga	15	14	14	16	14	14	14	13	14	15	15	13	16
Rb	2	2	1	2	3	2	3	1	1	3	1	4	5
Sr	61	64	67	68	65	68	64	62	76	64	58	61	61
Y	21	23	22	25	24	22	23	25	22	24	26	24	25
Zr	46	47	44	50	40	44	45	49	40	51	52	53	51
Nb	<1	<1	2	<1	<1	<1	1	2	<1	<1	2	2	<1
Ba	<8	8	9	14	12	13	9	14	17	19	18	25	26
Mg <sup>+</sup> -value	0.657	0.642	0.616	0.627	0.638	0.627	0.624	0.656	0.65	0.651	0.673	0.655	0.62

Piece 1; -7R-1, 135–139 cm, Piece 22). Most of the fibrous carbonate veins also contain some parallel clay fibers, typically along the vein walls but sometimes alternating with carbonate fibers (vein subparallel to pillow margin).

Clay fibers have their (001) plane orthogonal to the vein wall, resulting in uniform extinction when viewed with crossed nicols. In some fibrous clay veins, the fibers extending from each wall meet along an irregular suture line located near the center of the vein. Clay fibers may be straight or curved (Samples 148-896A-1R-1, 47–55 cm, Piece 11, and 148-896A-12R-2, 31–37 cm, Piece 3), and locally they are crenulated (Sample 148-896A, 1R-1, 47–55 cm, Piece 11). In Sample 148-896A, 1R-1, 47–55 cm, Piece 11, clay veins contain solid inclusions (“inclusion bands;” Ramsay, 1980), which are visible only at high magnification and are arranged in bands parallel to the vein walls. The elongated direction of clay fibers is generally orthogonal to the vein walls, but examples of oblique clay fibers have also been observed, particularly in sinuous or irregular veins. Clay fibers also occur in some veins filled by blocky carbonate, where the clay is commonly distributed along the vein walls, and the carbonate material occupies the central part of the veins suggesting that the carbonate was deposited during reopening of the vein.

Composite veins characterized by the coexistence of both non-fibrous and fibrous minerals appear to have formed by reopening of veins. In Sample 148-896A-5R-2, 20–23 cm, Piece 1B, a composite vein about 8 mm wide is filled with blocky carbonate crystals in the center and carbonate and clay fibers along the vein walls (Fig. 52). The fibers are generally oriented with their long axis orthogonal to vein walls and both the clay and carbonate fibers appear to be curved. Some carbonate veins have large crystals (probably calcite) that have partially or completely replaced aragonite fibers due to recrystallization (Sample 148-896A-21R-1, 33–38 cm, Piece 7), as evidenced by

the existence of relict grain boundaries of the original carbonate (aragonite?) crystals. The occurrence of both aragonite and calcite in Sample 148-896A-21R-1, Piece 10, is confirmed by XRD results (see “Alteration” section, this chapter) and is consistent with the interpretation of recrystallization of aragonite to calcite.

### Vein Morphology

Thin carbonate and clay veins display overlapping segments, triple junctions, and T-shape intersections. Veins with T-intersections are common throughout the cores and seem to occur mainly between carbonate-and/or carbonate-clay-filled veins (Fig. 53). Intersections of three vein segments (triple junctions) were observed in several core samples (Figs. 37 and 54). In some cases all three arms of the triple junctions are composed of the same material (carbonate or carbonate + clay fibers) having similar vein thicknesses (e.g., Sample 148-896A-7R-1, 21–44 cm), whereas in other samples two arms are filled predominantly with one mineral while the thinner arm is composed of a different mineral (Sample 148-896A-14R-2, 16–38 cm). The observed triple-junction geometry and T-shaped intersections are reminiscent of thermal contraction fractures (e.g., columnar basalt; Pollard and Aydin, 1988).

Overlapping vein segments are very common in fibrous veins (Fig. 50), and in some samples numerous bridged overlapping segments form an en echelon pattern (Sample 148-896A-12R-1, 24–33 cm). Vein tips in the overlapping segments display mainly a convergent geometry, and anastomosing hairline fractures at and ahead of the convergent vein tips are locally well developed as evident in thin section (Sample 148-896A-7R-1, 135–139 cm, Piece 22). Overlapping vein segments are characteristic of “mode III” cracks, formed during propagation of a surface in which en-echelon cracks at the

Table 6 (continued).

Leg																	
Hole	148	148	148	148	148	148	148	148	148	148	148	148	148	148	148	148	148
Core	896A	896A	896A	896A	896A	896A	896A	896A									
Section	18R	18R	19R	19R	20R	20R	21R	21R	21R	22R	22R	22R	22R	23R	23R	23R	23R
Interval (cm)	1	2	1	2	1	1	1	2	3	1	2	2	4	4	1	3	3
Piece	72-75	60-68	23-25	28-34	14-20	73-77	11-19	27-29	22-24	64-66	81-88	134-138	31-35	43-49	81-85	7-13	128-132
Unit	6B	10	5	6	5	16	3	3B	4A	7A	12A	18A	4	6	11	1	17
Lithology	29	30	30	30	30	31	31	32	32	32	32	33	33	34	36	36	36
Grain size	M-PO	H-PO	H-PO	H-PO	H-POC	H-POC	H-POC	H-PO	H-POC	H-POC		H-POC	H-PO	M-PO		H-OP	
Depth	M-F	M-F	M-F	M-F	M-F	F	M-F	M-F									
	353.82	355.15	356.23	357.76	363.64	364.23	373.11	374.75	376.2	383.24	384.9	385.43	387.33	387.45	392.91	395.07	396.28
SiO <sub>2</sub> (wt %)	49.88	50.37	49.71	50.17	49.65	49.70	49.38	49.50	49.59	49.55	49.16	49.77	49.53	48.76	48.83	48.31	49.05
Al <sub>2</sub> O <sub>3</sub>	15.55	15.40	15.43	15.90	16.06	16.06	16.12	17.56	16.58	15.75	16.05	16.22	16.01	16.54	17.12	16.12	15.77
TiO <sub>2</sub>	0.95	0.90	0.90	0.89	0.91	0.93	0.90	0.88	0.85	0.87	0.89	0.89	0.92	0.91	0.83	0.83	0.83
Fe <sub>2</sub> O <sub>3</sub> *	9.89	9.90	10.03	9.36	9.49	9.45	9.82	8.64	9.27	9.84	9.82	9.55	9.95	9.44	9.83	9.40	9.44
MgO	8.38	8.61	8.73	8.46	8.24	8.01	8.13	6.85	8.15	8.51	8.44	7.92	8.49	7.84	7.24	7.57	9.14
CaO	12.66	12.73	12.66	12.60	12.67	12.92	12.43	12.97	12.90	12.71	12.58	13.01	11.78	12.29	12.60	13.41	12.21
Na <sub>2</sub> O	1.69	1.61	1.81	1.92	1.80	1.96	1.97	2.17	1.79	1.97	1.91	1.79	1.83	2.26	2.09	2.11	1.82
K <sub>2</sub> O	0.05	0.03	0.04	0.13	0.07	0.06	0.16	0.09	0.05	0.06	0.08	0.10	0.12	0.08	0.08	0.04	<0.01
MnO	0.19	0.18	0.20	0.18	0.18	0.18	0.17	0.15	0.17	0.19	0.15	0.16	0.14	0.15	0.16	0.19	0.15
P <sub>2</sub> O <sub>5</sub>	0.05	0.05	0.06	0.05	0.06	0.06	0.06	0.05	0.05	0.06	0.06	0.06	0.06	0.06	0.05	0.04	0.03
LOI	0.30	-0.13	0.15	0.38	0.45	0.40	0.53	0.90	0.66	0.63	0.78	0.43	0.80	1.23	1.08	1.66	1.11
Total	99.59	99.65	99.72	100.04	99.58	99.73	99.67	99.76	100.06	100.14	99.92	99.90	99.63	99.56	99.91	99.68	99.55
H <sub>2</sub> O*	n.a.	n.a.	1.45	0.88	1.46	1.47	1.68	1.68	1.59	1.65	1.65	1.42	2.01	1.98	2.38	1.92	2.17
CO <sub>2</sub>	n.a.	n.a.	0.07	0.15	0.21	0.20	0.17	0.31	0.34	0.10	0.09	0.11	0.20	0.33	0.21	0.98	0.19
SO <sub>2</sub>	n.a.	n.a.	n.d.	n.d.	n.d.	n.d.	n.d.	n.d.	n.d.	0.01							
S (ppm)	1347	1565	1195	502	989	1149	581	550	1252	993	121	650	425	125	183	146	1904
Sc	45	45	43	38	41	39	46	39	39	46	38	42	41	43	39	39	27
V	277	268	266	269	273	273	267	220	252	259	262	256	266	232	214	204	199
Cr	318	331	316	306	320	336	324	395	332	371	326	343	324	327	387	349	321
Ni	120	129	121	181	102	93	109	138	118	120	102	122	106	110	126	149	157
Cu	74	74	66	83	71	77	79	89	72	72	59	83	134	68	95	70	83
Zn	73	73	66	71	67	71	67	66	68	70	63	71	71	68	65	59	67
Ga	17	15	14	16	16	15	14	15	15	13	16	16	13	16	14	14	16
Rb	3	1	3	4	3	<1	3	3	1	2	2	2	3	3	3	5	3
Sr	58	54	53	56	58	61	61	81	58	56	59	59	63	80	78	76	67
Y	26	24	26	25	26	26	25	22	23	24	26	25	27	23	21	22	22
Zr	47	50	47	48	50	53	52	49	48	43	48	52	50	48	46	41	46
Nb	<1	3	2	<1	<1	2	<1	3	<1	<1	<1	<1	<1	2	1	<1	1
Ba	28	<8	22	16	34	22	29	13	28	18	22	9	22	13	22	13	25
Mg*-value	0.651	0.657	0.657	0.665	0.656	0.651	0.646	0.636	0.659	0.656	0.654	0.646	0.652	0.646	0.618	0.639	0.681

propagation front become linked to form a continuous surface. The propagating surface may represent a new fracture, or a preexisting fracture that becomes reactivated and enlarges its surface area along its margins.

### Mechanism of Vein Formation

Textural arrangement of the vein-filling minerals provides information about the evolution of veins. Veins filled with blocky carbonate and/or vermicular clay have characteristics suggesting growing of crystals into open spaces. In contrast, fibrous veins have features pointing to their formation by the crack-seal mechanism, where a vein grows by cycles of hydraulic fracturing followed by sealing due to mineral precipitation from the fluid (Ramsay, 1980; Ramsay and Huber, 1983). In addition to carbonate fibers, this origin is inferred for clay fibers based on their well-developed fiber morphology, and "inclusion bands" parallel to the vein walls. Clay-rich inclusion bands have been observed within a vein filled with stretched carbonate fibers (Sample 148-896A-21R-1, 33-38 cm, Piece 7), where they form a 0.05-mm-wide band near the center of the vein. The inclusion band parallels the vein walls as they curve.

The arrangement of vein-filling fibers suggest that veins can be interpreted as filled extension fissures with fibers growing in the direction of extension. Veins filled by straight fibers perpendicular to vein walls suggest that the displacement vector was orthogonal to the vein walls as in the case of simple extension. The majority of the cores in the upper extrusive sequence include fibrous veins with different orientations that contain wall-perpendicular fibers suggesting extension and hence volume expansion in all directions in these rocks. A change in this style of strain with depth is suggested by the presence in a few samples from the deeper cores of both normal and oblique fibers

occurring within differently oriented segments of the same vein, and fibers subparallel to vein walls (slickenfibers). Some extension veins also have curved fibers, which may indicate deviations in the relative orientations of principal stress directions during vein evolution.

Reopening of veins appears to have occurred frequently, especially for early-formed dark-clay veins, but also for the blocky-carbonate/vermicular clay veins. The coexistence of two textural types are common and suggest reopening in veins characterized by the following: (1) non-fibrous clay along the margins of some fibrous carbonate veins; (2) fibrous clay along the margins of some blocky carbonate veins; (3) dark-green clay along vein margins and light-green vermicular clay + carbonate in the center; and (4) very thin fibrous clay veins anastomosing through some vermicular-clay veins. In addition, much of the original fracturing appears to have been by thermal contraction as discussed above. Figure 55 illustrates the three main types of veins, as observed in thin section, which may correspond to sequential crack-sealing episodes.

### Deformation of Veins

Most of the veins observed in thin section do not show any evidence of significant deformation (brittle or ductile). The occurrence of very localized microfaulting within some veins is observed, however, and this phenomenon is interpreted to have resulted from sliding of clay fibers (Sample 148-896A-6R-3, 6-9 cm, Piece 1). Similar features have also been observed in hand specimen within fibrous carbonate + clay-filled veins (Sample 148-896A-10R-1, Piece 8) where carbonate fiber packets are faulted within a clay matrix in an extended "domino-like" style. This deformation is probably related to different rheological behavior of the "softer" clays and "harder" carbonate fibers after crack-seal processes and healing occurred.

Table 6 (continued).

Leg																148	
Hole	148	148	148	148	148	148	148	148	148	148	148	148	148	148	148	148	896A
Core	896A	896A	896A	896A	896A	896A	896A	896A	896A	896A	896A	896A	896A	896A	896A	896A	30R
Section	24R	24R	25R	26R	26R	26R	27R	27R	27R	28R	29R	29R	29R	30R	30R	30R	1
Interval (cm)	1	3	2	1	1	2	1	1	2	1	1	1	2	1	1	1	137-141
Piece	21-24	23-25	123-134	92-95	134-139	89-88	22-25	71-75	109-112	54-58	49-53	123-126	1-5	5-8	103-107		
Unit	1	3	22	13	19	15	1C	8	13	9	6	18	1B	2	12C	18	
Lithology	36	36	37	39	41	42	42	43	45	47	48	49	50	50	50	51	
Grain size	M-P		M-PO					H-PO	M-PO	H-PO						H-PO	
Depth	M-F		M-F					F	M-F	M-F						M-F	
	402.01	405.01	414.03	421.92	422.34	423.39	430.72	431.21	433.04	440.54	450.19	450.93	451.13	459.35	460.33	460.67	
SiO <sub>2</sub> (wt %)	48.90	49.35	49.01	49.05	49.17	48.66	48.91	49.82	48.91	48.65	50.38	50.13	50.11	50.14	50.10	50.40	
Al <sub>2</sub> O <sub>3</sub>	15.95	16.05	16.96	17.26	17.30	16.90	16.56	15.66	16.34	16.05	14.75	15.68	15.61	15.84	14.71	15.06	
TiO <sub>2</sub>	0.80	0.83	0.85	0.84	0.87	0.85	0.88	0.79	0.63	0.63	0.82	0.82	0.81	0.82	0.83	0.83	
Fe <sub>2</sub> O <sub>3</sub> *	9.26	9.22	9.72	9.34	9.46	9.56	9.89	9.76	9.50	9.74	9.80	9.14	9.07	9.31	10.11	9.54	
MgO	9.74	8.34	7.05	6.91	6.69	6.99	7.21	8.42	7.90	8.50	8.84	8.03	8.56	8.35	8.62	8.68	
CaO	12.18	12.82	12.99	13.06	13.17	13.21	12.98	12.63	13.70	13.24	12.79	13.27	13.05	13.05	12.99	13.05	
Na <sub>2</sub> O	1.85	2.07	1.94	2.04	2.17	1.91	2.07	1.82	1.53	1.75	1.89	2.06	1.90	1.82	1.86	1.98	
K <sub>2</sub> O	<0.01	0.01	0.04	0.05	0.05	0.03	0.05	0.29	0.03	0.11	0.25	0.19	0.08	0.06	0.14	0.15	
MnO	0.16	0.18	0.16	0.14	0.15	0.16	0.16	0.18	0.15	0.16	0.19	0.18	0.19	0.19	0.20	0.20	
P <sub>2</sub> O <sub>5</sub>	0.03	0.03	0.04	0.03	0.03	0.03	0.04	0.04	0.02	0.04	0.05	0.05	0.04	0.05	0.05	0.04	
LOI	1.08	0.83	1.06	1.08	0.88	1.34	1.00	0.40	0.83	0.99	0.13	0.35	0.10	0.03	-0.03	0.08	
Total	99.95	99.73	99.82	99.80	99.94	99.64	99.75	99.81	99.54	99.86	99.89	99.90	99.52	99.66	99.58	100.01	
H <sub>2</sub> O*	1.70	1.67	3.31	2.97	2.95	2.97	1.95	1.70	2.71	2.68	0.63	1.23	1.00	1.06	0.72	0.89	
CO <sub>2</sub>	0.15	0.38	0.28	0.19	0.21	0.41	0.20	0.19	0.18	0.59	0.05	0.10	0.11	0.07	0.05	0.06	
SO <sub>2</sub>	0.03	0.03	n.d.	n.d.	n.d.	n.d.	n.d.	n.d.	n.d.	n.d.	n.d.	n.d.	n.d.	n.d.	n.d.	n.d.	
S (ppm)	1911	1243	938	792	1210	946	885	327	582	267	220	135	404	1001	589	273	
Sc	35	35	43	41	44	37	39	39	41	38	46	39	40	45	42	41	
V	193	199	196	201	222	208	216	216	200	201	249	242	229	236	253	255	
Cr	305	313	347	373	394	367	364	378	366	395	341	384	357	366	368	346	
Ni	157	162	192	198	201	185	163	168	170	164	127	137	186	137	123	155	
Cu	83	82	81	88	93	81	89	74	78	71	93	63	106	91	95	72	
Zn	50	56	59	60	66	64	65	58	59	57	66	70	62	64	65	65	
Ga	15	14	15	13	14	14	15	14	15	14	14	14	14	15	14	13	
Rb	1	1	<1	2	2	2	1	7	2	2	7	4	2	3	4	5	
Sr	64	82	72	69	72	86	69	65	69	74	54	61	60	63	55	56	
Y	22	22	20	21	22	20	24	21	17	17	22	25	20	24	20	23	
Zr	47	49	48	48	50	48	49	43	32	32	47	45	47	45	42	47	
Nb	<1	2	<1	<1	<1	1	<1	2	2	<1	<1	2	1	<1	3	<1	
Ba	24	22	12	29	32	38	14	29	<8	<8	13	29	15	17	31	30	
Mg* -value	0.698	0.666	0.615	0.619	0.609	0.617	0.616	0.655	0.647	0.658	0.665	0.659	0.675	0.664	0.652	0.667	

Note: Unit rock names and grain size data are from the thin section description. Abbreviations for rock names: S: sparsely phytic; M: moderately phytic; H: highly phytic; P: plagioclase; O: olivine; C: clinopyroxene. Abbreviations for grain-size data: G: glassy; C: cryptocrystalline; M: microcrystalline; F: fine-grained. Fe<sub>2</sub>O<sub>3</sub> is the total amount of iron expressed as Fe<sub>2</sub>O<sub>3</sub>. The Mg\* value is the molar ratio MgO/MgO + FeO, where FeO is calculated to be 90% of the total iron as FeO; n.a. = not analyzed; n.d. = no data.

The occurrence of curved clay fibers and carbonate fibers filling the veins may also be attributed to changes in the relative orientations of principal strain directions as discussed above, rather than compression.

### Breccias

Several types of breccias have been observed in samples recovered from Hole 896A. The first type is considered to be hyaloclastite formed on the sea floor by fragmentation of glassy pillow rims (see "Alteration" section, this chapter). These breccias consist of clasts of volcanic glass surrounded by a matrix composed of clay and altered glass. Locally "clouds" of coarse-grained carbonate may occur in the matrix (Fig. 60).

A second type of breccia consists primarily of angular to sub-angular clasts of basalt and variable amounts of glass (Fig. 10). The clasts generally range from approximately 1 mm to 1 cm in size, cemented by coarse-grained carbonate and/or clay minerals (e.g., Sample 148-896A-8R-1, Piece 9). These typically have sharp contacts with unbrecciated basalt. Other breccias of this type consist primarily of basalt clasts showing evidence for alteration, oxidation, and vein development prior to cementation, and the fragments are sub-angular to sub-rounded in shape (Fig. 57) (Samples 148-896A-20R-1, 83-88 cm, Piece 18; -23R-3, 18-20 cm, Piece 3; -28R-2, 45-54 cm, Piece 4). Some clasts are cut by thin, commonly clay-filled veins, which do not appear in hand specimen to crosscut the matrix. These clasts generally have sharp, smooth boundaries, but locally they have irregular, diffuse boundaries with the matrix and their edges appear to grade into the matrix through thin microbreccia zones

containing abundant clay. The matrix of these breccias contains clasts of plagioclase, clinopyroxene, and clay cemented by green clay commonly associated with Fe-oxyhydroxides. These breccias are commonly matrix-supported. In thin section, the carbonate component of the matrix consists mainly of coarse-grained blocky aragonite, in addition to composite aggregates composed of finer grains of aragonite (e.g., Sample 148-896A-14R-2, 58-61 cm, Piece 7; -8R-1, 54-57 cm, Piece 12). The lack of preferred orientation of clasts, bending, or cracking of mineral grains in the matrix, and lack of a planar fabric in the matrix suggest these breccias did not form by frictional faulting. Instead, the characteristic of the breccias suggest formation on the seafloor by mass wasting on escarpments and existing slopes. Alternatively, these breccias could represent more disaggregated variety of the third type of breccia, interpreted to have formed by fragmentation beneath the seafloor.

The third type of breccia is characterized by a "jigsaw puzzle" fabric where the various clasts can be fitted back together. This breccia type ranges from incipient (e.g., Sample 148-896A-18R-1, Piece 6A) to advanced (Fig. 59, Sample 148-896A-14R-2, Piece 10) stages of fragmentation with clasts "floating" in a matrix of blocky carbonate and vermicular clay (Fig. 60, Sample 148-896A-8R-1, Piece 9). Where brecciation is incipient, the contact with the basalt host rock is commonly preserved and breccias pass into complex vein networks. The most common veins in these networks are of early(?) dark-green clay veins, but locally thick patches of vermicular clay and/or blocky calcite are present (light gray material in Fig. 60). Incipient brecciation is evident in some thick vermicular clay + carbonate (>0.5 cm) veins, where a few small basalt clasts are "floating" in the veins. The

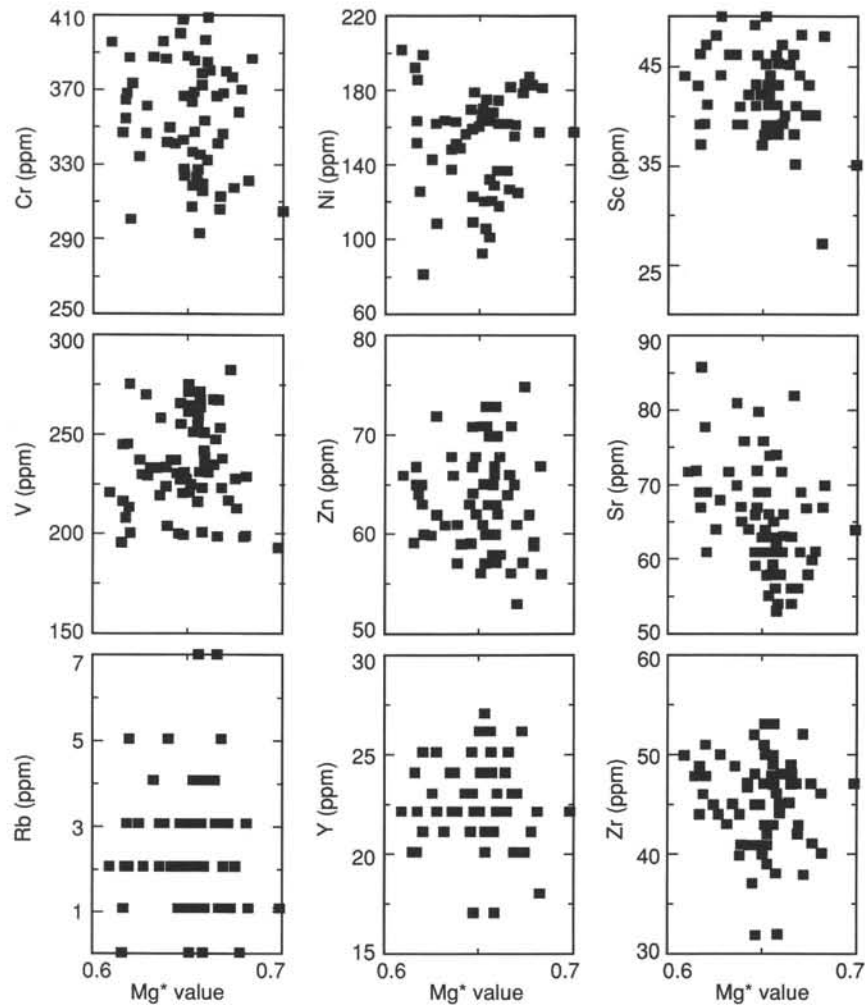


Figure 45. Trace element geochemistry plotted against  $Mg^*$  fractionation index of the basalts from Hole 896A drilled during Leg 148.

characteristics of this type of breccia indicate nearly in-situ formation, with fragmentation occurring along vein networks cutting intact basalt. Although a "cataclastic" matrix is present, there is no evidence of shearing. As discussed below, this type of brecciation also affects dike margins. It is likely that these breccias formed beneath the seafloor, probably by fragmentation in the uppermost crust related to extension. Disaggregation would be greatly aided by the development of cooling joints, especially in pillow lavas. Confining pressures at this level are very low, so that open voids (e.g., fissures) can be present. This type of sub-seafloor fragmentation should decrease rapidly with depth as confining pressure increases and fissuring is replaced by faulting. The cement-supported breccias require that the clasts be pushed apart, suggesting the presence of a high pore fluid pressure or fluids moving by turbulent flow (i.e., flow at high velocities).

### Crosscutting Relationships

A general sequence of veining is evident from crosscutting relationships, including reopening of veins discussed above (see also "Alteration" section, this chapter): (1) relatively uncommon brown clay + Fe-oxyhydroxide, commonly having wide alteration halos; (2) abundant thin, non-fibrous and non-vermicular dark-green clay veins; (3) blocky carbonate/vermicular clay veins; and (4) fibrous veins. Vein networks and associated breccias are also relatively old because they are cemented by (2) and/or (3). Fibrous veins (4) usually cut or reopen blocky carbonate/vermicular clay veins, but a few clear exam-

ples were observed where the latter cut the former. This suggests that textural types (3) and (4) alternated with time, which could simply reflect variations in pore-fluid pressure (fibrous veins forming during periods of high pore-fluid pressure) or different rates of opening of cracks (sudden versus progressive opening).

### Dike Margins

Moderately planar, steeply dipping ( $74^{\circ}$ – $78^{\circ}$ ) contacts between relatively coarse-grained massive units and cryptocrystalline to microcrystalline lithologies in Samples 148-896A-21R-2, Piece 9, and 148-896A-22R-4, Piece 5, are interpreted to be intrusive contacts between dikes and massive lavas. Contact relationships are complicated however, by brecciation and fragmentation of the samples. In Sample 148-896-21R-2, Piece 9B, the chilled margin is separated from host rock by a 0.5-cm-thick microbreccia comprised of clasts of fine-grained basalt, plagioclase and clinopyroxene crystal fragments, and altered glass in a cement of clay + phillipsite. There is considerable fragmentation but no displacement is evident across this breccia zone. At one end of Piece 9 (Piece 9C), the dike margin contact is very strongly brecciated and very irregular. The breccia consists of centimeter-size clasts of the host rock, with jigsaw-like fragmentation along the edge of the brecciated zone and millimeter- to centimeter-size clasts of the chilled margin cemented by clay and minor carbonate. A brecciated contact such as this could be interpreted as a fault contact between massive and pillowed lavas. We consider it more

likely that brecciation occurred during or after intrusion of a dike, similar to examples from the pillow lava sequence of Hole 504B (Anderson et al, 1985).

An approximately 1-cm thick, steeply dipping ( $82^\circ$ ) microcrystalline zone occurs in the same core (Sample 148-896A-21R-2, Piece 13B) and is interpreted to be either a thin dikelet or an interior chill zone within a larger dike. The dikelet(?) passes into a brecciated zone along the edge of the sample.

The dike margin in Sample 148-896A-22R-4 (Piece 5) appears to be sharp and planar. This piece only includes part of the full core width, however, so it is possible that a vein or breccia zone was associated with the dike margin.

### Vein Orientations

The majority of measured veins could only be partially re-oriented because many pieces preserve the core margins (vertical axis) but, because of their small size, may have rolled (i.e., the up direction is unknown), and the core is unoriented with respect to azimuth except samples oriented using the stable paleomagnetic declination (see "Structure and Deformation" section of the "Explanatory Notes" chapter, this volume). As a result, most of the spatial data consists of true dips. Interpretation of true-dip histograms must take into account a sampling bias due to a vertical drill hole (Fig. 61, curve B) and the effect of spherical geometry (Fig. 61, curve A) (Dick, Erzinger, Stokking, et al., 1992; Newmark et al, 1985). The combination of these effects is shown as curve C of Figure 61, corresponding to the predicted distribution of true-dips for a population of randomly oriented planes. In general, only the most planar and regular veins were measured, but multiple planar segments of irregular veins were commonly measured as well.

True-dip data for all measured veins, a paleomagnetically oriented subset of veins, and a contoured equal-area stereographic projection of oriented veins are shown in Figure 58. The histogram for all the data is distinct from the theoretical random distribution (Fig. 61) in that more steep dips are present. The histogram of 164 oriented veins (Fig. 58B), however, shows fewer steep dips and a more nearly random distribution. The source of the difference between the full true-dip data and the subset of oriented data is unknown. The stereographic projection for the oriented data (Fig. 58C) shows a strong maximum corresponding to shallow dips, in addition to weak NNE- and NNW-striking girdles. This data set is similar to a random distribution of planes intersected by a vertical drill hole, which biases the data strongly toward shallower dips (Fig. 61, curve B; note that curve A does not apply to stereographic projections). Because of the extensive fracturing in the pillow lava units, which probably originated largely as radially oriented cooling joints, oriented vein data from only the massive units were plotted separately. The plots, however, were similar to those for the entire oriented data set.

We were able to classify approximately 60% of the measured veins into the three subsets recognized from crosscutting relationships (from generally oldest to youngest): (1) clay + Fe-oxyhydroxide having wide alteration halos; (2) blocky aragonite and/or vermicular clay; and (3) fibrous aragonite and/or fibrous clay. Dip histograms for Fe-oxyhydroxide bearing veins (Fig. 56A) and all non-fibrous veins (Fig. 56B) show distributions that are clearly non-random (compare Figs. 56A and B with Fig. 61), with a tendency toward steeper dips. This is especially evident in the Fe-oxyhydroxide veins belonging to the earliest vein generation, whereas the non-fibrous veins include those formed during both the first and second vein generations. The former are common in massive lavas, and may represent steeply dipping cooling joints that were later filled with vein minerals. The histogram for fibrous vein dips (Fig. 56C) is also distinct from that predicted for random planes (Fig. 61), with a shallow dip being more common.

The oriented veins were subdivided into fibrous and non-fibrous. Second-generation blocky aragonite + clay veins mostly plot along a NE-striking girdle (Fig. 62A), but too little data and too much scatter

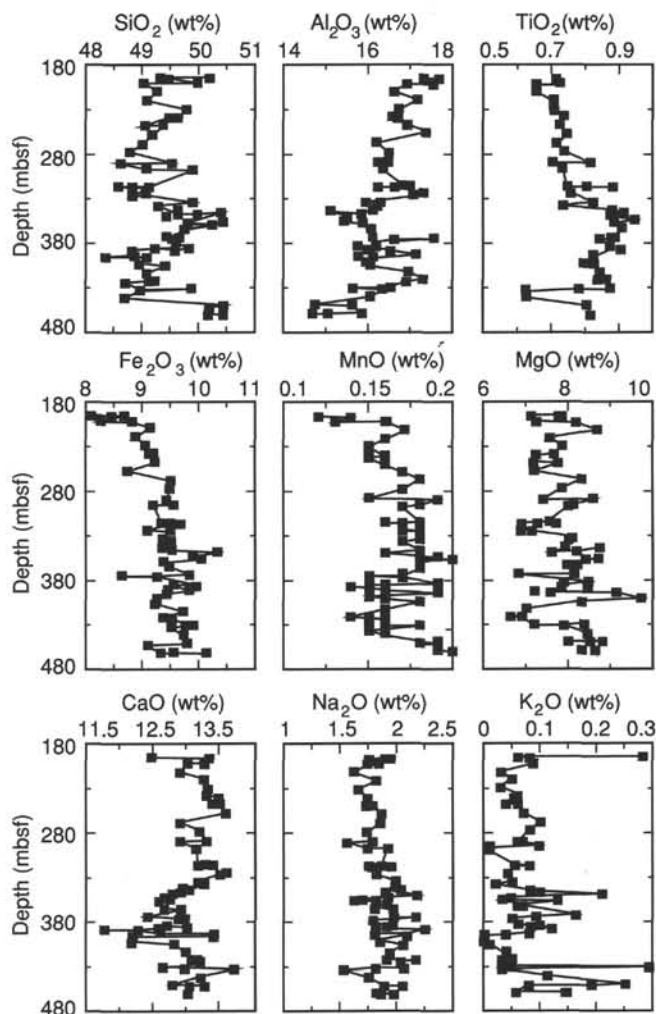


Figure 46. Downhole variation of the major elements' chemistry of the basalts from Hole 896A drilled during Leg 148.

is present to draw any definite conclusions. Several data sets for individual samples show a distinctly non-random vein orientation. For example, Figure 62B shows a plot of 14 non-fibrous clay veins (first generation?) where 12 of the veins plot along a girdle and the remaining veins plot near the pole to the girdle.

Oriented fibrous veins show considerable scatter on a stereographic projection (Fig. 63A), similar to the full set of oriented veins (Fig. 58C). Data for individual samples, however, often show a distribution along a girdle (Fig. 63B), similar to the non-fibrous samples. As discussed above, the vast majority of fibrous veins appear to have formed by extension normal to the vein walls (i.e., parallel to the pole of the vein, as shown in Fig. 63B). The wide variation in orientation of these veins apparent in the plot of all fibrous veins (Fig. 63A) implies extension in all directions during the third vein generation. The distribution of these veins along a girdle in an individual sample suggests extension was occurring within one plane. For six samples, the girdle (the plane containing all extension directions) is subvertical, but its strike is variable from one sample to another.

### Vein-faults and Fractures

Nine samples from depths of 335 to 406 mbsf have slickenfibers (Appendix H). These vein-faults have fibers that are very similar in texture and mineralogy to those in fibrous extension veins, and are thus considered to be part of the same vein generation. The sense of shear is readily determined for six of the vein-faults using step

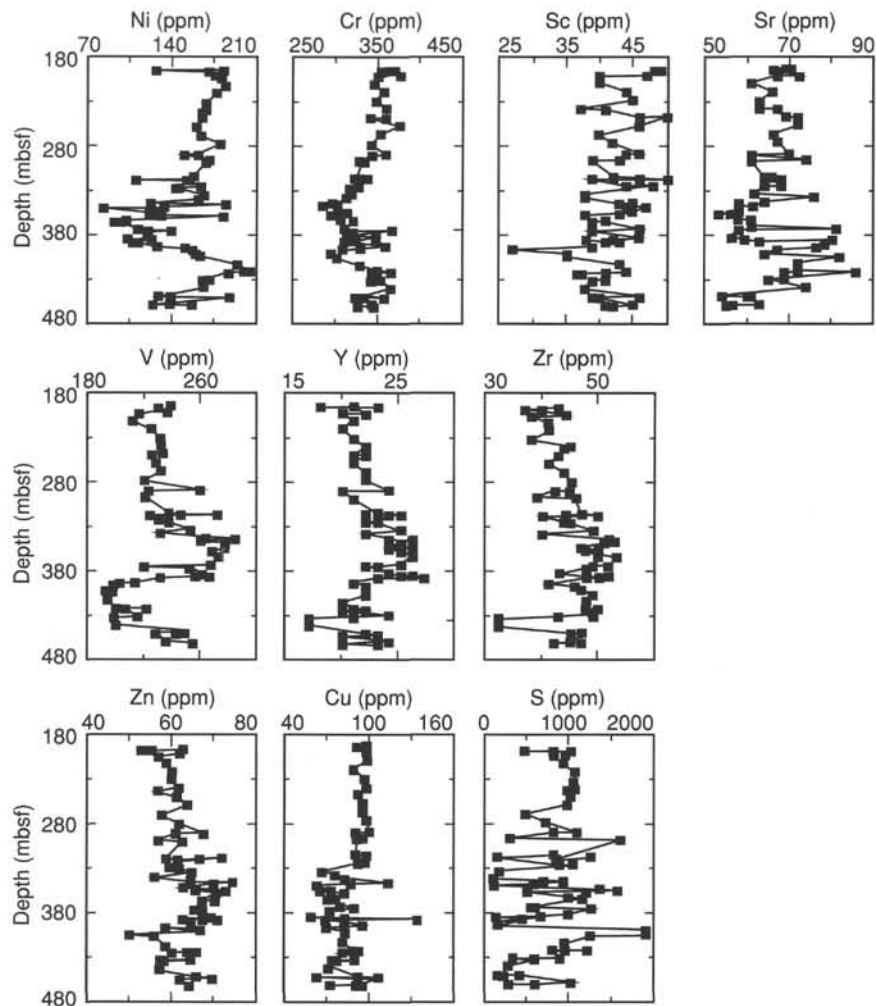


Figure 47. Downhole variation of the trace elements' chemistry of the basalts from Hole 896A drilled during Leg 148.

geometries and the obliquity of fibers to the vein wall ( $\sim 15^\circ$ ), although none of the samples are oriented with respect to azimuth. It is oblique-sinistral for samples and is oblique-reverse for four samples. The appearance of the vein-faults in the deeper cores may represent a gradual change in structural style with depth caused by increasing confining pressure. The vein faults, however, are uncommon, and the predominant strain recorded by fibrous veins throughout the drilled sequence is extension in virtually all directions.

Open fractures without vein material are rare, and the majority observed in rocks recovered from Hole 896A appear to be drilling-induced refracturing of veins. In addition, the samples tended to break along clay veins upon drying, so it is difficult to determine what fractures were present initially. Only 4 fracture orientations were recorded, and these had dips ranging from  $4^\circ$ – $88^\circ$ . All of these fractures were of the incipient type (see "Structure and Deformation" section, "Site 504" chapter, this volume) (i.e., discontinuous and not fully through-going). One probable drilling-induced "disking" fracture was recovered in Sample 148-896A-6R-2, Piece 10A. The saddle axis for this fracture was re-oriented using paleomagnetic data, and has a trend of  $126^\circ$ , approximately coincident with the BHTV defined breakout mode from Hole 504B (Morin et al., 1990). The coincidence of the saddle axis with a "principal" horizontal stress direction has been reported from the KTB deep hole in Germany (Roeckel et al., 1992) but the saddle axis is parallel to the minimum, rather than maximum, horizontal stress direction.

## Discussion

One of the most important results from this study is that extension occurred in virtually all directions, as indicated by complex vein geometry (especially fibrous veins). Secondly, the fibrous veins have features which may indicate formation by the crack-seal mechanism, thus implying periods of relatively high fluid pore-pressures needed to cause hydraulic fracturing. One of the common breccia types (associated with vein networks, affecting dike margins, and showing evidence for disaggregation without shearing) may have also formed by hydraulic fracturing.

## PALEOMAGNETISM

Paleomagnetic measurements were made on 71 oriented mini-cores sampled from cores recovered from the upper extrusive units of Hole 896A during Leg 148 in order to examine the variation in magnetic properties with alteration, lithology, and depth in the crustal section, and to make a comparison with similar data from Hole 504B. In general, the results of these measurements (Table 7) indicate that the magnetic properties of the extrusives in Hole 896A are similar to those of the extrusives sampled during DSDP Legs 69 and 70 from Hole 504B (Furuta and Levi, 1983; Smith and Banerjee, 1986). A significant change in magnetic properties is noted in Hole 896A below Unit 30.

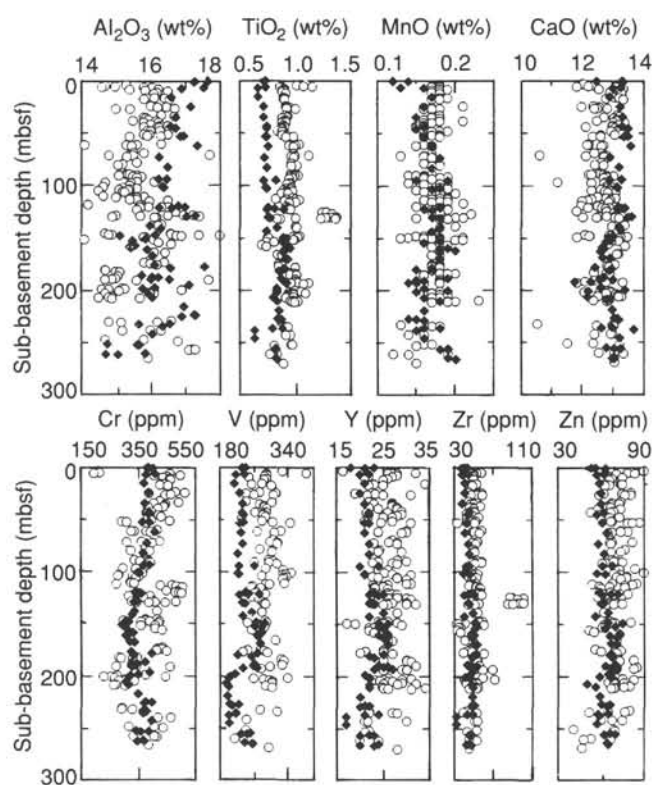


Figure 48. Downhole comparison of the major elements' chemistry of the basalts from Holes 504B (open circles) and 896A (solid diamonds), Leg 148.

### Natural Remanent Magnetization

The stability and direction of the natural remanent magnetization (NRM) have been studied using alternating field (AF) demagnetization techniques. Examples of orthogonal vector diagrams (Zijderveld, 1967) are included in Figure 64. The majority of samples show a single highly stable magnetic component that is almost completely demagnetized by 100 mT. This component typically has a shallow, negative inclination. A few samples contain a small viscous component, but a steeply inclined drilling-induced remanence (Ade-Hall and Johnson, 1976; Lowrie and Kent, 1978; and Johnson, 1978) is not evident. In the deeper parts of the hole some samples contain a small, high-coercivity component, which is not removed in fields of 100 mT (Figs. 64C and D). Initial intensities of the NRM are similar to those obtained from the extrusives from Hole 504B, although the distinction that Furuta and Levi (1983) draw between massive flows and pillowed flows is not apparent (Table 8). Above about 370 mbsf, maximum values of the initial NRM intensity ( $J_0$ ) are less than 17 A/m, except for Sample 148-896A-4R-1, 68–70 cm, for which  $J_0$  reaches a value of 20.7 A/m (Fig. 65A). A larger variation is noted between 195 and 240 mbsf and between 320 and 370 mbsf. Beneath about 370 mbsf,  $J_0$  drops to less than 5 A/m, except for two samples (148-896A-22R-1, 107–109 cm, and 148-896A-28R-2, 39–41 cm). Furuta and Levi (1983) record a similar drop in  $J_0$  below Core 69-504B-9R (332.2 mbsf) in Hole 504B.

The median destructive field (MDF) is a useful measure of the magnetic stability of the NRM during AF demagnetization. The MDF is relatively high (>60 mT) in some samples from pillowed flows above about 250 mbsf, although the range is great (Fig. 65B). There is a general decrease with depth below this point, in both pillowed units and massive flows, although the latter consistently have a lower MDF than adjacent pillows. Furuta and Levi (1983) observed a similar decrease in MDF in Hole 504B.

The stable magnetic inclination ( $I_s$ ) values determined for Hole 896A are plotted against depth in Figure 65C. The mean  $I_s$  value of  $-5.0^\circ \pm 21.9^\circ$  is similar to that observed in the upper part of Hole 504B (Furuta and Levi, 1983). Inclinations measured in samples from massive flows are similar to those in adjacent pillowed flows. A significant change in  $I_s$  is noted below about 370 mbsf. Above this depth, the stable inclinations show no consistent steepening or shallowing with depth in the hole, but there is a suggestion of a cyclic variation between about  $0^\circ$  and  $-20^\circ$ , although further measurements are required to confirm this observation. Some individual samples give anomalously steep directions (Samples 148-896A-8R-1, 29–31 cm, 148-896A-17R-1, 1–3 cm, 148-896A-18R-1, 72–74 cm, 148-896A-18R-2, 60–62 cm), although other samples within the same lithological unit have stable inclinations consistent with the general trend. The pieces from which these samples were taken are too large to have rotated during the drilling process, and we interpret these anomalous inclinations as the result of individual pillows breaking off the main lava pile after they had acquired their magnetization.

Below about 370 mbsf the range in  $I_s$  values increases, and there is a decrease in the quality of some of the demagnetization data, reflected in the delta values (Table 7), which largely corresponds to the occurrence of high-coercivity magnetic phases. The low-quality regressions (delta > 1.0) are shown as small symbols on Figure 65C. The large range in the magnetic inclinations cannot, however, be entirely explained by the quality of the data; some of the steep  $I_s$  values recorded are from highly linear demagnetizations (delta  $\leq 0.2$ ). The change in  $I_s$  corresponds to the first recovery of brecciated units (see "Igneous Petrology" section), and the range in inclinations may reflect a large-scale disruption of the units cored in the lower part of Hole 896A.

Three samples have been taken from brecciated units; these give low  $J_0$  values, and relatively chaotic demagnetization diagrams, consistent with each clast of the breccia carrying a magnetization which predated its formation.

Marine magnetic surveys (Langseth et al., 1983) suggest that Sites 504 and 896 are within the 3A reversed magnetic anomaly, and the majority of the crustal sequence is expected to carry a reversed magnetization. The mean inclination of the upper part of Hole 896A (above 370 mbsf) is  $-9.5^\circ$ , slightly steeper upwards than would be predicted from its paleolatitude. This may be the result of a gentle tilt of the extrusive sequence toward the spreading axis, so that the units dip gently to the north, consistent with models for the accretion of the upper oceanic crust (e.g., Cann, 1974).

### Induced Magnetization

Magnetic susceptibility ( $K$ ) is a measure of the instantaneous magnetization induced in a sample in the presence of an external field, and it is a function of composition, concentration, and grain size of the magnetic minerals within a rock. Values of  $K$  determined for Hole 896A samples are plotted against depth in Figure 66A and have a mean value of  $0.014 \pm 0.007$  SI units. This is similar to the mean  $K$  value of the extrusives obtained from Hole 504B (0.016–0.018 SI units). Above about 290 mbsf in Hole 896A, the maximum susceptibility is less than 0.015 SI units, whereas below this interval the susceptibility gradually increases, to a maximum of 0.034 SI units (Sample 148-896A-16R-2, 34–36 cm). A similar increase is seen in Hole 504B; Furuta and Levi (1983) ascribe this to a dominance of massive flow units in the lower part of the hole. In Hole 896A the increase in bulk susceptibility is also seen in the pillowed units, although the massive flows generally yield higher susceptibilities. The increase in bulk susceptibility may be related to an increase in grain size within the ground mass of the basalts. The highest values are obtained from the massive flows 31–36, corresponding to the occurrence of relatively large (20  $\mu\text{m}$ ) euhedral magnetites or titanomagnetites observed in thin section (e.g., 148-896A-22R-1, 64–66 cm, "Igneous Petrology" section).

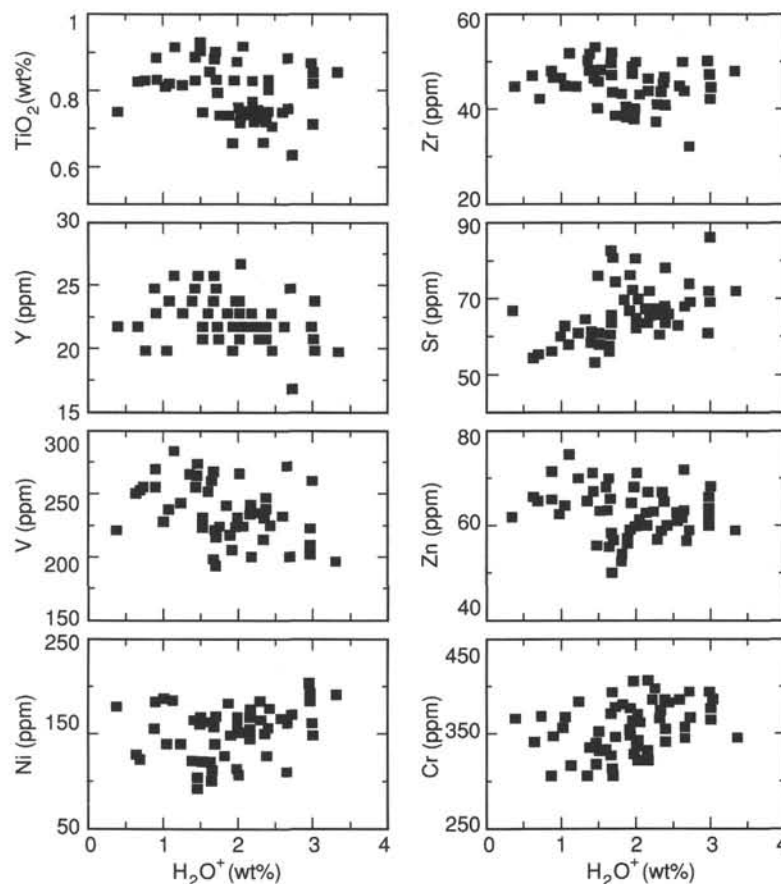


Figure 49.  $H_2O^+$  vs.  $TiO_2$ , Zr, Y, Sr, V, Zn, Ni, and Cr for the basalts from Hole 896A, Leg 148.

The Koenigsberger ratio ( $Q$ ) uses the ratio of  $J_0$  and  $K \cdot H$  to compare the strength of the remanent magnetization to that induced in the rock by the Earth's magnetic field (0.032 mT at Site 504).  $Q$  is generally high ( $32 \pm 32$ ) but decreases with depth (Fig. 66B), reflecting the increase in bulk susceptibility, and the decrease in  $J_0$  below about 370 mbsf. This trend is again similar to that observed in Hole 504B (Furuta and Levi, 1983).

### Rock Magnetic Measurements

A series of non-standard rock magnetic measurements were undertaken on some of the minicores sampled for shipboard analysis. Acquisition of isothermal remanent magnetization (IRM) is a relatively rapid technique, useful in discriminating between high- and low-coercivity magnetic phases. The majority of the samples exhibited a steep gradient of IRM acquisition up to the saturation level (defined as 95% of maximum IRM intensity), after which no significant increase in intensity was noted with increasing applied field (Fig. 67A). Samples saturated in fields between 70 and 200 mT, indicating the predominance of (titano)magnetite and/or (titano)maghemite. A few samples, mostly from massive flows, saturated in fields greater than 200 mT (Fig. 67B), suggesting the presence of additional, higher coercivity phases. Samples from the massive flow Units 31–36, and 49, and pillow Unit 47 commonly contain a high coercivity phase that is not removed during AF demagnetization. Hematite has been reported ("Alteration" section, this chapter) in some thin sections from the massive Units 31–36, which may be the carrier of this high-coercivity magnetization.

Comparison of the AF demagnetization of anhysteretic remanent magnetism (ARM) with the AF demagnetization of the NRM can provide valuable information on the origin of the NRM. ARMs were acquired in direct fields of 0.032 mT; a field similar to the present

Earth's field at Site 896. In most cases the samples were not fully saturated at 100 mT, the maximum alternating field applied, but were within approximately 20% of saturation. The shape of the ARM demagnetization curve was generally similar to that of the NRM, but the ARM intensity at 100 mT of AF demagnetization was always less than the initial NRM intensity.

### Anisotropy of Magnetic Susceptibility

Measurements of the anisotropy of magnetic susceptibility (AMS) have been made on the minicores from the Hole 896A core (Table 9). Although the recorded anisotropies ( $K_{max}/K_{min}$ ) are low,  $\leq 6\%$ , the recorded errors are smaller (Fig. 68), and the measurements are repeatable. The dominant fabric is prolate. The orientations of the AMS ellipses have been reoriented using the stable component of magnetization, assuming that this direction was approximately south-directed, as rocks at Site 896 are believed to have formed during a reversed magnetic epoch.

When the principal axes are plotted within the sample coordinate frame (Fig. 69A) there is a distinct grouping of the maximum principal axes of magnetic susceptibility ( $K_{max}$ ) in the  $x$ -axis; that is, parallel to the axis of the minicore. The minimum axes ( $K_{min}$ ) lie on a girdle in the  $y$ - $z$  plane. Such a distribution would be expected from a shape anisotropy produced by over-long samples. The ideal ratio for shape anisotropy in cylindrical samples is length/diameter = 0.86 (Collinson, 1983). The majority of samples now have a ratio slightly shorter than this, but after anisotropy measurements were made, the ends of the samples were ground for physical property measurements, so their original length is unknown. There is no clear correlation between the length of the sample and either the lineation ( $K_{max}/K_{int}$ ) or the declination in the sample coordinate system. To test this possibility further,



Fig. 50. Overlapping carbonate + clay-filled veins. The vein arms are filled mainly with clay. Sample 148-896A-7R-1, Piece 22.

vertical minicores were taken from three pieces already sampled for shipboard paleomagnetic analysis. AMS fabrics from these vertical samples are similar to those in the horizontal minicores (Table 9), confirming that the magnetic fabric is a property inherent in the rock, rather than a product of sampling.

After a correction using the stable remanence is applied, the maximum axes ( $K_{max}$ ) cluster with a dominant WNW-ESE, sub-horizontal trend (Declination =  $284^\circ \pm 12^\circ$ , inclination =  $0^\circ \pm 7^\circ$ , Bingham, 1974; Fig. 69B). The minimum axes are generally steep and lie on a girdle orthogonal to this trend. There is little distinction between the directions of the axes in the massive units compared to the pillowed units. Magnetic fabrics of volcanic rocks have been correlated with flow directions (Ellwood, 1978), but here the shallow prolate fabrics are difficult to reconcile with a flow fabric within the pillowed units, which generally erupt onto relatively steep slopes ( $>20^\circ$ ) and flow in a rather chaotic manner, with a wide range of flow directions. It seems improbable that a volcanic pile greater than 150 m thick should record such a narrow range of flow directions. Another point against these rocks preserving a flow fabric is that the three breccia samples give AMS fabrics with shallow ( $<15^\circ$ )  $K_{max}$  axes, similar to that observed in the massive flow and pillowed flow samples. These samples cannot be expected to carry a flow fabric.

One possibility is that the strong stable remanence is affecting the fabric. We have investigated this in one minicore (Sample 148-896A-7R-1, 80–82 cm) by inducing an ARM comparable in intensity to the

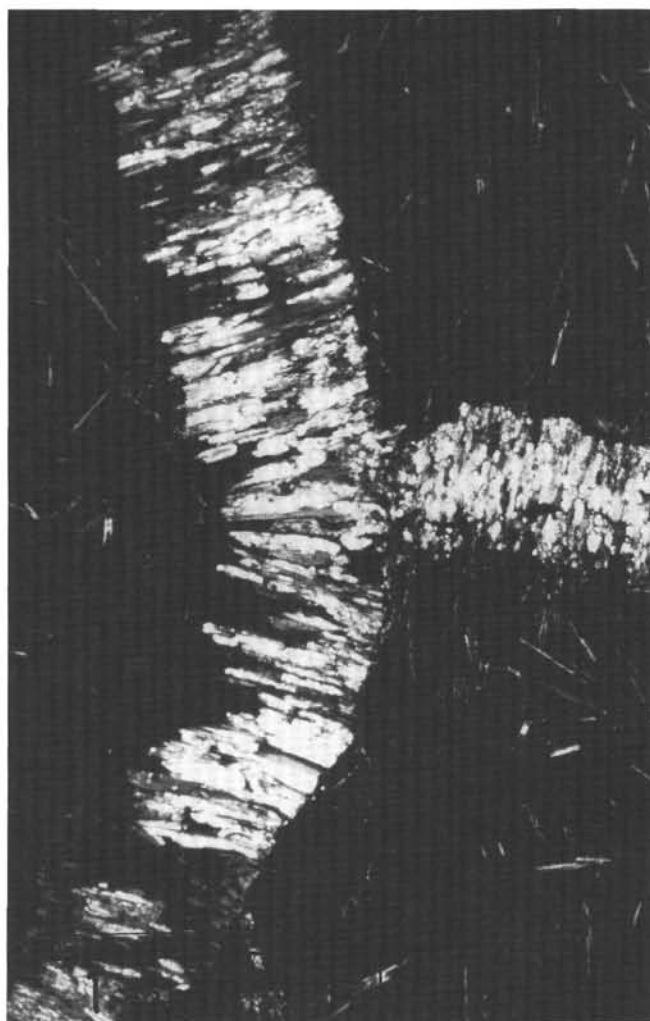


Figure 51. Stretched carbonate fibers filling veins forming a triple junction. Sample 148-896A-7R-1, 135–139 cm, Piece 22.

NRM in different axes, and measuring the AMS fabric. Although there is a small change in the magnitudes of the principal axes of the AMS, the orientations do not change significantly; remanence does not appear to control the AMS fabric in these rocks.

The orientation of the mean  $K_{max}$  direction is similar to that of the present minimum principal horizontal compressive stress ( $292^\circ \pm 16^\circ$ ) measured in Hole 504B (Newmark et al., 1984). The possibility that the stress field is controlling the orientation of the magnetic fabric should be investigated further.

## PHYSICAL PROPERTIES

Measurements of wet-bulk density, compressional wave velocity ( $V_p$ ), thermal conductivity, and electrical resistivity were made on selected water-saturated samples from Hole 896A in order to determine the changes in physical properties with depth at a site drilled in young crust on a buried basement topographic high and to compare the extent of alteration, as reflected in these properties, with that in Hole 504B, which was drilled in an adjacent basement low. Porosities and grain densities were calculated for the same samples from the differences between wet and dry weights, and formation factors were calculated from measured resistivities, assuming a pore-fluid (seawater) resistivity of  $0.20 \Omega\text{m}$  at room temperature (Table 10). Additional density measurements were made on irregular samples to assess changes in density with grain size, mineralogy, and alteration.



Figure 52. Curved carbonate fibers along the vein walls and coarse-grained blocky carbonate in the center. Sample 148-896A-6R-3, Piece 1.

As noted in earlier sections, the filling of cracks and interpillow voids by alteration products locally stabilized the formation for drilling and permitted high recovery in selected intervals in Hole 896A. Thus the physical properties shown in Table 10 include not only those of pillow and massive basalts, but those of other materials not commonly recovered in basement holes, including glassy pillow margins and interpillow hyaloclastite breccias cemented by carbonates and pale to dark green clays.

Bulk densities and porosities were determined for 41 saturated minicores taken for  $V_p$  studies and 24 re-saturated minicores taken for paleomagnetism studies. Bulk densities were also determined for 15 irregular samples shortly after recovery. With the exception of breccia Sample 148-896A-14R-1, 64–67 cm, which was kept saturated, the densities shown for these samples are minimum values since they may have partially dried between recovery and measurement.

As can be seen in Table 10 and Figure 70, the Hole 896A samples range widely in density from a low of about  $2.2 \text{ g/cm}^3$  for the green clays found in the matrix of the breccias to a high of nearly  $3.0 \text{ g/cm}^3$  in the basalts. Not surprisingly, the breccias, which consist of shards of altered glass and basalt fragments in a matrix of clay and calcite, have the lowest densities ( $2.2\text{--}2.7 \text{ g/cm}^3$ ), while the basalts have higher densities ( $2.6\text{--}3.0 \text{ g/cm}^3$ ) and increase in density with depth from a mean of about  $2.8 \text{ g/cm}^3$  at the top of the cored interval to about  $2.9 \text{ g/cm}^3$  at the base. Excluding breccias, which have extremely high apparent porosities (up to 33% in Sample 148-896A-14R-1, 64–67

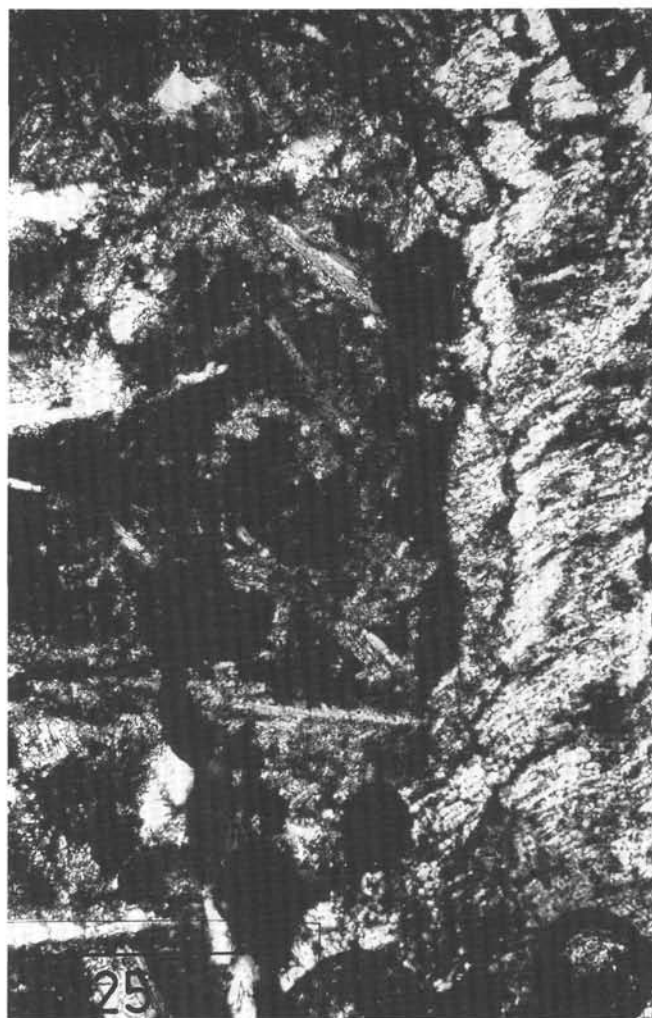


Figure 53. A vein filled with clay fibers oriented obliquely to the vein walls. Sample 148-896A-14R-2, 113–115 cm, Piece 16A.

cm) because of abundant clay and thus bound water content, porosities of the basalts range between 9.5% and 0.6%. As can be seen in Figures 70 and 71, porosities of the basalts decrease irregularly with depth as the rocks become increasingly fresh, and vary inversely with density for grain densities of  $2.95\text{--}3.0 \text{ g/cm}^3$ .

Velocity measurements on samples from Hole 896A were made at room temperature and pressure using the Hamilton Frame velocimeter and were limited to minicores for which other properties were measured. Even excluding the breccias, which have anomalously low compressional wave velocities ( $3.6\text{--}4.7 \text{ km/s}$ ) because of their high clay content, Hole 896A samples vary quite widely in velocity, with the massive and pillow basalts each ranging from  $5.2\text{--}6.4 \text{ km/s}$ . Interestingly, the samples with the highest velocities and densities are from glassy pillow margins, implying that the glasses are commonly still quite fresh, in agreement with thin section observations. Evidently the alteration of the glass has been delayed by its low permeability. As shown in Figure 70, the basalts tend to increase in velocity with depth in the top of the hole but show considerable scatter below 350 mbsf due to variations in alteration. Unlike the Leg 148 504B samples, the Hole 896A samples show a clear trend of increasing velocity with increasing density (Fig. 72).

Thermal conductivity measurements were made at room temperature and pressure on the archive halves of 37 samples, 17 of which were measured for other physical properties. Measurements were made using the half-space needle probe technique after extensive

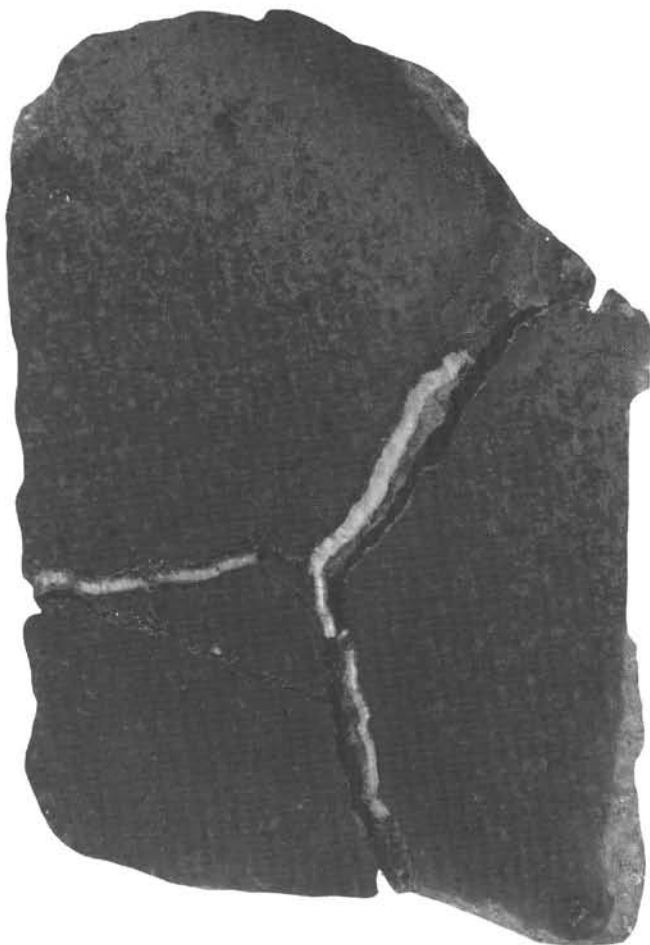


Figure 54. Triple junction intersection between carbonate-filled veins. Sample 148-896A-6R-3, Piece 4.

calibration against rubber, macor, and basalt standards. Most values fall between 1.6–2.0 W/(m · K) (Fig. 70), but the breccias display lower values (1.3–1.55 W/(m · K)) due to their high clay (water) content. One sample (a fresh massive basalt) has a value of nearly 2.0 W/(m · K). No discernible trend in thermal conductivity is observed with depth, other than a marked increase in scatter at about 350 mbsf.

Electrical resistivity was measured at room temperature (about 20°C) and pressure on 38 saturated minicores and 21 re-saturated minicores studied for paleomagnetism. The samples were measured using a 1 V current with a frequency of 50 Hz, similar to that used by the resistivity logging tool. The resistivities range from 10 to about 300 Ωm and show no particular trend with depth. As expected, however, the resistivities are strongly dependent on porosity ( $\phi$ ), since the formation factor (FF),

$$FF = R_o/R_w \approx 20/\phi, \quad (1)$$

where  $R_o$  is the measured resistivity of the sample and  $R_w$  is the resistivity of the pore water (Fig. 73).

Comparison of the densities, porosities, and velocities measured in samples from Hole 896A and the top 300 m of Hole 504B (Figs. 74 and 75; Hole 504B data from Karato, 1983; Wilkens et al., 1983; Christensen and Salisbury, 1985; Christensen et al., 1989; Shipboard Scientific Party, 1983, 1985, 1988a, 1992 a, b; Iturrino et al., in press) shows that the extent of alteration in the upper crust at both sites is fairly similar, despite their differences in basement elevation and burial history. The mean densities at the top of Hole 896A are slightly

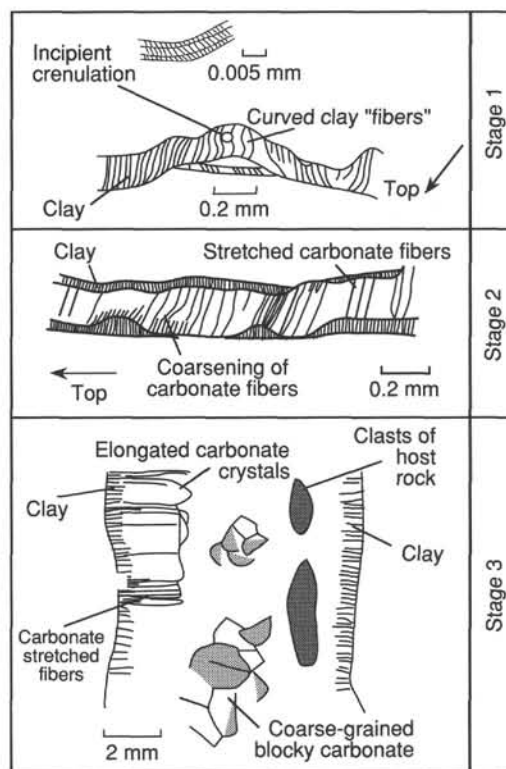


Figure 55. A schematic illustration depicting the evolution of three main types of veins in a sequential order as a result of crack-seal mechanism. Stage 1 indicates formation of monomineralic vein (clay). Clay fibers are arranged orthogonal to the vein walls. Some clay fibers are curved. Incipient crenulation of the clay has been observed at high magnification (from Sample 148-896A-1R-1, 47–55 cm, Piece 11). Stage 2 shows re-opening of the clay-filled vein is followed by its filling with stretched carbonate fibers. These fibers locally become wider toward the center of the vein (from Sample 148-896A-3R-1, 143–146 cm, Piece 17). Stage 3 illustrates further opening of the clay + carbonate vein followed by filling with coarse-grained blocky carbonate crystals (from Sample 148-896A-6R-3, Piece 1).

lower than those in Hole 504B (2.8 vs. 2.85 g/cm<sup>3</sup>) but converge to about 2.9 g/cm<sup>3</sup> and are indistinguishable by 200 m sub-basement. Similarly, porosities of the basalts generally range between 2% and 7% at both sites, while velocities range between 5.5–6.0 km/s and the thermal conductivities range between 1.6–1.8 W/(m · K).

Comparison with other holes which recovered cemented breccias (e.g., Holes 417A and 417D, which were drilled, respectively, on a buried basement high and a basement low in 110 m.y. old crust in the Atlantic Ocean; Shipboard Scientific Party, 1980) shows the breccias to have similar properties, but the basalts in Hole 896A to be slightly less altered than those in Hole 417D (mean density = 2.8 g/cm<sup>3</sup>) and considerably less altered than in Hole 417A (mean density = 2.75 g/cm<sup>3</sup>). From these observations, and examination of the core, we conclude that alteration in the upper oceanic crust is controlled by a complex interplay between topographic relief, water/rock ratio, temperature, and time of exposure to seawater or hydrothermal circulation.

## PHYSICAL PROPERTIES SUMMARY

One of the principle objectives of drilling Hole 896A was to compare the extent of alteration in young crust recovered from a buried basement ridge with that observed in Hole 504B, drilled in an adjacent basement low, the premise being that the ridge site would be more altered and perhaps, better sealed by alteration products, due to longer exposure to seawater and open hydrothermal circulation. As

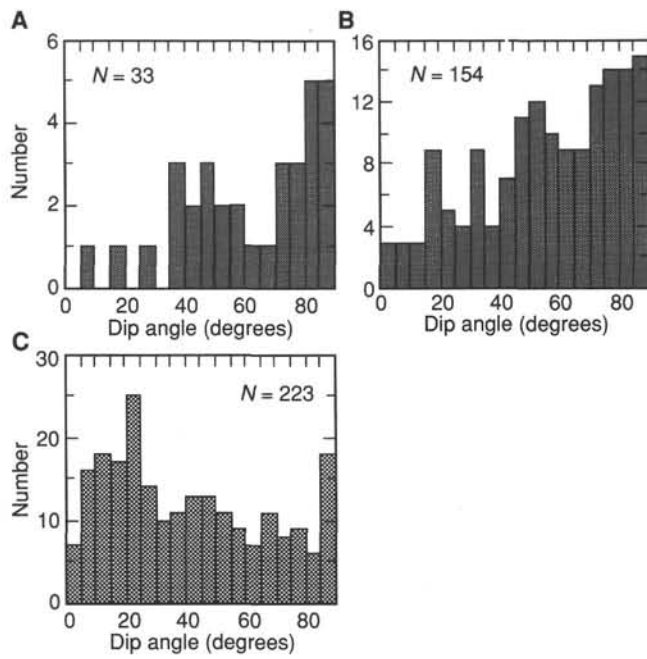


Figure 56. True dip histograms of (A) early Fe-oxyhydroxide-bearing veins, (B) non-fibrous veins, (C) fibrous veins.



Figure 57. Close-up photograph of a matrix-supported breccia with basaltic clasts in a fine-grained matrix cemented by clay. Note that veins in the center clast appear to be truncated at the edge of the clast. Sample 148-896A-28R-2, Piece 4.

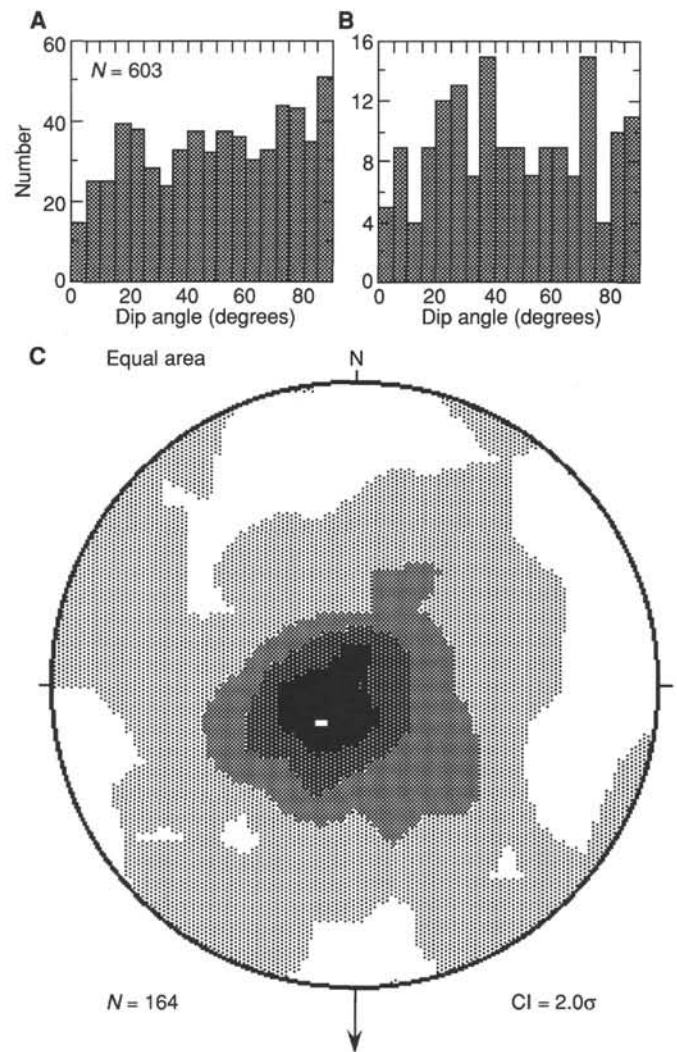


Figure 58. A. True-dip histogram of all measured veins. B. True-dip histogram of all veins that were oriented using paleomagnetic data. These data are plotted in C. C. Kamb-contour stereographic, equal-area projection of all oriented veins. Heavy arrow is the paleomagnetic reference direction used for reorienting azimuth.

anticipated, the physical properties of most of the samples from Hole 896A are typical of moderately altered basalt: bulk densities range for the most part, between 2.80 and 2.95 g/cm<sup>3</sup>; the porosities are moderately high (2%–10%); resistivities are low, ranging between 40–250 Ωm; velocities are fairly low, ranging largely from 5.5–6.0 km/s and thermal conductivities range between 1.6–1.8 W/(m · K). Also as expected, the unusual recovery of glassy pillow margins, interpillow hyaloclastic breccias and flow breccias cemented by clays and calcite suggests that the crust at Site 896 is at least partially sealed by alteration products. While these materials have very low densities (2.2–2.7 g/cm<sup>3</sup>), velocities (3.6–4.7 km/s) and resistivities (10–20 Ωm), they are much higher than those of seawater (1.035 g/cm<sup>3</sup>; 1.5 km/s; 0.2 Ωm at room temperature) and will strongly affect the overall properties of the formation, causing  $V_p$ , density and resistivity to rise, porosity to decrease and heat flow to approach conductive values.

While many of the physical property patterns observed in Hole 896A were anticipated, others were not: In most oceanic basement holes, alteration decreases with depth and this is seen as a decrease in  $V_p$  at the very top of the hole, but the most pronounced change is a marked increase in scatter in  $V_p$  and thermal conductivity below 350 mbsf, which we attribute to increasingly variable alteration with depth. Similarly, in most holes, massive basalts are the freshest



Figure 59. Vein network and incipient breccia cemented by dark-green clay. Light patches along the center veins consist of vermicular clay. Sample 148-896A-14R-2, Piece 10.

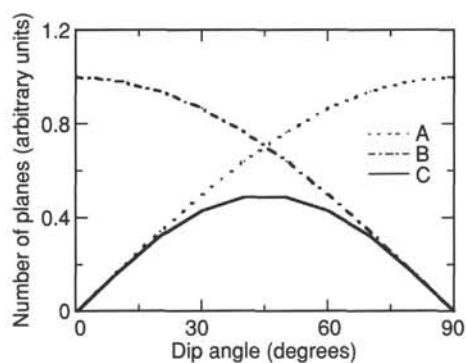


Figure 61. Distribution of true dips for a randomly oriented set of planes. Line A depicts the effect of spherical geometry on true-dip data. Line B shows the bias due to a vertically oriented drill hole. Line C gives the combination of these two effects.

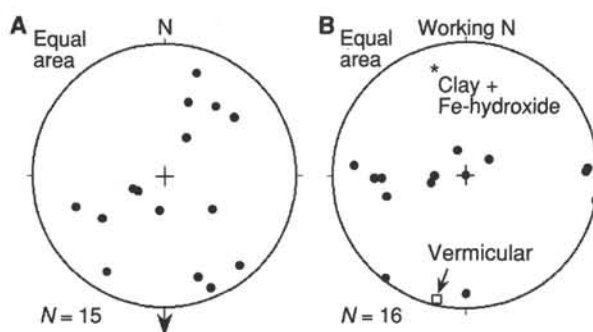


Figure 62. Hole 896A. **A.** Stereographic projection of all oriented blocky aragonite and vermicular clay veins. Heavy arrow is the paleomagnetic reference direction used for reorienting azimuth. **B.** Stereographic projection of non-fibrous chlorite veins from a single sample (Sample 148-896A-16R-3, Piece 1). This sample is not oriented with respect to azimuth.

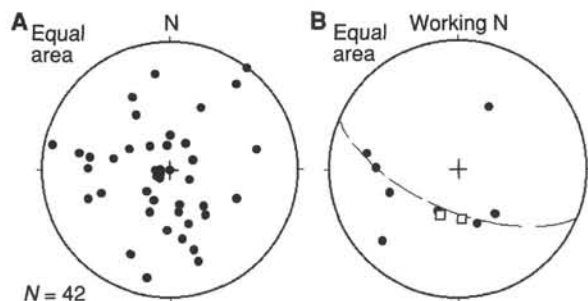


Figure 63. Hole 896A. **A.** Stereographic projection of all oriented fibrous veins. Heavy arrow is the paleomagnetic reference direction used for reorienting azimuth. **B.** Stereographic projection of fibrous veins from a single oriented sample (148-896A-16R-2, Piece 1). Filled circles are fibrous veins and squares represent the trend and plunge of fibers (derived from pitch measurements made with the aid of a binocular microscope). The fibers correspond closely in orientation of the pole of the corresponding veins (i.e., the fibers are essentially normal to the vein walls).



Figure 60. Cement-supported breccia consisting of basalt and glass fragments cemented by blocky carbonate (white) and vermicular clay (light gray). Sample 148-896A-8R-1, Piece 9.

materials recovered and pillow margins are the most altered, but in this hole, the glassy pillow margins and the cores of the thickest massive flows tend to have the highest densities ( $2.96 \text{ g/cm}^3$ ) and velocities ( $6.4 \text{ km/s}$ ). We speculate that while glassy pillow margins alter the most, coarse-grained massive basalts and pillow interiors alter first because of their higher permeability, and alteration was

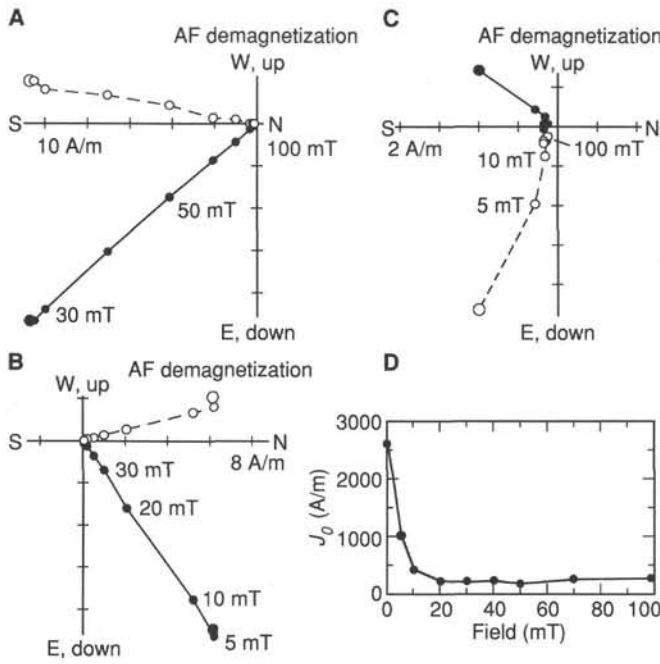


Figure 64. Orthogonal vector representations (Zijderveld, 1967) of AF demagnetization of NRM. Filled circles are projected onto horizontal plane; open circles onto a vertical plane. **A.** Sample 148-896A-4R-1, 68–70 cm (pillowed flow). **B.** Sample 148-896A-16R-1, 32–34 cm (massive flow). **C.** Sample 148-896A-23R-3, 132–134 cm (massive flow). Note high-coercivity component that is not removed during AF treatment to 100 mT. **D.** Sample 148-896A-23R-3, 132–134 cm (massive flow); intensity of remanent magnetization vs. AF demagnetizing field.

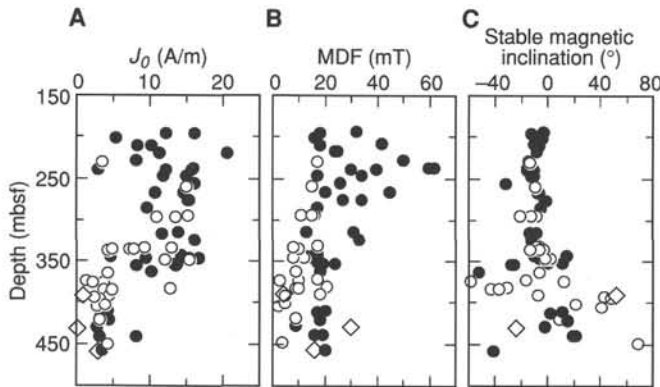


Figure 65. Magnetic properties of natural remanence vs. depth (mbsf) for samples from Hole 896A cored during Leg 148. Samples from massive flow units are shown as solid circles; those from pillow units as unfilled circles. Samples from breccias are shown as open diamonds. **A.**  $J_0$  vs. depth. **B.** MDF vs. depth. **C.** Stable magnetic inclination vs. depth. Samples from pillowed and massive units with poor regression fits on AF demagnetization diagrams ( $\Delta > 1.0$ ) are indicated by smaller symbols.

arrested at Site 896 by sealing and high sedimentation rates before the glass and the flow cores had begun to rot.

Comparison of the physical properties in Holes 896A and 504B shows that the densities in the upper 200 m of Hole 896A are slightly lower than in Hole 504B (2.8 vs. 2.85 g/cm<sup>3</sup>), but otherwise, the properties are quite similar. Thus, while the basalts in the top of Hole 896A are slightly more altered, the principal difference between the

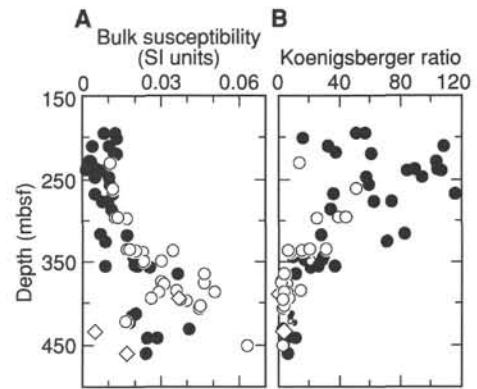


Figure 66. Magnetic properties of induced magnetization vs. depth (mbsf) for samples from Hole 896 cored on Leg 148. Samples from massive flow units are shown as solid circles; those from pillow units as unfilled circles. **A.** Bulk magnetic susceptibility (SI units) vs. depth. **B.** Koenigsberger ratio ( $Q$ ) vs. depth.

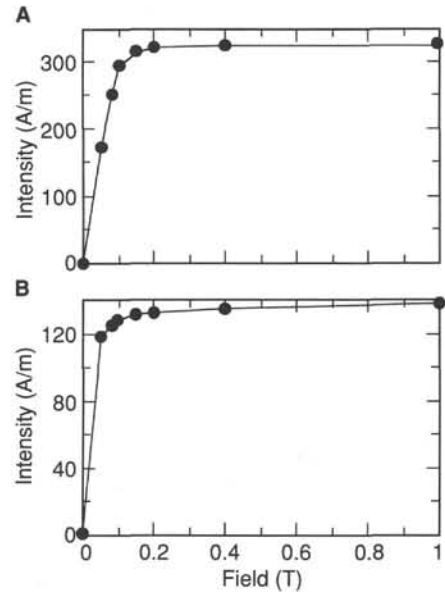


Figure 67. Intensity of IRM (normalized by the maximum intensity at saturation) against applied field (T). **A.** Sample 148-896A-7R-1, 82–84 cm. Note saturation before 0.2 T. **B.** Sample 148-896A-23R-3, 132–134 cm. Note small high-coercivity fraction not completely saturated by 1 T.

two sites is a greater degree of sealing at Site 896, perhaps due to deposition of secondary minerals in a zone of upwelling.

### DOWNHOLE MEASUREMENTS

A full program of downhole measurements including Schlumberger and magnetometer logs and packer experiments were conducted in Hole 896A. As these measurements were made so close to the end of the leg, this report includes only a brief operational summary and preliminary data presentation.

#### Operational Summary

Hole 896A was cored in two phases, separated by about eight days of fishing and logging in Hole 504B. The first log run in Hole 896A was a Schlumberger geochemical log (GLT) with Lamont temperature logging tool (TLT). This was run before the last core bit in Hole 896A,

Table 7. Magnetic data for Hole 896A samples.

Core, section, top (cm)	Depth (mbsf)	Piece	Unit	Dec	Inc	$J_0$ (A/m)	Stable dec	Stable inc	Delta stable	MDF (mT)	Susceptibility (SI)	$Q$	ARM (A/m) at 100 mT	MAF (mT)	ARM/NRM	Sat IRM A/m	Hsat (T)	Lithology
148-896A-																		
1R-1, 47	195.57	11	3	299.3	-1.6	12.4	299.4	-3.2	0.0	32	0.0086	56.8	3.03	50	0.40			Pillow
1R-1, 87	195.97	18	3	268.2	-11.5	16.2	269.4	-11.9	0.0	18	0.0125	51.0	3.22	28	0.24	220.1	0.11	Pillow
2R-1, 82	201.72	19	7	96.2	2.1	5.5	94.7	-3.9	0.0	16	0.0134	16.3	2.33	15	0.44	178.8	0.15	Pillow
3R-1, 38	210.28	7	8	67.2	-11.0	10.3	67.3	-10.4	0.0	42	0.0037	108.2	2.45	65	0.26			Pillow
3R-1, 78	210.68	9	9	118.3	-8.7	8.6	116.9	-6.4	0.0	18	0.0102	32.9	2.81	20	0.33	203.5	0.14	Pillow
4R-1, 44	219.34	9A	9	109.9	-7.6	11.5	110.0	-8.0	0.0	24	0.0121	37.3	3.65	38	0.36	206.3	0.14	Pillow
4R-1, 68	219.58	9C	9	139.1	-8.1	20.7	139.0	-7.9	0.0	25	0.0132	61.3	2.83	35	0.19			Pillow
5R-2, 38	229.70	1D	10	232.5	-14.9	8.3	232.5	-14.1	0.1	50	0.0032	103.3	2.55	75	0.39			Pillow
5R-3, 43	231.21	5B	11	329.3	-15.7	3.7	333.9	-13.1	0.0	17	0.0109	13.2	1.98	16	0.66	189.9	0.17	Massive
5R-3, 62	261.40	8	11	78.0	-9.9	15.2	235.3	-9.1	0.0	15	0.0117	50.9	3.64	18	0.28	292.2	0.16	Massive
6R-1, 52	238.42	5C	12	82.8	15.1	16.0	83.3	-15.4	0.0	62	0.0061	103.9	3.06	50	0.21			Pillow
6R-2, 3	239.41	1A	12	56.1	-16.7	3.1	281.9	-15.0	0.1	60	0.0014	89.7	0.99	100	0.33	51.2	0.29	Pillow
6R-2, 89	240.27	10A	12	43.1	-8.8	12.3	43.0	-10.0	0.0	40	0.0045	106.9	3.14	55	0.27			Pillow
6R-3, 8	240.86	1	12	255.9	-14.3	15.9	255.2	-15.5	0.0	30	0.0074	84.2	3.60	35	0.25	245.5	0.15	Pillow
7R-1, 58	247.98	10	13	271.9	-13.7	12.0	221.7	-12.4	0.0	34	0.0050	94.3	4.05	75	0.33	228.6	0.17	Pillow
7R-1, 80	248.20	13	14	87.9	-10.8	15.2	87.6	-9.8	0.0	17	0.0103	57.8	5.10	75	0.30	268.7	0.13	Pillow
8R-1, 29	257.39	7	14	181.2	-32.2	16.3	181.6	-32.2	0.0	26	0.0109	58.9	4.56	38	0.28	251.2	0.10	Pillow
9R-1, 138	268.08	25	14	70.8	-8.5	10.9	70.5	-6.1	0.0	20	0.0119	35.9	1.99	31	0.26	244.0	0.12	Pillow
9R-2, 4	268.18	1	14	211.8	-7.6	14.8	211.3	-7.3	0.0	45	0.0050	116.0	3.71	75	0.28	272.3	0.15	Pillow
10R-1, 85	277.25	8E	14	51.0	-1.6	15.6	51.0	-1.6	0.0	27	0.0097	62.7	3.34	37	0.21	265.0	0.11	Pillow
10R-1, 116	277.56	9D	14	16.5	-0.6	15.3	16.4	-1.4	0.0	34	0.0081	74.3	2.93	43	0.22	265.8	0.14	Pillow
11R-1, 32	286.32	3C	14	19.6	-5.7	9.8	19.3	-5.3	0.0	17	0.0112	34.2	3.04	22	0.31	216.5	0.08	Pillow
12R-1, 68	296.28	9C	16	222.1	-8.4	15.3	221.1	-6.7	0.0	15	0.0136	44.1	4.12	21	0.25	264.2	0.14	Massive
12R-1, 78	296.38	10B	16	110.6	-13.9	13.6	110.0	-12.0	0.1	16	0.0135	39.5	2.97	27	0.23	249.2	0.12	Massive
12R-1, 80	296.40	10B	16	108.6	-17.2	13.6	102.3	-20.6	0.4	16	0.0128	41.8						Massive
12R-2, 9	297.14	1C	16	253.7	-13.2	11.0	255.1	-8.2	0.0	11	0.0172	25.2	4.47	19	0.41	286.4	0.40	Massive
14R-2, 28	316.29	3	19	25.3	-13.1	14.1	25.1	-13.7	0.0	31	0.0067	82.6	4.01	55	0.31	239.6	0.15	Pillow
14R-2, 113	317.14	16A	21	92.5	-6.5	11.9	91.3	-7.8	0.0	13	0.0170	27.5	2.86	19	0.25	216.7	0.09	Pillow
15R-1, 103	325.33	15	23	23.0	-12.4	16.2	23.7	-11.9	0.0	33	0.0089	71.3	4.28	47	0.27	294.5	0.13	Pillow
16R-1, 21	334.10	3B	24	54.3	-6.2	13.2	54.0	-6.0	0.0	17	0.0169	30.7						Massive
16R-1, 32	334.21	3B	24	55.6	-10.9	9.4	55.9	-8.3	0.0	17	0.0181	20.3	3.36	22	0.31	253.0	0.09	Massive
16R-2, 34	335.59	1C	24	335.9	-16.5	5.0	338.6	-5.5	0.0	8	0.0344	5.7	2.36	15	0.47	179.3	0.11	Massive
16R-2, 130	336.55	4C	24	284.1	-14.8	7.9	283.9	-13.6	0.2	10	0.0204	15.1						Massive
16R-2, 132	336.57	4C	24	277.7	-7.7	7.4	278.8	-6.2	0.1	10	0.0193	15.0	2.60	15	0.40	223.3	0.58	Massive
16R-3, 88	337.58	4B	24	116.2	-15.6	4.4	110.7	-2.8	0.0	9	0.0230	7.6	2.65	17	0.62	211.0	0.25	Massive
17R-1, 1	343.51	1A	25	344.3	14.0	14.4	344.3	14.5	0.0	17	0.0193	29.2	3.84	21	0.28	273.0	0.09	Pillow
17R-1, 82	344.32	10B	26	204.9	-8.8	4.8	205.9	-10.3	0.0	16	0.0202	9.3	2.42	22	0.52	213.7	0.10	Pillow
17R-2, 126	346.26	11	27	46.4	-5.0	16.8	43.8	-5.7	0.0	13	0.0235	28.1	3.38	17	0.22	287.1	0.16	Pillow
17R-3, 37	346.81	4A	27	68.5	3.4	15.6	64.9	-2.6	0.0	13	0.0225	27.2	5.47	18	0.31	320.4	0.08	Pillow
17R-3, 89	347.33	8	27	215.5	-6.7	9.7	216.6	-6.5	0.0	14	0.0224	16.9	2.53	20	0.30	233.9	0.08	Pillow
17R-4, 28	348.18	2D	28	237.2	3.3	12.1	239.2	-2.0	0.0	12	0.0235	20.2	2.68	17	0.22	240.6	0.20	Massive
17R-4, 99	348.89	9	28	149.8	5.8	15.5	149.2	1.9	0.0	8	0.0303	20.0						Massive
18R-1, 72	353.82	6B	29	246.3	28.9	13.5	230.0	11.2	0.2	17	0.0201	26.4						Pillow
18R-1, 102	354.12	9B	29	167.0	3.1	13.8	166.0	-0.3	0.0	17	0.0210	25.7	3.54	20	0.26	275.9	0.08	Pillow
18R-2, 60	355.15	10	30	334.3	-32.8	8.3	332.0	-27.9	0.0	24	0.0088	37.2						Pillow
19R-1, 23	356.23	5A	30	116.0	-20.0	13.6	114.7	-25.5	0.0	19	0.0258	20.6	3.65	20	0.43	456.4	0.95	Pillow
20R-1, 63	364.13	15	30	255.2	-48.8	10.4	267.1	-52.3	0.0	18	0.0365	11.2						Pillow
20R-1, 108	364.51	22	31	270.4	20.0	4.4	287.6	-6.1	0.1	9	0.0470	3.6						Massive
21R-1, 58	373.58	10	31	344.8	11.3	1.4	337.8	-15.9	1.4	17	0.0300	1.9						Massive
21R-2, 85	375.33	13B	31	162.8	24.5	2.4	139.2	12.8	3.2	3	0.0470	2.0						Massive
21R-2, 133	375.81	13A	32	61.1	-56.9	3.8	58.0	-58.9	0.1	10	0.0310	4.9						Massive
22R-1, 107	383.67	13	32	227.9	-27.1	13.0	232.8	-30.6	0.0	21	0.0361	14.1						Massive
22R-3, 11	385.70	2	33	127.2	-28.6	3.8	115.8	-37.2	0.4	9	0.0295	5.1						Massive
22R-3, 26	385.85	3	33	107.1	-29.2	5.0	83.6	-43.6	0.0	10	0.0507	3.8						Massive
23R-1, 18	392.28	2	35	231.6	53.6	1.0	184.8	51.9	1.3	4	0.0368	1.1						Breccia
23R-1, 77	392.87	11	36	80.0	5.5	4.6	67.1	-6.7	0.1	18	0.0265	6.8						Massive
23R-3, 6	395.06	1	36	100.9	70.6	2.5	42.9	42.9	3.4	5	0.0377	2.6						Massive
23R-3, 132	396.32	17	33	215.6	61.8	3.3	186.9	48.0	1.0	5	0.0401	3.2	2.64	4	0.80	159.2	0.13	Massive
24R-1, 125	403.05	8	36	165.8	42.9	4.1	171.6	22.0	1.4	5	0.0453	3.5						Massive
24R-3, 140	406.18	14B	36	193.2	33.6	2.9	213.7	41.3	0.2	2	0.0447	2.6	3.07	5	1.06			Massive
25R-1, 49	411.75	6B	37	319.6	34.0	4.5	309.9	11.6	2.1	20	0.0203	8.7						Pillow
25R-3, 52	414.71	7	37	329.0	54.5	3.6	335.1	1.9	0.2	17	0.0192	7.3						Pillow
26R-1, 63	421.63	9B	38	123.8	41.0	3.4	95.3	9.8	1.6	9	0.0166	8.0						Massive
26R-2, 27	422.77	4	41	103.8	27.9	4.5	96.9	15.5	0.5	18	0.0182	9.8						Pillow
27R-1, 69	431.19	8	43	143.2	22.9	2.8	123.6	-2.3	1.9	9	0.0410	2.7						Pillow
27R-2, 64	432.59	7	44	102.2	-2.9	0.3	94.6	-24.0	1.1	30	0.0047	2.9						Pillow
																		(Breccia)
28R-2, 15	441.56	1B	47	103.8	27.6	3.3	93.6	21.6	3.3	19	0.0251	5.2						Pillow
28R-2, 39	441.80	3B	47	261.5	27.8	8.2	272.7	19.1	0.2	16	0.0290	11.1						Pillow
29R-1, 93	450.63	13	49	178.2	65.9	4.4	265.9	69.1	1.0	4	0.0632	2.7						Massive
30R-1, 36	459.66	6	50	148.4	-66.5	3.7	225.8	-41.4	0.2	20	0.0245	5.9						Pillow
30R-1, 44	459.74	7	50	265.2	-77.5	3.0				16	0.0169	6.9						Pillow
																		(Breccia)

Note: Declination (Dec) and inclination (Inc) are in degrees. Delta is a measure of the quality of the linear fit to the demagnetization data. Low values (<0.5) indicate highly linear data. MDF is median destructive field. Hsat is the field required to produce a saturation remanence. ARM = anhysteretic remanent magnetization; MAF = median destructive field of ARM; NRM = natural remanent magnetization; Sat IRM = saturation isothermal remanent magnetization.

**Table 8. Mean values of magnetic properties for samples from Hole 896A and the extrusives of Hole 504B (Furuta and Levi, 1983). N = number of samples.**

	$J_0$ (A/m)	$K$ (SI units)	$Q$	N	Stable inclination	MDF
<b>Hole 896A</b>						
Total	9.23 ± 5.2	0.021 ± 0.013	32 ± 32	71	-5.0 ± 21.9	19.1 ± 12.3
Pillows	10.7 ± 5.1	0.015 ± 0.009	44 ± 35	42	-8.2 ± 14.8	24.9 ± 12.5
Massive flows	6.7 ± 4.7	0.028 ± 0.014	13 ± 14	29	0.5 ± 27.6	11.9 ± 6.1
Above Unit 31	11.9 ± 4.0	0.015 ± 0.008	46 ± 31	46	-9.5 ± 10.4	22.6 ± 12.9
Unit 31 and below	3.9 ± 2.5	0.033 ± 0.014	5 ± 3	24	4.4 ± 33.8	12.3 ± 7.3
<b>Hole 504B</b>						
Pillows	10.2 ± 6.9	0.018 ± 0.008	28.1 ± 27.4	40		
Massive flows	4.7 ± 3.9	0.030 ± 0.014	7.4 ± 9.0	90		

Note: Uncertainties are expressed as standard deviations.

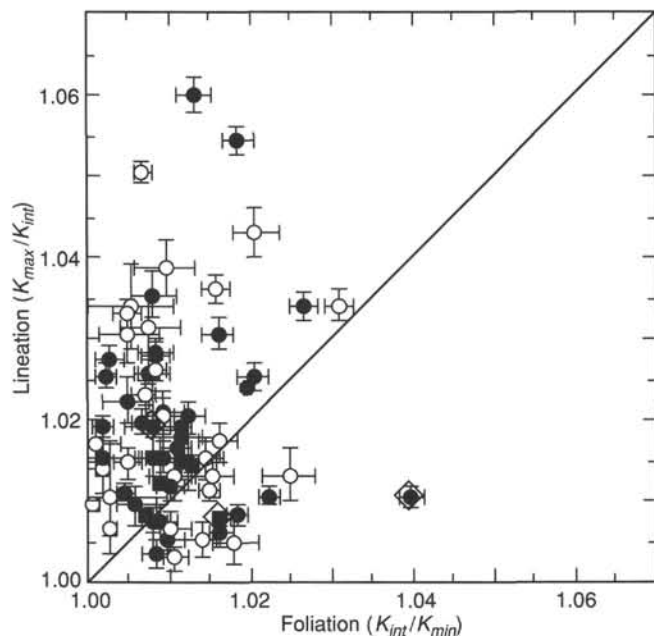


Figure 68. Anisotropy of magnetic susceptibility. Lineation ( $K_{max}/K_{int}$ ) vs. foliation ( $K_{int}/K_{min}$ ) for samples from Hole 896A. Samples from massive flow units are shown as solid circles; those from pillow units as unfilled circles; those from breccias as unfilled diamonds. Error bars are  $2 \times$  standard error.

immediately after the ship was offset from Hole 504B with the logging BHA kept near mudline. This procedure was followed because this was the only opportunity to measure temperatures in Hole 896A under conditions of reasonable recovery from the disturbance caused by the drilling process. The remainder of the downhole measurements in Hole 896A were conducted after the hole had been cored to its total depth of 469 mbsf. These included (in order of deployments) the Schlumberger geophysical combination (DLL/SDT), packer experiments at three inflation depths, a magnetometer log, and Schlumberger Formation MicroScanner (FMS).

### Temperature Log

As noted above, temperatures in Hole 896A were logged before the final 100 m of coring, immediately after 8 days of operations at Hole 504B. Thus, at the time of logging, Hole 896A had a total depth of 356 mbsf and had partially re-equilibrated from the thermal disturbance caused by drilling. This represented the best opportunity during Leg 148 to approximate the equilibrium thermal conditions in Hole 896A and to assess whether cold ocean bottom water was flowing down the hole as had occurred when Hole 504B was first drilled (Becker et al., 1983).

Temperatures were logged with the self-contained Lamont TLT attached to the bottom of the Schlumberger geochemical log. The TLT records pressure and the temperatures of two thermistors at 1 s intervals. The two thermistors are mounted in cases of different diameters and therefore have different thermal time constants. The thermistor with the faster time constant gave off-scale readings at seafloor temperatures, so the data from the thermistor with a somewhat slower time constant were used after a slight ( $0.64^\circ$ ) correction to match the known bottom water temperature. The profile recorded with this thermistor on the down-going run is shown in Figure 76. Depths were determined from the pressure readings and from the chronicle of events during the log. The pressure readings were somewhat noisy, which resulted in the apparent noise in the depth dimension of Figure 76.

The temperature profile measured in Hole 896A shows residual effects of the drilling disturbance, which ended 8 days before the log. Nevertheless the measured data (Fig. 76) would suggest a conductive heat flow on the order of  $275 \text{ mW/m}^2$ , and a temperature of about  $50^\circ\text{C}$  at the sediment-basement interface. These values are reasonably consistent with detailed heat flow surveys in the area (Langseth et al., 1988) and numerical modelling of off-axis hydrothermal circulation in the region (Fisher et al., 1990). In addition, the data do not display the depressed temperatures through the cased section that would be indicative of downhole flow as occurred when Hole 504B was first drilled.

### Schlumberger Logs

Three Schlumberger logs were successfully conducted in Hole 896A. First, as described above, the GLT was run with the TLT when the hole had been cored to a total depth of 356 mbsf. The DLL/SDT and two passes of the FMS were run after the final phase of coring, with the bottom of the hole at 469 mbsf. In running the DLL/SDT and FMS an obstruction was encountered at 423 mbsf, thus preventing the deepest 46 m of the hole from being logged.

Two passes of the GLT were required and excellent data were recorded on the second pass, both in the open hole and in casing. A Si-Fe crossplot of the recorded data (Fig. 77) shows the quality of the data set with a clear positive correlation between the two elements. The data recorded in casing have an expected higher Fe count through the sediments and upper 11 m of basement. This casing signal will be removed during post-cruise processing of the GLT data. The positive correlation between Fe and Si also appears in the general trend of the logs (Fig. 78), with a gradual decrease of both elements toward the top of the basement and into the sediments. The very low values measured below the casing shoe might be due to large hole size in this interval.

The DLL/SDT was run first at the end of coring operations in order to determine proper setting locations for the packer. Both electrical resistivity data and acoustic waveforms are of excellent quality throughout the recorded section (Fig. 79). Compressional velocities average  $5 \text{ km/s}$  (Fig. 80), with few excursions to values in the deeper half of the hole. In general, velocities are higher than those reported by Moos and Zuback (1990) in the upper part of Hole 504B, possibly reflecting a more important complete sealing of the upper basement at Site 896.

Electrical resistivities average  $10.0 \Omega\text{m}$  in the pillows and thin flows of upper half of the hole, similar to values obtained in the extrusive section of Hole 504B (Pezard, 1990). In the deeper section, resistivities are lower, down to  $3.0 \Omega\text{m}$ , probably reflecting the extent of groundmass alteration observed in the core ("Alteration" section, this chapter). Determining whether such low values reflect only the presence of alteration minerals or also an increase in the porosity of the basement will require post-cruise measurements of electrical resistivity and cation exchange capacity (CEC) of core samples.

The FMS was run last in the hole, and two successful passes were made. The images from these two passes will be processed and assembled during post-cruise processing. An overlay of the magnetic field vector and inclination obtained from the inclinometry section of

Table 9. Anisotropy of magnetic susceptibility (AMS) for samples from Hole 896A cored on Leg 148.

Sample	$K_{mean}$	$K_{max}$				$K_{int}$				$K_{min}$				Lineation $K_{max}/K_{min}$	Foliation $K_{int}/K_{min}$	Anisotropy $K_{max}/K_{min}$	Standard error
		Magnitude (SI)	Dec before	Dec after	Inc	Magnitude (SI)	Dec before	Dec after	Inc	Magnitude (SI)	Dec before	Dec after	Inc				
148-896A-																	
1R-1, 47-49	0.0580	0.0584	266.1	146.7	14.7	0.0581	159.4	40.0	47.7	0.0576	8.2	248.8	38.5	1.0051	1.0098	1.0149	0.0009
1R-1, 87	0.1116	0.1128	355.1	265.7	11.5	0.1111	242.5	153.1	62.2	0.1109	90.6	1.2	25.0	1.0152	1.0020	1.0172	0.0022
2R-1, 82	0.1388	0.1415	174.1	259.4	3.1	0.1380	264.8	350.1	13.8	0.1369	71.7	157.0	75.9	1.0257	1.0080	1.0338	0.0011
3R-1, 38	0.0381	0.0385	139.1	251.8	33.1	0.0382	231.0	343.7	2.9	0.0375	325.5	78.2	56.7	1.0084	1.0184	1.0270	0.0006
3R-1, 78	0.1112	0.1127	221.8	284.9	57.8	0.1111	28.4	91.5	31.5	0.1098	122.2	185.3	6.0	1.0147	1.0124	1.0272	0.0017
4R-1, 44	0.1180	0.1195	153.0	223.0	10.7	0.1177	60.8	130.8	11.4	0.1168	285.1	355.1	74.3	1.0154	1.0081	1.0236	0.0012
4R-1, 68	0.1020	0.1036	178.7	219.7	4.9	0.1018	87.7	128.7	10.9	0.1006	292.4	333.4	78.0	1.0181	1.0114	1.0297	0.0012
5R-2, 38	0.0273	0.0274	333.1	280.6	9.0	0.0273	70.1	17.6	37.8	0.0271	232.0	179.5	50.8	1.0035	1.0085	1.0121	0.0009
5R-3, 43	0.0981	0.0989	326.8	172.9	87.3	0.0978	83.6	289.7	1.2	0.0976	173.6	19.7	2.4	1.0105	1.0026	1.0131	0.0035
5R-3, 62	0.1084	0.1094	135.7	80.4	8.8	0.1089	19.8	324.5	70.4	0.1069	228.5	173.2	17.3	1.0051	1.0180	1.0231	0.0014
6R-1, 52	0.0594	0.0602	182.7	279.4	3.4	0.0593	274.8	11.5	32.1	0.0586	87.3	184.0	57.7	1.0146	1.0125	1.0272	0.0006
6R-2, 3	0.0142	0.0144	85.7	343.8	20.1	0.0142	186.4	84.5	27.0	0.0141	323.8	221.9	55.3	1.0096	1.0058	1.0154	0.0012
6R-2, 89	0.0476	0.0485	141.4	278.4	6.3	0.0472	51.4	188.4	0.0	0.0471	321.4	98.4	83.7	1.0273	1.0027	1.0301	0.0009
6R-3, 8	0.0753	0.0759	157.3	82.1	12.4	0.0753	63.3	348.1	17.2	0.0747	281.3	206.1	68.5	1.0076	1.0081	1.0157	0.0008
7R-1, 58	0.0553	0.0558	167.2	125.5	15.4	0.0554	32.0	350.3	68.8	0.0549	261.2	219.5	14.2	1.0073	1.0089	1.0162	0.0011
7R-1, 80	0.1253	0.1272	17.6	110.0	4.4	0.1248	172.9	265.3	85.2	0.1239	287.5	19.9	2.0	1.0197	1.0068	1.0266	0.0008
8R-1, 29	0.1187	0.1203	301.0	299.4	8.2	0.1185	31.6	30.0	4.4	0.1174	149.7	148.1	80.7	1.0154	1.0092	1.0248	0.0010
9R-1, 138	0.0920	0.0949	348.4	97.9	11.4	0.0918	240.6	350.1	56.7	0.0894	85.4	194.9	30.8	1.0341	1.0265	1.0615	0.0009
9R-2, 4	0.0499	0.0504	160.6	129.3	23.6	0.0498	36.5	5.2	52.0	0.0493	264.0	232.7	27.8	1.0116	1.0101	1.0219	0.0008
10R-1, 85	0.1115	0.1125	35.9	164.9	24.4	0.1113	268.8	37.8	53.0	0.1108	138.6	267.6	25.9	1.0111	1.0046	1.0158	0.0005
10R-1, 116	0.0789	0.0800	161.9	325.5	14.8	0.0785	62.7	226.3	31.1	0.0783	273.9	77.5	54.8	1.0192	1.0017	1.0209	0.0006
11R-1, 32	0.1257	0.1290	118.6	279.3	14.4	0.1246	10.9	171.6	49.6	0.1236	219.6	20.3	36.7	1.0355	1.0081	1.0439	0.0015
12R-1, 68	0.1635	0.1693	170.2	129.1	6.6	0.1612	58.4	17.3	72.8	0.1601	262.0	220.9	15.8	1.0504	1.0067	1.0575	0.0006
12R-1, 78	0.1399	0.1427	23.6	93.6	13.0	0.1391	116.1	186.1	10.8	0.1379	244.8	314.8	73.0	1.0261	1.0085	1.0348	0.0006
12R-1, 80	0.1392	0.1425	28.0	106.0	3.0	0.1379	297.0	15.0	21.0	0.1372	127.0	205.0	69.0	1.0330	1.0049	1.0380	0.0009
12R-2, 89	0.1884	0.1916	5.4	290.3	4.3	0.1891	273.3	198.2	26.7	0.1845	103.8	28.7	62.9	1.0132	1.0247	1.0383	0.0016
14R-2, 28	0.0679	0.0684	266.4	61.3	12.4	0.0679	165.0	319.9	42.1	0.0674	9.2	164.1	45.3	1.0082	1.0068	1.0151	0.0003
14R-2, 113	0.1770	0.1808	185.6	274.3	6.1	0.1758	94.4	183.1	11.7	0.1744	302.6	31.3	76.8	1.0280	1.0083	1.0366	0.0009
15R-1, 32	0.0968	0.0982	239.4	35.7	39.8	0.0966	148.0	304.3	1.7	0.0955	56.0	212.3	50.2	1.0168	1.0108	1.0278	0.0010
16R-1, 21	0.1841	0.1901	324.0	90.0	12.0	0.1838	233.0	359.0	5.0	0.1783	120.0	246.0	77.0	1.0341	1.0309	1.0661	0.0009
16R-1, 31	0.2292	0.2373	148.7	272.8	2.1	0.2275	58.4	182.5	7.3	0.2229	254.8	18.9	82.4	1.0429	1.0207	1.0645	0.0015
16R-2, 34	0.3827	0.3891	119.9	321.3	18.8	0.3825	215.5	56.9	16.2	0.3765	343.7	185.1	64.8	1.0173	1.0160	1.0335	0.0012
16R-2, 130	0.2223	0.2248	20.0	276.0	1.0	0.2216	110.0	6.0	28.0	0.2205	289.0	185.0	62.0	1.0146	1.0049	1.0197	0.0009
16R-2, 132	0.1858	0.1873	25.1	286.3	20.6	0.1863	143.7	44.9	51.8	0.1838	282.3	183.5	30.5	1.0053	1.0139	1.0193	0.0010
16R-3, 88	0.2440	0.2510	203.1	272.4	6.8	0.2416	90.9	160.2	72.5	0.2394	295.1	4.4	16.1	1.0389	1.0095	1.0488	0.0018
17R-1, 1	0.2042	0.2075	233.0	69.0	1.0	0.2030	324.0	160.0	50.0	0.2021	143.0	339.0	40.0	1.0224	1.0046	1.0272	0.0014
17R-1, 82	0.2173	0.2204	16.0	350.0	20.0	0.2181	285.0	259.0	2.0	0.2134	190.0	164.0	70.0	1.0107	1.0222	1.0331	0.0006
17R-2, 126	0.2337	0.2377	350.0	126.0	1.0	0.2328	260.0	36.0	17.0	0.2306	84.0	220.0	73.0	1.0210	1.0093	1.0305	0.0012
17R-3, 37	0.2838	0.2899	350.0	105.0	19.0	0.2819	255.0	10.0	12.0	0.2796	134.0	249.0	67.0	1.0282	1.0083	1.0367	0.0010
17R-3, 89	0.2134	0.2184	356.9	319.9	4.9	0.2130	88.8	51.8	21.3	0.2088	254.5	217.5	68.1	1.0252	1.0203	1.0460	0.0009
17R-4, 28	0.2587	0.2607	267.0	208.0	4.0	0.2590	357.0	298.0	4.0	0.2564	136.0	77.0	85.0	1.0065	1.0102	1.0167	0.0012
17R-4, 99	0.3190	0.3222	92.0	123.0	45.0	0.3177	184.0	215.0	2.0	0.3171	276.0	307.0	45.0	1.0142	1.0018	1.0160	0.0005
18R-1, 72	0.2097	0.2132	185.0	135.0	5.0	0.2092	93.0	43.0	26.0	0.2068	284.0	234.0	63.0	1.0191	1.0115	1.0308	0.0007
18R-1, 102	0.2248	0.2279	275.0	289.0	9.0	0.2245	181.0	195.0	24.0	0.2220	24.0	38.0	64.0	1.0150	1.0115	1.0267	0.0011
18R-2, 60	0.0875	0.0893	92.0	300.0	10.0	0.0870	1.0	209.0	1.0	0.0864	265.0	113.0	80.0	1.0259	1.0074	1.0334	0.0007
19R-1, 23	0.1785	0.1802	34.3	99.6	10.7	0.1791	301.0	6.3	16.6	0.1762	155.6	220.9	70.0	1.0060	1.0163	1.0225	0.0008
20R-1, 63	0.3114	0.3194	265.0	177.9	5.1	0.3099	173.1	86.0	20.8	0.3050	8.1	281.0	68.5	1.0306	1.0161	1.0472	0.0010
20R-1, 108	0.3712	0.3731	42.8	295.2	11.5	0.3708	180.5	72.9	74.7	0.3697	310.7	203.1	10.0	1.0064	1.0028	1.0093	0.0004
21R-1, 58	0.1615	0.1654	335.1	177.3	39.9	0.1600	214.0	56.2	31.7	0.1591	99.4	301.6	33.9	1.0341	1.0055	1.0398	0.0026
21R-2, 85	0.3396	0.3437	30.4	71.2	13.6	0.3393	138.2	179.0	51.6	0.3358	290.6	331.4	35.1	1.0130	1.0103	1.0234	0.0015
21R-2, 133	0.2648	0.2666	150.1	272.1	1.0	0.2640	240.3	2.3	17.3	0.2639	57.0	179.0	72.7	1.0097	1.0004	1.0101	0.0004
22R-1, 107	0.2506	0.2520	310.8	258.0	29.3	0.2512	209.4	156.9	19.4	0.2486	90.7	37.9	53.8	1.0030	1.0107	1.0137	0.0008
22R-3, 11	0.3303	0.3399	38.3	102.5	23.7	0.3281	140.7	204.9	26.2	0.3230	272.1	336.3	53.4	1.0360	1.0158	1.0524	0.0009
22R-3, 26	0.3694	0.3759	352.4	88.8	34.5	0.3674	237.7	334.1	31.3	0.3649	117.2	213.6	39.8	1.0233	1.0069	1.0303	0.0007
23R-3, 132	0.3492	0.3533	190.6	183.7	59.0	0.3474	19.7	12.8	30.7	0.3470	287.3	280.4	4.0	1.0171	1.0012	1.0183	0.0015
23R-1, 18	0.2503	0.2542	230.2	225.4	15.8	0.2493	139.2	134.4	3.4	0.2474	37.3	32.5	73.9	1.0194	1.0079	1.0274	0.0017
23R-1, 77	0.1974	0.1999	31.0	143.9	27.1	0.1976	300.2	53.1	1.6	0.1947	207.0	319.9	62.8	1.0116	1.0148	1.0266	0.0007
23R-3, 6	0.2837	0.2876	54.4	191.5	15.0	0.2839	159.7	296.8	44.5	0.2796	310.6	87.7	41.7	1.0130	1.0152	1.0284	0.0013
24R-1, 125	0.3673	0.3734	262.0	270.4	62.5	0.3659	81.1	89.5	27.5	0.3625	171.3	179.7	0.3	1.0205	1.0094	1.0301	0.0011
24R-3, 140	0.2956	0.3020	341.0	307.3	3.0	0.2931	247.7	214.0	47.8	0.2917	73.7	40.0	42.0	1.0305	1.0050	1.0356	0.0018
25R-1, 49	0.1595	0.1623	49.0	279.1	17.3	0.1583	315.8	185.9	10.0	0.1579	197.0	67.1	69.9	1.0255	1.0023	1.0279	0.0007
25R-3, 52	0.1532	0.1549	32.5	237.4	12.9	0.1530	125.0	329.9	10.9	0.1517	254.2	99.1	73.0	1.0123	1.0090	1.0214	0.0005
26R-1, 63	0.1																

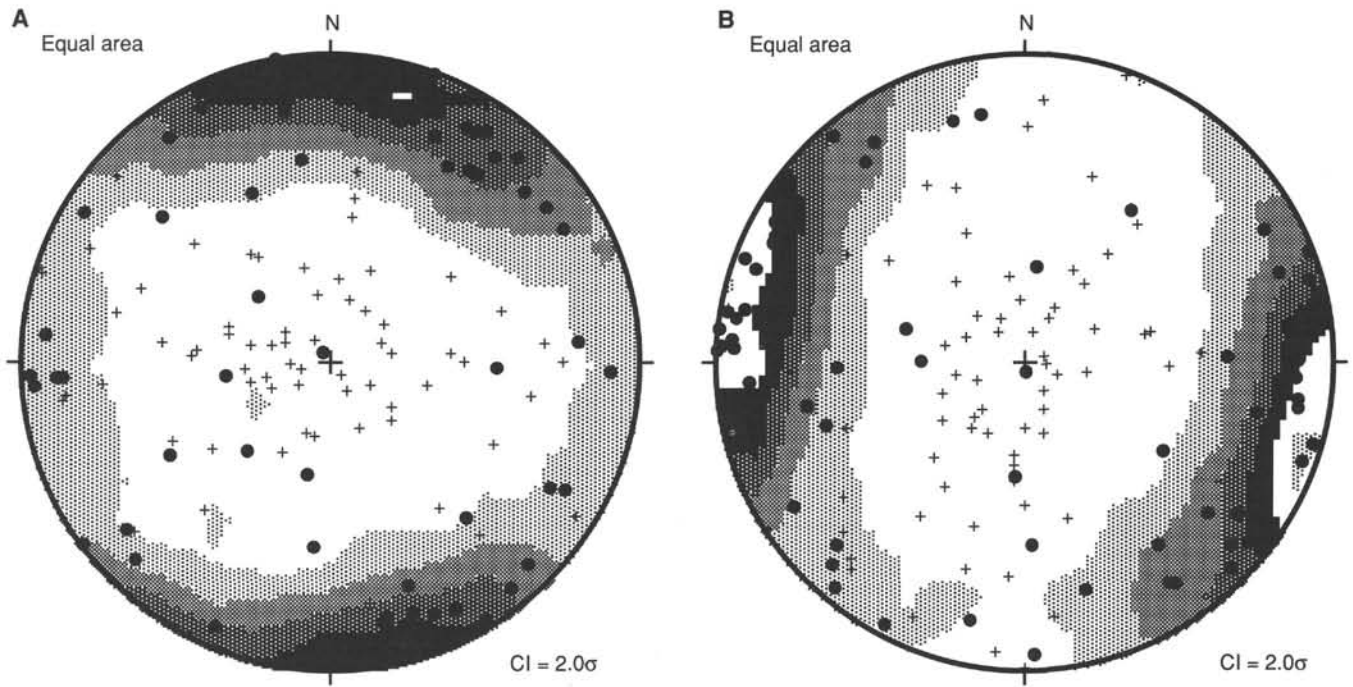


Figure 69. Lower hemisphere equal-area projection of principal axes of magnetic susceptibility anisotropy. Circles are  $K_{max}$  axes; crosses are  $K_{min}$  axes. Kamb contours at  $2\sigma$  intervals on  $K_{max}$  axes. **A.** In-situ core coordinates. **B.** Reoriented coordinates using the stable remanence direction.

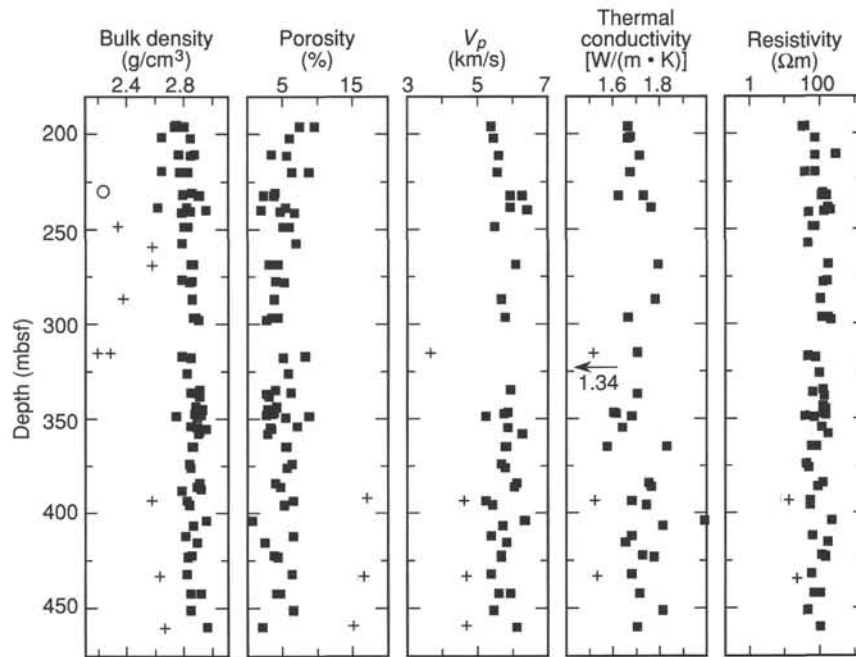


Figure 70. Wet-bulk density, porosity, compressional wave velocity ( $V_p$ ), thermal conductivity, and electrical resistivity of basalts (squares), cemented breccias (crosses), and clay fillings (open circle) from Hole 896A vs. depth.

Magnetic characterization by logging is continuous, in contrast to measurements on drill cores that are limited by the recovery rate. The location of Site 896, about 1 km south of Site 504, is closer to a transition in the surface magnetic anomaly pattern from reverse to normal polarity. Therefore, the chances of encountering normally magnetized basalts in the upper extrusives should be higher in Hole 896A than in

Hole 504B. The probability of finding mixed polarities depends not only on the lateral distance from the anomaly transition but also on the age distribution of the accumulated basalts. The magnetic logging data can also reveal to what degree the drilled section contributes to the magnetic anomalies measured at the surface. Thus, inferences can also be drawn about the magnetization of the underlying rocks.

**Table 10. Physical properties of samples collected from Hole 896A.**

Core, section, interval (cm)	Depth (mbsf)	Bulk density (g/cm <sup>3</sup> )	Grain density (g/cm <sup>3</sup> )	Porosity (%)	V <sub>p</sub> (km/s)	Thermal conductivity (W/(m • K))	Resistivity (Ωm)	Formation factor
148-896A-								
1R-1, 22-25	195.32	2.75						
1R-1, 47-50	195.57	2.74	2.92	9.5			30.3	151
1R-1, 55-63	195.65					1.66		
1R-1, 81-92	195.91	2.81	2.95	7.5	5.38	1.66	37.8	189
2R-1, 13-16	201.03	2.64						
2R-1, 41-44	201.31					1.67		
2R-1, 82-90	201.72	2.85	2.97	5.9	5.44	1.66	71.6	358
3R-1, 14-17	210.04	2.77						
3R-1, 38-41	210.28	2.88	2.95	3.2			271.2	1356
3R-1, 73-85	210.63	2.85	2.96	5.6	5.60	1.71	69.7	348
4R-1, 12-15	219.02	2.65						
4R-1, 43-58	219.33	2.83	2.95	6.2	5.54	1.67	71.1	355
4R-1, 68-71	219.58	2.77	2.94	8.7			35.1	175
5R-1, 11-14	228.51	2.23						
5R-2, 38-41	230.28	2.86	2.93	3.9			124.5	623
5R-3, 3-7	231.43	2.80						
5R-3, 39-49	231.79	2.90	2.98	3.7	5.92	1.73	107.5	538
5R-3, 58-67	231.98	2.92	2.96	2.2	6.25	1.62	148.5	742
6R-1, 1-4	237.91	2.62						
6R-1, 37-57	238.27	2.82	2.93	5.5	5.93	1.76	168.9	844
6R-2, 3-7	239.43	2.96	3.00	1.8	6.40		199.6	998
6R-2, 89-92	240.29	2.85	2.93	4.6			128.9	644
6R-3, 8-11	240.98	2.78	2.91	0.6			48.9	245
7R-1, 45-48	247.85	2.33						
7R-1, 58-61	247.98	2.80	2.91	5.9		5.49	61.7	309
7R-1, 80-83	248.20	2.83	2.93	5.0			74.4	372
8R-1, 29-32	257.39	2.79	2.92	6.9			42.2	211
8R-1, 52-55	257.62	2.56						
9R-1, 58-61	267.28	2.56						
9R-1, 138-141	268.08	2.85	2.93	4.3				
9R-2, 0-13	268.24	2.87	2.93	3.0	6.06	1.79	169.2	846
10R-1, 1-4	276.41	2.79						
10R-1, 85-88	277.25	2.86	2.94	3.8			151.9	760
10R-1, 116-119	277.56	2.84	2.94	5.2			114.9	575
11R-1, 26-36	286.26	2.86	2.93	3.7	5.68	1.78	99.1	495
11R-2, 50-53	288.00	2.37						
12R-1, 63-72	296.23	2.87	2.95	4.2	5.77	1.66	106.1	531
12R-1, 78-81	296.38	2.88	2.95	3.4			175.9	879
12R-2, 9-12	297.19	2.91	2.96	2.6			194.0	970
14R-1, 13-26	314.73					1.70		
14R-1, 64-72	315.24	2.28			3.58	1.34		
14R-2, 28-31	316.38	2.78	2.94	8.2			44.5	223
14R-2, 113-116	317.23	2.85	2.95	5.1			69.8	349
15R-1, 103-106	325.33	2.82	2.93	5.7			95.2	476
16R-1, 31-34	334.21	2.91	2.99	3.9	5.93		117.3	587
16R-2, 34-37	335.74	2.85	2.97	6.0			59.7	299
16R-2, 125-137	336.75	2.90	2.96	2.6	1.70			
16R-3, 88-91	337.78	2.91	2.97	2.9			128.8	644
17R-1, 1-4	343.51	2.89	2.97	4.1			117.7	588
17R-1, 82-85	344.32	2.94	2.99	2.8			137.6	688
17R-2, 120-134	346.20	2.90	2.97	3.6	5.87	1.60	131.7	658
17R-3, 29-37	346.79	2.88	2.95	3.5	5.74	1.61	115.2	576
17R-3, 89-92	347.39	2.92	2.97	2.5			146.5	733
17R-4, 27-35	348.27	2.75	2.92	8.7	5.23	1.68	37.8	189
17R-4, 99-102	348.99	2.90					65.5	327
18R-1, 72-75	353.82	2.85						
18R-1, 94-106	354.04	2.90	2.96	3.1	5.86	1.64	111.0	555
18R-2, 60-63	355.20	2.96	3.03	3.4				
19R-1, 23-26	356.23	2.91						
19R-2, 41-44	357.91	2.91	2.96	2.7	6.25		170.0	850
20R-1, 63-73	364.13	2.86	2.97	5.6	5.80	1.57	56.4	282
20R-1, 101-109	364.51	2.87	2.97	5.3	5.79	1.83	75.6	378
21R-1, 58-61	373.58	2.84	2.96	6.3	5.68		39.6	198
21R-2, 85-88	375.35	2.85	2.96	5.5	5.77		45.5	228
22R-1, 107-114	383.67	2.92	2.99	3.8	6.11	1.75	121.9	609
22R-3, 26-32	385.86	2.90	2.99	4.6	6.04	1.76	86.5	433
22R-3, 132-135	386.92	2.93						
22R-4, 44-47	387.54	2.79						
23R-1, 18-24	392.28	2.57	2.89	16.7	4.54	1.51	9.7	49
23R-1, 77-86	392.87	2.82	2.95	6.5	5.23	1.68	50.8	254
23R-3, 6-13	395.16	2.84	2.94	5.2	5.41	1.74	52.5	262
24R-1, 125-134	403.05	2.96	2.97	0.6	6.35	1.99	220.4	1102
24R-3, 140-145	406.20	2.87						
25R-1, 49-52	411.79	2.81	2.94	6.4	5.38	1.81		308
25R-1, 53-66	411.83					1.68		
25R-3, 52-56	414.82	2.90	2.95	2.4	5.81	1.65	165.2	826
26R-1, 63-69	421.63	2.86	2.93	3.7	5.65	1.72	108.7	543
26R-2, 27-30	422.77	2.83	2.91	4.2	5.66	1.77	141.9	709
27R-1, 69-75	431.19	2.82	2.95	6.3	5.38	1.68	54.7	274
27R-2, 64-70	432.64	2.63	2.95	16.3	4.66	1.53	18.0	90
28R-2, 15-20	441.65	2.85	2.94	4.6	5.59	1.71	103.2	516
28R-2, 39-42	441.89	2.92	3.00	4.0	5.92		64.4	322
29R-1, 93-97	450.63	2.85	2.98	6.6	5.43	1.81	41.4	207
30R-1, 36-39	459.66	2.97	3.01	2.0	6.12		102.4	512
30R-1, 44-49	459.74	2.67	2.95	14.6	4.63	1.70		

**Logging Procedure**

The BGR magnetometer, described in the “Explanatory Notes” chapter, this volume, measured the horizontal and vertical field components of the magnetic field in Hole 896A from 208 mbsf to 438 mbsf. The downhole logging speed was 20 m/min while the rate uphole was 10 m/min. At a sampling rate of 0.5 s these logging speeds resulted in sampling intervals of 16 cm and 8 cm, respectively. Since the logging

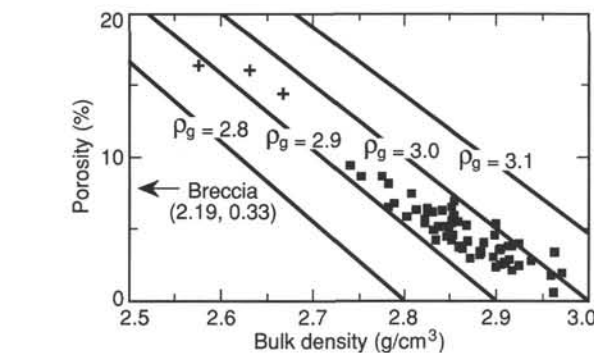


Figure 71. Wet-bulk density vs. porosity for basalts (squares) and breccia (crosses) from Hole 896A. The Hole 896A samples have a grain density, ρ<sub>g</sub>, of 2.95–3.00 g/cm<sup>3</sup>.

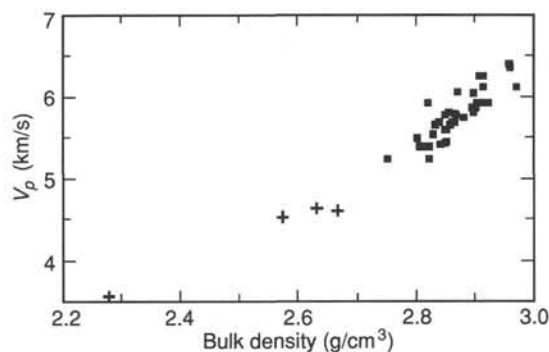


Figure 72. Wet-bulk density vs. velocity for basalts (squares) and breccia (crosses) from Hole 896A at room temperature and pressure.

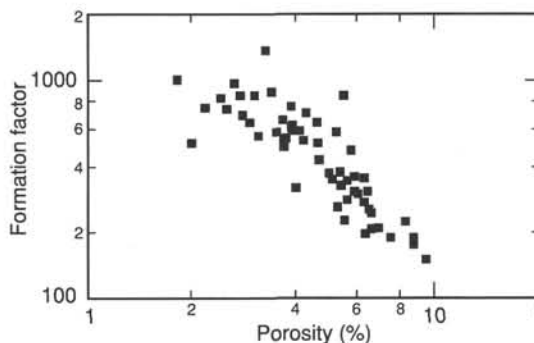


Figure 73. Formation factor vs. porosity for samples from Hole 896A.

time was <40 min, the effect of daily variations of the Earth’s magnetic field on the anomaly field should be negligible. In addition, the quality of the anomaly data can be judged by comparing downhole and up-hole measurements. The centralizers were modified to avoid a repetition of the problems that were encountered at the end of logging Hole 504B, when they jammed during reentry into the drill pipe. However, this change also reduced the maximum diameter of the centralizers, which resulted in frequent rotations of the tool during logging.

**Results**

Figure 83 displays the horizontal and vertical components and the total strength of the magnetic field as a function of depth in Hole 896A. Also indicated as straight lines are the components of the

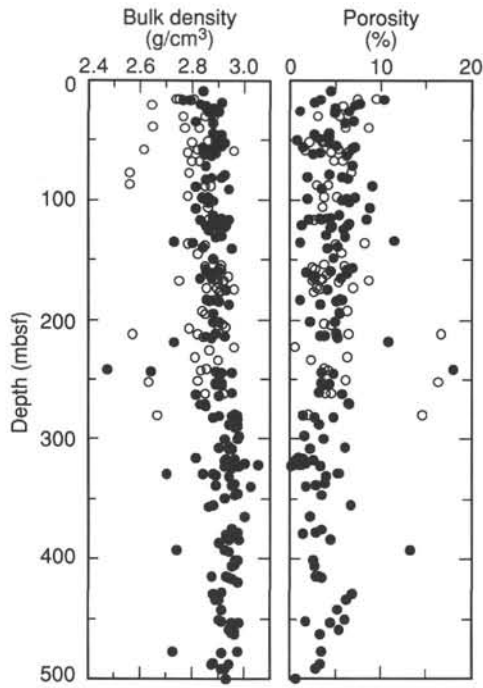


Figure 74. Comparison of wet-bulk densities and porosities of samples from Hole 896A (open circles) and Hole 504B (filled circles) vs. depth.

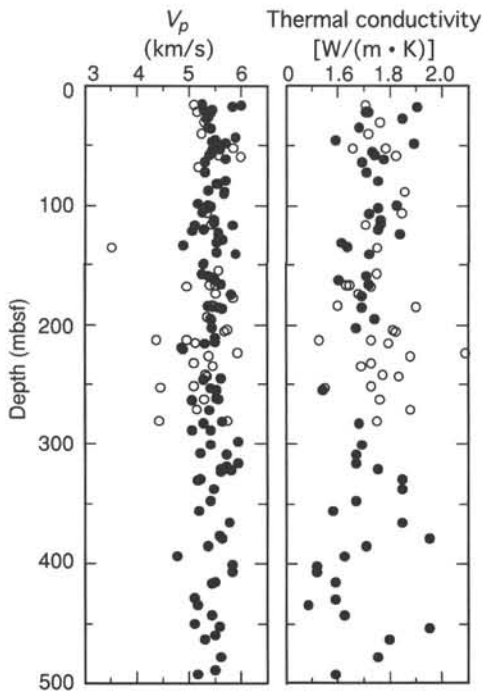


Figure 75. Comparison of compressional wave velocities ( $V_p$ ) and thermal conductivities of samples from Hole 896A (open circles) and Hole 504B (filled circles) vs. depth.

Earth's main field that would be measured if the surrounding rocks were non-magnetic. These are raw data, uncorrected for possible time and temperature drifts. The largest distortions, however, are probably due to rotations of the magnetometer, which resulted in small oscillations of the signals with wavelengths  $>10$  m. These artificial anomaly contributions can be identified by comparing downhole and

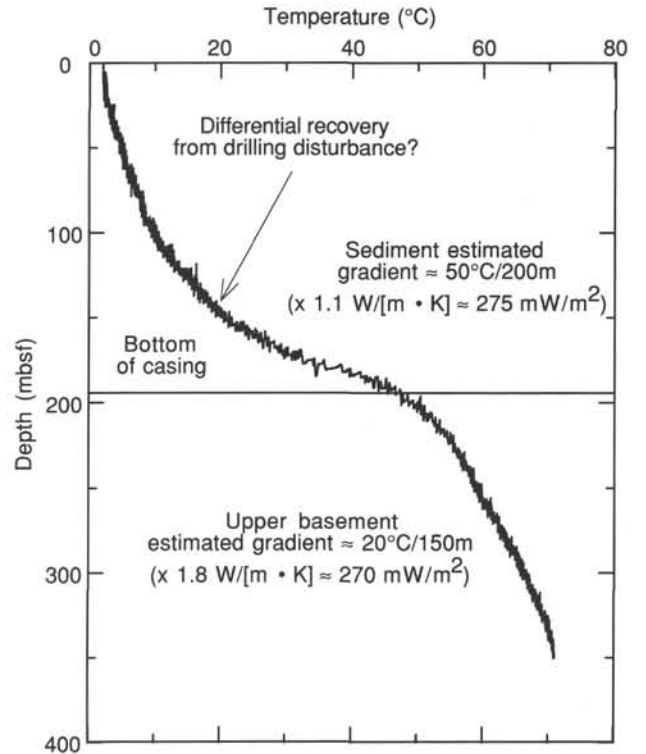


Figure 76. Temperatures in Hole 896A recorded with the Lamont TLT during the downgoing deployment of the geochemical logging tool, about eight days after the last disturbance to the hole by drilling.

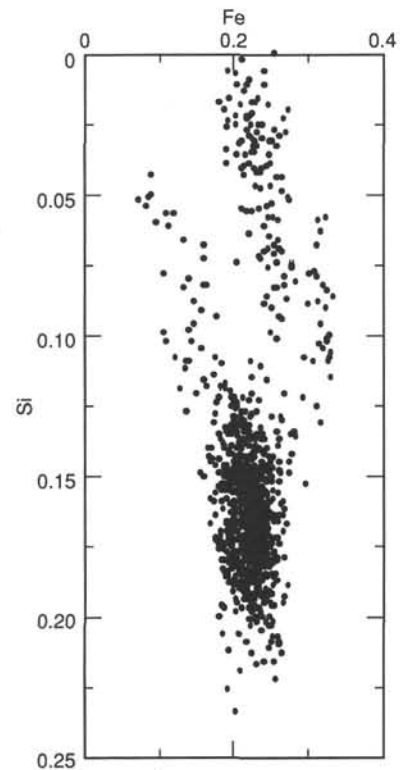


Figure 77. Cross-plot of raw silicon and iron counts from geochemical logs at Hole 896A. Relatively high-iron/low-silicon points are influenced by the presence of drillpipe.

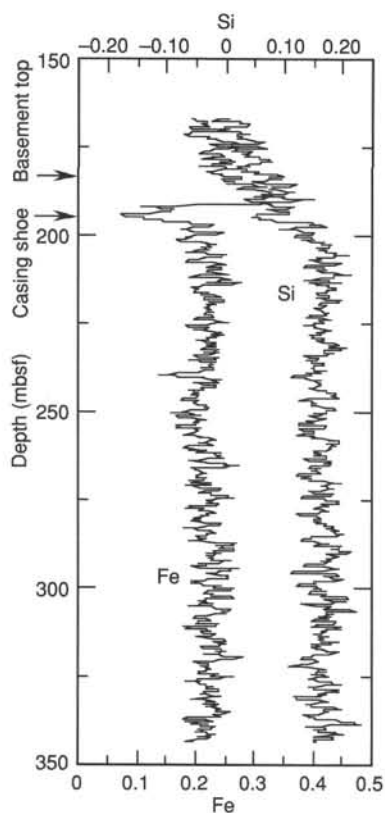


Figure 78. Raw silicon and iron counts from geochemical logs at Hole 896A plotted vs. depth below seafloor.

uphole measurements. These errors will be corrected by applying results of a laboratory calibration. Figure 84 displays downhole as well as uphole measurements of the horizontal and vertical field components in the depth range 280 to 320 mbsf.

### Interpretation

The measured anomalies are large for most of the hole with amplitudes of up to 5000 nT. Only in the bottom 30 m are the anomalies rather small with amplitudes <100 nT. The anomaly amplitudes are predominantly positive for the vertical and negative for the horizontal component. According to the models displayed in the "Downhole Measurements" section, Site 504 chapter (this volume), these indicate reverse magnetizations with negative inclinations. The paleomagnetic results obtained from minicores ("Paleomagnetism" section, this chapter) show intensities of the natural remanent magnetization (NRM) averaging about 11 A/m above Unit 31 (sub-bottom depth approximately 365 mbsf), with mostly negative inclinations, in good agreement with the anomaly measurements. Cores from Hole 896A were not azimuthally oriented, so the declination of the NRM could not be determined. The decrease in magnetization below Unit 31 at the bottom of the hole is equally well reflected in logging measurements. There are a few positive horizontal anomalies, possibly indicating normally magnetized rocks. However, the wide positive anomaly around 400 mbsf just above the weakly magnetic zone may also be a result of the 'shoulder' effect discussed in the "Downhole Measurements" section, Site 504 chapter, that occurs at the boundary of a magnetic layer whose thickness is on the order of its diameter. The large, narrow positive anomaly near 300 mbsf is recorded in both the downhole and uphole records and is therefore not an artifact. This is most likely caused by normally magnetized rocks, although other geometrical models with reverse magnetizations should be tested.

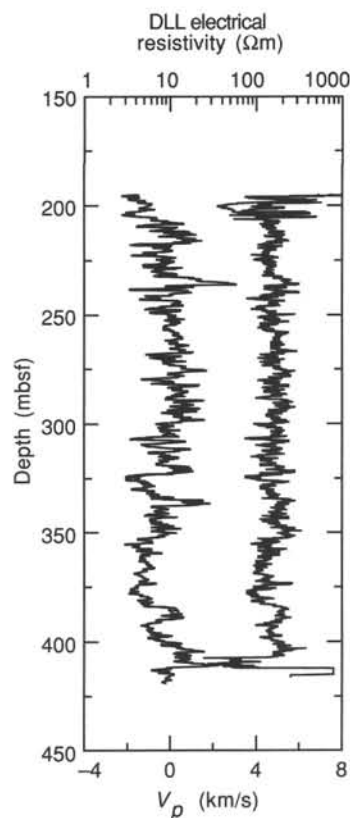


Figure 79. Deep resistivity and compressional sonic velocities in Hole 896A as recorded with the Schlumberger DLL/SDT.

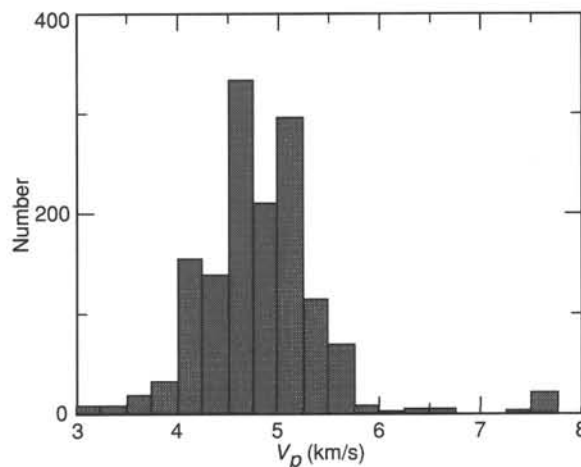


Figure 80. Histogram of sonic velocities recorded in Hole 896A.

The wavelength of the anomalies is on the order of meters. This implies that the magnetization of the surrounding rocks changes on the same scale although other factors such as borehole breakouts, dip of the layers, and lateral inhomogeneities add higher-frequency components to the total signal.

The magnetic anomalies measured in Hole 896A bear several similarities to those measured in Hole 504B, regarding amplitudes, polarities, and wavelengths. It may be concluded that the upper extrusives at both sites are very similar in their magnetic properties.

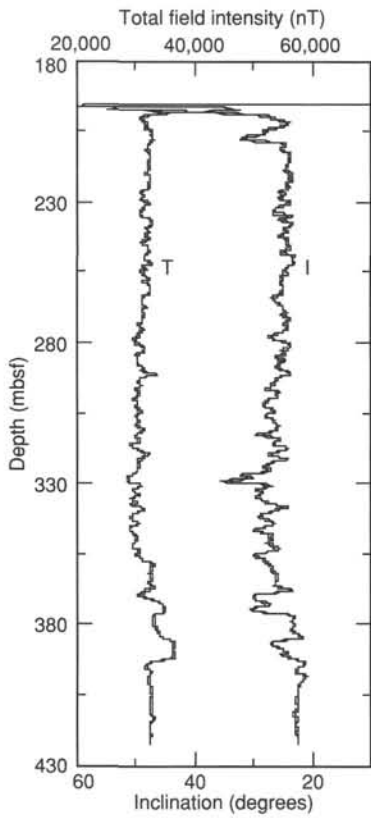


Figure 81. Total magnetic field intensity and inclination from the two passes of the FMS in Hole 896A.

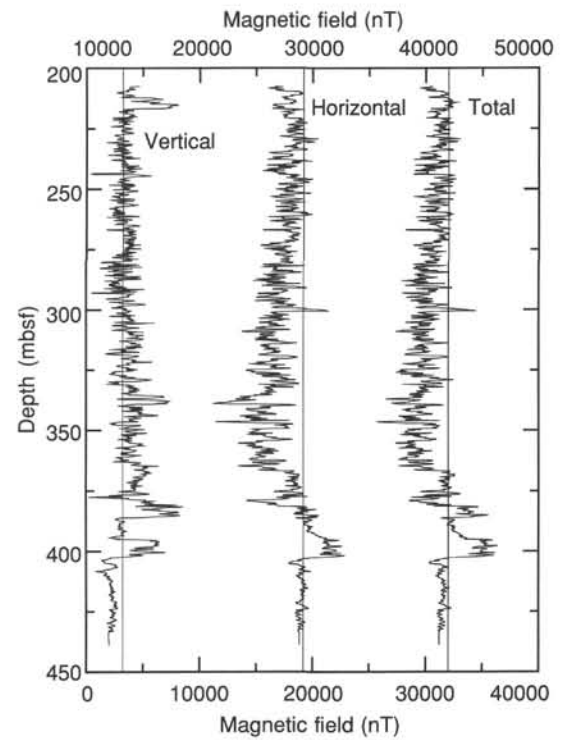


Figure 83. Downhole variations of the vertical, horizontal, and total magnetic field components in Hole 896A. The scale at the top axis applies to the vertical and horizontal components; the scale on the bottom axis applies to the total field. The straight lines are the main field components, as given in Table 14, "Site 504" chapter.

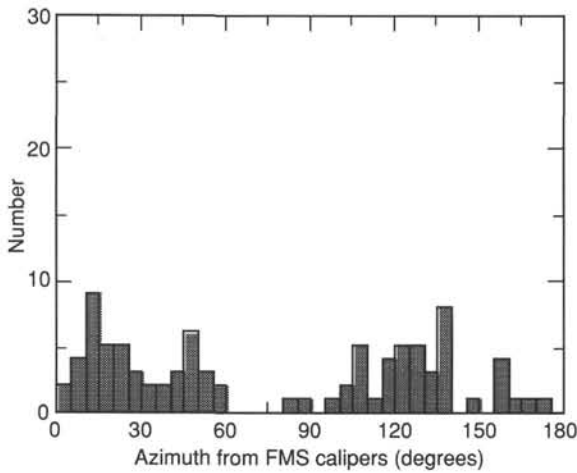


Figure 82. Histogram of borehole elongation azimuths at Hole 896A from filtered FMS calipers.

**Packer Experiments**

Packer experiments were conducted in Hole 896A after the Schlumberger geophysical log was run, as this log was required for the selection of formations in which to inflate the packer. The caliper log was not registering reliable hole diameters, so the packer inflation depths were selected using the resistivity and sonic data. These data suggested only a few prospective inflation depths, so the packer was first inflated in casing before attempting open-hole inflations (where the risk of damage to the packer is greater). Three successful packer

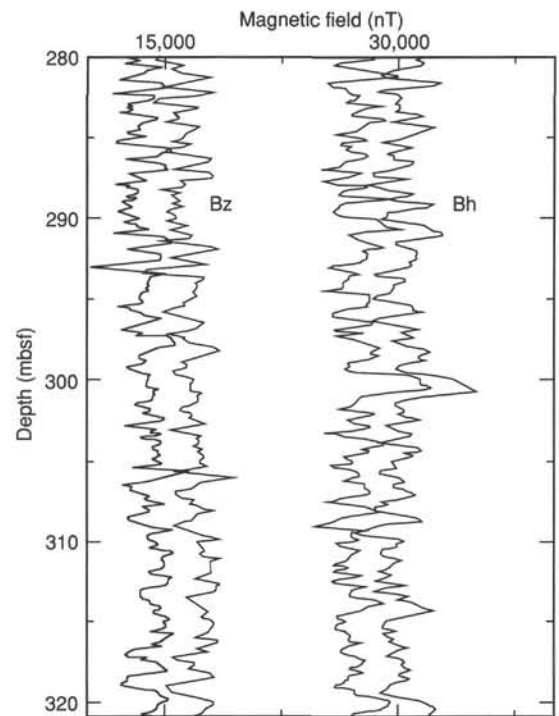


Figure 84. Comparison of downgoing and upgoing measurements of the magnetic field components for the depth range 280–320 mbsf. The downgoing traces have been offset by 3000 nT.

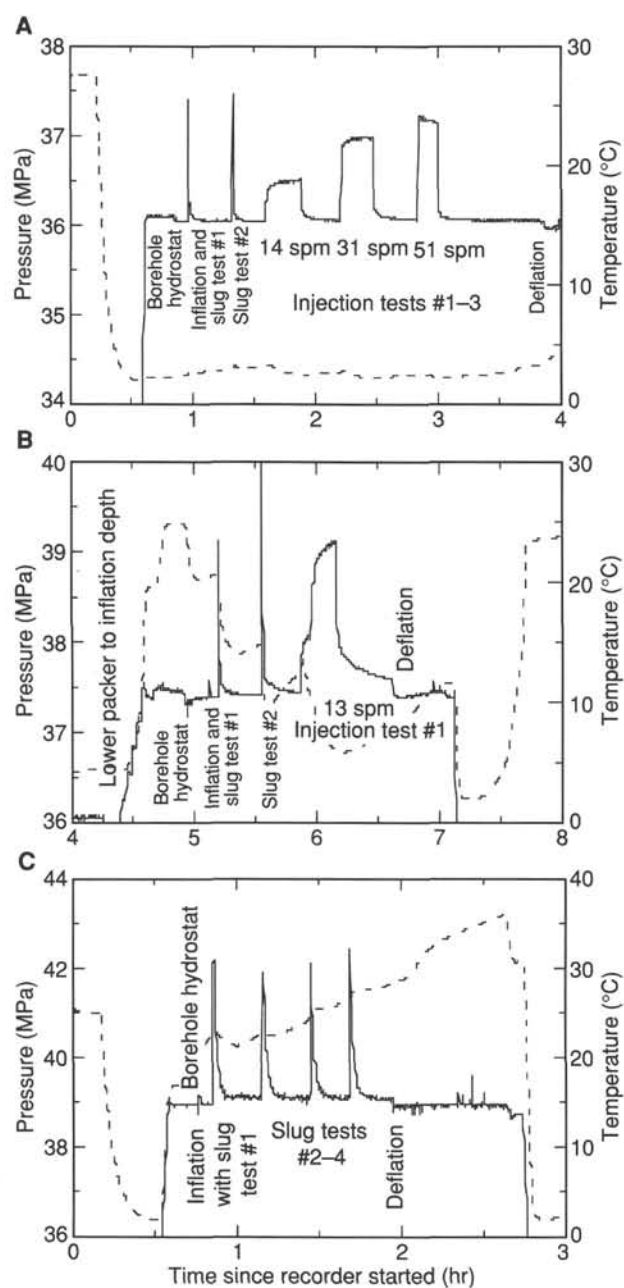


Figure 85. Pressure-time records recorded with a downhole electronic gauge during the three packer experiments in Hole 896A. A. Packer inflated in casing at 106 mbsf. B. Packer inflated in upper basement at 233 mbsf. C. Packer inflated deep in the hole at 385 mbsf.

inflations were conducted: (1) at 106 mbsf within casing; (2) at 233 mbsf in a zone of high resistivity about 40 m below the casing shoe; and (3) at 385 mbsf in another zone of high resistivity 71 m above the bottom of the hole.

Figure 85 shows the pressure records collected by the downhole gauges during the experiments conducted at each of the three inflation depths. With the packer inflated in casing (Fig. 85A), two slug tests decayed quickly, suggesting relatively high transmissivity for the entire open-hole interval (or the possibility of leakage past the grout between the casing and formation). Three constant-rate injection tests were conducted, at successively higher pumping rates (14, 31, and 51 strokes per minute, or spm). The first two injection tests show proper pressure-time records that should yield valid permeability informa-

tion; however, the last test at the highest pump rate shows pressure decreasing with time, suggesting that pre-existing cracks in the formation were being slowly opened or that the hydraulic integrity of the seal between packer and casing was being compromised.

Given that pumping rates of at least 50 spm are desirable for the packer/flowmeter experiment, it was decided not to attempt this experiment, but instead to run the packer into the hole for open-hole inflations. The first open-hole inflation was conducted at the first appropriate formation below the casing, to test the permeability of the upper basement section without the ambiguities introduced when inflating in casing. Two slug tests and a single constant-rate injection test were conducted at this inflation (Fig. 85B), and the results indicate lower transmissivity and average permeability than when the packer was inflated in casing. At the conclusion of the packer inflation at 233 mbsf, the go-devil was retrieved, and the pressure gauges were redressed while the packer was moved to the inflation point at 385 mbsf, to test the permeability of the deepest section of the hole. Four slug tests were conducted (Fig. 85C); these decayed fairly slowly, indicating that this section of the hole is less transmissive and probably less permeable than the upper section.

The unprocessed pressure-time records suggest some tentative, qualitative interpretations about the permeability structure in Hole 896A, as follows: It appears that the uppermost few tens of meters of basement in Hole 896A are quite permeable, much like in Hole 504B (Becker et al., 1983). Permeabilities decrease deeper in Hole 896A, but probably remain large enough to support the kind of off-axis circulation concentrated in the upper few hundred meters of basement as modeled by Fisher et al., (1990). The deepest section of Hole 896A probably does not show the sharp reduction of permeability reported below 260 m into basement in Hole 504B by Anderson et al. (1985).

#### REFERENCES\*

- Adamson, A.C., 1985. Basement lithostratigraphy, Deep Sea Drilling Project Hole 504B. In Anderson, R.N., Honnorez, J., Becker, K., et al., *Init. Repts. DSDP, 83*: Washington (U.S. Govt. Printing Office), 121-127.
- Ade-Hall, J.M., and Johnson, H.P., 1976. Paleomagnetism of basalts, Leg 34. In Yeats, R.S., Hart, S.R., et al., *Init. Repts. DSDP, 34*: Washington (U.S. Govt. Printing Office), 513-532.
- Anderson, R.N., Honnorez, J., Becker, K., et al., 1985. *Init. Repts. DSDP, 83*: Washington (U.S. Govt. Printing Office).
- Anderson, R.N., and Zoback, M.D., 1982. Permeability, underpressures, and convection in the oceanic crust near the Costa Rica Rift, eastern equatorial Pacific. *J. Geophys. Res.*, 87:2860-2868.
- Anderson, R.N., Zoback, M.D., Hickman, S.H., and Newmark, R.L., 1985. Permeability versus depth in the upper oceanic crust: in situ measurements in DSDP Hole 504B, eastern equatorial Pacific. *J. Geophys. Res.*, 90:3659-3669.
- Autio, L.K., and Rhodes, J.M., 1983. Costa Rica Rift Zone basalts: geochemical and experimental data from a possible example of multistage melting. In Cann, J.R., Langseth, M.G., Honnorez, J., Von Herzen, R.P., White, S.M., et al., *Init. Repts. DSDP, 69*: Washington (U.S. Govt. Printing Office), 729-746.
- Autio, L.K., Sparks, J.W., and Rhodes, J.M., 1989. Geochemistry of Leg 111 basalts: intrusive feeders for highly depleted pillows and flows. In Becker, K., Sakai, H., et al., *Proc. ODP, Sci. Results, 111*: College Station, TX (Ocean Drilling Program), 3-16.
- Ballard, R., Bryan, W., Dick, H., Emery, K.O., Thompson, G., Uchupi, E., Davis, K.E., Boer, J., Delong, S., Fox, P., Malcolm, F., Spydell, R., Stroup, J., Melson, W., and Wright, R., 1979. Geological and geophysical investigation of the Midcayman Rise Spreading Center: initial results and observations. In Talwani, M., Harrison, C.G., and Hayes, D.E. (Eds.), *Deep Drilling Results in the Atlantic Ocean: Ocean Crust*. Am. Geophys. Union, 66-93.
- Becker, K., Langseth, M.G., and Von Herzen, R.P., 1983. Deep crustal geothermal measurements, Hole 504B, Deep Sea Drilling Project Legs 69 and

\* Abbreviations for names of organizations and publication titles in ODP reference lists follow the style given in *Chemical Abstracts Service Source Index* (published by American Chemical Society).

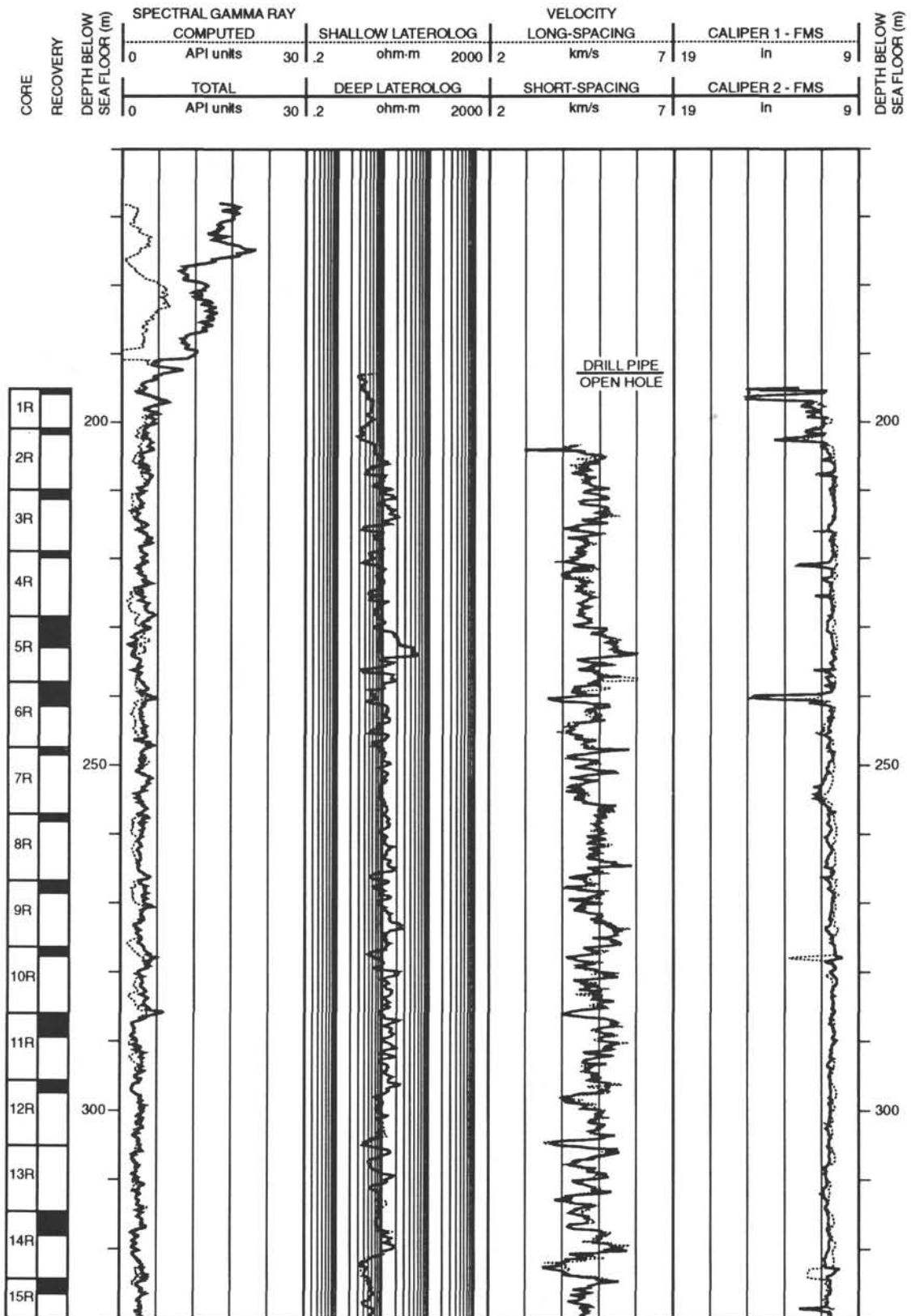
70. In Cann, J.R., Langseth, M.G., Honnorez, J., Von Herzen, R.P., White, S.M., et al., *Init. Repts. DSDP*, 69: Washington (U.S. Govt. Printing Office), 223–236.
- Becker, K., Sakai, H., et al., 1988. *Proc. ODP, Init. Repts.*, 111: College Station, TX (Ocean Drilling Program).
- Bender, J.F., Hodges, F.N., and Bence, A.E., 1978. Petrogenesis of basalts from the Project FAMOUS area: experimental study from 0 to 15 kbars. *Earth Planet. Sci. Lett.*, 41:277–302.
- Biggar, G.M., and Clarke, D.M., 1976. Reaction rate of xenocrysts in synthetic basaltic melts. *NERC Prog. Exp. Petrol.*, D6:227–230.
- Bingham, C., 1974. An antipodally symmetric distribution on a sphere. *Ann. Statist.*, 2:1201–25.
- Bryan, W.B., 1972. Morphology of quench crystals in submarine basalts. *J. Geophys. Res.*, 77:5812–5819.
- , 1983. Systematics of model phenocryst assemblages in submarine basalts: petrologic implications. *Contrib. Mineral. Petrol.*, 83:62–74.
- Bryan, W.B., and Moore, J.G., 1977. Compositional variations of young basalts in the Mid-Atlantic rift valley near latitude 36°49'N. *Geol. Soc. Am. Bull.*, 88:556–570.
- Cann, J.R., 1974. A model for oceanic crustal structure developed. *Geophys. J. R. Astron. Soc.*, 39:169–187.
- Cann, J.R., Langseth, M.G., Honnorez, J., Von Herzen, R.P., White, S.M., et al., 1983. *Init. Repts. DSDP*, 69: Washington (U.S. Govt. Printing Office).
- Christensen, N.I., and Salisbury, M.H., 1985. Seismic velocities, densities and porosities of Layer 2B and Layer 2C basalts from Hole 504B. In Anderson, R.N., Honnorez, J., Becker, K., et al., *Init. Repts. DSDP*, 83: Washington (U.S. Govt. Printing Office), 367–370.
- Christensen, N.I., Wepfer, W.W., and Baud, R.D., 1989. Seismic properties of sheeted dikes from Hole 504B, ODP Leg 111. In Becker, K., Sakai, H., et al., *Proc. ODP, Sci. Results*, 111: College Station, TX (Ocean Drilling Program), 171–174.
- Collinson, D.W., 1983. *Methods in Rock Magnetism and Palaeomagnetism: Techniques and Instrumentation*: London (Chapman and Hall).
- Cox, S.F., and Etheridge, M.A., 1983. Crack-seal fiber growth mechanisms and their significance in the development of oriented layer silicate microstructures. *Tectonophysics*, 92:147–170.
- Delaney, P.T., and Pollard, D.P., 1982. Solidification of basaltic magma during flow in a dike. *Am. J. Sci.*, 282:856–885.
- Dick, H.J.B., Erzinger, J., Stokking, L.B., et al., 1992. *Proc. ODP, Init. Repts.*, 140: College Station, TX (Ocean Drilling Program).
- Ellwood, B.B., 1978. Flow and emplacement direction determined for selected basaltic bodies using magnetic susceptibility anisotropy measurements. *Earth Planet. Sci. Lett.*, 41:254–264.
- Emmertmann, R., 1985. Basement geochemistry, Hole 504B. In Anderson, R.N., Honnorez, J., Becker, K., et al., *Init. Repts. DSDP*, 83: Washington (U.S. Govt. Printing Office), 183–199.
- Fehn, U., Green, K.E., Von Herzen, R.P., and Cathles, L.M., 1983. Numerical models for the hydrothermal field at the Galapagos spreading center. *J. Geophys. Res.*, 88:1033–1048.
- Fisher, A.T., Becker, K., Narasimhan, T.N., Langseth, M.G., and Mottl, M.J., 1990. Passive, off-axis convection through the southern flank of the Costa Rica rift. *J. Geophys. Res.*, 95:9343–9370.
- Fisk, M.R., and Bence, A.E., 1980. Experimental crystallization of chrome spinel in FAMOUS basalt 527-1-1. *Earth Planet. Sci. Lett.*, 48:111–123.
- Furuta, T., and Levi, S., 1983. Basement paleomagnetism of Hole 504B. In Cann, J.R., Langseth, M.G., Honnorez, J., Von Herzen, R.P., White, S.M., et al., *Init. Repts. DSDP*, 69: Washington (U.S. Govt. Printing Office), 697–703.
- Furuta, T., and Tokuyama, H., 1983. Chromian spinels in Costa Rica basalts, Deep Sea Drilling Project Site 505—a preliminary interpretation of electron microprobe analyses. In Cann, J.R., Langseth, M.G., Honnorez, J., Von Herzen, R.P., White, S.M., et al., *Init. Repts. DSDP*, 69: Washington (U.S. Govt. Printing Office), 805–810.
- Gieskes, J., and Lawrence, J.R., 1981. Interstitial water chemistry in deep sea sediments. *Geochim. Cosmochim. Acta*, 45:1687–1703.
- Hagen, H., and Neumann, E.-R., 1990. Modeling of trace-element distribution in magma chambers using open-system models. *Comput. Geosci.*, 16:549–586.
- Honnorez, J., Laverne, C., Hubberten, H.-W., Emmertmann, R., and Muehlenbachs, K., 1983. Alteration processes in Layer 2 basalts from Deep Sea Drilling Project Hole 504B, Costa Rica Rift. In Cann, J.R., Langseth, M.G., Honnorez, J., Von Herzen, R.P., White, S.M., et al., *Init. Repts. DSDP*, 69: Washington (U.S. Govt. Printing Office), 509–546.
- Iturrino, G.J., Christensen, N.I., Becker, K., Boldreel, L.D., Harvey, P.K.H., in press. Physical properties and elastic constants of upper crystal rocks from core-log measurements in Hole 504B. In Erzinger, J., Becker, K., Dick, H.B.J., Stokking, L.B., et al., *Proc. ODP, Sci. Results*, 140: College Station, TX (Ocean Drilling Program).
- Johnson, H.P., 1978. Paleomagnetism of igneous rock samples—DSDP Leg 45. In Melson, W.G., Rabinowitz, P.D., et al., *Init. Repts. DSDP*, 45: Washington (U.S. Govt. Printing Office), 387–396.
- Karato, S., 1983. Physical properties of basalts from Deep Sea Drilling Project Hole 504B, Costa Rica Rift. In Cann, J.R., Langseth, M.G., Honnorez, J., Von Herzen, R.P., White, S.M., et al., *Init. Repts. DSDP*, 69: Washington (U.S. Govt. Printing Office), 687–695.
- Kempton, P.D., 1985. An interpretation of contrasting nucleation and growth histories from the petrographic analysis of pillow and dike chilled margins, Hole 504B, Deep Sea Drilling Project, Leg 83. In Anderson, R.N., Honnorez, J., Becker, K., et al., *Init. Repts. DSDP*, 83: Washington (U.S. Govt. Printing Office), 165–181.
- Kempton, P.D., Autio, L.K., Rhodes, J.M., Holdaway, M.J., Dungan, M.A., and Johnson, P., 1985. Petrology of basalts from Hole 504B, Deep Sea Drilling Project, Leg 83. In Anderson, R.N., Honnorez, J., Becker, K., et al., *Init. Repts. DSDP*, 83: Washington (U.S. Govt. Printing Office), 129–164.
- Langseth, M.G., Cann, J.R., Natland, J.H., and Hobart, M., 1983. Geothermal phenomena at the Costa Rica Rift: background and objectives for drilling at Deep Sea Drilling Project Sites 501, 504, and 505. In Cann, J.R., Langseth, M.G., Honnorez, J., Von Herzen, R.P., White, S.M., et al., *Init. Repts. DSDP*, 69: Washington (U.S. Govt. Printing Office), 5–29.
- Langseth, M.G., Mottl, M.J., Hobart, M.A., and Fisher, A., 1988. The distribution of geothermal and geochemical gradients near Site 501/504: implications for hydrothermal circulation in the oceanic crust. In Becker, K., Sakai, H., et al., *Proc. ODP, Init. Repts.*, 111: College Station, TX (Ocean Drilling Program), 23–32.
- Lofgren, G., 1971. Spherulitic textures in glassy and crystalline rocks. *J. Geophys. Res.*, 76:5635–5648.
- , 1980. Experimental studies on the dynamic crystallization of silicate melts. In Hargraves, R.B. (Ed.), *Physics of Magnetic Processes*: Princeton (Princeton Univ. Press), 487–551.
- , 1983. Effect of heterogeneous nucleation on basaltic textures: a dynamic crystallization study. *J. Petrol.*, 24:229–255.
- Lowrie, W., and Kent, D.V., 1978. Characteristics of VRM in ocean basalts. *J. Geophys. Res.*, 83:297–315.
- MacKenzie, W.S., Donaldson, C.H., and Guilford, C., 1982. *Atlas of Igneous Rocks and Their Textures*: New York (Wiley).
- Marsh, B.D., 1988. Crystal size distribution (CSD) in rocks and the kinetics and dynamics. I. Theory. *Contrib. Mineral. Petrol.*, 99:277–291.
- Marsh, N.G., Tarney, J., and Hendry, G.L., 1983. Trace element geochemistry of basalts from Hole 504B, Panama Basin, Deep Sea Drilling Project Legs 69 and 70. In Cann, J.R., Langseth, M.G., Honnorez, J., Von Herzen, R.P., White, S.M., et al., *Init. Repts. DSDP*, 69: Washington (U.S. Govt. Printing Office), 747–763.
- Meyer, P.S., and Shibata, T., 1990. Complex zoning in plagioclase feldspars from ODP Site 648. In Detrick, R., Honnorez, J., Bryan, W.B., Juteau, T., et al., *Proc. ODP, Sci. Results*, 106/109: College Station, TX (Ocean Drilling Program), 123–142.
- Michael, P.J., and Chase, R.L., 1987. The influence of primary magma composition, H<sub>2</sub>O and pressure on mid-ocean ridge basalt differentiation. *Contrib. Mineral. Petrol.*, 96:245–263.
- Moos, D. and Zoback, M., 1990. Utilization of observations of well-bore failure to constrain the orientation and magnitude of crustal stresses; application to continental Deep Sea Drilling Project and Ocean Drilling Program boreholes. *J. Geophys. Res.*, 95:9305–9325.
- Morin, R.H., Newmark, R.L., Barton, C.A., and Anderson, R.N., 1990. State of lithospheric stress and borehole stability at Deep Sea Drilling Project Site 504B, eastern Equatorial Pacific. *J. Geophys. Res.*, 95:9293–9303.
- Mottl, M.J., 1989. Hydrothermal convection, reaction, and diffusion in sediments on the Costa Rica Rift flank: pore-water evidence from ODP Sites 677 and 678. In Becker, K., Sakai, H., et al., *Proc. ODP, Sci. Results*, 111: College Station, TX (Ocean Drilling Program), 195–213.
- Mottl, M.J., Lawrence, J.R., and Keigwin, L.D., 1983. Elemental and stable-isotope composition of pore waters and carbonate sediments from Deep Sea Drilling Project Sites 501/504 and 505. In Cann, J.R., Langseth, M.G., Honnorez, J., Von Herzen, R.P., White, S.M., et al., *Init. Repts. DSDP*, 69: Washington (U.S. Govt. Printing Office), 461–473.

- Natland, J.H., Adamson, A.C., Laverne, C., Melson, W.G., and O'Hearn, T., 1983. A compositionally nearly steady-state magma chamber at the Costa Rica Rift: evidence from basalt glass and mineral data, Deep Sea Drilling Project Sites 501, 504, and 505. *In* Cann, J.R., Langseth, M.G., Honnorez, J., Von Herzen, R.P., White, S.M., et al., *Init. Repts. DSDP*, 69: Washington (U.S. Govt. Printing Office), 811–858.
- Newmark, R.L., Anderson, R.N., Moos, D., and Zoback, M.D., 1985. Sonic and ultrasonic logging of Hole 504B and its implications for the structure, porosity, and stress regime of the upper 1 km of the oceanic crust. *In* Anderson, R.N., Honnorez, J., Becker, K., et al., *Init. Repts. DSDP*, 83: Washington (U.S. Govt. Printing Office), 479–510.
- Newmark, R.L., Zoback, M.D., and Anderson, R.N., 1984. Orientation of in situ stresses in the oceanic crust. *Nature*, 311:424–428.
- Nielsen, R.L., 1990. Simulation of igneous differentiation processes. *In* Nicholl, J., and Russell, J.K. (Eds.), *Modern Methods of Igneous Petrology: Understanding Magmatic Processes*. Mineral. Soc. Am., Rev. in Min., 24:65–105.
- Niu, Y., and Batiza, R., 1991. DENSICAL: a program for calculating melt densities of silicate melts and mantle minerals in melting range. *Comput. Geosci.*, 17:679–687.
- Parsons, B., and Sclater, J.G., 1977. An analysis of the variation of ocean floor bathymetry and heat flow with age. *J. Geophys. Res.*, 82:803–827.
- Perfit, M.R., and Fornari, D.J., 1983. Geochemical studies of abyssal lavas recovered by DSRV *Alvin* from eastern Galapagos Rift, Inca Transform, and Ecuador Rift. 2. Phase chemistry and crystallization history. *J. Geophys. Res.*, 88:10530–10550.
- Pezard, P.A., 1990. Electrical properties of mid-ocean ridge basalt and implications for the structure of the upper oceanic crust in Hole 504B. *J. Geophys. Res.*, 95:9237–9264.
- Pollard, D.D., and Aydin, A., 1988. Progress in understanding jointing over the past century. *Geol. Soc. Am. Bull.*, 100:1181–1204.
- Ramsay, J.G., 1980. The crack-seal mechanism of rock deformation. *Nature*, 284:135–139.
- Ramsay, J.G., and Huber, M., 1983. *The Techniques of Modern Structural Geology* (Vol. 1): *Strain Analysis*: London (Academic Press).
- Rhodes, J.M., Dungan, M.A., Blanchard, D.P., and Long, P.E., 1979. Magma mixing at mid-ocean ridges: evidence from basalts drilled near 22°N on the Mid-Atlantic Ridge. *Tectonophysics*, 55:35–61.
- Roeckel, T., Nataou, O., and Dietrich, H.-G., 1992. Core reorientation by comparison of core instabilities and borehole instabilities. *In* Emmermann, R., Dietrich, H.-G., et al., *KTB Hauptbohrung, Results of Geoscientific Investigation in the KTB Field Laboratory, 0–6000 m*. KTB Rep. 92-2:F1–F17.
- Saltykov, S.A., 1967. The determination of the size distribution of particles in an opaque material from measurement of the size distribution in their section. *In* Helias, H. (Ed.), *Stereology: Proc. Second Int. Congr. Stereology*: New York (Springer).
- Searle, R.C., 1983. Gloria survey over Costa Rica Rift Sites 501, 504, and 505. *In* Cann, J.R., Langseth, M.G., Honnorez, J., Von Herzen, R.P., White, S.M., et al., *Init. Repts. DSDP*, 69: Washington (U.S. Govt. Printing Office), 217–222.
- Shipboard Scientific Parties, 1980. Site 417. *In* Donnelly, T., Francheteau, J., Bryan, W., Robinson, P., Flower, M., Salisbury, M., et al., *Init. Repts. DSDP*, 51, 52, 53: Washington (U.S. Govt. Printing Office), 23–350.
- Shipboard Scientific Parties of Leg 68 (Site 501), Leg 69, and Leg 70, 1983. Sites 501 and 504: sediments and ocean crust in an area of high heat flow on the southern flank of the Costa Rica Rift. *In* Cann, J.R., Langseth, M.G., Honnorez, J., Von Herzen, R.P., White, S.M., et al., *Init. Repts. DSDP*, 69: Washington (U.S. Govt. Printing Office), 31–174.
- Shipboard Scientific Party, 1985. Hole 504B, Leg 83. *In* Anderson, R.N., Honnorez, J., Becker, K., et al., *Init. Repts. DSDP*, 83: Washington (U.S. Govt. Printing Office), 13–118.
- , 1988a. Site 504: Costa Rica Rift. *In* Becker, K., Sakai, H., et al., *Proc. ODP, Init. Repts.*, 111: College Station, TX (Ocean Drilling Program), 35–251.
- , 1988b. Site 648. *In* Detrick, R., Honnorez, J., Bryan, W.B., Juteau, T., et al., *Proc. ODP, Init. Repts.*, 106/109: College Station, TX (Ocean Drilling Program), 35–134.
- , 1989. Site 758. *In* Peirce, J., Weissel, J., et al., *Proc. ODP, Init. Repts.*, 121: College Station, TX (Ocean Drilling Program), 359–453.
- , 1992a. Site 504. *In* Becker, K., Foss, G., et al., *Proc. ODP, Init. Repts.*, 137: College Station, TX (Ocean Drilling Program), 15–55.
- , 1992b. Site 504. *In* Dick, H.J.B., Erzinger, J., Stokking, L.B., et al., *Proc. ODP, Init. Repts.*, 140: College Station, TX (Ocean Drilling Program), 37–200.
- Smith, G.M., and Banerjee, S.K., 1986. The magnetic structure of the upper kilometer of the marine crust at Deep Sea Drilling Project Hole 504B, Eastern Pacific Ocean. *J. Geophys. Res.*, 91:10337–10354.
- Sparks, R.S.J., Huppert, H.E., and Sigurdsson, H., 1980. Density variation amongst mid-ocean ridge basalts: implications for magma mixing and the scarcity of primitive magmas. *Earth Planet. Sci. Lett.*, 46:419–430.
- Sun, S.-S., and McDonough, W.F., 1989. Chemical and isotopic systematics of oceanic basalts: implications for mantle composition and processes. *In* Saunders, A.D., and Norry, M.J. (Eds.), *Magmatism in the Ocean Basins*. Geol. Soc. Spec. Publ. London, 42:313–345.
- Thorseth, I.H., Furnes, H., and Heldal, M., 1992. The importance of microbiological alteration of natural basaltic glass. *Geochim. Cosmochim. Acta.*, 56:845–850.
- van Andel, T.H., and Ballard, R.D., 1979. The Galapagos Rift at 86°W: 2. Volcanism structure and evolution of the rift valley. *J. Geophys. Res.*, 84:5379–5406.
- Wilkens, R.H., Christensen, N.I., and Slater, L., 1983. High-pressure seismic studies of Leg 69 and 70 basalts. *In* Cann, J.R., Langseth, M.G., Honnorez, J., Von Herzen, R.P., White, S.M., et al., *Init. Repts. DSDP*, 69: Washington (U.S. Govt. Printing Office), 683–686.
- Zijderveld, J.D.A., 1967. AC demagnetization of rocks: analysis of results. *In* Collinson, D.W., Creer, K.M., and Runcorn, S.K. (Eds.), *Methods in Palaeomagnetism*: New York (Elsevier), 254–286.

Ms1481R-103

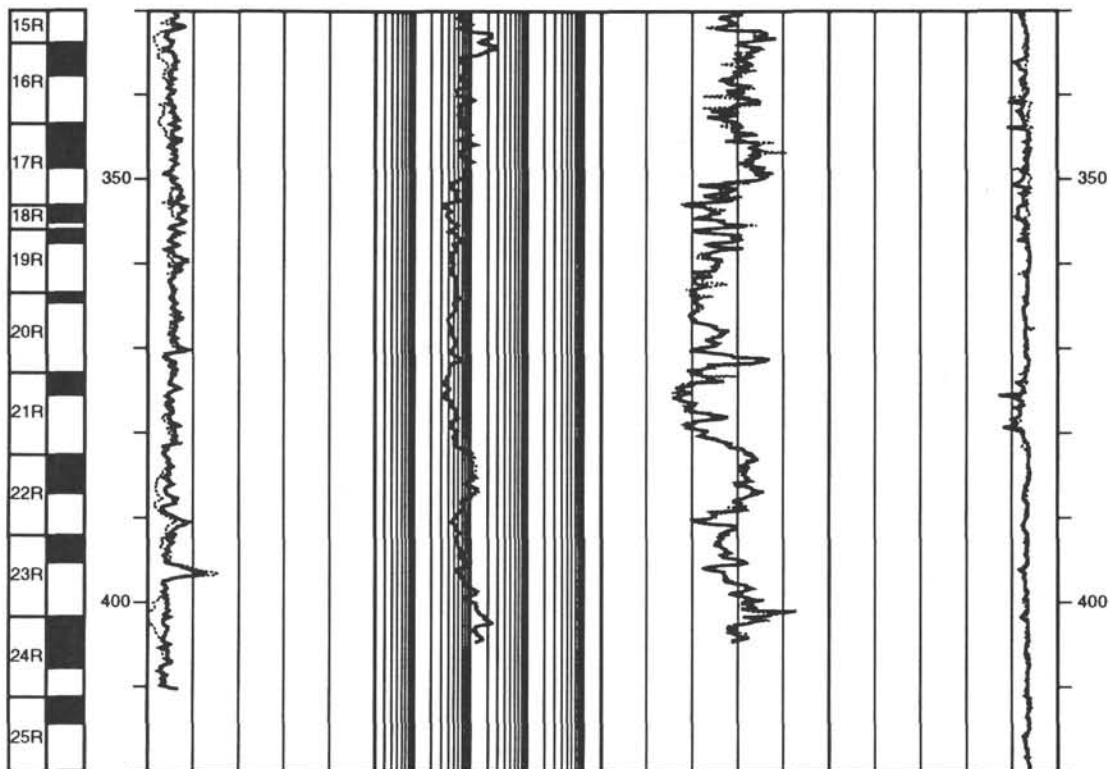
**NOTE: For all sites drilled, hard-rock core-description forms and core photographs can be found in Section 3, beginning on page 195. Thin-section data are given in Section 4, beginning on page 291. Conventional-log and FMS data can be found in the CD-ROM (back pocket). As a guide to the reader, only the first page of the nine Appendixes to this chapter is printed, following the text. All nine Appendixes are given in their entirety in the accompanying CD-ROM.**

Hole 896A: Natural Gamma Ray-Resistivity-Velocity Log Summary

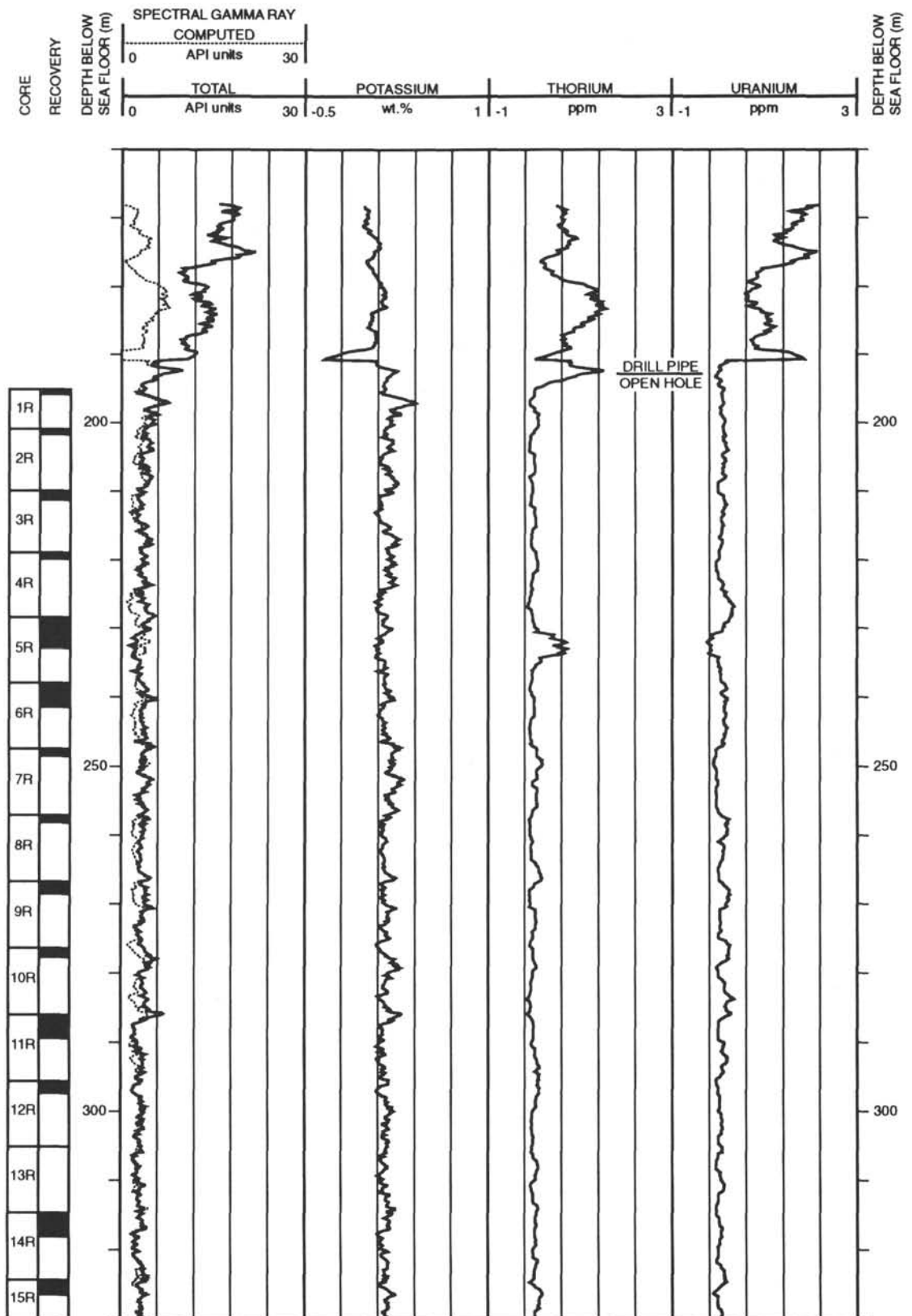


Hole 896A: Natural Gamma Ray-Resistivity-Velocity Log Summary (continued)

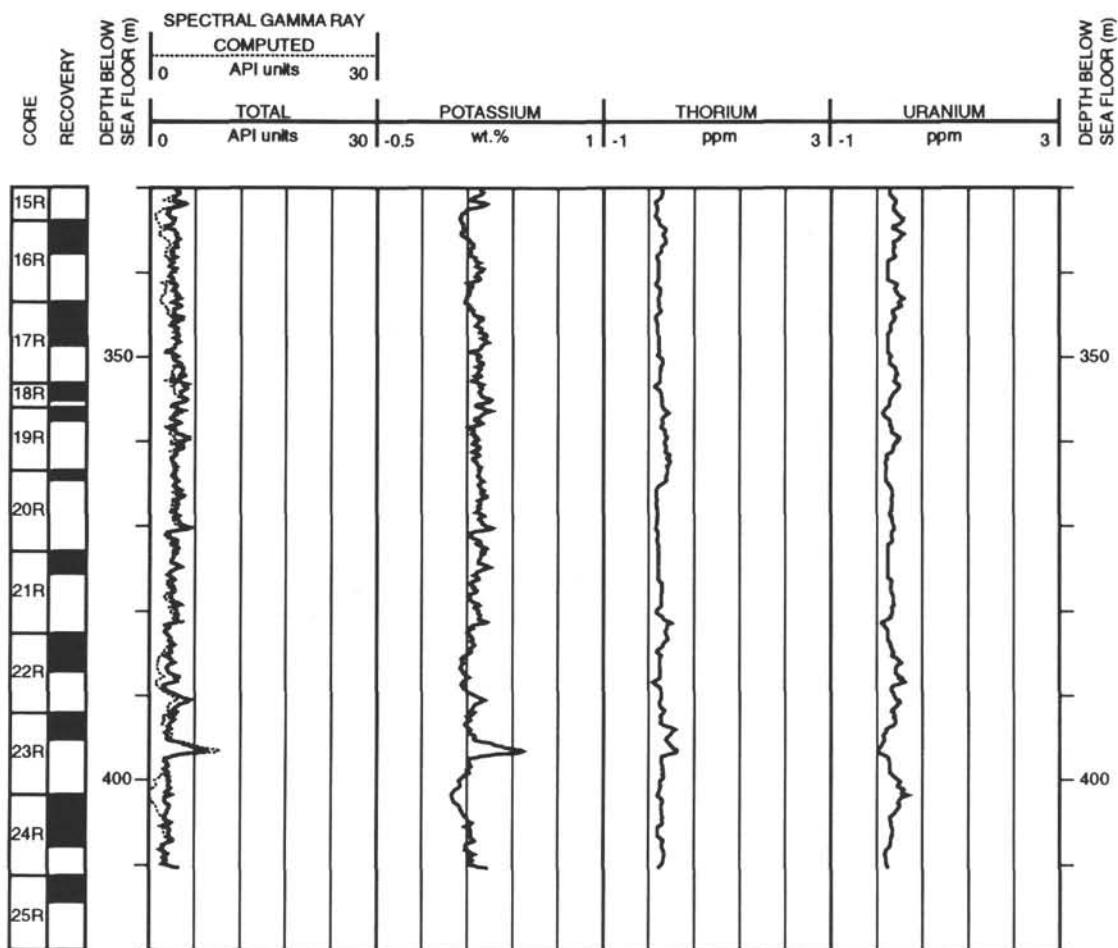
CORE RECOVERY	DEPTH BELOW SEA FLOOR (m)	SPECTRAL GAMMA RAY				VELOCITY				DEPTH BELOW SEA FLOOR (m)
		COMPUTED		SHALLOW LATEROLOG		LONG-SPACING		CALIPER 1 - FMS		
		0	API units	30	.2 ohm-m	2000	2	km/s	7	
CORE RECOVERY	DEPTH BELOW SEA FLOOR (m)	TOTAL		DEEP LATEROLOG		SHORT-SPACING		CALIPER 2 - FMS		DEPTH BELOW SEA FLOOR (m)
		0	API units	30	.2 ohm-m	2000	2	km/s	7	



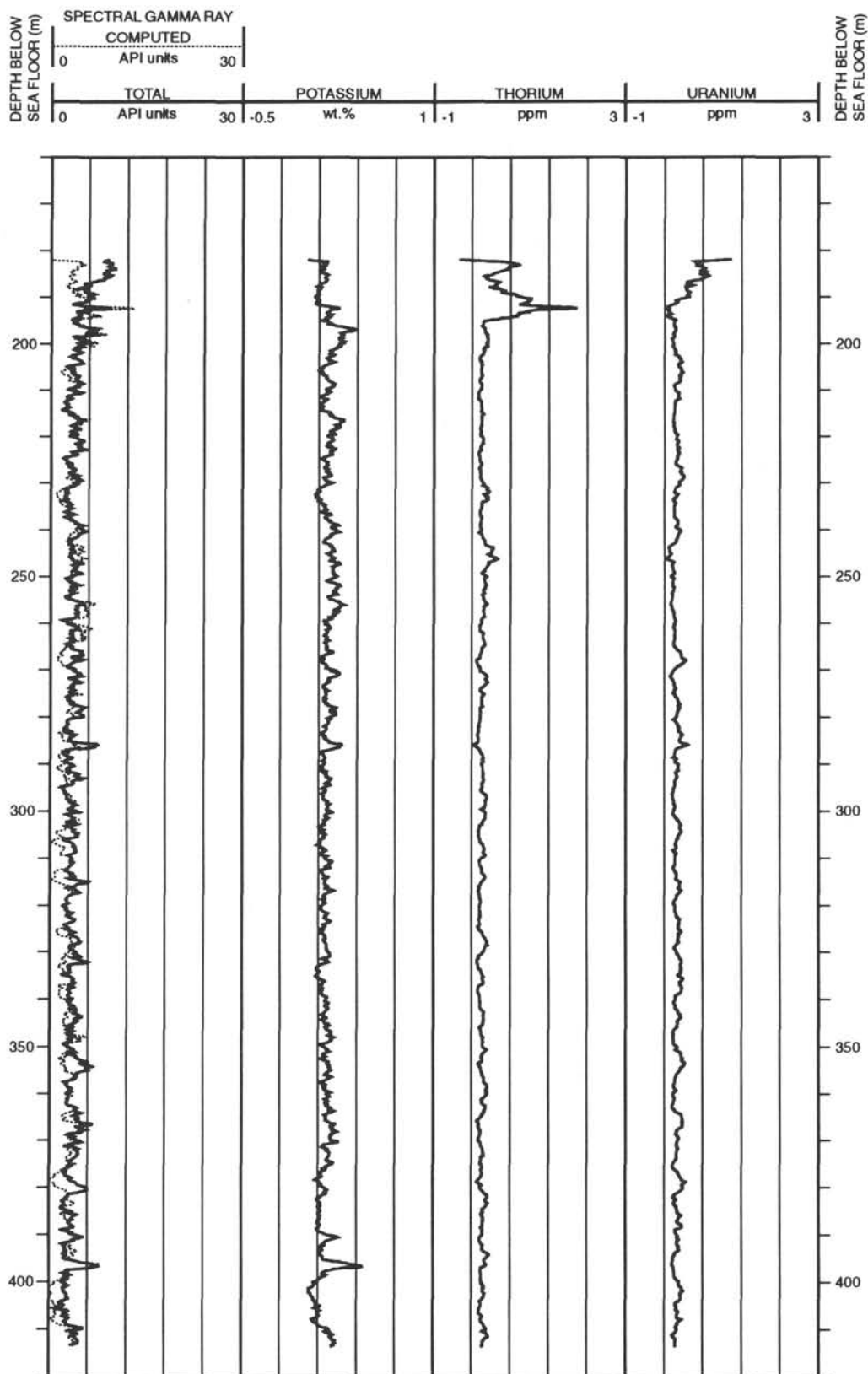
### Hole 896A: Natural Gamma Ray Log Summary



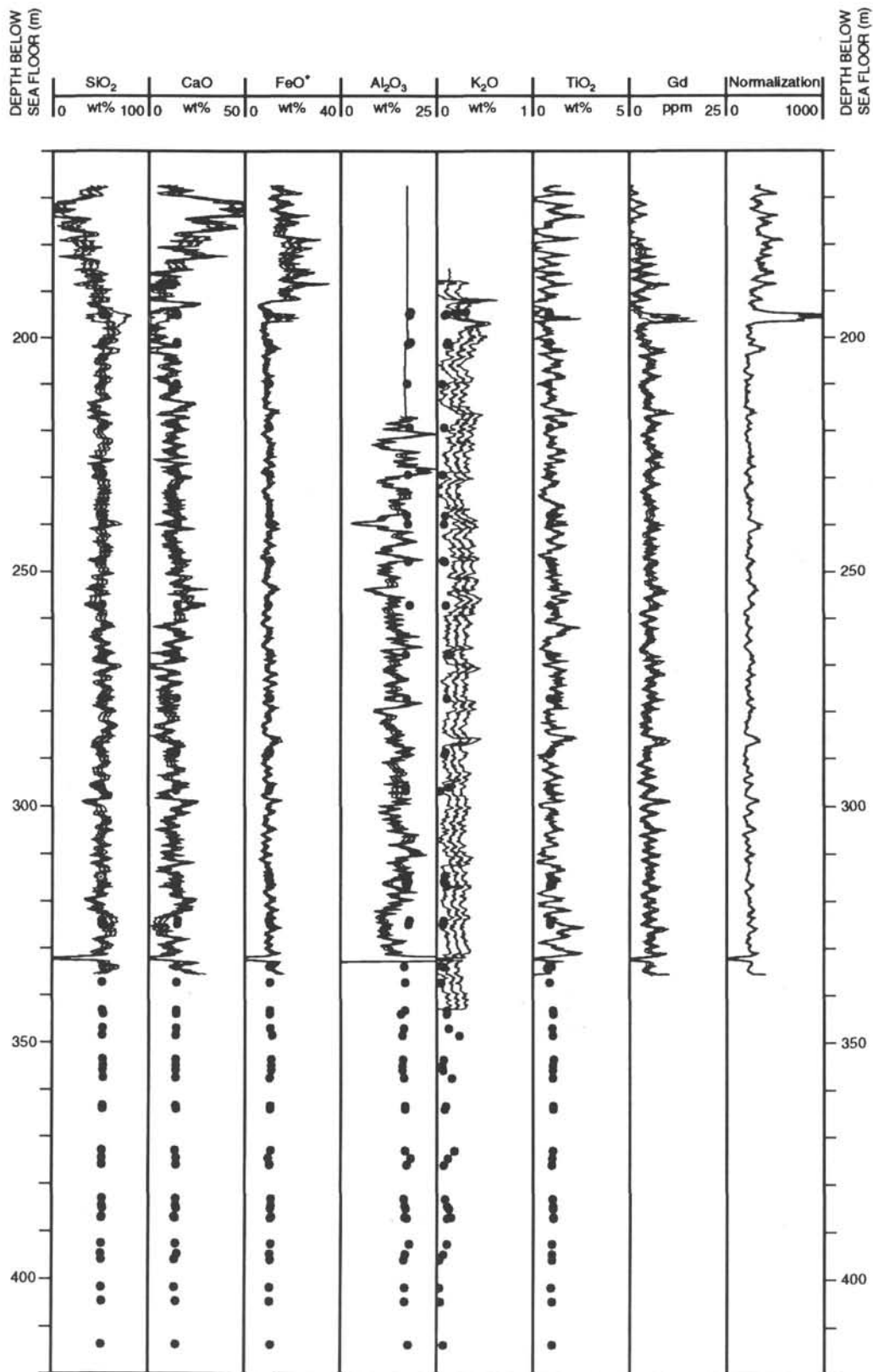
Hole 896A: Natural Gamma Ray Log Summary (continued)



Hole 896A: Natural Gamma Ray Log Summary



Hole 896A: Geochemical Log Summary



Appendix A. Leg 148 Hole 896A. Igneous mineralogy log. The core, section, interval, and pieces of each unit are given. Ph = phenocryst; Gm = intergranular material; GS = grain size; Mor = morphology; Ox = opaque minerals; and S = sulfides; Tr = trace. Phenocryst and intergranular material abundances are in percent. Phenocryst and intergranular grain sizes are in millimeters; — = not observed. Morphology 1 = phenocryst, *a* is euhedral, *b* is subhedral, and *c* is anhedral. The estimates are based on observations made with the unaided eye and with binocular microscopes with magnification up to 50×. In most samples the groundmass was microcrystalline or finer, so mineral identification and abundance of these minerals were not estimated. Two massive units, however, have intergranular groundmass. Unit 36 is massive and the mesostasis is made up of 45% plagioclase, 38% clinopyroxene, and 5% olivine. Average grain sizes are 0.4 mm, 0.15 mm, and 0.10 mm for plagioclase, clinopyroxene, and olivine, respectively. These groundmass grains are euhedral to subhedral, except for pyroxene, which is anhedral. In Unit 51 plagioclase grains about 0.2 mm long constitute 50% of the rock, and 0.2 mm subophitic clinopyroxene that are subhedral to anhedral constitute about 45% of the rock.

Core	Section	Piece	Interval (cm)	Unit	Plagioclase		Phenocrysts			Augite		Phenocrysts			Olivine		Phenocrysts			Spinel (%)	Ox (%)	S (%)	Ves. (%)
					Min	Max	Avg	GS	Mor	Min	Max	Avg	GS	Mor	Min	Max	Avg	GS	Mor				
1R	1	1-3	0-14	1	2	5	3.3	1	1a,b laths	—	—	—	—	—	2	2.5	2.3	0.5	1a equant	Tr	—	—	1
1R	1	4-5	14-25	2	4	5	4.5	1.2	1a,b laths	—	—	—	—	—	2	3	2.5	0.5	1a equant	—	—	—	<1
1R	1	6-18	25-93	3	1	5	2.3	0.8	1a,b	—	—	—	—	—	2	5	2.7	0.6	1a,b equant	Tr	0	—	—
2R	1	1-2	0-11.5	4	2	2	2	0.7	1a,b	—	—	—	—	—	3	3	3	0.5	1a,b	—	—	—	—
2R	1	3-8	11.5-37	5	2	1	1.5	0.9	1a,b	—	—	—	—	—	3	5	4	0.5	1a	—	0.2	—	—
2R	1	9	37-40.5	6	0	0.2	0.1	0.8	1a	—	—	—	—	—	4	4	4	0.8	1a,b	—	—	—	—
2R	1	10-22	40.5-107	7	2	5	3	0.8	1a,b	—	—	—	—	—	1	3	2.3	—	—	—	—	—	—
3R	1	1-3	0-14	7	2	5	3	0.8	1a,b	—	—	—	—	—	1	3	2.3	0.4	1a	—	—	—	—
3R	1	4-8	14-73	8	3	2	2.5	0.8	1a,b	—	—	—	—	—	1	2	1.5	0.5	1a	—	—	—	—
3R	1	9-17	73-148	9	2	3	2.3	0.9	1 a,b	—	—	—	—	—	1	2	1.7	0.6	1a	—	—	—	1
3R	2	1-3	0-16	9	2	3	2.3	0.9	1a,b	—	—	—	—	—	1	2	1.7	0.6	1a	—	—	—	1
4R	1	1-16	0-107	9	2	3	2.3	0.9	1a,b	—	—	—	—	—	1	2	1.7	0.6	1a	—	—	—	1
4R	1	17	107-114	10	4	5	4.5	1	1a	—	—	—	—	—	1	3	2	0.4	1 a,b	—	—	—	1
5R	1	1-16	0-92	10	4	5	4.5	1	1a	—	—	—	—	—	1	3	2	0.4	1 a,b	—	—	—	1
5R	2	1-17	0-146	10	4	5	4.5	1	1a	—	—	—	—	—	1	3	2	0.4	1 a,b	—	—	—	1
5R	3	1	0-17	10	4	5	4.5	1	1a	—	—	—	—	—	1	3	2	0.4	1a,b	—	—	—	1
5R	3	2-8	17-68	11	3	5	4	1	1a,b	—	—	—	—	—	4	7	5	0.3	1a/lc	Tr	—	—	—
6R	1	1-13	0-147	12	5	8	6	1.5	1a,b plates, laths	—	—	—	—	—	1	1	1	0.5	1a,b equant	—	—	—	—
6R	2	1-12	0-140	12	5	8	6	1.5	1a,b plates, laths	—	—	—	—	—	1	1	1	0.5	1a,b equant	—	—	—	—
6R	3	1-13	0-80	12	5	8	6	1.5	1a,b plates, laths	—	—	—	—	—	1	1	1	0.5	1a,b equant	—	—	—	—
6R	3	14-23	80-117	13	4	6	5	1.5	1a	—	—	—	—	—	2	2	2	0.6	1a,b	—	—	—	—
7R	1	1-10	0-67	13	4	6	5	1.5	1a	—	—	—	—	—	2	2	2	0.6	1a,b	—	—	—	—
7R	1	11-22	67-144	14	2	8	6	1.3	1a,b	—	—	—	—	—	5	2	3	0.6	1a	Tr	—	—	—
8R	1	1-29	0-144	14	2	8	6	1.3	1a,b	—	—	—	—	—	5	—	—	—	—	—	—	—	—
9R	1	1-25	0-144	14	2	8	6	1.3	1a,b	—	—	—	—	—	5	—	—	—	—	—	—	—	—
9R	2	1-5	0-52	14	2	8	6	1.3	1a,b	—	—	—	—	—	5	—	—	—	—	—	—	—	—
10R	1	1-13	0-146	14	2	8	6	1.3	1a,b	—	—	—	—	—	5	—	—	—	—	—	—	—	—
11R	1	1-14	0-144	14	2	8	6	1.3	1a,b	—	—	—	—	—	5	—	—	—	—	—	—	—	—
11R	2	1-16	0-107	14	2	8	6	1.3	1a,b	—	—	—	—	—	5	2	3	0.6	1a	Tr	—	—	—
11R	2	17-22	107-148	15	0.2	1	0.6	0.5	1a,b	—	—	—	—	—	1	1	1	0.4	1a	—	—	—	—
11R	3	1-5	0-36	15	0.2	1	0.6	0.5	1a,b	—	—	—	—	—	1	1	1	0.4	1a	—	—	—	—
11R	3	6-15	36-94	16	2.5	5	3.3	1	1a,b	—	—	—	—	—	1	5	2	0.5	1a	Tr	—	—	—
12R	1	1-10	0-90	16	2.5	5	3.3	1	1a,b	—	—	—	—	—	1	5	2	0.5	1a	Tr	—	—	—
12R	1	11-18	90-145	17	3	4	3.5	0.5	1a,b	—	—	—	—	—	2	5	3.5	0.4	1a	—	—	—	—
12R	2	1-7	0-68	17	3	4	3.5	0.5	1a,b	—	—	—	—	—	2	5	3.5	0.4	1a	—	—	—	—
13R	1	1-5	0-20.5	17	3	4	3.5	0.5	1a,b	—	—	—	—	—	2	5	3.5	0.4	1a	—	—	—	—
14R	1	1-2	0-49	18	5	5	5	1	1a,b	—	—	—	—	—	1	1	1	0.3	1a	—	—	—	—
14R	1	3-16	49-141	19	4	7	5.3	1	1a,b	—	—	—	—	—	4	6	4.5	0.5	1a	—	—	—	—

NOTE: As a guide to the reader, only the first page of this Appendix is reproduced here. The entire Appendix is given in the CD-ROM (back pocket).

Appendix B. Leg 148 Site 896A. Igneous lithology log. The lithology (rock name) is determined using the conventions given in the "Explanatory Notes."

Core	Section	Piece	Interval (cm)	Unit	Lithology	Texture	Structure	Munsell color
1R	1	1-3	0-14	1	Moderately phyrlic PO basalt	Microcrystalline, porphyritic	Pillow	5B 5/1 Bluish gray
1R	1	4-5	14-25	2	Moderately phyrlic PO basalt	Microcrystalline, subglomerophyritic	Massive	5R 4/1 Dark reddish gray
1R	1	6-18	25-93	3	Moderately phyrlic OP basalt	Microcrystalline, porphyritic	Pillow	5B 5/1 Bluish gray
2R	1	1-2	0-11.5	4	Moderately phyrlic OP basalt	Microcrystalline, porphyritic	Massive	5R 4/1 Dark reddish gray
2R	1	3-8	11.5-37	5	Moderately phyrlic OP basalt	Microcrystalline, porphyritic, trachytic	Massive	5B 4/1 Dark bluish gray
2R	1	9	37-40.5	6	Moderately phyrlic O basalt	Microcrystalline, porphyritic, trachytic	Massive	5B 4/1 Dark bluish gray
2R	1	10-22	40.5-107	7	Moderately phyrlic PO basalt	Microcrystalline, porphyritic	Pillow, massive	5BG 5/1 to 7.5YR 5/6 Dark blue-gray to strong brown
3R	1	1-3	0-14	7	Moderately phyrlic PO basalt	Microcrystalline, porphyritic	Pillow, massive	5BG 5/1 to 7.5YR 5/6 Dark blue-gray to strong brown
3R	1	4-8	14-73	8	Moderately phyrlic PO basalt	Microcrystalline, porphyritic	Pillow	5B 4/1 to 7.5 YR 6/6 or 5R 4/4 Bluish gray to reddish yellow or weak red
3R	1	9-17	73-148	9	Moderately phyrlic PO basalt	Microcrystalline, porphyritic	Massive massive pillow	5B 5/1 to 5R 5/1 or 7.5 YR 4/6 Bluish gray to reddish gray or reddish yellow
3R	2	1-3	0-16	9	Moderately phyrlic PO basalt	Microcrystalline, porphyritic	Massive massive pillow	5B 5/1 to 5R 5/1 or 7.5 YR 4/6 Bluish gray to reddish gray or reddish yellow
4R	1	1-16	0-107	9	Moderately phyrlic PO basalt	Microcrystalline, porphyritic	Massive massive pillow	5B 5/1 to 5R 5/1 or 7.5 YR 4/6 Bluish gray to reddish gray or reddish yellow
4R	1	17	107-114	10	Moderately phyrlic PO basalt	Microcrystalline, porphyritic, subglomerophyritic	Pillow, pillow-breccia	5B 5/1 to 5B 4/1 Bluish gray to dark bluish gray
5R	1	1-16	0-92	10	Moderately phyrlic PO basalt	Microcrystalline, porphyritic, subglomerophyritic	Pillow, pillow-breccia	5B 5/1 to 5B 4/1 Bluish gray to dark bluish gray
5R	2	1-17	0-146	10	Moderately phyrlic PO basalt	Microcrystalline, porphyritic, subglomerophyritic	Pillow, pillow-breccia	5B 5/1 to 5B 4/1 Bluish gray to dark bluish gray
5R	3	1	0-17	10	Moderately phyrlic PO basalt	Microcrystalline, porphyritic, subglomerophyritic	Pillow, pillow-breccia	5B 5/1 to 5B 4/1 Bluish gray to dark bluish gray
5R	3	2-8	17-68	11	Moderately phyrlic OP basalt	Microcrystalline, porphyritic	Massive	5B 5/1 to 7.5 YR 5/3 Bluish gray to brown
6R	1	1-13	0-147	12	Moderately phyrlic PO basalt	Microcrystalline, porphyritic, subglomerophyritic	Pillow	5B 5/1 Bluish gray
6R	2	1-12	0-140	12	Moderately phyrlic PO basalt	Microcrystalline, porphyritic, subglomerophyritic	Pillow	5B 5/1 Bluish gray
6R	3	1-13	0-80	12	Moderately phyrlic PO basalt	Microcrystalline, porphyritic, subglomerophyritic	Pillow	5B 5/1 Bluish gray
6R	3	14-23	80-117	13	Moderately phyrlic PO basalt	Microcrystalline, porphyritic, glomerophyritic	Pillow, pillow-breccia	5B 5/1 to 5BG 5/1 Bluish gray
7R	1	1-10	0-67	13	Moderately phyrlic PO basalt	Microcrystalline, porphyritic, glomerophyritic	Pillow, pillow-breccia	5B 5/1 to 5BG 5/1 Bluish gray
7R	1	11-22	67-144	14	Moderately phyrlic PO basalt	Microcrystalline, porphyritic	Pillow, pillow-breccia	5B 5/1 to 2.5YR 5/1 Bluish gray to reddish gray
8R	1	1-29	0-144	14	Moderately phyrlic PO basalt	Microcrystalline, porphyritic	Pillow, pillow-breccia	5B 5/1 to 2.5YR 5/1 Bluish gray to reddish gray
9R	1	1-25	0-144	14	Moderately phyrlic PO basalt	Microcrystalline, porphyritic	Pillow, pillow-breccia	5B 5/1 to 2.5YR 5/1 Bluish gray to reddish gray
9R	2	1-5	0-52	14	Moderately phyrlic PO basalt	Microcrystalline, porphyritic	Pillow, pillow-breccia	5B 5/1 to 2.5YR 5/1 Bluish gray to reddish gray
10R	1	1-13	0-146	14	Moderately phyrlic PO basalt	Microcrystalline, porphyritic	Pillow, pillow-breccia	5B 5/1 to 2.5YR 5/1 Bluish gray to reddish gray
11R	1	1-14	0-144	14	Moderately phyrlic PO basalt	Microcrystalline, porphyritic	Pillow, pillow-breccia	5B 5/1 to 2.5YR 5/1 Bluish gray to reddish gray
11R	2	1-16	0-107	14	Moderately phyrlic PO basalt	Microcrystalline, porphyritic	Pillow, pillow-breccia	5B 5/1 to 2.5YR 5/1 Bluish gray to reddish gray
11R	2	17-22	107-148	15	Sparsely phyrlic OP basalt	Microcrystalline	Massive, pillow	5B 5/1 to 5Y 5/2 Bluish gray to olive gray
11R	3	1-5	0-36	15	Sparsely phyrlic OP basalt	Microcrystalline	Massive, pillow	5B 5/1 to 5Y 5/2 Bluish gray to olive gray
11R	3	6-15	36-94	16	Moderately phyrlic PO basalt	Microcrystalline, porphyritic	Pillow, massive	5B 5/1 to 2.5Y 5/2 Bluish gray to grayish brown
12R	1	1-10	0-90	16	Moderately phyrlic PO basalt	Microcrystalline, porphyritic	Pillow, massive	5B 5/1 to 2.5Y 5/2 Bluish gray to grayish brown
12R	1	11-18	90-145	17	Moderately phyrlic PO basalt	Microcrystalline, porphyritic to variolitic	Pillow, massive	5B 5/1 to 2.5Y 5/3 Bluish gray to light olive gray
12R	2	1-7	0-68	17	Moderately phyrlic PO basalt	Microcrystalline, porphyritic to variolitic	Pillow, massive	5B 5/1 to 2.5Y 5/3 Bluish gray to light olive gray
13R	1	1-5	0-20.5	17	Moderately phyrlic PO basalt	Microcrystalline, porphyritic to variolitic	Pillow, massive	5B 5/1 to 2.5Y 5/3 Bluish gray to light olive gray
14R	1	1-2	0-49	18	Moderately phyrlic PO basalt	Microcrystalline, porphyritic	Massive	5B 4/1 to 7.5YR 5/8 or 2.5YR 5/8 Dark bluish gray to strong brown or red
14R	1	3-16	49-141	19	Moderately phyrlic PO basalt	Microcrystalline, porphyritic	Pillow, pillow-breccia	5B 4/1 to 5B 6/1 Dark bluish gray to bluish gray
14R	2	1-5	0-52	19	Moderately phyrlic PO basalt	Microcrystalline, porphyritic	Pillow, pillow-breccia	5B 4/1 to 5B 6/1 Dark bluish gray to bluish gray
14R	2	6-8	52-67	20	Moderately phyrlic O basalt	Microcrystalline	Breccia, Piece 7 is massive	5B 4/1 Dark bluish gray
14R	2	9-20	67-148	21	Moderately phyrlic PO basalt	Microcrystalline, porphyritic	Pillow, massive	5B 5/1 to 7.5YR 6/8 or 2.5YR 4/8 Bluish gray to reddish yellow or red
14R	3	1-11	0-69	21	Moderately phyrlic PO basalt	Microcrystalline, porphyritic	Pillow, massive	5B 5/1 to 7.5YR 6/8 or 2.5YR 4/8 Bluish gray to reddish yellow or red
15R	1	1-8	0-51.5	22	Highly phyrlic OP basalt	Intergranular, porphyritic	Massive, pillow	5B 4/1 to 2.5YR 4/8 Dark bluish gray to red
15R	1	9-18	51.5-130	23	Highly phyrlic PO basalt	Microcrystalline, porphyritic	Pillow	5B 4/1 to 7.5YR 5/8 or 2.5YR 5/8 Dark bluish gray to strong brown or red
15R	2	1-16	0-138	23	Highly phyrlic PO basalt	Microcrystalline, porphyritic	Pillow	5B 4/1 to 7.5YR 5/8 or 2.5YR 5/8 Dark bluish gray to strong brown or red
16R	1	1-9	0-132	24	Moderately phyrlic PO basalt	Intergranular, porphyritic	Massive	5B 4/1 to 2.5YR 4/8 Dark bluish gray to red
16R	2	1-6	0-145	24	Moderately phyrlic PO basalt	Intergranular, porphyritic	Massive	5B 4/1 to 2.5YR 4/8 Dark bluish gray to red
16R	3	1-8	0-129	24	Moderately phyrlic PO basalt	Intergranular, porphyritic	Massive	5B 4/1 to 2.5YR 4/8 Dark bluish gray to red
17R	1	1-5	0-55	25	Highly phyrlic PO basalt	Microcrystalline, porphyritic	Pillow	5B 4/1 to 5B 5/1 Dark bluish gray to bluish gray
17R	1	6-14	55-126	26	Moderately phyrlic PO basalt	Microcrystalline, porphyritic	Pillow	5B 4/1 to 5B 5/1 Dark bluish gray to bluish gray
17R	1	15-16	126-150	27	Highly phyrlic PO basalt	Microcrystalline, porphyritic	Pillow	5B 4/1 to 5B 5/1 Dark bluish gray to bluish gray
17R	2	1-12	0-144	27	Highly phyrlic PO basalt	Microcrystalline, porphyritic	Pillow	5B 4/1 to 5B 5/1 Dark bluish gray to bluish gray
17R	3	1-4	0-47	27	Highly phyrlic PO basalt	Microcrystalline, porphyritic	Pillow	5B 4/1 to 5B 5/1 Dark bluish gray to bluish gray
17R	3	5-16	47-148	28	Moderately phyrlic OP basalt	Intergranular, porphyritic	Massive	5B 5/1 to 2.5YR 5/8 Bluish gray to red
17R	4	1-16	0-148	28	Moderately phyrlic OP basalt	Intergranular, porphyritic	Massive	5B 5/1 to 2.5YR 5/8 Bluish gray to red
17R	5	1-5	0-34	28	Moderately phyrlic OP basalt	Intergranular, porphyritic	Massive	5B 5/1 to 2.5YR 5/8 Bluish gray to red
18R	1	1-12	0-146	29	Moderately phyrlic PO basalt	Microcrystalline, porphyritic	Pillow	5B 5/1 Bluish gray

NOTE: As a guide to the reader, only the first page of this Appendix is reproduced here. The entire Appendix is given in the CD-ROM (back pocket).

**Appendix C. Occurrence of spinel. Thin sections are identified by core, section, and interval. The location of spinels within phenocrysts or groundmass is indicated with the spinel size, shape, color, and comments about the spinel or its associated minerals. E = euhedral; s = subhedral; and a = anhedral. All grains are equant. Colors, r = red, y = yellow, b = brown, b l = black, g = green.**

Spinel thin section ID	Depth (mbsf)	Unit	Oliv	Plag	Ground mass	Length ( $\mu$ m)	Width ( $\mu$ m)	Shape (c, s, a)	Color (drawing)	Comment
148-896A										
IR-1, 14-21 (4)	195.97			1		150	150	s	yb	In core. With olivine and spinel 2. Corroded.
IR-1, 14-21 (4)	195.97		2			20	20	a		Altered olivine.
IR-1, 14-21 (4)	195.97			x	3	50	50	a		Corroded.
IR-1, 14-21 (4)	195.97			4		30	30	s	yb	In lath with grain 5 plus third smaller grain.
IR-1, 14-21 (4)	195.97			5		30	30	s	yb	With grain 4.
IR-1, 14-21 (4)	195.97				6,7	20	20	e		
IR-1, 14-21 (4)	195.97				8	30	30	s	rb	Corroded.
IR-1, 14-21 (4)	195.97			9		60	50	s	yb	Has glass inclusion.
IR-1, 47-55 (11)	198.03				1	55	55	e	yb	Part of olivine-plagioclase clot.
IR-1, 47-55 (11)	198.03				2	35	35	e	yb	With grain 1.
IR-1, 47-55 (11)	198.03		3			20	20	e	yg yb	In plagioclase in clot with grains 1 and 2.
IR-1, 47-55 (11)	198.03				4	20	20	e	rb	
IR-1, 47-55 (11)	198.03			5		30	30	e	yb	In plagioclase lath near grains 1 to 4.
IR-1, 47-55 (11)	198.03				6	40	40	e	yb	
IR-1, 47-55 (11)	198.03				7	30	30	e	yb	
IR-1, 47-55 (11)	198.03		x		8-10	40	40	e	rb	Grains 9 and 10 are smaller. With groundmass plagioclase.
IR-1, 47-55 (11)	198.03			11		170	80	a	yb rb	Connects plagioclase in clot. Y where inside plagioclase.
IR-1, 47-55 (11)	198.03				12-13	70	70	s, a	drb	Near grain 11.
IR-1, 47-55 (11)	198.03		14			50	50	a		Olivine altered.
IR-1, 47-55 (11)	198.03			15		120	70	a		Plagioclase clot.
IR-1, 47-55 (11)	198.03		16			35	35	a	drb	In largest olivine (0.35 mm) in thin section.
IR-1, 47-55 (11)	198.03			17,18		15	15	a		Anhedral plagioclase.
IR-1, 47-55 (11)	198.03				x					10 more grains in groundmass.
IR-1, 47-55 (11)	198.03			x						6 more grains in or attached to olivine.
IR-1, 7-14 (3)	198.03				3	30	10	e		
IR-1, 7-14 (3)	198.03		x		1	40	40	e	rb	Olivine altered.
IR-1, 7-14 (3)	198.03			x	2	30	30	e	rb	
IR-1, 7-14 (3)	198.03				3	30	30	e	drb	
2R-1, 5-12 (2)	201.32				1	100	70	e	br	Has glass inclusions. Photo
2R-1, 5-12 (2)	201.32				2	20	20	e	yb	Magnetite overgrowth.
2R-1, 5-12 (2)	201.32				3	30	20	e	yb	Thin magnetite overgrowth.
2R-1, 5-12 (2)	201.32				4	100	80	s	rb	At edge of plagioclase; corroded, indented, carries texture.
2R-1, 5-12 (2)	201.32				5	80	60	s	rb	With dark inclusions; With Piece 5 in plagioclase glomerocryst.
2R-1, 5-12 (2)	201.32				6,7					6 attached to plagioclase, 7 in groundmass.
2R-1, 5-12 (2)	201.32		8			20	20	e	y	In altered olivine.
2R-1, 5-12 (2)	201.32			9		60	30	e	b	In same olivine as 8.
2R-1, 5-12 (2)	201.32		10			20	20	e	yb	Perfect octahedron.
2R-1, 5-12 (2)	201.32		4	7	14					Also 14 in groundmass, 4 in olivine, 7 attached to plagioclase.
2R-1, 41-50	204.35				1	40	40	s	yb	Corroded.
2R-1, 41-50	204.35		2			20	20	a	yb	Plus second similar grain. Olivine altered.
2R-1, 41-50	204.35			X	3	50	50	e	yb	Four grains touch plagioclase megacryst with glass inclusions.
2R-1, 41-50	204.35				4	80	80	a	yb	Two grains.
2R-1, 82-90	207.8			x	1	40	40	e	b	Touching plagioclase megacryst.
2R-1, 82-90	207.8				2	60	50	a	b	
2R-1, 82-90	207.8				3	50	50	s	yb	
2R-1, 82-90	207.8		4			80	80	a	yb	Three grains together; plus a grain in adjacent olivine.
2R-1, 94-101 (24)	208.81				1	70	60	e	rb	
2R-1, 94-101 (24)	208.81			2		80	70	s	rb	Symplectic; plus grain at edge of plagioclase.
2R-1, 94-101 (24)	208.81				3	40	40	e	rb	Perfect truncated pyramid.
2R-1, 94-101 (24)	208.81				4	120	80	e	rb	With olivine-plagioclase clot; plus 2 smaller spinels.
2R-1, 94-101 (24)	208.81		5			60	60	s	yb rb	Altered olivine.
2R-1, 94-101 (24)	208.81			6		30	30	e-s	rb	With plagioclase and altered olivine.
2R-1, 94-101 (24)	208.81			7		70	70	e	rb	With olivine-plagioclase clot.
2R-1, 94-101 (24)	208.81			8		100	80	s	rb	Large plagioclase with melt inclusion.
2R-1, 94-101 (24)	208.81		9			30	30	s	rb	In altered olivine associated with plagioclase 8.
2R-1, 94-101 (24)	208.81				x					Associated with plagioclase.

**NOTE: As a guide to the reader, only the first page of this Appendix is reproduced here. The entire Appendix is given in the CD-ROM (back pocket).**

## Appendix D. Point-count data for thin sections from Site 896.

Core	Section	Top (cm)	Bottom (cm)	Piece	Unit	Depth (mbsf)	Phenocrysts					Megacrysts						
							Plag (%)	Ol (%)	Cpx (%)	Sum (%)	Plag/ Ol	Plag (%)	Max (mm)	Ol (%)	Max (mm)	Cpx (%)	Max (mm)	Sum (%)
1	1	7	14	3	1	195.54	3.8	0.8		4.6	4.8	1.8	2.3	0.1	0.8			1.9
1	1	14	21	4	2	195.97	5.8	1.8		7.6	3.2	1.6	3.0					1.6
1	1	47	55	11	3	198.03	5.6	0.6		6.2	9.3	1.8	3.0					1.8
2	1	5	12	2	4	201.32	5.0	1.4		6.4	3.6	0.9	1.7					0.9
2	1	41	50	10	7	204.35	4.0	1.6		5.6	2.5							0.0
2	1	82	90	19	7	207.80	3.2	1.8		5.0	1.8	3.1	4.0					3.1
3	1	41	44	7	8	212.15	2.2	0.2		2.4	11.0	0.9	2.0					0.9
3	1	83	86	9	9	214.45	4.2	1.0		5.2	4.2	1.1	2.0					1.1
3	1	143	146	17	9	217.75	2.4	2.6		5.0	0.9	0.9	1.9	0.1	1.0			1.0
4	1	5	8	1	9	219.32	5.6	2.2		7.8	2.5	1.3	2.6					1.3
4	1	75	80	9	9	225.15	2.2	0.8		3.0	2.8	0.5	1.7					0.5
5	1	49	52	9	10	229.92	5.2	0.6		5.8	8.7							0.0
5	2	20	23	1	10	231.88	8.8	1.0		9.8	8.8	2.6	2.4					2.6
5	2	35	37	1	10	232.34	6.8	1.0		7.8	6.8	1.4	1.9					1.4
5	3	1	5	1	10	235.82	4.0	1.2		5.2	3.3	1.5	3.8					1.5
5	3	63	67	8	11	237.74	7.0	1.2		8.2	5.8	2.9	2.1					2.9
6	1	52	54	5	12	239.12	7.8	2.4		10.2	3.3	2.9	3.0	0.1	0.8			3.0
6	2	89	91	10	12	243.45	9.0	1.4		10.4	6.4	2.3	2.4					2.3
6	2	130	133	11	12	244.41	7.2	1.6		8.8	4.5							0.0
6	3	6	9	1	12	244.79	6.8	1.8		8.6	3.8	2.4	2.6	0.1	1.3			2.5
7	1	52	55	10	13	250.90	4.6	0.8		5.4	5.8							0.0
7	1	80	83	13	14	252.79	5.2	1.6		6.8	3.3	2.6	2.6					2.6
7	1	135	139	22	14	256.49	5.8	1.4		7.2	4.1	1.0	3.4	0.1	0.9			1.1
8	1	29	32	7	14	259.03	6.6	4.0		10.6	1.7	1.4	2.6					1.4
8	1	54	57	12	14	260.70	4.8	0.0		4.8								0.0
9	1	138	141	25	14	273.53	10.0	2.4		12.4	4.2	1.9	2.2					1.9
10	1	36	39	4	14	278.77	5.6	2.2		7.8	2.5							0.0
10	1	116	118	9	14	284.03	5.0	1.0		6.0	5.0	2.1	2.6	0.2	0.8			2.3
10	1	129	134	11	14	284.88	9.6	0.8		10.4	12.0	2.2	2.6	0.3	1.2			2.5
11	1	64	71	7	14	287.59	5.0	1.6		6.6	3.1							0.0
11	3	12	17	3	15	293.56	0.8	0.2		1.0	4.0							0.0
11	3	48	53	8	16	294.46	10.0	2.2		12.2	4.5	2.9	3.8					2.9
12	1	68	71	9	16	298.63	7.8	3.6		11.4	2.2	2.5	3.2					2.5
12	1	78	81	10	16	299.08	8.9	5.6		14.5	1.6	2.0	2.4					2.0
12	2	9	12	1	17	302.47	11.4	3.0		14.4	3.8	1.2	1.9					1.2
12	2	31	37	3	17	303.45	5.8	2.4		8.2	2.4	1.3	2.4					1.3
14	1	38	41	2	18	315.63	10.8	1.2		12.0	9.0	2.1	2.6					2.1
14	2	28	31	3	19	319.18	14.4	1.8		16.2	8.0	2.2	2.0	1.2	2.3			3.4
14	2	58	61	7	20	319.99	0.2	1.4		1.6	0.1							0.0
14	2	113	115	19	21	321.48	9.4	1.0		10.4	9.4	3.4	3.0					3.4
14	2	135	137	16	21	322.08	11.6	3.6		15.2	3.2	2.6	2.9					2.6
15	1	23	29	4	22	325.12	10.2	2.4		12.6	4.3	3.9	2.6	0.6	1.3			4.5
15	1	101	106	15	23	327.92	9.8	3.2		13.0	3.1	3.0	3.0					3.0
16	1	31	34	3	24	334.63	5.8	2.6		8.4	2.2	0.9	1.5					0.9
16	3	88	91	4	24	342.53	8.2	8.0		16.2	1.0	3.5	2.2	0.3	0.9			3.8
17	1	1	3	1	25	343.52	9.8	2.8		12.6	3.5							0.0
17	1	82	84	9	26	344.76	4.0	2.4		6.4	1.7							0.0
17	2	16	19	2	27	346.06	9.8	1.8		11.6	5.4	1.4	2.3	0.1	1.2			1.5
17	3	89	93	8	28	349.40	11.2	4.2		15.4	2.7	1.7	1.9					1.7
17	4	80	84	7	28	351.53	2.8	1.4		4.2	2.0							0.0
17	4	99	102	9	28	351.82	4.0	2.6		6.6	1.5	3.0	2.0					3.0
17	4	118	123	12	28	352.11	12.2	4.0		16.2	3.1	2.5	2.6					2.5
18	1	72	75	6	29	354.07	6.2	2.8		9.0	2.2							0.0
18	1	83	86	8	29	354.22	9.0	2.0		11.0	4.5	1.4	3.8					1.4
18	2	60	68	10	30	355.88	10.6	3.8		14.4	2.8	3.6	3.0	1.3	2.1			4.9
19	1	23	25	5	30	356.89	9.2	3.2		13.4	2.9	1.2	2.1	0.5	1.2	0.3	1.1	2.0
19	1	140	144	22	30	361.44	8.8	2.4		11.2	3.7	1.9	3.2	0.2	1.1	0.4	3	2.5
19	2	28	34	6	30	362.84	9.2	3.2		12.4	2.9	0.8	1.7	1.2	1.9	0.6	3	2.6
20	1	14	20	5	30	364.29	9.8	4.4	0.2	14.4	2.2	1.7	2.4	0.3	1.1	0.3	1.1	2.3
20	1	73	77	16	31	367.63	10.2	2.4		12.6	4.3	2.7	3.0	0.4	1.1	0.3	1.8	3.4
20	1	83	88	18	31	368.19	7.0	0.8	0.8	8.6	8.8	1.2	1.6	0.2	0.9			1.4
21	1	11	19	3	31	373.32	15.2	3.2	0.4	18.8	4.8	1.4	1.9	0.1	1.1	0.2	0.9	1.7
21	1	33	38	7	31	373.96	11.4	3.8		15.2	3.0	2.1	2.5	0.2	1.4			2.3
21	2	27	29	3B	31	378.09	10.6	4.0		14.6	2.7	1.4	2.1					1.4
21	2	87	89	10C	32	379.84	10.8	4.2	0.2	15.2	2.6	0.7	2.4	0.4	1.5			1.1
21	3	22	24	4	32	382.31	12.2	6.6	0.4	19.2	1.8	2.8	2.6	0.2	1.0	1.2	7.1	4.2
22	1	64	66	7A	32	383.75	14.8	5.0	2.0	21.8	3.0	3.7	2.6	0.1	0.8	0.2	1.6	4.0
22	2	133	134	18B	33	387.68	16.2	3.2		19.4	5.1	8.6	3.6	1.9	1.9	1.4	1.2	11.9
22	4	26	29	4	33	391.02	10.6	1.8		12.4	5.9	1.3	2.1	0.6	1.2	0.1	0.8	2.0
22	4	43	46	6	34	391.33	6.0	3.6		9.6	1.7	1.0	1.5					1.0
23	2	5	7	1	36	395.55	7.6	6.8		14.4	1.1	1.1	1.8					1.1
23	3	18	20	3	36	399.10	10.2	14.2		24.4	0.7	0.7	2.0	1.2	2.4			1.9
24	1	24	25	1	36	402.11	7.8			7.8		2.3	2.0					2.3
24	5	145	148	14	36	411.16	22.6	10.8		33.4	2.1	2.3	3.2	1.7	2.3			4.0
25	2	123	134	22	37	417.92	6.4	2.4		8.8	2.7	1.3	1.5	0.3	0.9			1.6
27	1	69	71	8	43	432.40	8.4	6.4		14.8	1.3	1.9	1.9	2.2	3.4	1.0	4.9	5.1
27	2	107	112	13	45	437.49	7.0	1.4		8.4	5.0	3.8	2.4	0.1	0.8			3.9
28	1	54	58	9	47	442.36	7.2	5.2		12.4	1.4	1.8	2.3	0.1	0.8			1.9
30	1	137	141	18	51	467.55	9.2	6.8		16.0	1.4	0.3	3.4					0.3

Appendix E. Glomerocryst, classified by mineralogical type. The number of grains in each glomerocryst are indicated with the modal proportions and the maximum and minimum dimensions of the glomerocryst. Mineral abbreviations: pl = plagioclase; cpx = clinopyroxene; ol = olivine; mt = magnetite. + = present, (+) = megacryst. In the comments the following abbreviations are used: oscil = oscillatory; z = zoning; euhed = euhedral; subhed = subhedral; anhedral = anhedral; incl = inclusion; Ol = olivine; Pl = plagioclase; Cpx = clinopyroxene; Sp = spinel; tex = texture.

	Glomerocryst type						Number of grains	Size (mm)	Relative abundance				Comments	
	Piece	Pl	Pl-ol	Pl-cpx	Pl-ol-cpx	Others			Pl	Ol	Cpx	Sp		
148-896A-1R-1, 7-14	3	+					6	0.9-0.1	100					
		+					14	1-0.2	100					Resorbed core.
			+				6	0.9-0.15	85	15				Euhed, glass inc.
		+					14	1.4-0.15	100					Euhed, resorped core, oscil. z. mantle.
		+					16	0.6-0.15	100					Euhed-anhed, sutured boundary.
1R-1, 14-21	4	+					3	2.7-0.3	100					Big pl: undulatory z. core mantled by oscil. z.
		+					8	1.6-0.15	100					Oscil. z.
		+					11	1.4-0.2	100					Subhed-anhed.
1R-1, 47-55	11	+	+				13	2.6-0.3	85	14		1		Subhed-anhed, sp within pl.
		+					10	3-0.3	100					Oscil. z.
		+					35	0.6-0.1	100					Oscil. z.
		+					13	1-0.3	100					Euhed, oscil. z.
		+					5	1.3-0.3	100					Euhed, oscil. z.
		+					22	0.6-0.1	100					Subhed-anhed, oscil. z.
2R-1, 5-12	2	+					15	1.3-0.2	100					Euhed, oscil. z. core.
			+				13	0.6-0.1	40	60				Weakly normal z., subhed.
			+				10	2.5-0.15	89	10		1		Euhed, sp included in pl.
		+					7	1.4-0.2	100			tr		Euhed, resorbed core with mantle.
2R-1, 41-50	10	+					5	1.5	95		5	tr		Euhed, glass inc., resorbed core.
		+					16	0.7-0.15	50		49	1		Oscil. z. mantle.
		+					32	2-0.15	95		5	tr		Euhed-subhed, preferred alignment, oscil. z.
		+					5	0.5-0.2	100					Euhed.
2R-1, 82-90	19	+					10	1.1-1.15	100					Euhed.
		+					10	1-0.2	100					Preferred alignment, euhed-subhed.
		+					5	1-0.2	100					Grain boundary: ambiguous.
2R-1, 94-101	24	+					7	1.2-0.2	100					Subhed, inc. in mantle.
		+					8	1.8-0.3	99			1		Sp included in the rim of Pl.
		+					21	2-0.2	100					Resorbed core, oscil. z.
		+					11	2-0.3	100			tr		Multiple oscil. z., glass inc.
3R-1, 41-44	7	+					8	0.8-0.3	100					Euhed.
		+					4	1.5-0.3	100					Euhed, oscil. z.
		+					10	1-0.2	100					Euhed.
		+					8	1.5-0.4	100					Euhed, oscil. z.
3R-1, 83-86	9A	+					6	1.5-0.3	100					Euhed-subhed, oscil. z.
		+					15	1.2-0.15	100					Euhed, loosely packed, cumulus tex.
		+					7	1-0.3	100					Euhed, undulatory z. core, oscil. z. mantle.
		(+)					1	1.3 x 0.8						Zoning structure is truncated, finely embayed.
4R-1, 5-8	1	+					16	1-0.2	100					Euhed-subhed, resorbed core.
		+					12	0.9-0.15	100					Euhed-subhed, oscil. z.
		+					15	1.0-0.15	100					Euhed, oscil. z.
		+	+				15	1.0-0.2	84	15		1		Euhed equant, rounded subhed, oscil. z.
		(+)					1	2.7 x 1.0						Rounded, dusty incl.
4R-1, 75-80	9C	+					11	0.7-0.3	100					Euhed, oscil. z.
		+					8	0.8-0.1	100					Euhed, oscil. z.
		+					4	1.6-0.5	100					Euhed.
5R-1, 49-52	9A	+	+				8	0.8-0.2	75	25				Euhed, oscil. z.
		+					8	1.6-0.3	100					Subhed: no z., euhed: oscil. z.
		+					10	2.2-0.3	95		5			Euhed, fine oscil. z.
5R-2, 20-23	1B	+					5	0.8-0.3	100					Euhed, resorbed core.
		+					12	0.9-0.15	100					Subhed, rounded.
		+					13	0.6-0.15	100					Euhed-subhed, rev. z.
		(+)					1	1.1 x 0.9						Numerous glass inc., anhed.
5R-2, 35-37	1D	+	+				10	1.2-0.15	90	10				Euhed, resorbed core.
		+					20	0.8-0.2	100					Euhed-subhed, fine oscil. z.
		+					8	0.9-0.2	100					Euhed.
		(+)					1	1.7x0.6						Patchy irregular z., anhed.

NOTE: As a guide to the reader, only the first page of this Appendix is reproduced here. The entire Appendix is given in the CD-ROM (back pocket).

Appendix F. Leg 148 Hole 896A. Alteration Log. Abbreviations are defined in Table 3, "Explanatory Notes" chapter, this volume.

Unit	Core	Section	Piece	Length (cm)	Depth (mbsf)	Exp (mbsf)	After olivine	% Gray g'mass	Total Oxid. (%) g'mass	Red (%) g'mass	Yellow (%) g'mass	Red-brown (%) g'mass	% Dark grey g'mass	Comments
1	001R	1	1	3	195.1	195.1	dk grn	99	1	1				Fine-grained basalt; distinctive brown-gray. Very minor spots of oxidation.
1	001R	1	2	2.5	195.1	195.3		95	5	5				Minor spots of oxidation; brownish gray in background.
1	001R	1	3	6	195.2	195.5		90	10	10				Near chilled margin.
2	001R	1	4	6	195.2	195.9		60	40	10	30			Medium grained.
2	001R	1	5	3.5	195.3	196.4		10	90		90			Yellow alteration area with less oxidized rim.
3	001R	1	6	4.5	195.3	196.6		90	10		10			Fine grained, near chill. small patch of red/yellow alteration.
3	001R	1	7	6	195.4	197.0		100						Fine grained, brownish gray.
3	001R	1	8	4	195.4	197.4		100						Fine grained, brownish gray.
3	001R	1	9	2.5	195.5	197.7		100						Rubble.
3	001R	1	10	3	195.5	197.9		100						Fine grained, brownish gray.
3	001R	1	11	7	195.5	198.1		95	5	5				Fine grained, brownish gray.
3	001R	1	12	8	195.6	198.6		100						Fine grained, brownish gray.
3	001R	1	13	3.5	195.7	199.2		95	5	5				Fine grained, brownish gray. Minor alteration zones along veins.
3	001R	1	14	3	195.7	199.4		100						Rubble.
3	001R	1	15	1.5	195.7	199.7		100						Fine grained, brownish gray.
3	001R	1	16	1.5	195.7	199.8		100	<1	<1				Fine grained, brownish gray.
3	001R	1	17	3	195.8	199.9		100						Fine grained, brownish gray.
3	001R	1	18	11	195.8	200.1		100						Fine grained, brownish gray.
4	002R	1	1	4	200.9	200.9	iddings.	50	50	50				Brown alteration, highly oxidized around black dots in groundmass.
4	002R	1	2	6	200.9	201.3	iddings.		100	100				Highly oxidized.
5	002R	1	3	3	201.0	201.9	dk grn	90	10	10				Partially oxidized, scattered black dots with red rims.
5	002R	1	4	3.5	201.0	202.2	dk grn	80	20	20				Fine grained.
5	002R	1	5	2.5	201.1	202.5	dk grn	100						Fine grained, brownish gray.
5	002R	1	6	3	201.1	202.8	dk grn	100						Fine grained, brownish gray.
5	002R	1	7	5.5	201.1	203.1	dk grn	100						Fine grained, brownish gray.
5	002R	1	8	4.5	201.2	203.6	dk grn	100						Fine grained, brownish gray.
6	002R	1	9	3	201.2	204.1	dk grn	100						Fine grained, brownish gray.
7	002R	1	10	8	201.3	204.4	dk grn	98	2	2				Fine grained, brownish gray.
7	002R	1	11	4	201.3	205.2		100						Fine grained, brownish gray. Porphyritic.
7	002R	1	12	3	201.4	205.6			100	100				Highly oxidized.
7	002R	1	13	4	201.4	205.9			100	100				Highly oxidized.
7	002R	1	14	3	201.4	206.3		100						Rubble.
7	002R	1	15	2.5	201.5	206.6	grn, red	100						Fine grained, brownish gray.
7	002R	1	16	2.5	201.5	206.8	grn, red	95	5	5				Fine grained, brownish gray. Oxidation around black spots.
7	002R	1	17	5.5	201.5	207.1	grn, red	100						Fine grained, brownish gray. Chill down one edge.
7	002R	1	18	3.5	201.6	207.6	grn, red	100						Fine grained, brownish gray. Near chill.
7	002R	1	19	7	201.6	208.0	grn, red		100	100				Highly oxidized.
7	002R	1	20	3	201.7	208.7	grn, red	10	90	60		30		Red halo around dark oxidized halo.
7	002R	1	21	3.5	201.7	209.0	grn, red	95	5	5				Medium grained, some oxidation in groundmass.
7	002R	1	22	6	201.7	209.3	green	40	60	60				Medium grained. Red/yellow oxidation in patches.
7	003R	1	1	5	209.9	209.9		60	60	60				Patchy oxidation.
7	003R	1	2	3.5	210.0	210.2		100						Greenish-gray; vein, though no halo.
7	003R	1	3	2.5	210.0	210.5		100						Greenish-gray; appears fresh, very fine grained.
8	003R	1	4	10	210.0	210.6		95	1	1				Chilled at top, cross-cut by vein; oxidation along halo.
8	003R	1	5	5	210.1	211.3		100						20% is greenish gray; >1 cm glassy rim; green coating of groundmass, gray at core.
8	003R	1	6	2	210.2	211.6		95	5	5				Margin defined by smectite + carbonate veins with 1-1.5 mm halos.
8	003R	1	7	22	210.2	211.7		95	5	5				20 cm pillow with upper and lower chill rims; oxidation around smectite + carbonate veins.
8	003R	1	8	13	210.4	213.2		60	40	40				Top 60% gray, lower part red; intense red core with ochre margin.
9	003R	1	9a	31	210.5	214.1		1	99	99				Highly oxidized; 2 cm patches of gray background.
9	003R	1	9b		210.8	216.1	grn clay	5	95	95				3-4 cracks, but bulk rock oxidized; vein halos not significant; green clay after olivine in gray patch.
9	003R	1	10-11	4	210.8	216.1								Rubble.
9	003R	1	12	3	210.9	216.4			100	100				Patchy alteration, partially oxidized (red facies).
9	003R	1	13	3	210.9	216.6			100	100				Patchy alteration, partially oxidized (red facies).
9	003R	1	14	4.5	210.9	216.8			100	100				Patchy alteration, partially oxidized (red facies).
9	003R	1	15	2.5	211.0	217.1			100	100				Patchy alteration, partially oxidized (red facies).

NOTE: As a guide to the reader, only the first page of this Appendix is reproduced here. The entire Appendix is given in the CD-ROM (back pocket).

Appendix G. Leg 148, Hole 896A. Vein log. Abbreviations are defined in Table 3, "Explanatory Notes" chapter, this volume.

Unit	Core	Section	Piece	Length	Top cm	Bottom cm	Type	Minerals	Total (%)	AW	Orient	Az	Halo	Alt (%)	W	%h	Comments
1	1	1	1	3	0	3	med gm+w	clay+carb	<1	<1							On exposed surface.
1	1	1	3	5	0	10	frac	?	<1	<1			bm	<1	<1		Brown halo extends from the larger diffuse bm halo that flanks one surface.
1	1	1			10	11	frac	?	<1	<1			bm	<<1	<<1		
1	1	1			11	13	med gm	clay	<1	<1							On exposed surface.
1	1	1			11	11	med gm	clay	<1	<1							On exposed surface and fracture
3	1	1	7	6	29	34	med gm	clay	<1	<1			bm	<1	<1		On exposed surface.
3	1	1			34	35	med gm	clay	<1	<1			bm	<1	<1		On exposed surface.
3	1	1	8	4	37	38	med gm	clay	<1	<1			bm	<1	<1		On exposed surface.
3	1	1	9	2	41	42	med gm	clay	<1	<1			bm	<1	<1		On exposed surface.
3	1	1	11	7	47	53	dk gm+w	clay+carb	6	2			bm	1-2	1		
3	1	1			52	52	dk gm+w	clay+carb	6	2			bm	1-2	<1		
3	1	1			51	51	dk gm+w	clay+carb	6	2			bm	1-2	<1		
3	1	1			49	49	med gm	clay	<1	<1							
3	1	1			51	53	med gm	clay	<1	<1							
3	1	1			52	52	med gm	clay+carb	<1	<1							
3	1	1	12	8	55	59	med gm, w	clay+carb	<1	<1							
3	1	1			58	63	med gm, w	clay+carb	<1	1							
3	1	1			61	63	med gm+w	clay+carb	<1	1.5							
3	1	1			59	60	med gm+w	clay+carb	<1	<1							
3	1	1			59	60	med gm+w	clay+carb	<1	<1							
3	1	1			61	63	med gm+w	clay+carb	<1	<1							On exposed surface.
3	1	1	13	4	64	67	med gm	clay	<1	<1			bm	1	2		Halo stops 1/2 thickness sample.
3	1	1			65	65	med gm	clay	<1	<1							
3	1	1			65	65	med gm+w	clay+carb	<1	<1							Crosses a thin bm halo.
3	1	1			64	65	med gm+w	clay+carb	<1	<1			bm	<1-1	<1		On exposed surface, irregular shape.
3	1	1	14	1	68	70	med gm+w	clay+carb	<1	<1							On exposed surface.
3	1	1	16	1	76	76	dk gm+w	clay+carb	<1	<1			bm	<1	<1		On exposed surface.
3	1	1	17	3	78	78	w	carb	6	1.5							On exposed surface.
3	1	1			80	80	med gm+w	clay	<1	1							
3	1	1			78	80	med gm	clay+carb	<1	<1			bm	<1	<1		On exposed surface.
3	1	1	18	11	86	86	dk gm+w	clay+carb	<1	<1							These three veins change color from w to gm.
3	1	1			81	91	dk gm+w	clay+carb	<1	<1							These three veins change color from w to gm.
3	1	1			86	88	dk gm+w	clay+carb	<1	<1							These three veins change color from w to gm.
4	2	1	1	4	0	0	med gm	clay	<1	<1							On exposed surface.
4	2	1	2	6	5	7	med gm+w	clay+w	<1	<1							
5	2	1	5	2	20	20	med gm	carb+?	<1	<1			bm	<1	<1		On exposed surface (working half).
5	2	1	7	6	26	27	w (+black dots)	clay+carb	<1	<1							On exposed surface, One of them only in working half.
5	2	1			27	28	dk gm+med gm	clay	<1	<1			bm	<1	<1		On exposed surface.
5	2	1	8	5	33	33	med gm+w	clay+carb	<1	<1			bm	<1	<1		On exposed surface.
6	2	1	9	3	38	38	dk gm+med gm spots	clay	8	1-3							On exposed surface.
6	2	1			38	39	med gm	clay	<1	<1							On exposed surface.
7	2	1	11	3	50	50	breccia		2	<1-2							Med gm clay cements dk gm pieces of altered basalt (glass?) and gray basalt.
7	2	1	12	2	55	57	breccia	clay+carb	14	3-4							Med gm clay cements dk gm pieces of altered basalt (glass?) and gray basalt.
7	2	1			55	58	breccia	clay									
7	2	1	13	4	58	58	breccia (2)	clay	<5	2			bm	<1	<1		Med gm clay cements dk gm pieces of altered basalt (glass?) and gray basalt.
7	2	1	14	1	64	64	breccia	clay	<1	<1							On exposed surface.
7	2	1			64	64	med gm	clay	<1	<1							On exposed surface.
7	2	1			64	64	w	carb	<1	<1							On exposed surface.
7	2	1	15	2	66	66	med gm	clay	<1	<1			bm	<1	<1		On exposed surface.
7	2	1	16	2	70	70	dk gm	clay	<1	<1							
7	2	1	17	5	74	74	lt gm+w	clay+carb	4	2							Clay at the wall, carbonate in the center.
7	2	1	18	3	78	81	med gm+w	clay+carb	2	1							
7	2	1			81	81	med gm	clay	1	<1			bm				On exposed surface.

NOTE: As a guide to the reader, only the first page of this Appendix is reproduced here. The entire Appendix is given in the CD-ROM (back pocket).

Appendix H. Leg 148, Hole 896A. Structure log.

Core	Type	Section	Piece	Oriented?	Top (m)	Bottom (m)	Depth (mbsf)	Feature	Composition	Dir.	Angle	Dir.	Angle	Angle	Dir.	Mag. dec	Mag. inc	Angle	Dir.	Sense	SBA	Comments	
001	R	1	7	N	29	34	195.4	Vein	Clay					90								On working half only.	
001	R	1	7	N	34	35	195.4	Vein	Clay	090	22	000	23	30								On working half only.	
001	R	1	7	N	34	36	195.4	Vein	Clay	090	0	180	27	27								On working half only.	
001	R	1	11	Y	48	54	195.6	Vein	clay/Carb.					90	100	299	-3.20	90	341		TM	Cuts vein below.	
001	R	1	11	Y	51		195.6	Vein	clay/Carb.	270	0	180	27	27	180	299	-3.20	27	061		TM	Offset by vein above, apparent movement is normal.	
001	R	1	12	Y	55	60	195.7	Vein	clay/Carb.	270	42	180	0	42	270								
001	R	1	12	Y	59	63	195.7	Vein	clay/Carb.	090	64	174	0	66	084								Discontinuous.
001	R	1	18	Y	83	87	195.9	Vein	clay/Carb.	270	9	200	39	75	122	269	-	75	033		M	Sinuuous.	
001	R	1	18	Y	86	89	196.0	Vein	clay/Carb.	090	48	220	32	64	148	269	11.90	-	64	059		M	Branches from vein above.
002	R	1	14	N	74		201.6	Vein	clay/Carb.					90									
002	R	1	22	N	103	106	201.9	Vein	clay/Carb.					69									
003	R	1	4	Y	16	24	210.1	Vein	clay/Carb.					90	083								
003	R	1	4	Y	18		210.1	Vein	Carb.	270	17	183	18	24	225								
003	R	1	4	Y	23		210.1	Vein	Carb.	090	15	162	48	48	166								
003	R	1	7	Y	42	46	210.3	Vein	clay/Carb.	270	21	335	35	35	327	067	-	35	080		TM	Continuous, overlapping segments.	
003	R	1	7	Y	42	45	210.3	Vein	clay/Carb.					75	270	067	10.40	-	75	023		TM	Alteration halo, planar, discontinuous, terminated by veins described above and below.
003	R	1	7	Y	45	48	210.4	Vein	clay/Carb.					45	206	067	-	45	319		TM	Forms fracture face between pieces.	
003	R	1	7	Y	49	55	210.4	Vein	clay/Carb.					42	030	067	10.40	-	42	143		TM	Forms face of core, discontinuous against vein described above.
003	R	1	7	Y	49	55	210.4	Vein	clay/Carb.					39	085	067	10.40	-	39	198		TM	Planar, continuous, fractured face of core.
003	R	1	7	Y	50		210.4	Vein	clay/Carb.					45	088	067	10.40	-	45	201		TM	Planar to weakly irregular, forms fractured face of core.
003	R	1	8	Y	61		210.5	Vein	Carb.					22	087								
003	R	1	8	Y	63	73	210.5	Vein	clay/Carb.					90	053								
003	R	1	8	Y	67		210.6	Vein	Carb.	090	10	182	28	30	162								
003	R	1	9a	Y	74	79	210.6	Vein	clay/Carb.					55	280	117	-6.40	55	343		TM	Continuous, weakly curvilinear, fibers normal to vein walls.	
003	R	1	9a	Y	79	84	210.7	Vein	Carb.	270	45	017	0	46	287	117	-6.40	46	350		TM	Discontinuous, smooth to irregular, "en echelon"	
003	R	1	9a	Y	87		210.8	Vein	Carb.	000	0	027	32	54	090	117	-6.40	54	153		TM	Irregular, continuous, planar.	
003	R	1	14	N	122	126	211.1	Vein	clay					78									
003	R	1	17	Y	143	147	211.3	Vein	Carb.	270	57	188	30	58	257								
003	R	1	17	Y	145		211.4	Vein	Carb.	090	17	338	65	68	007								
004	R	1	1	Y	2	4	218.9	Vein	clay/Carb.					71	073								
004	R	1	1	Y	7	9	219.0	Vein	clay					82	153								
004	R	1	1	Y	8		219.0	Vein	clay/Carb.	090	16	175	18	23	136								
004	R	1	9a	Y	54	58	219.4	Vein	lgt. gn. clay	090	29	006	5	29	087	110	-8.00	29	157		TM	Continuous, irregular, variable thickness, planar to curvilinear.	
004	R	1	9a	Y	58	68	219.5	Vein	lgt. gn. clay					63	182	110	-8.00	63	252		TM	Planar, continuous, weakly irregular, fractured face.	
004	R	1	9a	Y	58	70	219.5	Vein	lgt. gn. clay					84	062	110	-8.00	84	132		TM	Continuous, planar to irregular.	
004	R	1	9a	Y	64		219.5	Vein	dark gn. clay	090	30	000	5	6	031	110	-8.00	6	101		TM	Continuous, planar to irregular.	

NOTE: As a guide to the reader, only the first page of this Appendix is reproduced here. The entire Appendix is given in the CD-ROM (back pocket).

## Appendix I. Leg 248, Site 896. Deformation log. ODP visual core description.

Core	Section	Interval	Piece	Unit	Depth (mbsf)	Lithol.	Magmatic	Ductile	Cataclast.	Fracture	Vein	Comments
1R	1	0-7	1-2	1	195.1	basalt	0	0	0	0/0	0/0	
1R	1	7-14	3	1	195.1	basalt	0	0	0	1/1	1/0	Planar vein filled by clay, in the exposed surface.
1R	1	14-29	4-6	2/3	195.2	basalt	0	0	0	1/1	0/0	Tiny fractures perpendicular to chilled margin.
1R	1	29-47	7-10	3	195.2	basalt	0	0	0	1/1	1/0	Thin veins on the exposed surface.
1R	1	47-55	11	3	195.6	basalt	0	0	0	1/1	2-3/0	T-intersection of the main veins.
1R	1	55-63	12	3	195.6	basalt	0	0	0	1/1	2-3/0	Calcite fibers orthogonal to the vein walls.
1R	1	63-68	13	3	195.7	basalt	0	0	0	1/1	3/0	Nearly orthogonal vein system. Overlapping veins.
1R	1	68-77	14-16	3	195.7	basalt	0	0	0	1/1	1/0	Irregular veins, mostly in the exposed surface.
1R	1	77-81	17	3	195.8	basalt	0	0	0	1/1	2/0	All veins in the exposed surface. Two orthogonal veins.
1R	1	81-93	18	3	195.8	basalt	0	0	0	2/1	3/2	Sinuuous to irregular veins.
2R	1	0-15	1-3	4/5	200.9	basalt	0	0	0	1/1	1/0	Veins in the exposed surface.
2R	1	15-26	4-6	5/6	201	basalt	0	0	0	1/1	1/0	Veins in the exposed surface.
2R	1	26-41	7-9	6/7	201.1	basalt	0	0	0	1/1	1/0	Planar veins in the exposed surface.
2R	1	41-49	10	7	201.3	basalt	0	0	0	2/1	0/0	Irregular, open fractures.
2R	1	49-62	11-13	7	201.3	basalt	0	0	0	1/1	0/0	Breccia/hyalocl. in the exposed surface.
2R	1	62-72	14-16	7	201.5	basalt	0	0	0	1/1	1/0	Veins in the exposed surface.
2R	1	73-82	17-18	7	201.6	basalt	0	0	0	1/1	2/0	Planar; fibers orthogonal to the vein walls.
2R	1	82-94	19-20	7	201.7	basalt	0	0	0	1/1	1/0	Veins mostly in the exposed surface.
2R	1	94-101	21	7	201.8	basalt	0	0	0	0/0	1/0	Veins on the exposed surface.
2R	1	101-108	22	7	201.9	basalt	0	0	0	1/1	3/0	Planar veins.
3R	1	0-14	1-3	7	209.9	basalt	0	0	0	1/1	1/0	On the exposed surface, piece #2.
3R	1	14-25	4	8	210	basalt	0	0	0	1/1	3/0	Overlapping calcite veins. Orthogonal vein arrays.
3R	1	25-31	5	8	210.1	basalt	0	0	0	3/1	1/0	On the outside surface. Broken pieces.
3R	1	31-34	6	8	210.2	basalt	0	0	0	1/1	2/0	On the exposed surface.
3R	1	35-73	7-8	8	210.2	basalt	0	0	0	2/1	3/0	Planar to sinuous veins; T-intersection; some triple junctions; fibers orthogonal to vein walls.
3R	1	73-104	9A-9B	9	210.6	basalt	0	0	0	1/1	2-3/0	Planar to irregular and curvilinear veins.
3R	1	104-110	10-11	9	210.9	basalt	0	0	0	1/1	1/0	Rollers; outside surface.
3R	1	110-122	12-13	9	211	basalt	0	0	0	0/0	2/0	Planar to curvilinear veins; fractures in the veins.
3R	1	122-131	14-15	9	211.1	basalt	0	0	0	1/1	1/0	Mainly on the exposed surface.
3R	1	131-135	16	9	211.2	basalt	0	0	0	0/0	0/0	
3R	1	135-146	17	9	211.2	basalt	0	0	0	1/1	2-3/0	Curvilinear to sinuous veins.
3R	2	0-10	1-2	9	211.4	basalt	0	0	0	1/1	1/0	Hairline fractures.
3R	2	11-15	3	9	211.5	basalt	0	0	0	0/0	2/0	
4R	1	0-9	1	9	218.9	basalt	0	0	0	1/1	3/0	Curvil linear to irregular veins. Complex crosscutting relations between veins.
4R	1	10-15	2-3	9	219	basalt	0	0	0	0/0	1/0	
4R	1	15-30	4-5	9	219	basalt	0	0	0	3/1	3/0	Cm-sized veins filled by microcrystalline disintegrated piece.
4R	1	30-37	6-7	9	219.2	basalt	0	0	0	1/1	2/0	Most veins are in the outside surface. Planar veins.
4R	1	37-43	8	9	219.3	basalt	0	0	0	1/1	2-3/0	Fractures along veins. Calcite fibers nearly orthogonal to vein walls.
4R	1	43-80	9	9	219.3	basalt	0	0	0	3/1	3/0	Most of fractures are along veins. Planar to irregular veins.
4R	1	80-93	10-12	9	219.7	basalt	0	0	0	0/0	1/0	Irregular thin veins.
4R	1	93-107	13-16	9	219.8	basalt	0	0	0	1/1	2/0	Overlapping veins with calcite fibers orthogonal to the vein walls. Veins are planar to curvilinear. Some irregular veins.
4R	1	107-114	17	10	219.9	basalt	0	0	0	1/1	1/0	
5R	1	0-7	1-2	10	228.4	basalt	0	0	0	1/1	1/0	One vein on the outside surface.
5R	1	7-17	3-4	10	228.5	basalt	0	0	0	1/1	2/0	Fractures along veins. Planar to curvilinear veins. T-intersections.
5R	1	17-27	5-7	10	228.6	basalt	0	0	0	0/0	1/0	Veins in the exposed surface.
5R	1	27-48	8	10	228.9	basalt	0	0	0	3/1	3/0	Curvilinear to irregular vein. Calcite-veins cut clay-veins. Calcite fibers are orthogonal to the vein walls. Chilled margin and edge of interpillow breccia (continuation of piece 9).
5R	1	49-57	9	10	228.9	basalt	0	0	0	3/1	3/0	Highly brecciated. Angular clasts; altered glassy material.
5R	1	57-64	10	10	229	basalt	0	0	0	2/1	1/0	Edge of chilled margin and glassy altered material.
5R	1	64-68	11	10	229	basalt	0	0	0	0/0	0/0	Brecciated material in altered glass.
5R	1	79-92	14-16	10	229.2	basalt	0	0	0	1/1	1/0	Veins on the outside surface.

**NOTE: As a guide to the reader, only the first page of this Appendix is reproduced here. The entire Appendix is given in the CD-ROM (back pocket).**